

Enhancing Wind Energy Assessment and Optimization through Airborne Observations: Insights from Onshore and Offshore Measurements

DISSERTATION

der Mathematisch-Naturwissenschaftlichen Fakultät
der Eberhard Karls Universität Tübingen
zur Erlangung des Grades eines
Doktors der Naturwissenschaften
(Dr. rer. nat.)

vorgelegt von
KJELL ZUM BERGE
aus Achim

Tübingen
2024

Gedruckt mit Genehmigung der Mathematisch-Naturwissenschaftlichen Fakultät der
Eberhard Karls Universität Tübingen.

Tag der mündlichen Qualifikation: 24.04.2024

Dekan:	Prof. Dr. Thilo Stehle
1. Berichterstatter:	Prof. Dr. Jens Bange
2. Berichterstatter:	Prof. Dr. Stefan Emeis

Licencing

Enhancing Wind Energy Assessment and Optimization through Airborne Observations: Insights from Onshore and Offshore Measurements © 2024 by Kjell zum Berge is licensed under CC BY-NC-ND 4.0. To view a copy of this license, visit <https://creativecommons.org/licenses/by-nc-nd/4.0/>

The two articles „A Two-Day Case Study: Comparison of Turbulence Data from an Unmanned Aircraft System with a Model Chain for Complex Terrain“ and „Seasonal Changes in Boundary-Layer Flow Over a Forested Escarpment Measured by an Uncrewed Aircraft System“ attached to this cumulative dissertation are not part of the overall licence but are licensed under CC-BY 4.0. The article named „Evaluation of Engineering Models for Large Scale Cluster Wakes with the Help of in Situ Airborne Measurements“ also attached to this dissertation is licensed under CC BY-NC-ND 4.0.

Abstract

The expansion of wind energy is set to increase significantly over the next few years. This will lead to challenges both onshore and offshore, such as the influence of wind farms on downstream wind farms in the German Bight or the change of the wind field of wind turbines in complex terrain. This thesis investigates the influence of orography on the wind field in a wind energy test site in the Swabian Alb and the effects of wakes from large wind farm clusters on downstream wind turbines in the German Bight. The measurements carried out with crewed and uncrewed aerial systems (UAS) are also used to validate and compare model data.

Complex terrain, such as small hills or the edges of slopes, changes the flow considerably. Above the highest point of the obstacle, there is an increase in wind speed, known as a speed-up. In addition, recirculation zones can form downstream of the elevation. Both of these often lead to strong shear (turbulence) at the boundary between the flow that is accelerated by the slope and the flow that is slowed down below it. The lower part of modern wind turbines is usually located in this height range. The roughness of the slope surface also has an effect. For example, if the slope is overgrown with forest, this will further increase turbulence and flow velocity and therefore affect the yield and life time of wind turbines in such areas. In this work, flight measurements with the UAS MASC-3 (Multi-Purpose Airborne Sensor Carrier, Version 3) are presented to analyse the wind field over a 200 m high slope and compared with a model chain consisting of a WRF (Weather Research and Forecast) model and an openFOAM (Open Source Field Operation and Manipulation) model. The results show that there is a significant increase in wind speed over the highest point of the west-facing slope, in the area of the future research wind turbines (FWEA). The resulting shear also increases the turbulent kinetic energy (TKE) at the lowest measurement heights many times compared to the undisturbed flow at 200 m above ground. The seasonal influence, i.e. the presence or absence of foliage cover on the slope, is clearly evident. Both velocity and TKE are higher in summer. The model chain simulated the wind field above the slope edge in two case studies with good agreement.

Based on flight measurements with the crewed aircraft D-IBUF of the TU Braunschweig over the German Bight to investigate the wake effects of large wind farm clusters and their influence on downstream wind farms, the industrial model FOXES (Farm Optimisation and eXtended yield Evaluation Software) is compared in different configurations. The measurement results show clearly pronounced wake effects under stable atmospheric conditions. In comparison, the simulation results show good results in the immediate vicinity downstream of the wind farm clusters. The model quality decreases with increasing distance to the wind farms.

Zusammenfassung

Der Ausbau der Windenergie wird in den nächsten Jahren stark zunehmen. Dies führt sowohl onshore als auch offshore zu Herausforderungen, wie z.B. dem Einfluss von Windparks auf nachgelagerte Windparks in der Deutschen Bucht oder der Veränderung des Windfeldes von Windenergieanlagen (WEA) in komplexem Gelände. Diese Dissertation untersucht den Einfluss der Orographie auf das Windfeld in einem Windenergie-Testfeld auf der Schwäbischen Alb und die Auswirkungen von Nachläufen (Wakes) großer Windpark-Cluster auf stromabwärts gelegene Windenergieanlagen in der Deutschen Bucht. Die mit bemannten und unbemannten Luftfahrtsystemen (UAS) durchgeführten Messungen werden zudem genutzt um Modelldaten zu validieren und zu vergleichen.

Komplexes Gelände wie kleine Hügel oder Hangkanten verändern die Strömung erheblich. Über dem höchsten Punkt des Hindernisses kommt es zu einer Erhöhung der Windgeschwindigkeit, dem so genannten Speed-Up. Außerdem können sich Rezirkulationszonen stromabwärts der Erhebung bilden. Beides führt häufig zu starker Scherung (Turbulenz) an der Grenze zwischen der beschleunigten Strömung durch den Hang und der langsamen Strömung darunter. In diesem Höhenbereich befindet sich meist auch der untere Teil moderner Windkraftanlagen. Einen weiteren Einfluss hat die Rauigkeit der Hangoberfläche. Ist der Hang z.B. mit Wald bewachsen, erhöht dieser die Turbulenz und die Geschwindigkeit der Strömung weiter und hat somit auch Einfluss auf den Ertrag und die Lebensdauer von Windkraftanlagen in solchen Gebieten. In dieser Arbeit werden Flugmessungen mit dem UAS MASC-3 (Multi-Purpose Airborne Sensor Carrier, Version 3) zur Analyse des Windfeldes über einem ca. 200 m hohen Hang vorgestellt und mit einer Modellkette bestehend aus einem WRF (Weather Research and Forecast) Modell und einem openFOAM (Open Source Field Operation and Manipulation) Modell verglichen. Die Ergebnisse zeigen, dass über dem höchsten Punkt des nach Westen ausgerichteten Hanges, im Bereich der zukünftigen Forschungswindenergieanlagen (FWEA), eine deutliche Erhöhung der Windgeschwindigkeit vorliegt. Die daraus resultierende Scherung erhöht auch die turbulente kinetische Energie (TKE) in den untersten Messhöhen um ein Vielfaches im Vergleich zur ungestörten Strömung in 200 m über Grund. Der jahreszeitliche Einfluss, d.h. die Belaubung bzw. Nichtbelaubung des Waldes am Hang, ist deutlich zu erkennen. Sowohl Speed-Up als auch TKE sind im Sommer stärker erhöht. Die Modellkette simulierte das Windfeld über der Hangkante in zwei Fallstudien mit guter Übereinstimmung.

Basierend auf Flugmessungen mit dem Forschungsflugzeug D-IBUF der TU Braunschweig über der Deutschen Bucht zur Untersuchung der Nachläufe von großen Windpark-Clustern und deren Einfluss auf nachgelagerte Windparks wird in dieser Arbeit das Industriemodell FOXES (Farm Optimization and eXtended yield Evaluation Software) in verschiedenen Konfigurationen verglichen. Die Messergebnisse zeigen deutlich ausgeprägte Nachläufe bei stabilen atmosphärischen Bedingungen. Im Vergleich dazu zeigen die Simulationsergebnisse gute Übereinstimmung im Nahbereich stromabwärts der Windparkcluster. Mit zunehmender Entfernung nimmt die Modellgüte ab.

Contents

1	List of Publications	1
1.1	Peer-reviewed publications, first author	1
1.2	Peer-reviewed publications, co-author	1
1.3	Conference contributions	2
2	Introduction	3
2.1	Atmospheric Boundary Layer	7
2.2	Turbulence in the ABL	9
2.2.1	The ABL and Flow Regimes over Complex Terrain	10
2.2.2	The ABL and Flow Regimes over the Sea	12
2.3	Wind Energy in Complex Terrain and Offshore	13
2.4	Airborne Measurements in the ABL	14
2.4.1	MASC-3	16
2.4.2	D-IBUF	17
2.5	Open Questions and Objectives	17
3	Results	19
3.1	Publication I	19
3.2	Publication II	24
3.3	Publication III	28
4	Discussion	31
5	Future Perspectives	35
A	Peer-reviewed first-author publications	43
A.1	Publication I	44
A.2	Publication II	71
A.3	Publication III	95

Chapter 1

List of Publications

This thesis is showcased as a consolidated compilation of three peer-reviewed publications. All three manuscripts have either already been published or are scheduled for publication in peer-reviewed journals in the near future.

1.1 Peer-reviewed publications, first author

- I **zum Berge K.**, Schoen M., Mauz M., Platis A., van Kesteren B., Leukauf D., El Bahlouli A., Letzgus P., Knaus H. and Bange J. (2021) A Two-Day Case Study: Comparison of Turbulence Data from an Unmanned Aircraft System with a Model Chain for Complex Terrain, *Boundary-Layer Meteorology* 180, 53–78
- II **zum Berge K.**, Gaiser A., Platis A., Knaus H. and Bange J. (2023) Seasonal Changes in Boundary-Layer Flow Over a Forested Escarpment Measured by an Uncrewed Aircraft System, *Boundary-Layer Meteorology* 186, 69-91
- III **zum Berge K.**, Centurelli G., Dörenkämper M., Platis A. and Bange J. (2024) Evaluation of Engineering Models for Large Scale Cluster Wakes with the Help of in Situ Airborne Measurements, *Wind Energy under review, 2nd round*

1.2 Peer-reviewed publications, co-author

- Rautenberg A., Schön M., **zum Berge K.**, Mauz M., Manz P., Platis A., van Kesteren B., Suomi I., Kral S.T. and Bange J. (2019), The Multi-Purpose Airborne Sensor Carrier MASC-3 for Wind and Turbulence Measurements in the Atmospheric Boundary Layer, *Sensors* 19
- El Bahlouli A., Rautenberg A., Schön M., **zum Berge K.**, Bange J. and Knaus H. (2019) Comparison of CFD Simulation to UAS Measurements for Wind Flows in Complex Terrain: Application to the WINSENT Test Site, *Energies* 12
- Leukauf D., El Bahlouli A., **zum Berge K.**, Schön M., Knaus H. and Bange J. (2019) The impact of a forest parametrization on coupled WRF-CFD simulations during the passage of a cold front over the WINSENT test-site, *Wind Energy Science, Preprint*

- El Bahlouli A., Leukauf D., Knaus H., Platis A., **zum Berge K.** and Bange J. (2020) Validating CFD Predictions of Flow over an Escarpment Using Ground-Based and Airborne Measurement Devices, *Energies* 13
- Schulz-Stellenfleth J., Emeis S., Dörenkämper M., Bange J., Canadillas B., Neumann T., Schneemann J., Weber I., **zum Berge K.**, Platis A., Djath B., Gottschall J., Vollmer L., Rausch T., Barekzai M., Hammel, J., Steinfeld G. and Lampert A. (2022) Coastal impacts on offshore wind farms – a review focussing on the German Bight area, *Meteorologische Zeitschrift* 31
- Schoen M., Suomi I., Harm-Altstädter B., van Kesteren B., **zum Berge K.**, Platis A., Wehner B., Lampert A. and Bange J.(2022) Case studies of the wind field around Ny-Ålesund, Svalbard, using unmanned aircraft, *Polar Research* 41

1.3 Conference contributions

- **zum Berge K.**, Schön M., Rautenberg A., Mauz M. and Bange J., Using airborne measurements to investigate the impact of mast structures on its sonic measurements, EMS Annual Meeting, 3–7 September 2018, Budapest, Hungary
- **zum Berge K.**, Schön M., Rautenberg A., Mauz M. and Bange J., In-situ wind measurements over complex terrain using an UAS, DACH Meteorologentagung, 18–22 March 2019, Garmisch-Partenkirchen, Germany
- **zum Berge K.**, Schön M., Rautenberg A., Mauz M. and Bange J., In-situ wind measurements over complex terrain using an UAS, ISARRA Meeting, 15–19 Juli 2019, Lugo, Spain
- **zum Berge K.**, Schön M., Rautenberg A., Mauz M. and Bange J., In-situ wind measurements over complex terrain using an UAS, EMS Annual Meeting, 9–13 September 2019, Kopenhagen, Denmark
- **zum Berge K.**, Platis A., Schön M., Savvakis V., Büchau Y., Bange J., Hochschild V., Braun A., Mauz M., Warth G., Hager K., Geske F., Schlettig C. and Anger M., UnLuBW - Pollutant monitoring through technological development of UAS applications, EMS Annual Meeting 4–9 September 2022, Bonn, Germany
- **zum Berge K.**, Platis A., Mauz M., Geske F. and Bange J., Air Quality Measurements within Cities using a Multirotor System, ISARRA Meeting, 1–4 August 2023, Bergen, Norway
- **zum Berge K.**, Platis A., Mauz M., Geske F. and Bange J., Air Quality Measurements within Cities using a Multirotor System, AK Klima Konferenz, 12–14 October 2023, Tübingen, Germany

Chapter 2

Introduction

Climate change is making it increasingly clear that humans need to switch to non-fossil, renewable energies. In addition to solar energy, this also includes wind energy as one of the main drivers of the energy transition in Germany and around the world. The switch to renewable energy sources is in full swing and will continue to be driven forward. The German government, like other EU countries, is planning to reduce net greenhouse gas emissions to zero. Figure 2.1 shows a clear trend of reducing greenhouse gas emissions in the European Union (EU) in the last 30 years. Projections with current measures and even additional measures are still failing to reach targets of 55% less emissions in the year 2030 and 0 net emission in the year 2050 for Europe.

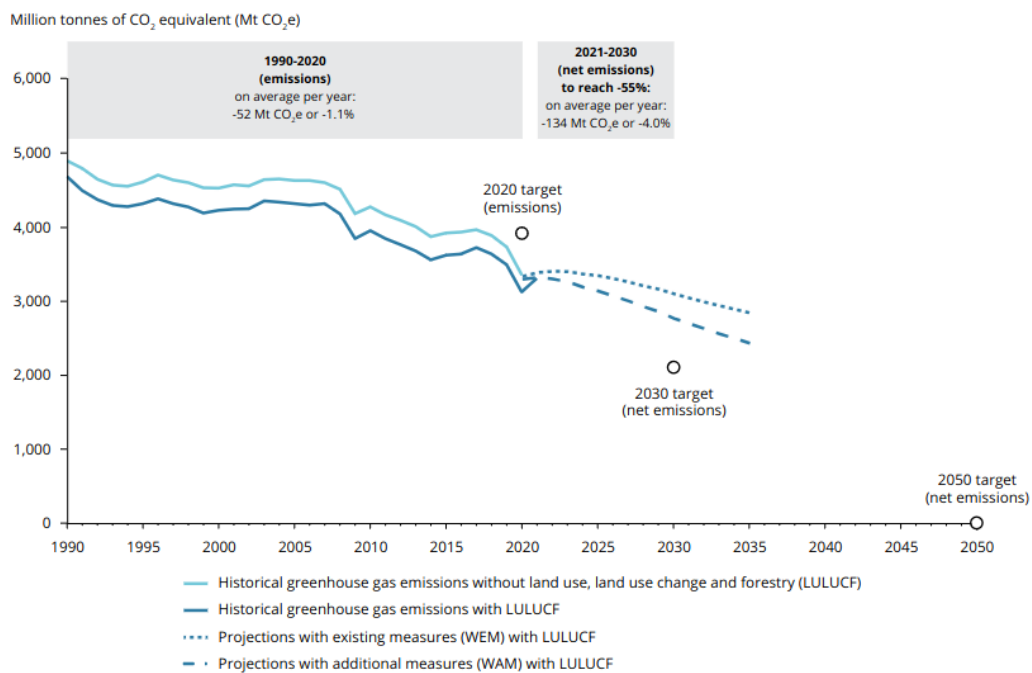


Figure 2.1: Development of the GHG emissions since 1990 without land use, land use change and forestry (LULUCF) shown as a solid light blue line and with LULUCF shown as a solid dark blue line. The dashed lines indicate two different future scenarios with existing measures (dotted line) and additional measures (dashed line). The black dots show the target emissions for the years 2020, 2030 and 2050. Source: European Environment Agency (2022)

Measures to reach these goals in Germany are among other things a strong focus on wind energy built up on- and offshore. Germany's share of renewable energies was ever increasing over the last years being now the biggest portion of energy production. Figure 2.2 illustrates the growth of renewable energies in Germany from 1990 to 2022. The gross electricity generation grew from 20 TWh in 1990 to more than 250 TWh in 2022 while other energy sources like coal and nuclear decreased. Especially nuclear power sources are not producing any power from 2023 on. This and the decline in other power sources has to be intercepted by renewable energy sources.

Renewable energy production today is mainly driven by wind and solar power. These are also the only two areas that have seen strong growth in recent years. Other energy sources, such as hydropower and energy from biomass, have reached their maximum yield due to limited space for large hydroelectric power plants and crops for biomass (Umweltbundesamt 1996). The potential for renewable energy expansion in Germany therefore lies in solar and wind energy.

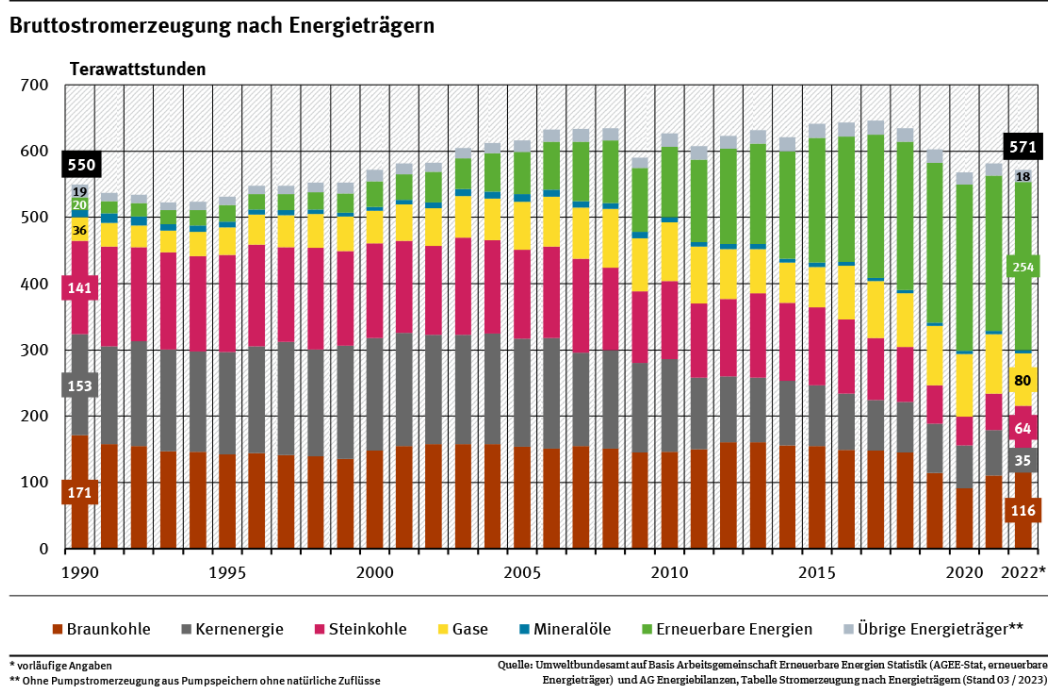


Figure 2.2: Gross electricity generation in Germany broken down by energy source in the years 1990 to 2022. Source: Umweltbundesamt - Arbeitsgemeinschaft Energiebilanzen (2023)

Wind energy can be divided into two areas: Onshore and Offshore. Onshore wind energy expanded strongly, especially until the 2010s, but since then the number of new installations has stagnated somewhat. At the same time, the expansion of wind energy in the North and Baltic Seas has increased. However, there has been no significant growth since 2018. Onshore, there are several reasons for this stagnation. Wind turbines, or even entire wind farms on land, often have space problems. Germany is a densely populated country with

a lot of agricultural land. Lack of public acceptance, nature conservation and the need for space are therefore the main reasons for land-based installations. As a result, potential sites for wind turbines are often located in mountainous, complex terrain that cannot be used for agriculture or settlement. This type of terrain poses problems such as access to construction sites or increased loads on turbine structures due to increased turbulence (Emeis 2018). However, it can also lead to a higher yield of wind energy due to higher wind speeds and therefore more time where the turbine runs within its designated power range. To evaluate the problems and opportunities of wind energy sites in complex terrain and to validate and improve numerical models for such sites, measurements are essential. Section 2.3 gives more details about the challenges and positive aspects of wind energy in complex terrain and why measurements are important.

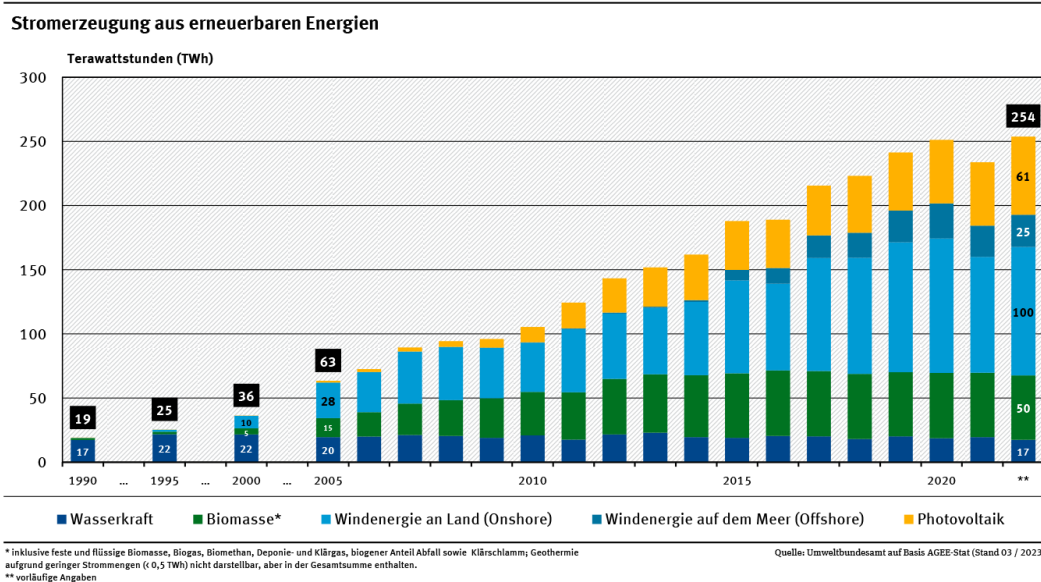


Figure 2.3: Energy production from renewable energies in Germany in the years 1990 to 2022. Source: Umweltbundesamt - Arbeitsgemeinschaft Energiebilanzen (2023)

Offshore in the North and Baltic Sea the main concerns are space and installation costs. The spatial development plan for the Exclusive Economic Zone in the German Bight provides for the expansion of offshore wind energy in the North Sea, as shown in Figure 2.4. With the prevailing wind direction from the south-west, some of the newly planned and existing wind farm clusters are located in the lee of other wind farm clusters. This shading can reduce the yield of the downstream wind turbines by up to 30% (Vollmer et al. 2023). The distances between individual wind farms are sometimes less than 10-20 km. Studies using research aircraft and satellite data have shown that under stable atmospheric conditions, the wake, an area of reduced wind speed in the lee of wind farm clusters, can be up to 70km long (Platis et al. 2021). And even at these distances, wind speed reductions can still be expected, reducing the output of the wind turbines (Platis et al. 2018).

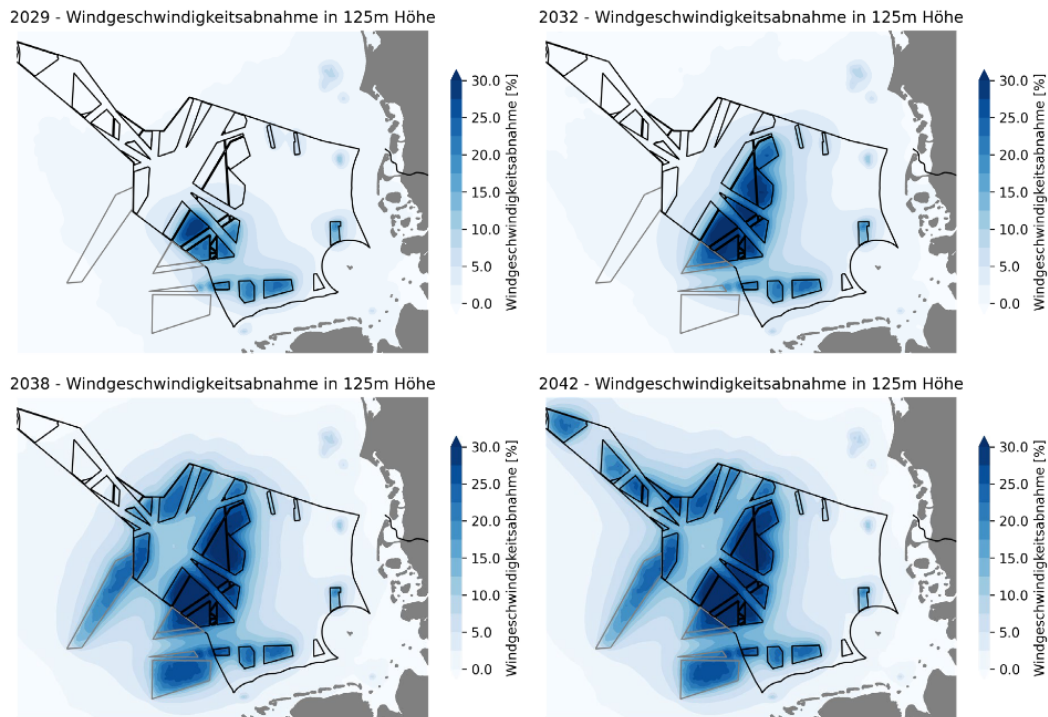


Figure 2.4: *The decrease in average wind speed in the German Bight as a result of the expansion status in specific years. Source: Vollmer et al. (2023)*

The results shown in the following chapters of this thesis consist of three publications in the field of high-resolution wind measurement in complex terrain using small uncrewed aerial vehicles (zum Berge et al. 2021, zum Berge et al. 2022) and over the German Bight behind offshore wind farm clusters using a crewed research aircraft (zum Berge et al. 2024). For wind energy applications it is important to know the ambient conditions of the locations for planned wind turbines. This applies for onshore as well as for offshore turbines. The parameters to be analysed and the scope of the measurement area to be covered differ in the two scenarios. When determining the wind field over the open sea, significantly larger areas need to be covered, as in most cases entire wind farms or even wind farm clusters are to be set up here. On land and especially in mountainous and complex terrain, the size scales are significantly smaller. For this reason, it makes sense to use smaller aircraft for measurements. Small automatic flying measurement platforms such as the Multi-Purpose Airborne Sensor Carrier Version 3 (MASC-3; Rautenberg et al. 2019) allow the wind field to be measured on a fine scale and at very low altitudes above ground. This enabled measurements of the flow over a slope edge on the Swabian Alb at the WINSSENT (Wind Science and Engineering Test Site in Complex Terrain) wind energy test site with regard to wind speed increase due to the orography and subsequent validation of a model chain for complex terrain in the first publication. The second publication built on these results and used further measurement flights in summer and winter, i.e. with and without foliage of the forest on the slope, to draw conclusions about a seasonal difference in the overflow of the slope

edge. The third publication investigated the interaction among wind farm clusters situated in the German Bight region, employing the research aircraft D-IBUF from the Technical University of Braunschweig. The primary focus was on evaluating multiple engineering model configurations against aircraft-derived data, employing innovative methodologies for utilizing wind farm production data. This entailed accounting for advection time across the extensive domain under examination and validating various engineering model calibrations using a mesoscale model.

The following sections give a broad overview of what the ABL (Atmospheric Boundary Layer) is, how it behaves over complex and maritime regions, how the quantities in the ABL are measured using airborne systems, and a brief explanation of second-order statistics to give the reader a basic background for understanding the three publications.

2.1 Atmospheric Boundary Layer

The Earth's atmosphere is a complex and dynamic system consisting of several distinct layers. A crucial region where the atmosphere interacts with the Earth's surface is known as the Atmospheric Boundary Layer (ABL). The ABL is a critical component in meteorology, playing a significant role in various environmental processes, weather patterns, and air quality. It is the lowest part of the Earth's atmosphere, extending from the Earth's surface up to an altitude where its properties differ significantly from those above, typically to 1000-3000 m above the surface. This layer is characterized by a dynamic and turbulent exchange of energy, momentum, and mass between the Earth's surface and the overlying atmosphere at a timescale of one hour or less (Stull 1988). The effective exchange between the Earth's surface and the atmosphere is significantly influenced by the stratification of the boundary layer. Consequently, obtaining comprehensive details about the vertical and horizontal structure of the atmospheric boundary layer (ABL), particularly in terms of temperature, humidity, wind, and their turbulent variations, is essential for a thorough understanding of the associated exchange mechanisms. In the ABL three different stratifications types are possible. Several factors contribute to the development of thermal stratification in the ABL. These include solar radiation, surface properties, humidity, and synoptic-scale weather patterns. Understanding the intricate relationships among these factors is crucial for accurately predicting and modeling the evolution of the ABL's thermal structure.

Stable stratification occurs when a layer of cool, dense air is situated near the Earth's surface, suppressing vertical motion. This stratification commonly forms during nighttime radiative cooling, leading to the development of a stable boundary layer. The inhibition of vertical mixing and turbulence during stable stratification has significant implications for air quality and the dispersion of pollutants.

Conversely, unstable stratification arises when the surface layer becomes warmer than the overlying air. Daytime heating often induces this condition, promoting vertical motion and convective processes. Unstable stratification fosters the development of a well-mixed

boundary layer, characterized by enhanced turbulence, vertical transport, and convective cloud formation.

Neutral stratification occurs when there is minimal or no temperature difference between the surface and the overlying air. This condition is common during transitional periods, such as dawn and dusk. Neutral stratification allows for increased vertical mixing and turbulence, influencing atmospheric dispersion and boundary layer dynamics.

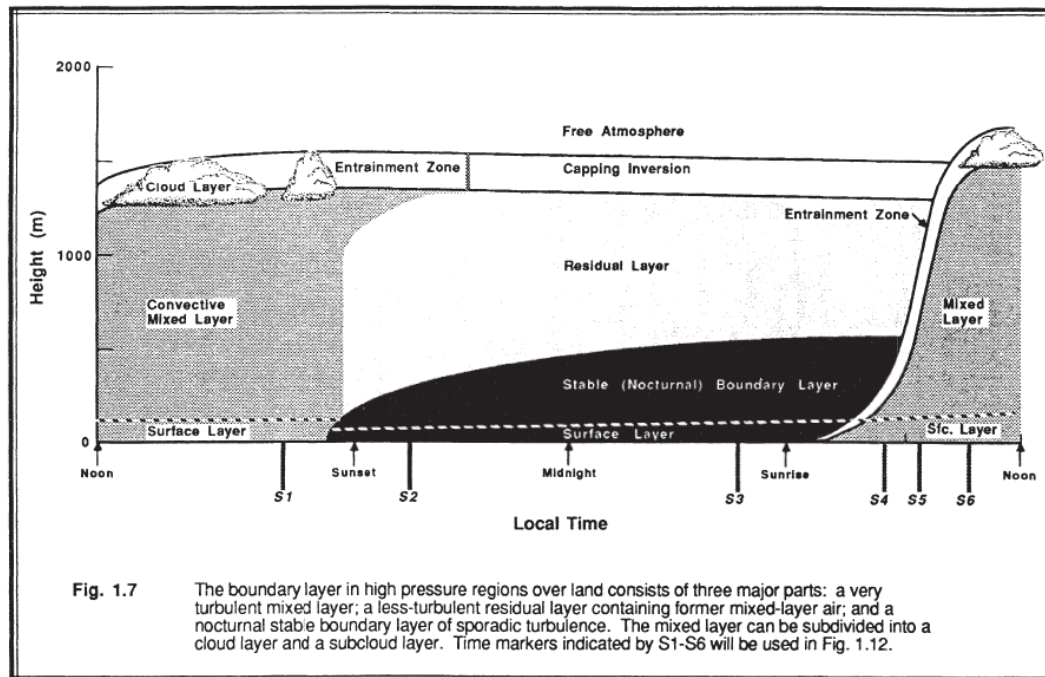


Figure 2.5: *The atmospheric boundary layer in a diurnal cycle. Source: Stull (1988)*

The ABL undergoes distinct diurnal variations, with daytime heating causing increased turbulence and mixing. During the night, the ABL can become stable, limiting vertical motion and leading to the development of a nocturnal boundary layer. This scheme is depicted by Figure 2.5.

Over land and under a high pressure system, the shown diurnal cycle can develop. The separate stages of the diurnal cycle are explained as follows.

Nighttime radiative cooling sets in in the early evening to late night time. As the sun sets, the Earth's surface begins to lose heat through radiative cooling. The ground emits infrared radiation, causing the surface temperature to decrease. This cooling effect is most pronounced during the early to light night hours. Towards the early morning hours the radiative cooling leads to a development of stable stratification near the surface, characterized by a decrease in turbulent mixing and vertical motion. It is possible that a temperature inversion occurs, trapping cool air near the surface and leading to the accumulation of pollutants. When the sun rises, solar radiation begins to warm the Earth's surface beginning the morning transition, marking the period when the atmosphere transitions from stable to neutral or slightly

unstable conditions. Vertical mixing increases, and the boundary layer starts to deepen. As solar heating continues, the boundary layer becomes convectively unstable. Turbulent mixing intensifies, and thermals form as warm air rises from the surface. Cloud formation may occur in response to convective processes, leading to the development of cumulus clouds. During the afternoon the peak of daytime heating typically occurs, maximum temperatures are reached as solar radiation input surpasses radiative cooling. As the sun starts to set, the energy input decreases, leading to a reduction in surface heating. The boundary layer gradually stabilizes, convective processes diminish, and radiative cooling resumes. The atmosphere transitions back to stable conditions, and the boundary layer begins to cool. The cycle repeats, with the atmosphere becoming more stable during late evening and early night.

2.2 Turbulence in the ABL

Atmospheric turbulence, a complex and dynamic phenomenon, manifests in the Atmospheric Boundary Layer (ABL) with significant implications for diverse atmospheric processes. Turbulence in the ABL spans a spectrum of spatial and temporal scales, from small-scale microturbulence to larger-scale phenomena influencing the overall mixing and transport of atmospheric properties. Convective turbulence, driven by buoyancy-induced instabilities, and mechanical turbulence, generated by surface roughness and obstacles, are key mechanisms shaping ABL turbulence. Additionally, shear-induced turbulence arises from wind speed variations with height. Pioneering contributions by Richardson (2007) and Kolmogorov (1941) have profoundly advanced our understanding of turbulence. Kolmogorov, in particular, proposed a universal scaling law for the energy spectrum in isotropic turbulence, offering insights into the cascade of energy from larger to smaller scales. The so-called inertial subrange is the range of scales in a turbulent flow where the transfer of energy occurs primarily through inertial forces rather than viscous forces. In the inertial subrange, turbulent eddies are characterized by a balance between the inertial forces that drive the cascade of energy from larger to smaller scales and the viscous forces that dissipate the energy at the smallest scales. The energy spectrum exhibits a power-law behavior, known as the Kolmogorov -5/3 law in three-dimensional isotropic turbulence. This power-law scaling describes the relationship between the turbulent kinetic energy and the spatial scale of the fluctuations within the inertial subrange.

The turbulence kinetic energy, denoted as k , represents the average kinetic energy per unit mass attributed to eddies within a turbulent flow. It is calculated by using the velocity fluctuations of the mean flow from the variance Var or its square root, the standard deviation (σ) of the three wind components (u, v , and w).

$$k = \frac{1}{2}(\text{Var}_u + \text{Var}_v + \text{Var}_w) = \frac{1}{2}(\sigma_u^2 + \sigma_v^2 + \sigma_w^2). \quad (2.1)$$

The variance (Var) of a variable X is calculated, using Reynolds decomposition where the

fluctuations X' are separated from the mean, with

$$\text{Var}_X = \frac{1}{N-1} \sum_{i=1}^N (X_i - \bar{X})^2. \quad (2.2)$$

These statistical moments (k, VAR) are used to describe the turbulence structure and processes in the ABL and how complex terrain (Sec. 3.1 and Sec. 3.2) or artificial structures like wind turbines change the flow (Sec. 3.3).

2.2.1 The ABL and Flow Regimes over Complex Terrain

Depending on where you look at the atmosphere, the ABL can differ in vertical expansion, degree of turbulence, thermal effects and other parameters. The basic observation is based on a flat surface over land. If the ABL is observed over complex mountainous terrain, the orography plays a decisive role. It deflects the flow in a vertical and horizontal direction, leading to changes in wind speed, direction, and turbulence. These flow disruptions can result in the formation of eddies, vortices, and localised wind patterns, which significantly impact the vertical and horizontal transport of momentum, heat, moisture, and pollutants.

Flow over hills or mountains is an area of research that has been studied for several decades. Jackson and Hunt (1975) and Finnigan (1988) have developed analytical models that represent the flow over certain types of hills. The so-called fractional speed-up ΔS at the highest point of a symmetrical hill (Jackson and Hunt 1975) plays an important role in analyzing such flows. It is determined by $U(x, z)$ as the wind profile U over height z at the point x , which is the lateral distance between the profile above the apex and the undisturbed wind profile U_B upstream:

$$\Delta S(x, z) = \frac{U(x, z) - U_B(z)}{U_B(z)}. \quad (2.3)$$

The speed-up on low altitudes, depending on the shape of the hill, creates a separation bubble where the flow can reverse direction (Finnigan et al. 2020). The area between the reversed flow and the accelerated flow of the updraft creates shear and therefore increased turbulence. These models define the shape of the hill by the hill length L and the hill height H and always define ideal hills with symmetrical slopes and a smooth shape. Such mounds are very rare in the real world, making the flow over them difficult to determine analytically. In order to calculate loads and determine the potential yield of wind turbines in the speed-up, it is important to simulate using numerical models or measure the flow in order to make a well-founded statement about the influence of the terrain in front of the turbines. If the hill is covered with a canopy, the flow structure gets even more complex: Low wind speeds within the canopy, but a speed-up directly above the canopy that is located at the crest of the hill. The wind speeds then also depend on the type of canopy. Are there mainly bushes and small trees like in the Askervein Hill experiment by Taylor and Teunissen (1987) or does

the canopy consist of mainly large trees? Are the trees deciduous trees or coniferous trees? Does the foliage start at ground level or higher up at the trunk? All these factors together with the hill shape and the surrounding orography have an impact on the local flow field. Finnigan et al. (2020) compared two model results for a symmetric hill with a uniform canopy. Figure 2.6 shows the results of two analytical models by Finnigan and Belcher (2004) and Hunt et al. (1988) to analyse the flow over a symmetrical Gaussian hill covered by a uniform canopy. The modified flow over the ridge in (a) and (b) shows the acceleration of the two models (solid and dashed lines) compared to the wind speed profile of the flow without the hill. The perturbations in (b) show the complexity of the flow within the canopy sublayer and the modified flow due to the hill. These flow features are valid for idealised hills, but become more complex in real scenarios with different hill shapes and canopies.

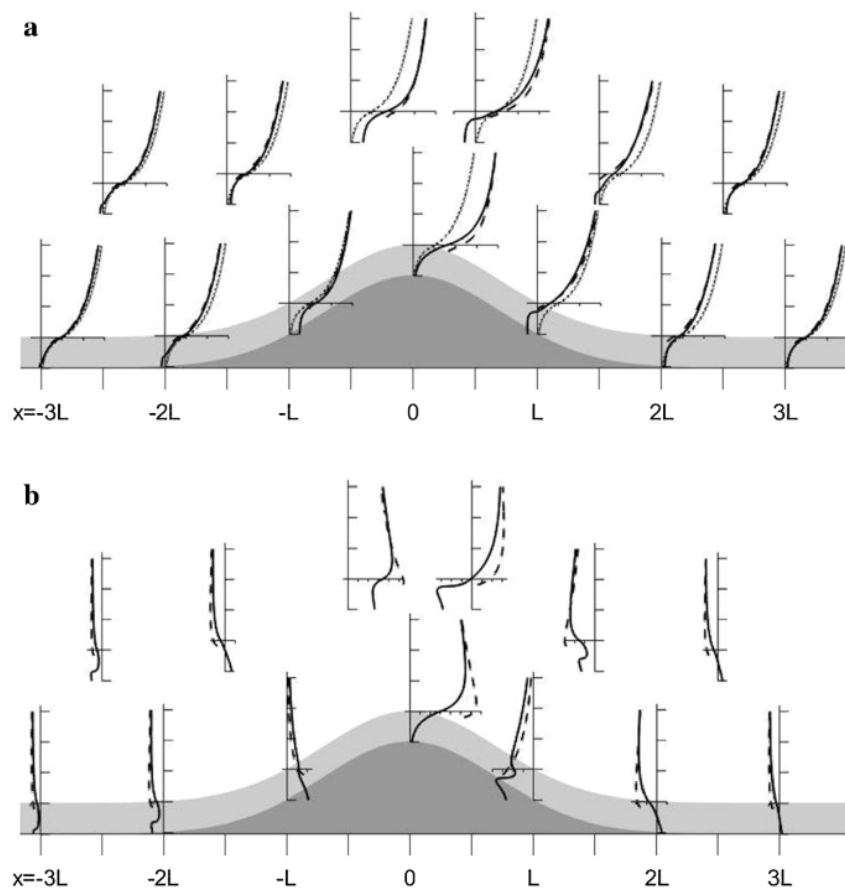


Figure 2.6: Profiles of wind speed (a) and stream-wise velocity perturbations (b) above a Gaussian hill covered with a canopy. Source: Finnigan et al. (2020)

In addition to orographically induced changes in flow direction and velocity, differences in elevation and steep slopes mean that the ground is heated differently by incoming radiation, as some areas are in the shade for longer. This leads to differences in the vertical mixing of the lower atmosphere and favours the development of thermally driven circulations, such as valley, slope (e.g., Zardi and Whiteman 2012) or mountain plain winds (e.g., Jackson et al. 2018, Serafin et al. 2018, Zardi and Whiteman 2012). These circulations can enhance

vertical mixing, affect cloud formation and change local weather patterns.

2.2.2 The ABL and Flow Regimes over the Sea

Over the ocean, the MBL (Marine Boundary Layer) tends to be shallower because the sea surface has a higher thermal inertia compared to land, leading to a relatively stable temperature profile near the surface. This stability suppresses vertical mixing and turbulence, resulting in a shallower boundary layer. The MBL typically reaches heights of a few hundred meters. This is of course dependent on other factors like wind patterns and the presence of coastal features.

The wind speed over the open sea is stronger, more consistent and less turbulent than over land. This is due to two factors: The low surface roughness of the sea in the order of 10^{-4} m and the more consistent sea surface temperature (SST) due to the much higher heat capacity of a large body of water (Emeis 2018).

The surface roughness of water was described by Charnock (1955) as

$$z_0 = \alpha \frac{u_*^2}{g}, \quad (2.4)$$

with the Charnock parameter α for the open sea with 0.011 after Smith (1980), gravitational acceleration g and the friction velocity u_* . With low surface roughness the wind speed is higher and the vertical gradient in wind speed is low resulting in less shear. Another source for turbulence is buoyancy. Due to the high heat capacity and the vertical circulation of the water, low temperature changes of the sea surface are present during diurnal cycles. This limits the development of large eddies and reduces the turbulence when compared to land surface (Bodini et al. 2019a). An exception to this are conditions in coastal regions where the wind blows from the land advecting warmer or colder air over the water. This effect is seen in annual variations rather than in diurnal variations. An unstable marine boundary layer is more likely in autumn and early winter while a stable boundary layer is more likely in spring and early summer (Emeis 2018, Shaw et al. 2022). These effects of altering the boundary layer are only valid for coastal regions to an extent of up to 50 km for warmer air from land advected over colder water causing a stable thermal stratification, and only a few kilometres for colder air blown over warmer water causing an unstable boundary layer. These layers are called internal boundary layers (IBL) as they form within the MBL due to a change in surface roughness or surface temperature (Emeis 2018). The extent and how strong these layers grow depends on the change in roughness or surface temperature. After a certain distance downstream of the roughness or temperature change, the IBL reaches its maximum extent and becomes indistinguishable from other IBLs. This height is called the blending height and is usually well within the Prandtl layer or constant flux sublayer.

The relative humidity over the sea surface and within the MBL is typically above 70 % (Abraham and Goldblatt 2023). This results nearly always in dryer air above more humid air directly above the sea surface creating upward directed humidity fluxes (Platis et al.

2023). Because the humid air is less dense than dry air at a given temperature, the upward humidity fluxes help in destabilizing the MBL (Sempreviva and Gryning 1996).

2.3 Wind Energy in Complex Terrain and Offshore

In the German Bight offshore wind energy is influenced by strong thermal stratification, with a dependence on wind direction (Platis et al. 2018, Cañadillas et al. 2020, Platis et al. 2022). The stability of the atmosphere in the marine boundary layer (MBL) in the German Bight is often directly linked to advection of warmer air from land over the cold sea surface (Emeis 2018). Hence, southern and south-westerly winds are due to the direct proximity of land masses associated with stable stratification. Conversely, cold air from northern wind directions over warm water tends to create an unstable stratification Emeis 2018.

The spacing between wind farms and turbines within a wind farm must be considered for different wind directions. Closer spacing is feasible for northern wind directions, while for southern and south-westerly wind directions, larger spacing is recommended due to the likelihood of stable stratification and resulting longer wakes (Platis et al. 2020, Vollmer et al. 2023).

Another essential factor affecting wind turbine yield and durability is the boundary layer height and turbulence. The boundary layer height of the MBL is often limited to a few hundred meters and due to less surface roughness and the large water body with its stable temperatures, turbulence is low (Emeis 2018), wind speeds are higher and more consistent with height and in time than over land, resulting in less vertical wind shear and less stress on the turbine structures. This is true for single turbines. The lower turbulence intensity is on the other hand a problem for wind farms built in offshore regions, such as the German Bight, because the kinetic energy provided by vertical turbulent fluxes is much lower (Emeis 2018, Cañadillas et al. 2020, Platis et al. 2021).

Wind energy faces several challenges in complex terrain, which refers to hills, mountains, valleys or escarpments, the so-called “orography”. Other features like trees, buildings or bushes that change the surface properties (e.g., roughness) are here called “topography”. Both are strongly influencing the flow in complex terrain (Jackson and Hunt 1975, Finnigan et al. 2020).

The orography, e.g. an escarpment, changes the approaching flow in terms of wind speed and turbulence. Vertical shear is significantly higher, primarily due to the hill shape (Taylor and Teunissen 1987, Fernando et al. 2019). This increase in turbulence exerts higher loads on wind turbine structures. The area of highest turbulence is at the border of the inner and outer layer where also the maximum speed-up is to be found (Emeis 2018). Depending on the orography dimensions and type (e.g., hill, escarpment or ridge) the inner layer has a different thickness (Finnigan et al. 2020) which places the border to the outer layer at different altitudes above the crest. Modern wind turbines hub heights often exceed this layer of

increased turbulence, which reduces the load and increases the yield as it operates in higher wind speeds. Smaller wind turbines on the other hand can reach into the region of higher turbulence increasing the load and decreasing the lifetime.

Another factor influencing the turbulence and speed-up in complex terrain is the diurnal cycle and the topography. The diurnal cycle introduces additional turbulence due to buoyancy during daytime and prelinenry in summer (Bodini et al. 2019b) and the topography in changing the roughness length. The flow over an escarpment covered with large trees shows even stronger turbulence and speed-up (zum Berge et al. 2021). Depending on the kind of trees, deciduous or coniferous, the wind can flow through the forest or is deflected upwards acting like an extension of the escarpment height, also changing the area of high turbulence and speed-up.

An upside of the increased turbulence around wind energy sites is the downward momentum of the flow, replenishing the energy loss from wind turbines and therefore the distance between turbines and wind parks does not need to be as extensive as offshore (Emeis 2018, Cañadillas et al. 2020, Platis et al. 2021).

These factors and the dependence on the complexity of the region, the application of wind profile laws is not expedient and more advanced tools have to be applied, such as analytical or numerical models. The results from those simulations are typically only applicable for one given site. Measurements at future wind energy sites are often crucial to analyze the wind field and to validate the model results.

Measurements in complex terrain are more challenging when compared to flat homogeneous terrain. Steep slopes make it more difficult to place measurement systems like towers or remote sensing devices. In a country like Germany with its dense population and high agricultural land use (Sec. 2) such slopes, hills and escarpments are among the only places covered with large forests. Large trees are big obstacles for measurement techniques like lidar (Light Detection and Ranging) or sodar (Sound Detection and Ranging) and depending on the setting those are often also only point/vertical measurements and limited in their temporal resolution of the data. The internal assumptions of lidars for their wind vector reconstruction algorithms are based on homogeneous flat terrain, which creates errors in the measurement results (Klaas-Witt and Emeis 2022). UAS are a great way to collect measurement data of the whole wind field (Rautenberg et al. 2019) around a wind turbine location (Mauz et al. 2019) during different meteorological conditions to serve as a validation source or input data for numerical models like LES (Large Eddy Simulation, Letzgun et al. 2022).

2.4 Airborne Measurements in the ABL

Historically, airborne measurements have undergone significant advancements with the evolution of aircraft and measurement technology. Crewed aircraft have played a crucial role in early atmospheric studies (Bemis 1951). The first attempts at airborne wind measurements

can be traced back to the early 20th century when pioneering aviators and scientists began utilizing aircraft to explore the vertical structure of the atmosphere (Bemis 1951). However, these early efforts were constrained by the limited capabilities of both aircraft and measurement instruments.

As technology progressed, crewed aircraft became more sophisticated, enabling more precise and comprehensive wind measurements. The development of specialized instruments, including anemometers and probes such as multi-hole probes or open path analyzers, enhanced the accuracy of wind and gas data collected during atmospheric research missions (Brümmer et al. 2012, Lampert et al. 2020). Crewed research aircraft have since become invaluable tools for atmospheric scientists, providing a platform for conducting in-depth studies of wind patterns, turbulence, and atmospheric phenomena.

In parallel, the emergence of uncrewed aircraft systems (UAS) has opened new opportunities for atmospheric research and wind measurements (Rautenberg et al. 2019). Uncrewed aircraft systems equipped with advanced sensors have proven to be particularly adept at collecting data in challenging environments, such as low altitudes and confined spaces. The integration of modern autopilots further refined the ability of UAS to follow precise flight paths, contributing to enhanced spatial coverage in wind measurement campaigns.

The synergy between crewed and uncrewed aircraft has become increasingly apparent in recent years. While crewed aircraft continue to excel in certain mission scenarios, uncrewed systems offer unique advantages, including cost-effectiveness, reduced operational risks, and the ability to access hard-to-reach locations. This collaborative approach, leveraging the strengths of both crewed and uncrewed platforms, has enriched our understanding of atmospheric dynamics and improved the accuracy of wind measurements across diverse spatial and temporal scales.

The spatial gap between ground stations and ground-based/satellite-based remote sensing is addressed by uncrewed aircraft systems (UAS) equipped with fast and accurate sensors. Unlike crewed research aircraft and radiosondes, UAS can navigate low-altitude and confined spaces with precise flight paths and altitudes, thanks to modern autopilots. Their smaller size and motors contribute to lower disturbance of the atmosphere, but their endurance for measurements is limited.

Crewed and uncrewed aircraft complement each other well in various mission scenarios and applications, but the purchase, operation, and logistics of UAS are comparatively smaller than those of crewed aircraft.

For measuring the 3D wind vector and turbulence, a common method involves using a small five-hole probe, pressure transducers (van den Kroonenberg et al. 2008, Rautenberg et al. 2019), and an inertial measurement unit (IMU). Fast temperature measurements (Wildmann et al. 2013) for flux determination utilize NTC (Negative Temperature Coefficient), finewire thermometers, or semiconductor sensors.

However, measuring the relative humidity of the atmosphere on small UAS poses challenges. Traditional devices like Lyman-Alpha, dew point mirrors, or open path analyzers

are bulky and heavy for UAS. Instead, UAS employ capacitive sensors and in-house developed sensors (Mauz et al. 2020) for humidity measurements, which are lightweight but may have slower response times.

2.4.1 MASC-3

MASC-3 is the third iteration of the Multipurpose Airborne Sensor-Carrier (MASC) of the Environmental Physics group at the University of Tübingen (Rautenberg et al. 2019). This UAS was primarily used in the investigations presented in this thesis. It is a fixed-wing UAS with a wingspan of 4 m and a take-off weight of 6-8 kg, depending on the configuration of the sensor system and the flight battery carried. With the electric pusher motor at the rear of the aircraft, the MASC-3 achieves a flight duration of 1-1.5 hours at a flight speed of 18.5 m s^{-1} . In addition, the rear-mounted motor reduces potential sources of interference from pressure fluctuations and changes in ambient air. The Pixhawk 2.1 autopilot is used to maintain a constant altitude and a precise path above ground. To successfully measure flow conditions and turbulence in particular, the measurement system mounted on the front of the fuselage (Figure 2.7) is equipped with fast analog and digital sensors. These include a five-hole probe with pressure sensors in combination with a precise and fast IMU to measure wind speed, wind direction and turbulence with a temporal resolution of up to 30 Hz. A proprietary FineWire Platinum Resistance Thermometer (FWPRT) is used for fast temperature measurements (Wildmann et al. 2013). Other commercially available sensors for measuring air temperature and water vapour content (Sensirion SHT31) are also available. Sensors such as optical particle counters or gas sensors can also be easily integrated into the measurement system.

The high-resolution measurement data is collected by a Raspberry Pi directly on board the aircraft and made available in low temporal resolution via a downlink to a ground station for observation.



Figure 2.7: *The Multi-Purpose Airborne Sensor Carrier in its 3rd iteration (MASC-3), operated by the University of Tübingen in the left panel (Photo: © Ines Weber) and the Dornier-128 (Do-128) research aircraft D-IBUF (Photo: © Florian Szczepek), operated by the Technical University Braunschweig in the right panel. Source:*

2.4.2 D-IBUF

The Dornier-128 (Do-128) research aircraft from the Technical University of Braunschweig (Lampert et al. 2020) was used over the German Bight to survey the wakes of wind farms and wind farm clusters located close to the coast (Platis et al. 2018, Schulz-Stellenfleth et al. 2022). As this is a crewed aircraft, it can cover large areas over the sea with a flight speed of about 60 m s^{-1} . The Do-128 is equipped with a nose boom containing a variety of sensors for determining meteorological parameters. These include wind, air temperature and humidity with high temporal resolution (Corsmeier et al. 2001). Turbulence, wind direction and wind speed are measured in the same way as on MASC-3, using a five-hole probe, pressure sensors and an IMU. The sensors are mounted in the nose boom to minimise the distance to the engines and thus the pressure fluctuations in the ambient air.

Other sensors, such as a Lidar to measure wave height or temperature sensors to measure surface temperature, can also be accommodated in the fuselage of the research aircraft.

2.5 Open Questions and Objectives

With the increase in wind energy production onshore and offshore, questions arise that can often only be answered through measurements and simulations of the corresponding situation. Due to the increasingly smaller area for the erection of wind turbines on land and the potentially higher yield in complex mountainous terrain, such areas are more frequently proposed for the generation of wind energy. Measurements over flat terrain without strong changes in surface roughness have often been made over the last decades (Kaimal et al. 1972, Højstrup 1999, Shaler et al. 2019). However, little research has been carried out into the effects of flow changes across a slope or similar orographic changes, especially covered with large deciduous trees, on the wind turbines, their structures and the yield (Thomsen 1996, Troldborg et al. 2022).

Additionally, the expansion of wind energy in the open sea is being driven forward worldwide. The German government is planning to greatly expand wind energy generation in the German Bight over the next few years. However, the planned targets pose a problem with regard to the planned areas (Vollmer et al. 2023). In the future scenarios, the wind farms will be located close to each other, which will reduce the yield for wind farms located downwind due to the spreading wakes and the associated reduction of wind speed. This thesis aims to answer the following research questions:

- How does an escarpment (complex terrain) influence the wind field in its vertical structure and downstream of the crest above a plateau?
- What is the difference in boundary layer flow and speed-up above the crest of a forested escarpment in different seasons?
- Are engineering models capable of simulating large scale cluster wakes over very

long distances by comparing the results to aircraft measurements?

The first two questions, relating to measurements by UAS and simulations in complex terrain, are addressed in Chapters 3.1 and 3.2. Chapter 3.3 explores the third question on the simulation of long wind farm cluster wakes with engineering models.

Chapter 3

Results

This section provides a concise outline and summary of the key findings, which are elaborated further in the associated peer-reviewed publications found in Sections 3.1 through 3.3.

3.1 Publication I -

A Two-Day Case Study: Comparison of Turbulence Data from an Uncrewed Aircraft System with a Model Chain for Complex Terrain

The first study dealt with the investigation of the wind field on a slope of the Swabian Alb near the town of Geißlingen an der Steige in south-west Germany. The slope faces west and is, to a large extent, covered with tall trees. A wind energy test field was planned and built on the plateau in the immediate vicinity of the slope edge. The results presented here were used to determine the wind field on and around this planned wind energy test field (<https://www.windfors.de/en/projects/test-site/>). To limit the number of plots, only results from the first day of measurement are shown.

Measurements were carried out with the UAS of type MASC-3 (Sec. 2.4.1) on two consecutive days in September 2018. Wind direction and wind speed were determined with high temporal and spatial resolution in order to characterise the overflow of the slope edge in westerly winds. The resulting wind field was then compared with simulation results from a model chain consisting of a WRF (Weather Research and Forecast) model with coarse resolution and an openFOAM (Open Source Field Operation and Manipulation) model with finer resolution based on the WRF output.

A flight between 20 and 200 m above ground (reference altitude is the starting point on the plateau behind the slope edge) was analysed for both measurement days. The 21st September 2018 was characterised by high wind speeds of 10–14 m s⁻¹ from westerly directions, while the wind speed on 22 September was significantly lower at 5–7 m s⁻¹. The data on wind speed, wind direction and air temperature for the course of the day came from meteorological measuring masts that were already erected and in operation on the wind test field at the time of the flight measurements.

The UAS measurements were carried out repeatedly on the same flight route over the edge

of the slope in altitudes of 20, 30, 40, 50, 60, 80, 100, 120, 160 and 200 m above the plateau. Due to the more densely staggered measurement heights of the UAS at low altitudes above ground, the flow area mainly influenced by the slope (Emeis et al. 1995, Berg et al. 2011) could be analysed in more detail. For statistical significance, each of the flight legs was repeated four times. The vertical sections in Figure 3.1a and 3.4a are interpolated values between each of the flight legs using inverse distance weighted (IDW) interpolation (Lu and Wong 2008).

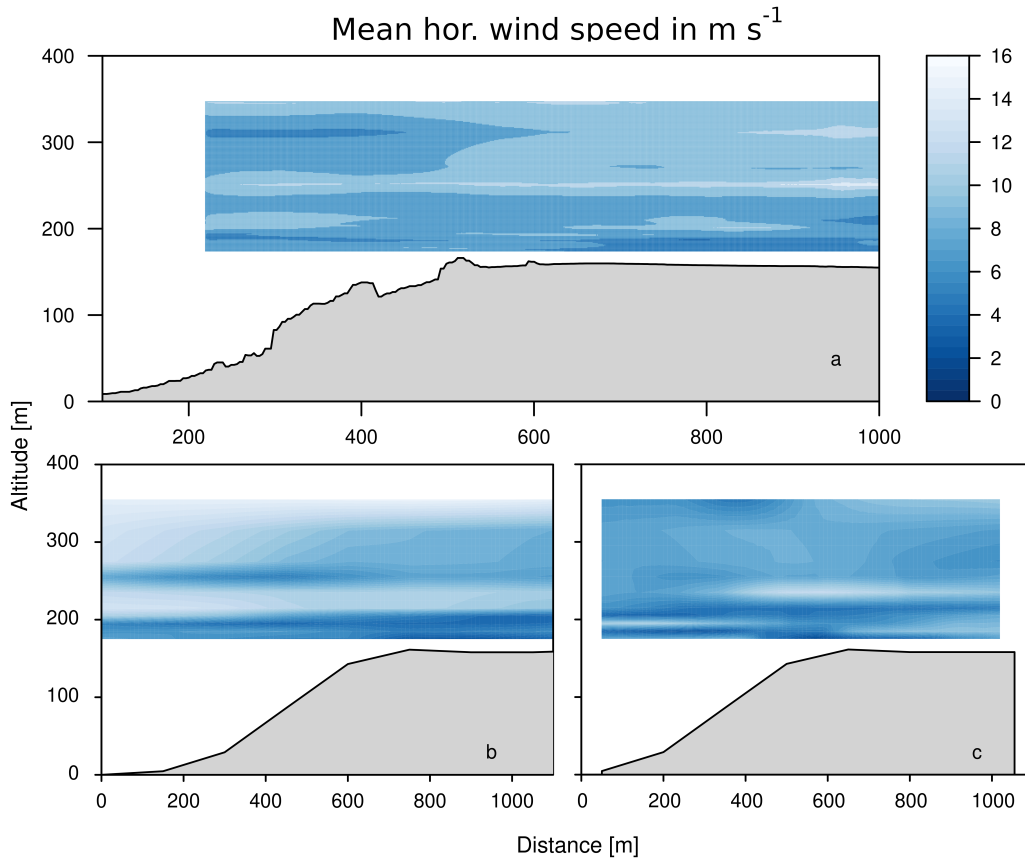


Figure 3.1: Wind speed measurements of a) MASC-3 on 21st of September 2018 between 1055–1229 UTC in heights between 20 and 200 m above ground. Corresponding model results for the same time frame of b) WRF and c) openFOAM. Adapted from zum Berge et al. (2021)

The results of the flight measurements show an increase in flow velocity in the area of the highest point of the slope edge compared to the layers below and above. The range of increased wind speeds is between 40 and 80 m above ground. The intensity of the increase in wind speed depends heavily on the wind direction and the wind speed of the free flow. Even small changes in wind direction can lead to significant changes in the wind field and flow velocity over the slope edge given the prevailing orography. This is due not only to the orography, but also to the forest on the escarpment (Belcher et al. 2012). In westerly

wind directions with a northerly or southerly component, this also changes the distances and gradient angles of the flow along the slope. In the event of prolonged overflow or flow through the forest, this can lead to a reduction in the flow velocity near the ground in the lee of the escarpment.

Figure 3.1 show the UAS measurements of the wind speed in subplot a), the results of the WRF simulation in subplot b) and the results of the openFOAM simulation based on them in subplot c) for the 21st of September 2018. There is good agreement between the measurements and the simulations. The openFOAM model identifies the strengths and areas with increased velocity more precisely, while the WRF model does not give that level of accuracy and only shows a large area with increased flow velocity over the whole length of the plot. The second day showed a similar picture of a speed-up above the crest of the escarpment, but less pronounced due to the generally lower wind speed.

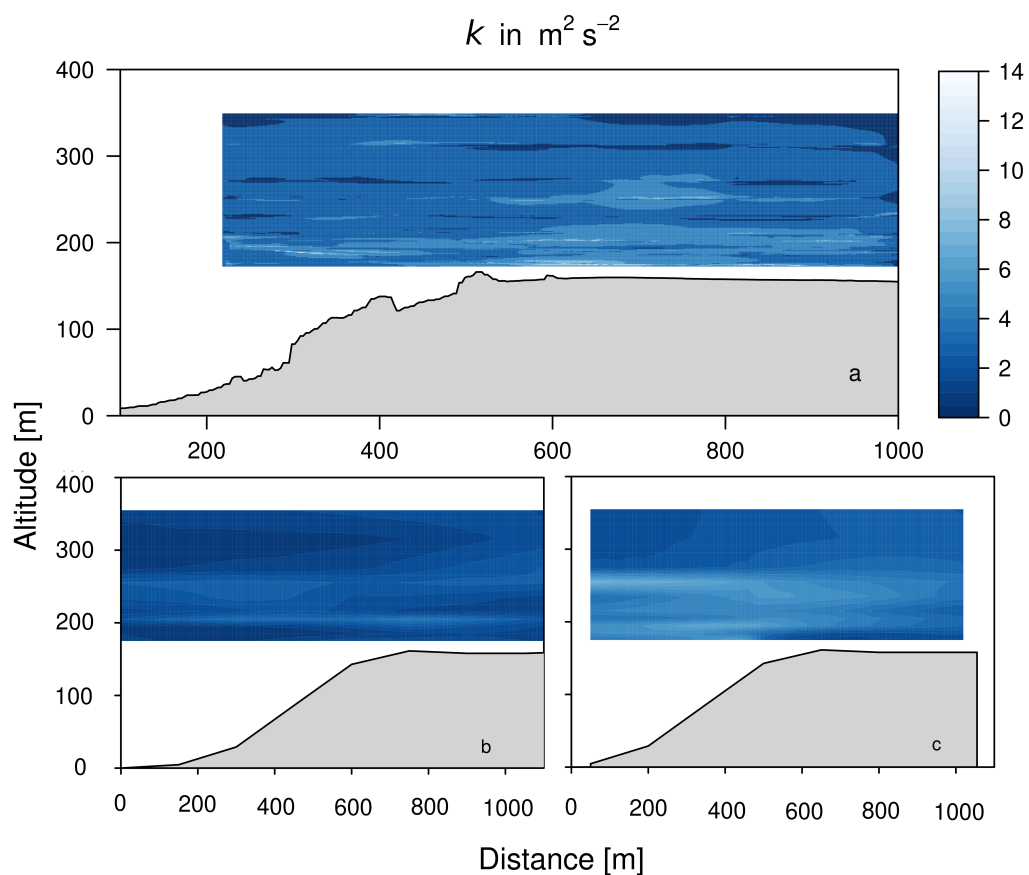


Figure 3.2: *Turbulence kinetic energy measurements of a) MASC-3 on 21st of September 2018 between 1055–1229 UTC in heights between 20 and 200 m above ground. Corresponding model results for the same time frame of b) WRF and c) openFOAM. Adapted from zum Berge et al. (2021)*

In addition to the wind speed, the degree of turbulence, which is expressed in this study by the TKE, is of decisive importance for the yield and service life of wind turbines. The UAS

measurements showed a significantly increased TKE at the lowest measurement heights, just above the canopy, and a lateral extent of several hundred metres above the plateau downstream of the crest (Fig. 3.2). The values reached up to $14 \text{ m}^2 \text{ s}^{-2}$ on 21 September 2018 and thus a multiple of the undisturbed flow at a height of 200 m. This is due to the high wind speeds on this day. The strong shear winds between the slower flow in the lee of the trees and the accelerated air layer directly above lead to a strong increase in the TKE in this area. Both models have problems simulating the TKE. On 22 September 2018, the results compared to the UAS data are better than on 21 September 2018, where both the intensity and the position of the increased TKE do not match the measurements.

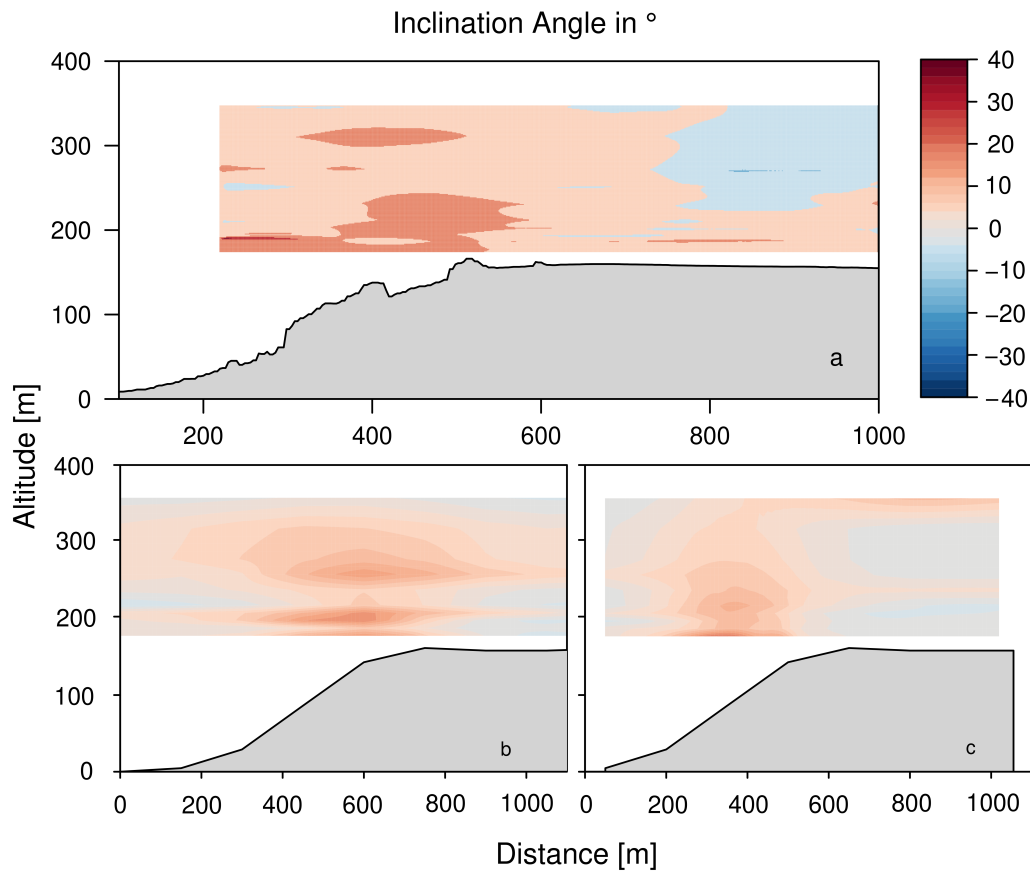


Figure 3.3: *Inclination angle measurements of a) MASC-3 on 21st of September 2018 between 1055–1229 UTC in heights between 20 and 200 m above ground. Corresponding model results for the same time frame of b) WRF and c) openFOAM. Adapted from zum Berge et al. (2021)*

The last variable analysed in this study, which also has a major influence on wind turbines, is the inclination angle (Fig. 3.3). It refers to the angle by which the flow is deflected from the horizontal. If the flow has to overcome an obstacle, the inclination angle becomes positive as the flow is deflected upwards. Behind the obstacle, the inclination angle becomes negative as the air masses flow downwards again. This effect was visible both in the measurements

and in the simulations. In front of the apex of the slope and above it, the inclination angle was clearly positive; above the plateau, it tended to be negative or neutral. OpenFOAM was able to identify the areas with positive and negative inclination angles of more than 20° but did not calculate the location of the highest positive inclination correctly. WRF was also able to correctly model the strength and location of the upward diverted flow, but had difficulty calculating the downward flow over the plateau.

The knowledge gained about the wind field in complex terrain under different westerly wind conditions shows a clearly pronounced velocity maximum at low altitude, a strongly increased TKE and pronounced inclination angles in the area of the planned wind turbines and thus a valuable source of knowledge about the complex flow conditions on a forested escarpment.

3.2 Publication II - Seasonal Changes in Boundary-Layer Flow Over a Forested Escarpment Measured by an Uncrewed Aircraft System

In the second study, the same methodology was used as in the first study. The measurements were also carried out at the same location, the wind energy test field on the Swabian Alb. However, the focus of this study was not on analysing individual case studies for comparison with a model chain, but on the influence of the foliage of the forest on the slope on the overflow of the slope edge. A total of 14 of the 60 measurement flights with 30 to 40 flight legs carried out on the test field were selected for this purpose. The main selection criteria were the foliage of the deciduous trees (LAI, Shaw and Schumann 1992) on the slope (full foliage vs. no foliage) and westerly wind conditions. Measurements in the transition area between no and full foliage were excluded from the analysis, as these would have falsified the results. As the data was averaged over all flights of a season, the wind speed itself was not decisive, but should neither be too high nor too low. Table 3.1 provides an overview of the conditions of the measurement flights used.

Table 3.1: *Lapse rate, Bulk Richardson Number, Mean wind speed and Mean wind direction calculated from flight data for heights between 30–200 m, calculated using the equations in zum Berge et al. (2022)*

Date	Time UTC	LAI	γ [10^{-2}K m^{-1}]	Ri_B	Mean v [m s^{-1}]	Mean dir [$^\circ$]
26/10/2018	1420–1537	Low	0.03	0.033	3.5	285
10/12/2019	1247–1355	Low	-0.20	-0.740	2.0	267
12/12/2019	1352–1458	Low	0.16	0.358	3.1	266
02/11/2020	1446–1609	Low	-0.02	-0.045	5.5	250
10/03/2021	0911–1020	Low	1.24	2.848	6.0	282
10/03/2021	1108–1234	Low	0.30	0.198	5.8	285
14/08/2018	1108–1230	High	-0.37	-3.860	5.3	284
21/09/2018	1055–1229	High	-0.35	-0.089	8.5	262
22/09/2018	1255–1417	High	0.02	0.110	4.5	276
08/07/2019	1251–1416	High	-0.31	-1.435	4.4	297
08/07/2019	1632–1810	High	-0.09	-0.161	4.2	316
29/07/2021	0630–0811	High	0.49	1.051	3.5	252
29/07/2021	0841–1012	High	0.65	2.422	7.2	260
29/07/2021	1636–1803	High	-0.71	-1.552	3.7	300

The average wind speeds were mostly between 4 and 7 m/s, which is a normal wind speed for this area (Hahmann et al. 2020, Dörenkämper et al. 2020). In addition to the wind direction, which was southwest to northwest during the measurement flights, the thermal stability of the atmosphere is another parameter that influences the flow and, in particular, the TKE. To ensure that the turbulence generated is mainly mechanical due to the orography and not to buoyancy, both the lapse rate

$$\gamma = \frac{\Delta\theta_v}{\Delta z} \quad (3.1)$$

with the difference in virtual potential temperature $\Delta\theta_v$ over the height Δz , as well as the Bulk Richardson Number

$$Ri_B = \frac{(\frac{g}{T_v})\Delta\theta_v\Delta z}{(\Delta u)^2 + (\Delta v)^2} \quad (3.2)$$

with the absolute virtual temperature T_v , the virtual potential temperature θ_v , the gravitational acceleration g , the difference across a layer Δz and the changes in the horizontal wind components Δu and Δv were calculated. Both provide clues as to whether the atmosphere was neutral, stable or unstable stratified at the time of the measurements. The former would lead to an attenuation of the turbulence, while the latter would generate additional turbulence due to rising air parcels and thus increase the orographic effect of the slope edge on the TKE. This would influence an isolated consideration of the effect of the slope edge on the wind field. The results in Tab. 3.1 show that some days have a slightly unstable stratification resulting in some of the turbulence generated coming from buoyancy. The amount is small, so mostly negligible, but should be kept in mind when analyzing the measurements. The results of the six flights in winter with no foliage and the eight flights in summer with full foliage showed a significant increase in wind speed over crest. This increase in wind speed over the highest point of a slope or hill is called speed-up and is calculated as follows according to Jackson and Hunt (1975):

$$\Delta S(x, z) = \frac{U(x, z) - U_B(z)}{U_B(z)}. \quad (3.3)$$

$U(x, z)$ is the wind profile U over height z at a location x , which is the lateral distance between the profile over the crest and U_B , the undisturbed approaching wind profile upstream of the escarpment. The greatest speed-up ΔS was found at the lowest measurement altitude of 30 m above ground (Figure 3.4). With increasing altitude, the speed-up of the wind speed over the top of the slope decreases further until it has almost the same value as the undisturbed flow upstream at 200 m above ground. As the flow in the undisturbed area was not measured with the UAS, it was extrapolated from the measurement data at 200 m altitude using an idealized logarithmic wind profile:

$$\mathbf{v}_2 = \mathbf{v}_1 \frac{\ln(\frac{h_2}{z_0})}{\ln(\frac{h_1}{z_0})} \quad (3.4)$$

Figure 3.4 also distinguishes between summer (red line) and winter (blue line) results. The difference in the wind speed increase above the slope edge is clearly visible between these

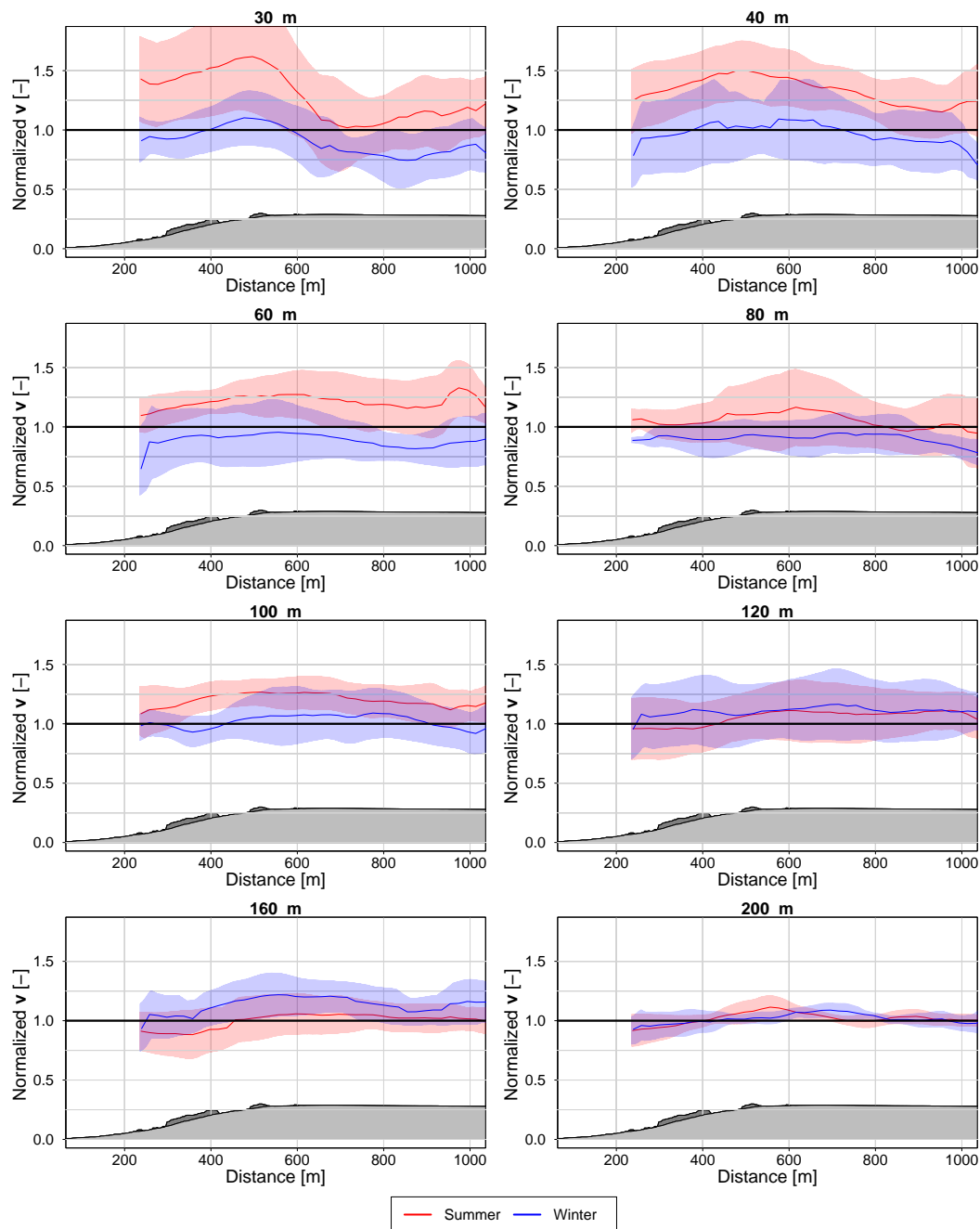


Figure 3.4: Wind speed measurement from MASC-3 between 30 and 200 m above ground for a total of 14 flights during the summer (red line) and winter (blue line) season normalized with the idealized logarithmic wind profile. The shaded areas are the standard deviation of the mean of all flights of each season combined. Adapted from zum Berge et al. (2022)

two seasons. At the lowest measurement heights, the wind speed increase in winter is significantly lower than in summer. This is most likely due to the foliage itself. A fully leafed forest at the edge of a slope makes it much harder for the wind to flow through, which changes the ratio between slope height and slope length, as the trees act as an artificial

elevation of the slope. According to Jackson and Hunt (1975) and Taylor et al. (1987), this new ratio increases velocity. In winter, however, the wind can flow more easily through the forest, reducing the artificial elevation of the slope.

Similar results can be seen when evaluating the turbulence kinetic energy and the angle of inclination. For both, the values at the lowest altitudes in summer are in some cases significantly higher than those in winter. The effect of the slope also decreases with increasing altitude. In the case of the TKE, the forest itself has an increasing effect in addition to the shear caused by the faster flow. In summer the leaves also increase the turbulence of the air masses and thus increase the TKE.

The results of the study agree well with the theoretical values for escarpments postulated by Jackson and Hunt (1975) and Taylor et al. (1987). Only the winter values differ from theory. This is most likely due to the complex orography and forest cover which were not taken into account in the analytically determined values of Jackson and Hunt (1975) and Taylor et al. (1987).

3.3 Publication III - Evaluation of Engineering Models for Large Scale Cluster Wakes with the Help of in Situ Airborne Measurements

The third publication was on wind measurement and simulation using engineering models over the North Sea in the German Bight within the X-Wakes project (<https://www.iwes.fraunhofer.de/de/forschungsprojekte/aktuelle-projekte/x-wakes-.html>). The aim was to measure and model the wakes of wind farm clusters. Previous studies have already shown that wind farm wakes can be detected up to 70 km downstream (Platis et al. 2018). Due to the mission scenario of covering such a large area (Fig. 3.5), the previously used UAS are no longer an option. In order to reliably cover such a large measurement area, crewed aircraft are required as the measurement system. The DO-128 measurement aircraft D-IBUF (Sec. 2.4.2) operated by the Technical University of Braunschweig was used for this study.

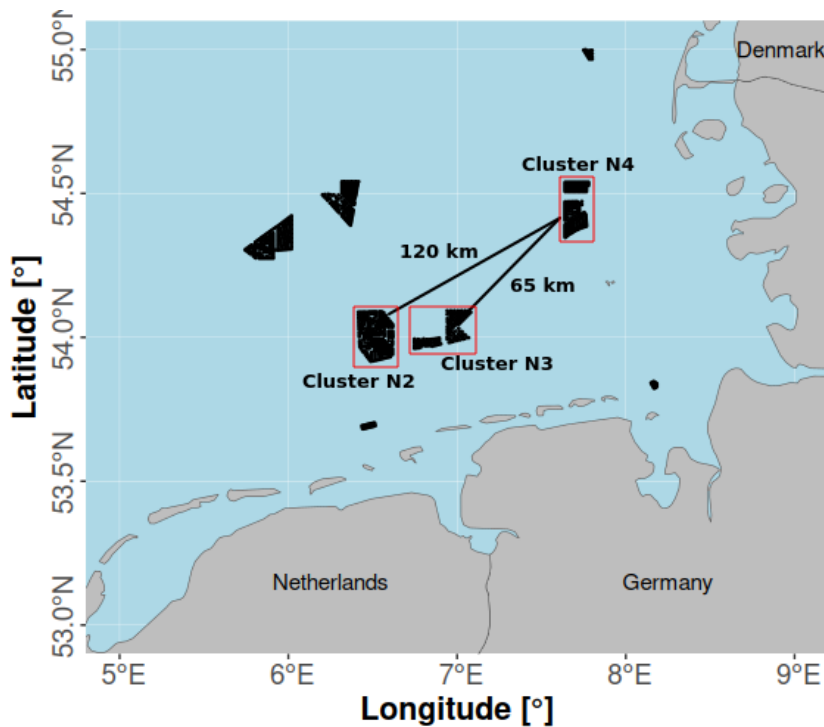


Figure 3.5: The wind farm cluster in the German Bight. Marked with red rectangles are the clusters analyzed in this study. Adapted from zum Berge et al. (2024)

As explained in the introduction (Section 2), the planned increase in wind energy development in the German Bight could lead to issues with interference between different wind farms (Vollmer et al. 2023). A key question arises: Can the turbulence caused by one group of wind turbines reduce the power output of nearby clusters, even if they are still quite far apart (Fig. 3.5)? To answer this question for specific cases, we can use measurements taken

during flight. However, in order to make a more general statement, it is necessary to use simulations. A high-resolution simulation of the flow conditions in the German Bight for as many weather conditions as possible is costly and time-consuming. The models used by industry, on the other hand, work quickly and are more cost-effective because they require much less computing power. However, these engineering models are designed to simulate the flow and yield of individual turbines within a wind farm and the effects in the immediate vicinity using long time series. For future yield assessments, it would be useful to be able to simulate the wake of individual or multiple wind farm clusters using engineering models. The innovative approaches used in the study to tune the FOXES (<https://github.com/FraunhoferIWES/foxes>) engineering model to detect long wakes of entire wind farm clusters using SCADA (Supervisory Control and Data Acquisition) and WRF data are, to the authors' knowledge, new and have not been used before.

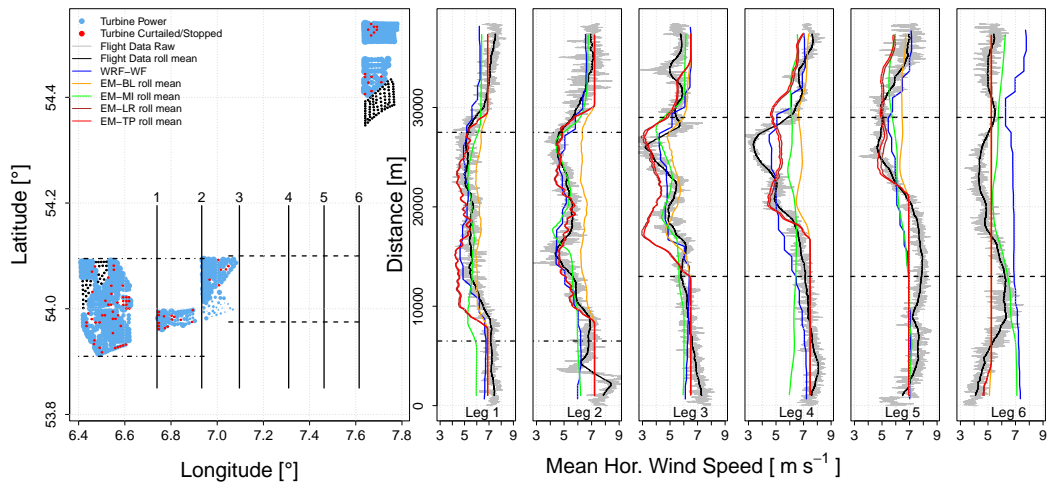


Figure 3.6: *Flight data, WRF-WF, engineering model results and SCADA data on 14.07.2020. The Left panel shows the flight legs in respect to the wind farm cluster N2, N3 and N4. Each wind turbine is depicted as a dot. The size of the blue dots shows the average power during the time of the flight measurement relative to the whole wind park output. Black dots are wind turbines where no SCADA data was available. The smaller panels to the right show the wind speed measured by the aircraft in grey with a running mean in black. The coloured lines show results for WRF-WF and a variety of EM setups. The point-dashed-line and the dashed line indicate the projected wake area for the wind direction during the airborne measurement for cluster N2 and N3, respectively. Caption and plot adapted from zum Berge et al. (2024)*

The selected measurement flights took place in July 2020 and July 2021. In order to minimise the influence of the coast, the investigations were carried out with average wind directions from the west and south-west. The mean wind speeds measured were between 6 and 11 m/s and the thermal stratification was stable during all flight measurements. Figure 3.6 shows an example of the results of the measurement flight on 14th July 2020 behind wind farm clusters N2 and N3. The average wind direction during the measurement flight was

about 260°.

In the left part of the plot, each turbine is represented by a blue dot. The size of the dots indicates the power generated by each turbine relative to the total power generated by the wind farm. The black dots are turbines for which no SCADA data was available at the time of publication. The red dots represent turbines that were not in operation or only partially in operation. In particular, the southern part of Godewind (cluster N3) shows a significant reduction in the power generated by the turbines located there. This is most likely due to the presence of the Nordsee 1 wind farm and its wake. A similar picture can be seen within Nordsee 1, where the power of the turbines also decreases the further downstream they are located.

The vertical solid lines are the straight sections of each flight leg behind the wind farms. A total of six flight legs were flown over a total distance of just under 60 km. The dashed and dotted lines show the area of the expected wake behind each wind farm cluster. These are also plotted on the right-hand side of the figure, along with the aircraft measurements and simulation results, for reference. The measured and modelled wind speeds for each of the six legs flown are plotted from left to right. Clear wakes can be seen in the measured data in the areas close to the wind farms (the grey line is the raw mean wind speed signal and the black line is the rolling mean of the raw signal). The deficit in wind speed is particularly pronounced very close to the turbines, so much so that the layout of the wind farms can be seen (leg 3). As the distance to the wind farms increases, the intensity of the wind speed reduction decreases visibly.

The models deliver very good results in the vicinity of the wind farm clusters, although the different model variants differ in their quality. While the EM-MI version tuned with mesoscale model data (WRF) gave the best results over all distances, EM-TP and EM-LR often overestimated the wind speed deficit. The basic version of the engineering model (EM-BL) gave the worst results. In the southern part of the fifth and sixth flight legs, all models except EM-MI failed to deliver results (straight line) because they no longer recognised the influence of the wind farms.

The other comparisons with the flight measurements also showed very similar results. Again, the engineering model initialised with WRF performed best, while the other variants significantly over- or under-estimated the measurements.

Chapter 4

Discussion

In this thesis, the flow conditions related to wind energy in complex terrain and over the sea have been investigated using airborne in-situ measurements. In particular, the first publications have shown the benefits of UAS in measuring small scale wind fields.

A significant increase in wind speed was observed above a forested escarpment. This increase, or speed-up, is found above the highest point of elevation. Analytical solutions were determined early by Jackson and Hunt (1975) and Taylor et al. (1987). Experiments such as those of Bradley (1980) have shown that the analytical values of the acceleration are applicable to the real world. However, the measurements carried out in this thesis have also shown that other factors play an essential role in the evaluation of flow over complex terrain. In addition to the shape of the orography (hill, slope or ridge) and the environment, i.e. whether the orography to be analysed in the surrounding area has any further complexity, the surface texture also plays an important role. The UAS measurements have shown that the difference in the foliage of a forest on a slope produces a clear difference in the strength of the wind speed exaggeration, the TKE and the vertical deflection (angle of inclination). The speed-up was about 50 % higher in summer than in winter. This is true for low altitudes up to 40 m above ground. Above that, the values converge between the seasons. The TKE was also almost 50 % higher in summer at an altitude of 30 m. This effect quickly diminished with height, so that the values converged correspondingly faster. It can therefore be assumed that a forest with foliage changes the relationship between the length and height of the hill and thus also the position and strength of the speed-up, i.e. makes the hill artificially higher. According to Jackson and Hunt (1975), this increases the speed-up accordingly.

The two measurement flights in September 2018, which took place at an altitude of 20 m above ground level, just above the canopy, showed that an even higher TKE can probably be expected at altitudes below 30 m. The measurements in the second publication also suggest that the increase in wind speed in winter is greater at lower altitudes than those measured. However, the measurement flights used in this study were not conducted below 30 m above ground.

Measurements taken by the crewed aircraft D-IBUF over the German Bight showed clear wakes behind the wind farm clusters. These wakes reduced the wind speed in a stable atmosphere over more than 70 km downwind of the wind farm clusters. For example, some wakes from clusters N2 and N3 reached cluster N4 in southwesterly winds. In the close

vicinity (up to 10 km) behind the wind farms, the wind speed was reduced by more than 20 % in some cases. In addition to the in-situ data from the flight measurements, this effect was also observed in the SCADA data of the individual wind turbines.

The data obtained from the flight measurements were also used to validate the mesoscale model WRF with the wind farm parameterisation according to Fitch et al. (2012) and the engineering model FOXES with different adjustments. The comparison of the different setups with the aircraft data provided good results for the close range behind the wind farm clusters. With increasing distance to the wind turbines, the quality of the simulation results decreased. On the most distant legs, some of the models no longer calculated any influence, while the measurements still showed this.

TKE measurements from the research aircraft were not included in publication III, but can be provided by the measurement system in high resolution. Figure 4.1 shows the TKE of measurement flight 44 on 27 July 2021 with a south-westerly wind and wind speeds between 8 and 10 m s^{-1} . A band of increased TKE can be clearly recognised behind the northern part of cluster N3, which extends to the southern part of cluster N4. Behind this cluster, the TKE is significantly higher, especially in the northern area. This is due to the close proximity of the turbines and the particularly dense arrangement of the turbines in this wind farm. An investigation of the TKE and the extent to which it is maintained in the wake is an interesting topic with regard to the planned expansion of wind energy in the German Bight and should be analysed and compared with model results in future work.

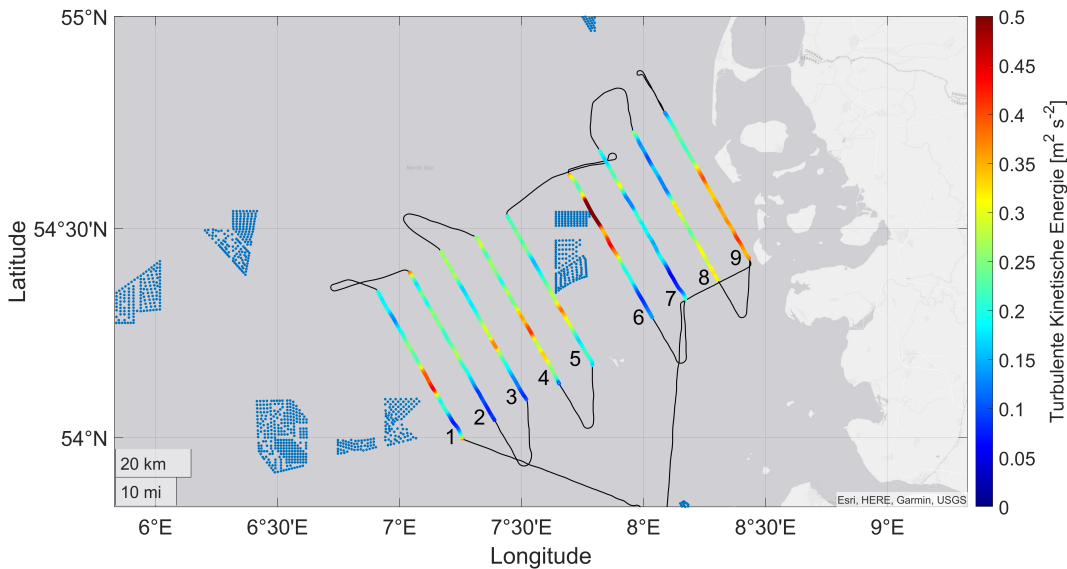


Figure 4.1: Contour plot of the turbulence kinetic energy of flight 44 of the research aircraft D-IBUF of the Technical University of Braunschweig on 27 July 2021 in the lee of cluster N3 and N4. Adapted from the master thesis of Lukas Gruchot

Flight measurements are always a snapshot of a situation, but the atmosphere can change during the measurement period. It is therefore possible that the flight measurement on the last leg measures a lower wind speed, but that this was caused by the changing atmosphere

and no longer by the reduction in wind speed of the wake of a wind farm cluster.

This is one of the major problems with flight measurements. The atmosphere is dynamic and during a flight measurement the atmosphere can change so much that the beginning of a measurement can no longer be directly compared with the end. To counteract this problem, it is helpful to repeat the measurement legs flown as often as possible in order to obtain sufficient statistics and thus reduce the measurement error. Further problems, especially with UAS, are the limited measurement duration and the current regulations for the operation of UAS. These very often stipulate operation within visual range. Very long flight legs, which are often necessary to determine all eddy sizes when measuring second order moments (TKE) are, depended on the area of measurement, sometimes hard to get approval for. The same applies to night flights.

The advantage of in-flight measurements, however, is the ability to measure the situation directly in the medium of interest. This is not possible with simulations or remote sensing measurements such as lidar. A single UAS can therefore measure a large number of meteorological variables directly at the measurement site. Due to the low logistical effort and the fact that it is largely independent of infrastructure, this measurement site can be located in a variety of places that are difficult to access. UAS also offer the possibility of covering large areas at very low altitudes above the ground (Sec. 3.1, 3.2). In contrast, crewed aircraft can use other or additional instruments that are too large and heavy for UAS and cover much larger areas due to the propulsion system.

It was possible to answer the scientific questions posed above within the scope of this dissertation:

- An escarpment significantly influences the flow above it by generating an increase in wind speed in the lower 60 m above the top of the slope. In addition, recirculation zones were identified in the flow over the plateau behind it. Wind speed and wind direction have a decisive influence on the strength of the wind speed increase.
- Further investigations in complex terrain have also shown that the slope gradient, if forested, has a strong influence on the strength and vertical position of the speed-up. Due to the density of foliage, the characteristics differ greatly between the seasons without foliage and with complete foliage. This is particularly visible in the wind speed and the TKE.
- This study of the wakes of large wind farm clusters in the German Bight has shown that, under stable conditions, wakes of more than 70 kilometres in length can occur. Some of these reach wind farms that are far away. The comparison with engineering models and WRF has shown that these can satisfactorily simulate the wakes of large

wind farm clusters in the immediate vicinity, but quickly lose quality with increasing distance from the wind farm cluster.

Chapter 5

Future Perspectives

Both measurement systems have shown that they can measure wind fields with high temporal and spatial resolution and are therefore important for research in the wind energy sector, thus making a valuable contribution to the development of wind energy. It is important to know the inflow conditions upstream of wind turbines in complex terrain and offshore both for flight measurements with UAS and with crewed flight systems. This is especially the case if the measured data are to be compared with simulations. For future measurements it would therefore make sense to use more than one system simultaneously, e.g. at the wind energy test site on the Swabian Alb, a multi-copter will be used to determine the inflow conditions a few hundred metres in front of the test site. It is therefore not necessary to use the same systems for both measurements, different systems which can measure the same variables can supplement each other as well. However, using two MASC-3s at the same time would also improve the results. For example, it would be possible to fly in front of and behind wind turbines or at different heights at the same time. With the same measurement profile, a single MASC-3 could perform more repetitions on a flight leg, thus increasing the statistical significance of the overall measurement. The same is possible for crewed flight measurements and has already been done at the end of the X-Wakes project. Here the D-IBUF was used together with the new research aircraft of the TU Braunschweig. In this way it was possible to carry out simultaneous measurements upstream and downstream of the wind farm cluster, thus obtaining the corresponding inflow conditions for each measurement leg in the wake. Such a procedure would be very useful for future measurements, but also very expensive and therefore difficult to implement. In the area of UAS, this is easier and cheaper to implement to improve the results.

The development of new sensor technology will also improve the results of future measurements. For example, the University of Tübingen is currently researching a fast humidity measurement with a measurement speed of 5 - 10 Hz. A dew-point mirror is being adapted in size and weight to meet the requirements of small UAS, while still providing accurate and fast humidity measurements.

Bibliography

- Abraham C, Goldblatt C (2023) Changes in relative humidity profiles over earth's oceans in a warming climate: A satellite-data-based inference. *Journal of the Atmospheric Sciences* 80(7):1847 – 1866, DOI 10.1175/JAS-D-22-0119.1, URL <https://journals.ametsoc.org/view/journals/atsc/80/7/JAS-D-22-0119.1.xml>
- Belcher S, Harman I, Finnigan J (2012) The wind in the willows: Flows in forest canopies in complex terrain. *Annual Review of Fluid Mechanics* 44(1):479–504, DOI <https://doi.org/10.1146/annurev-fluid-120710-101036>
- Bemis AC (1951) *Aircraft Meteorological Instruments*, American Meteorological Society, Boston, MA, pp 1223–1231. DOI 10.1007/978-1-940033-70-9_99, URL https://doi.org/10.1007/978-1-940033-70-9_99
- Berg J, Mann J, Bechmann A, Courtney MS, Jørgensen HE (2011) The Bolund experiment, part I: Flow over a steep, three-dimensional hill. *Boundary Layer Meteorol* 141:219–243, DOI <https://doi.org/10.1007/s10546-011-9636-y>
- zum Berge K, Schoen M, Mauz M, Platis A, van Kesteren B, Leukauf D, El Bahlouli A, Letzgus P, Knaus H, Bange J (2021) A two-day case study: Comparison of turbulence data from an unmanned aircraft system with a model chain for complex terrain. *Boundary-Layer Meteorology* 180, DOI <https://doi.org/10.1007/s10546-021-00608-2>
- zum Berge K, Gaiser A, Platis A, Knaus H, Bange J (2022) Seasonal changes in boundary-layer flow over a forested escarpment measured by an uncrewed aircraft system. *Boundary-Layer Meteorology* 186, DOI <https://doi.org/10.1007/s10546-022-00743-4>
- zum Berge K, G C, M D, Bange J, Platis A (2024) Towards the improvement of engineering models for large scale cluster wakes with the help of in situ airborne measurements. *Wind Energy*
- Bodini N, Lundquist JK, Kirincich A (2019a) U.s. east coast lidar measurements show offshore wind turbines will encounter very low atmospheric turbulence. *Geophysical Research Letters* 46(10):5582–5591, DOI <https://doi.org/10.1029/2019GL082636>
- Bodini N, Lundquist JK, Krishnamurthy R, Pekour M, Berg LK, Choukulkar A (2019b) Spatial and temporal variability of turbulence dissipation rate in complex terrain. *Atmospheric Chemistry and Physics* 19(7):4367–4382, DOI 10.5194/acp-19-4367-2019, URL <https://acp.copernicus.org/articles/19/4367/2019/>

- Bradley E (1980) An experimental study of the profiles of wind speed, shearing stress and turbulence at the crest of a large hill. *Q J R Meteorol Soc* 106(447):101–123, DOI <https://doi.org/10.1002/qj.49710644708>
- Brümmer B, Kruspe G, Rump B, Müller G, Brecht H, Bakan S, Reuter A, Manschke A, Busack B (2012) Berichte aus dem Zentrum für Meeres- und Klimaforschung: Arktis 91 report on the field phase with examples of measurements. DOI <https://doi.org/10.1594/WDCC/UNIHHMIARKTIS1991>
- Cañadillas B, Foreman R, Barth V, Siedersleben S, Lampert A, Platis A, Djath B, Schulz-Stellenfleth J, Bange J, Emeis S, Neumann T (2020) Offshore wind farm wake recovery: Airborne measurements and its representation in engineering models. *Wind Energy* 23(5):1249–1265, DOI <https://doi.org/10.1002/we.2484>, URL <https://onlinelibrary.wiley.com/doi/abs/10.1002/we.2484>
- Charnock H (1955) Wind stress on a water surface. *Quarterly Journal of the Royal Meteorological Society* 81(350):639–640, DOI <https://doi.org/10.1002/qj.49708135027>, URL <https://rmets.onlinelibrary.wiley.com/doi/abs/10.1002/qj.49708135027>, <https://rmets.onlinelibrary.wiley.com/doi/pdf/10.1002/qj.49708135027>
- Corsmeier U, Hankers R, Wieser A (2001) Airborne turbulence measurements in the lower troposphere onboard the research aircraft Dornier 128-6, D-IBUF. *Meteorologische Zeitschrift* 10(4):315–329, DOI 10.1127/0941-2948/2001/0010-0315, URL <http://dx.doi.org/10.1127/0941-2948/2001/0010-0315>
- Dörenkämper M, Olsen BT, Witha B, Hahmann AN, Davis NN, Barcons J, Ezber Y, García-Bustamante E, González-Rouco JF, Navarro J, Sastre-Marugán M, Sile T, Trei W, Žagar M, Badger J, Gottschall J, Sanz Rodrigo J, Mann J (2020) The making of the new european wind atlas – part 2: Production and evaluation. *Geoscientific Model Development* 13(10):5079–5102, DOI 10.5194/gmd-13-5079-2020, URL <https://gmd.copernicus.org/articles/13/5079/2020/>
- Emeis S (2018) *Wind Energy Meteorology*. Springer
- Emeis S, Frank H, Fiedler F (1995) Modification of air flow over an escarpment - results from the Hjardemal experiment. *Boundary-Layer Meteorol* 74:131–161, DOI <https://doi.org/10.1007/BF00715714>
- European Environment Agency (2022) Trends and projections in Europe 2022. Tech. rep., European Environment Agency, URL <https://www.eea.europa.eu/publications/trends-and-projections-in-europe-2022>
- Fernando HJS, Mann J, Palma JMLM, Lundquist JK, Barthelmie RJ, Belo-Pereira M, Brown WOJ, Chow FK, Gerz T, Hocut CM, Klein PM, Leo LS, Matos JC, Oncley SP,

- Pryor SC, Bariteau L, Bell TM, Bodini N, Carney MB, Courtney MS, Creegan ED, Dimitrova R, Gomes S, Hagen M, Hyde JO, Kigle S, Krishnamurthy R, Lopes JC, Mazzaro L, Neher JMT, Menke R, Murphy P, Oswald L, Otarola-Bustos S, Pattantyus AK, Rodrigues CV, Schady A, Sirin N, Spuler S, Svensson E, Tomaszewski J, Turner DD, van Veen L, Vasiljević N, Vassallo D, Voss S, Wildmann N, Wang Y (2019) The Perdigão: Peering into microscale details of mountain winds. *Bull Am Meteorol Soc* 100(5):799 – 819, DOI 10.1175/BAMS-D-17-0227.1, URL <https://journals.ametsoc.org/view/journals/bams/100/5/bams-d-17-0227.1.xml>
- Finnigan J (1988) Air flow over complex terrain. In: Steffen WL, Denmead OT (eds) *Flow and Transport in the Natural Environment: Advances and Applications*, Springer Berlin Heidelberg, pp 183–229
- Finnigan J, Ayotte K, Harman I, Katul G, Oldroyd H, Patton E, Poggi D, Ross A, Taylor P (2020) Boundary-layer flow over complex topography. *Boundary-Layer Meteorol* 177:247–313, DOI <https://doi.org/10.1007/s10546-020-00564-3>
- Finnigan JJ, Belcher SE (2004) Flow over a hill covered with a plant canopy. *Quarterly Journal of the Royal Meteorological Society* 130(596):1–29, DOI <https://doi.org/10.1256/qj.02.177>
- Fitch AC, Olson JB, Lundquist JK, Dudhia J, Gupta AK, Michalakes J, Barstad I (2012) Local and mesoscale impacts of wind farms as parameterized in a mesoscale NWP model. *Monthly Weather Review* 140(9):3017 – 3038, DOI 10.1175/MWR-D-11-00352.1, URL <https://journals.ametsoc.org/view/journals/mwre/140/9/mwr-d-11-00352.1.xml>
- Hahmann AN, Sile T, Witha B, Davis NN, Dörenkämper M, Ezber Y, García-Bustamante E, González-Rouco JF, Navarro J, Olsen BT, Söderberg S (2020) The making of the new european wind atlas – part 1: Model sensitivity. *Geoscientific Model Development* 13(10):5053–5078, DOI 10.5194/gmd-13-5053-2020, URL <https://gmd.copernicus.org/articles/13/5053/2020/>
- Hunt JCR, Richards KJ, Brighton PWM (1988) Stably stratified shear flow over low hills. *Quarterly Journal of the Royal Meteorological Society* 114(482):859–886, DOI <https://doi.org/10.1002/qj.49711448203>
- Højstrup J (1999) Spectral coherence in wind turbine wakes. *Journal of Wind Engineering and Industrial Aerodynamics* 80(1):137–146, DOI [https://doi.org/10.1016/S0167-6105\(98\)00198-6](https://doi.org/10.1016/S0167-6105(98)00198-6), URL <https://www.sciencedirect.com/science/article/pii/S0167610598001986>
- Jackson D, Gadian A, Hindley N, Hoffmann L, Hughes J, King J, Moffat-Griffin T, Moss A, Ross A, Vosper S, et al. (2018) The south georgia wave experiment: A means for

- improved analysis of gravity waves and low-level wind impacts generated from mountainous islands. *Bulletin of the American Meteorological Society* 99(5):1027–1040
- Jackson PS, Hunt JCR (1975) Turbulent wind flow over a low hill. *Q J R Meteorol Soc* 101(430):929–955, DOI <https://doi.org/10.1002/qj.49710143015>
- Kaimal JC, Wyngaard JC, Izumi Y, Coté OR (1972) Spectral characteristics of surface-layer turbulence. *Quarterly Journal of the Royal Meteorological Society* 98(417):563–589, DOI <https://doi.org/10.1002/qj.49709841707>
- Klaas-Witt T, Emeis S (2022) The five main influencing factors for lidar errors in complex terrain. *Wind Energy Science* 7(1):413–431, DOI 10.5194/wes-7-413-2022, URL <https://wes.copernicus.org/articles/7/413/2022/>
- Kolmogorov AN (1941) Dissipation of energy in the locally isotropic turbulence. *Proceedings: Mathematical and Physical Sciences* 434(1890):15–17, URL <http://www.jstor.org/stable/51981>
- van den Kroonenberg A, Martin T, Buschmann M, Bange J, Vörsmann P (2008) Measuring the wind vector using the autonomous mini aerial vehicle M2AV. *Journal of Atmospheric and Oceanic Technology* 25(11):1969 – 1982, DOI <https://doi.org/10.1175/2008JTECHA1114.1>, URL https://journals.ametsoc.org/view/journals/atot/25/11/2008jtecha1114_1.xml
- Lampert A, Bärfuss K, Platis A, Siedersleben S, Djath B, Canadillas B, Hunger R, Hankers R, Bitter M, Feuerle T, Schulz H, Rausch T, Angermann M, Schwithal A, Bange J, Schulz-Stellenfleth J, Neumann T, Emeis S (2020) In situ airborne measurements of atmospheric and sea surface parameters related to offshore wind parks in the German Bight. *Earth System Science Data* 12(2):935–946, DOI 10.5194/essd-12-935-2020, URL <https://essd.copernicus.org/articles/12/935/2020/>
- Letzgus P, Guma G, Lutz T (2022) Computational fluid dynamics studies on wind turbine interactions with the turbulent local flow field influenced by complex topography and thermal stratification. *Wind Energy Science* 7(4):1551–1573, DOI 10.5194/wes-7-1551-2022, URL <https://wes.copernicus.org/articles/7/1551/2022/>
- Lu GY, Wong DW (2008) An adaptive inverse-distance weighting spatial interpolation technique. *Computers & Geosciences* 34(9):1044–1055, DOI <https://doi.org/10.1016/j.cageo.2007.07.010>, URL <https://www.sciencedirect.com/science/article/pii/S0098300408000721>
- Mauz M, Rautenberg A, Platis A, Cormier M, Bange J (2019) First identification and quantification of detached-tip vortices behind a wind energy converter using fixed-wing unmanned aircraft system. *Wind Energy Science* 4(3):451–463, DOI 10.5194/wes-4-451-2019, URL <https://wes.copernicus.org/articles/4/451/2019/>

- Mauz M, van Kesteren B, Junkermann W, zum Berge K, Schön M, Platis A, Bange J (2020) Miniature high-frequency chilled-mirror hygrometer for atmospheric measurements aboard fixed wing uas. *Meteorologische Zeitschrift* 29(6):439–449, DOI 10.1127/metz/2020/1026, URL <http://dx.doi.org/10.1127/metz/2020/1026>
- Platis A, Siedersleben SK, Bange J, Lampert A, Bärfuss K, Hankers R, Canadillas B, Foreman R, Schulz-Stellenfleth J, Djath B, Neumann T, Emeis S (2018) First in situ evidence of wakes in the far field behind offshore wind farms. *Scientific Reports* 8, DOI 10.1038/s41598-018-20389-y, URL <https://www.mdpi.com/1996-1073/8/6/541>
- Platis A, Bange J, Bärfuss K, Canadillas B, Hundhausen M, Djath B, Lampert A, Schulz-Stellenfleth J, Siedersleben S, Neumann T, Emeis S (2020) Long-range modifications of the wind field by offshore wind parks - results of the project wipaff. *Meteorologische Zeitschrift* 29(5):355–376, DOI 10.1127/metz/2020/1023, URL <http://dx.doi.org/10.1127/metz/2020/1023>
- Platis A, Hundhausen M, Mauz M, Siedersleben S, Lampert A, Bärfuss K, Djath B, Schulz-Stellenfleth J, Canadillas B, Neumann T, et al. (2021) Evaluation of a simple analytical model for offshore wind farm wake recovery by in situ data and weather research and forecasting simulations. *Wind Energy* 24(3):212–228
- Platis A, Hundhausen M, Lampert A, Emeis S, Bange J (2022) The role of atmospheric stability and turbulence in offshore wind-farm wakes in the german bight. *Boundary Layer Meteorology* 182, DOI 10.1007/s10546-021-00668-4
- Platis A, Büchau Y, Zuluaga S, Bange J (2023) The impact of offshore wind farms on the latent heat flux; the impact of offshore wind farms on the latent heat flux. *Meteorologische Zeitschrift* 32(4):261–277
- Rautenberg A, Schoen M, zum Berge K, Mauz M, Manz M, Platis A, van Kesteren B, Suomi I, Kral S, Bange J (2019) The Multi-purpose Airborne Sensor Carrier MASC-3 for wind and turbulence measurements in the atmospheric boundary layer. *Sensors* 19(10), DOI <https://doi.org/10.3390/s19102292>
- Richardson LF (2007) *Weather Prediction by Numerical Process*, 2nd edn. Cambridge Mathematical Library, Cambridge University Press
- Schulz-Stellenfleth J, Emeis S, Dörenkämper M, Bange J, Cañadillas B, Neumann T, Schneemann J, Weber I, zum Berge K, Platis A, Djath B, Gottschall J, Vollmer L, Rausch T, Barekzai M, Hammel J, Steinfeld G, Lampert A (2022) Coastal impacts on offshore wind farms - a review focussing on the german bight area. *Meteorologische Zeitschrift* 31(4):289–315, DOI 10.1127/metz/2022/1109, URL <http://dx.doi.org/10.1127/metz/2022/1109>

-
- Sempreviva AM, Gryning SE (1996) Humidity fluctuations in the marine boundary layer measured at a coastal site with an infrared humidity sensor. *Boundary-Layer Meteorology* 77:331–352, DOI <https://doi.org/10.1007/BF00123531>
- Serafin S, Adler B, Cuxart J, De Wekker SF, Gohm A, Grisogono B, Kalthoff N, Kirshbaum DJ, Rotach MW, Schmidli J, et al. (2018) Exchange processes in the atmospheric boundary layer over mountainous terrain. *Atmosphere* 9(3):102
- Shaler K, Kecskemety KM, McNamara JJ (2019) Benchmarking of a free vortex wake model for prediction of wake interactions. *Renewable Energy* 136:607–620, DOI <https://doi.org/10.1016/j.renene.2018.12.044>, URL <https://www.sciencedirect.com/science/article/pii/S0960148118314757>
- Shaw RH, Schumann U (1992) Large-eddy simulation of turbulent flow above and within a forest. *Boundary-Layer Meteorol* 61:47–64, DOI <https://doi.org/10.1007/BF02033994>
- Shaw WJ, Berg LK, Debnath M, Deskos G, Draxl C, Ghate VP, Hasager CB, Kotamarthi R, Mirocha JD, Muradyan P, Pringle WJ, Turner DD, Wilczak JM (2022) Scientific challenges to characterizing the wind resource in the marine atmospheric boundary layer. *Wind Energy Science* 7(6):2307–2334, DOI 10.5194/wes-7-2307-2022, URL <https://wes.copernicus.org/articles/7/2307/2022/>
- Smith SD (1980) Wind stress and heat flux over the ocean in gale force winds. *Journal of Physical Oceanography* 10(5):709 – 726, DOI [https://doi.org/10.1175/1520-0485\(1980\)010<0709:WSAHFO>2.0.CO;2](https://doi.org/10.1175/1520-0485(1980)010<0709:WSAHFO>2.0.CO;2), URL https://journals.ametsoc.org/view/journals/phoc/10/5/1520-0485_1980_010_0709_wsahfo_2_0_co_2.xml
- Stull R (1988) *An Introduction to Boundary Layer Meteorology*. Kluwer Academic Publisher, Dordrecht
- Taylor P, Teunissen H (1987) Askervein hill project: Overview and background data. DOI 10.1007/BF00121863
- Taylor P, Mason PJ, Bradley E (1987) Boundary-layer flow over low hills. *Boundary-Layer Meteorol* 39:107–132, DOI <https://doi.org/10.1007/BF00121870>
- Thomsen K (1996) Loads for wind turbines in complex terrain. *Wind Engineering* 20(4):233–240, URL <http://www.jstor.org/stable/43749617>
- Troldborg N, Andersen SJ, Hodgson EL, Meyer Forsting A (2022) Brief communication: How does complex terrain change the power curve of a wind turbine? *Wind Energy Science* 7(4):1527–1532, DOI 10.5194/wes-7-1527-2022, URL <https://wes.copernicus.org/articles/7/1527/2022/>
- Umweltbundesamt (1996) *Hydroelectric Power Plants as a Source of Renewable Energy - legal and ecological aspects*. Tech. rep., Umweltbundesamt,

- URL <https://www.umweltbundesamt.de/sites/default/files/medien/publikation/long/2544.pdf>
- Umweltbundesamt - Arbeitsgemeinschaft Energiebilanzen (2023) Erneuerbare und Konventionelle Stromerzeugung. Tech. rep., Umweltbundesamt, URL <https://www.umweltbundesamt.de/daten/energie/erneuerbare-konventionelle-stromerzeugung#zeitliche-entwicklung-der-bruttostromerzeugung>
- Vollmer L, Dörenkämper M, B L (2023) Ad-Hoc Analyse: Modellierung der Langzeitstatistiken und des Einflusses eines kontinuierlichen Ausbaus auf die Windenergieerträge in der deutschen AWZ der Nordsee. Tech. rep., Fraunhofer IWES, URL https://www.bsh.de/DE/THEMEN/Offshore/Meeresfachplanung/Flaechenentwicklungsplan/_Anlagen/Downloads/Ad-HocAnalyse_FEP_Langzeitstatistik_kontinuierlicherAusbau.pdf?__blob=publicationFile&v=2
- Wildmann N, Mauz M, Bange J (2013) Two fast temperature sensors for probing of the atmospheric boundary layer using small remotely piloted aircraft (RPA). *Atmospheric Measurement Techniques* 6(8):2101–2113, DOI 10.5194/amt-6-2101-2013, URL <https://amt.copernicus.org/articles/6/2101/2013/>
- Zardi D, Whiteman CD (2012) Diurnal mountain wind systems. *Mountain weather research and forecasting: Recent progress and current challenges* pp 35–119


Appendix A

Peer-reviewed first-author publications

A.1 A Two-Day Case Study: Comparison of Turbulence Data from an Unmanned Aircraft System with a Model Chain for Complex Terrain - Publication I



A Two-Day Case Study: Comparison of Turbulence Data from an Unmanned Aircraft System with a Model Chain for Complex Terrain

Kjell zum Berge¹  · Martin Schoen¹ · Moritz Mauz¹ · Andreas Platis¹ · Bram van Kesteren¹ · Daniel Leukauf² · Asmae El Bahlouli³ · Patrick Letzgus⁴ · Hermann Knaus³ · Jens Bange¹

Received: 26 May 2020 / Accepted: 13 February 2021 / Published online: 29 March 2021
© The Author(s) 2021

Abstract

The airborne measurement platform MASC-3 (Multi-Purpose Airborne Sensor Carrier) is used for measurements over a forested escarpment in the Swabian Alps to evaluate the wind field. Data from flight legs between 20 and 200 m above the ground on two consecutive days with uphill (westerly) flow in September 2018 are analyzed. In the lowest 140 m above the ground a speed-up is found with increased turbulence and changes in wind direction directly over the escarpment, whereas in the lowest 20 to 50 m above the ground a deceleration of the flow is measured. Additionally, simulation results from a numerical model chain based on the Weather Research and Forecasting (WRF) model and an OpenFOAM (Open Source Field Operation and Manipulation) model, developed for complex terrain, are compared to the data captured by MASC-3. The models and measurements compare well for the mean wind speed and inclination angle.

Keywords Complex terrain · Turbulence measurement · Unmanned aircraft system · Wind energy

Kjell zum Berge
kjell.zumberge@unituebingen.de

¹ Center for Applied Geoscience, Eberhard-Karls-Universitaet Tuebingen, Schnarrenbergstr. 94-96, 72076 Tuebingen, Germany

² Institute of Meteorology and Climate Research Atmospheric Environmental Research (IMK-IFU), Karlsruhe Institute of Technology KIT, Campus Alpin, Kreuzeckbahnstraße 19, 82467 Garmisch-Partenkirchen, Germany

³ Faculty of Building Services-Energy-Environment, Esslingen University of Applied Sciences, Kanalstrasse 33, 73728 Esslingen, Germany

⁴ Institute of Aerodynamics and Gas Dynamics (IAG) University of Stuttgart, Pfaffenwaldring 21, 70569 Stuttgart, Germany

1 Introduction

In 2019, wind energy production covered 15% of the electricity demand for all 28 European Union member states (WindEurope 2019). Due to the increasing numbers of wind turbines erected, the wind-energy research focus is shifting from flat terrain and offshore locations towards complex topography. Orographic effects, such as channeling or the acceleration of near-surface flow, can lead to local increases in wind speed (Wagenbrenner et al. 2016) and thus improvement in wind resource (Clifton et al. 2014).

Compared to flat, homogeneous terrain, measurements and characterization of the atmospheric flow in complex terrain are more challenging. The flow is influenced by the heterogeneous orography, leading to higher levels of turbulence in the lower atmospheric boundary layer (ABL), wind shear, and a less predictable behaviour. These features rapidly change the wind field in both space and time (Wildmann et al. 2017). Lidar and sodar, with their comparatively large averaging volumes, have difficulties measuring the highly heterogeneous flow and its fine structure and turbulence over an escarpment. Static point measurements on towers close to the escarpment cannot be representative for the immediate vicinity (Ayotte et al. 2001) due to the heterogeneity and the non-stationarity of the flow. An unmanned aircraft system (UAS) however allows measurements of small-scale turbulence and the flow field over a larger area at multiple heights. This makes a UAS especially useful for measurements in complex terrain, as it captures the phenomena over certain areas of an escarpment or other complex structures.

In order to answer the questions on how to optimize turbines in complex terrain and extend their service life in such areas, the WindForS research cluster (<https://www.windfors.de>) has launched the WINSSENT (Wind Science and Engineering in Complex Terrain) project. The WINSSENT project uses a wind-energy test site at the top of a forested escarpment at the rim of the Swabian Alps in south-western Germany. The aim is to get a complete picture on how to operate wind turbines in complex terrain and develop software tools that simulate the turbines, turbulent structures, and the wind field, as well as changes introduced by the wind turbines. The present study analyzes the undisturbed wind field before the installation of wind turbines at and around the test site. It also compares the UAS measurements with data from a numerical-model chain developed by our project partners, consisting of the mesoscale Weather Research and Forecasting (WRF) model and the meso-microscale URANS (Unsteady Reynolds-Averaged Navier–Stokes) model OpenFOAM (Open Source Field Operation and Manipulation; El-Bahlouli et al. 2019, 2020).

High fidelity numerical airflow models, such as large-eddy simulation (LES) models, have been developed and applied for wind energy applications over the years. These models resolve most of the turbulence and require observational data with an equally high resolution for validation. However, since measurements require an extensive amount of material, personnel, funding, and time, there are only few observational datasets with sufficient spatial and temporal resolution of a wind field in complex terrain. One of these unique datasets can be found in Letson et al. (2018). Datasets such as these are of importance given that small-scale obstacles such as trees may have a significant impact. Such a new dataset is needed to reach high accuracy in model results for the future test site and for the analysis on fatigue loads onto the turbine structures, especially the blades. Apart from wind speed, wind direction, and turbulence, the inclination angle plays a major role for the site assessment of new wind turbines. According to the IEC 60400-1 (VDE 2019) it should not exceed values of $\pm 8^\circ$.

During the previous projects Lidar Complex (Hofsaess et al. 2018) and KonTest (Wildmann et al. 2017), measurements with UASs and numerical studies were carried out at this

site (Fig. 1). Measurements and simulations showed an accelerated flow over the escarpment with westerly winds. Due to surface roughness and the orography, the strongest turbulence fluctuations and flow acceleration were observed at the lowest 10 to 80 m above ground upstream of the escarpment (Knaus et al. 2018; Letzgus et al. 2018).

In this study, similar measurement flights were conducted. With the latest iteration of the MASC (Multi-Purpose Airborne Sensor Carrier) UAS, the MASC-3 (Rautenberg et al. 2019), we were able to fly much closer to the ground compared to previously (Wildmann et al. 2017) and could not gather these important data downstream the escarpment edge. Due to improved autopilot and more accurate sensors the UAS now provides a more stable flight path that enables measurement trajectories as low as 20 m above ground (Mauz et al. 2019). Thus MASC-3 covers most of the vertical region of the flow field influenced by the forested escarpment.

The long blades of modern wind turbines reach down into this area with stronger turbulence in the lee of the trees. Knaus et al. (2018) showed that not only orographic effects, but also lee effects of trees affect the flow over an escarpment at these heights. The model results show a significant increase of the turbulence kinetic energy (TKE, k) and a minimum in wind speed below 50 m above ground in the lee of the trees (Knaus et al. 2018). Thus, this study aims at answering the following questions:

- Is the MASC-3 able to measure small-scale flow phenomena in complex terrain (such as the propagation of turbulence introduced by the forested escarpment close to the ground), locate recirculation zones along the plateau, and detect differences in wind speed over a large area?
- How well do numerical models resolve small-scale phenomena in comparison to the MASC-3 data?

The results give insight into the turbulence and atmospheric flow within the lower atmospheric boundary layer behind the escarpment on two consecutive days in September 2018, with a focus on the lowest 60 m above the plateau and close to the future wind-turbine locations. These measurements will give valuable new data for model validation and load calculations within altitudes reached by the turbine blades, which have not been measured before with such a high spatial–temporal resolution.

2 Measurement System and Site

2.1 The Test Site

The test site (48.664°N, 9.836°E) is situated on top of a forested escarpment in the Swabian Alps close to the town of Geislingen an der Steige in southern Germany. The forested escarpment peaks at 200 m above the valley with the slope facing west with no other large obstacles in that direction, except a smaller hill about 2 km away (Fig. 1). This feature and the predominant westerly winds make this area interesting for building the test site.

Figure 1 shows a digital elevation model of the area with a zoomed view of the future test site. Two measurement masts have been erected close to the escarpment and two more will follow at a later point in time. The masts are equipped with wind vanes, cup anemometers, and pressure–temperature–humidity sensors at heights between 3 and 100 m, which cover the whole wind-turbine diameter. A wind turbine will be placed between each pair of masts. At the time of the measurements, only the north-western tower was equipped with a suite of instruments.

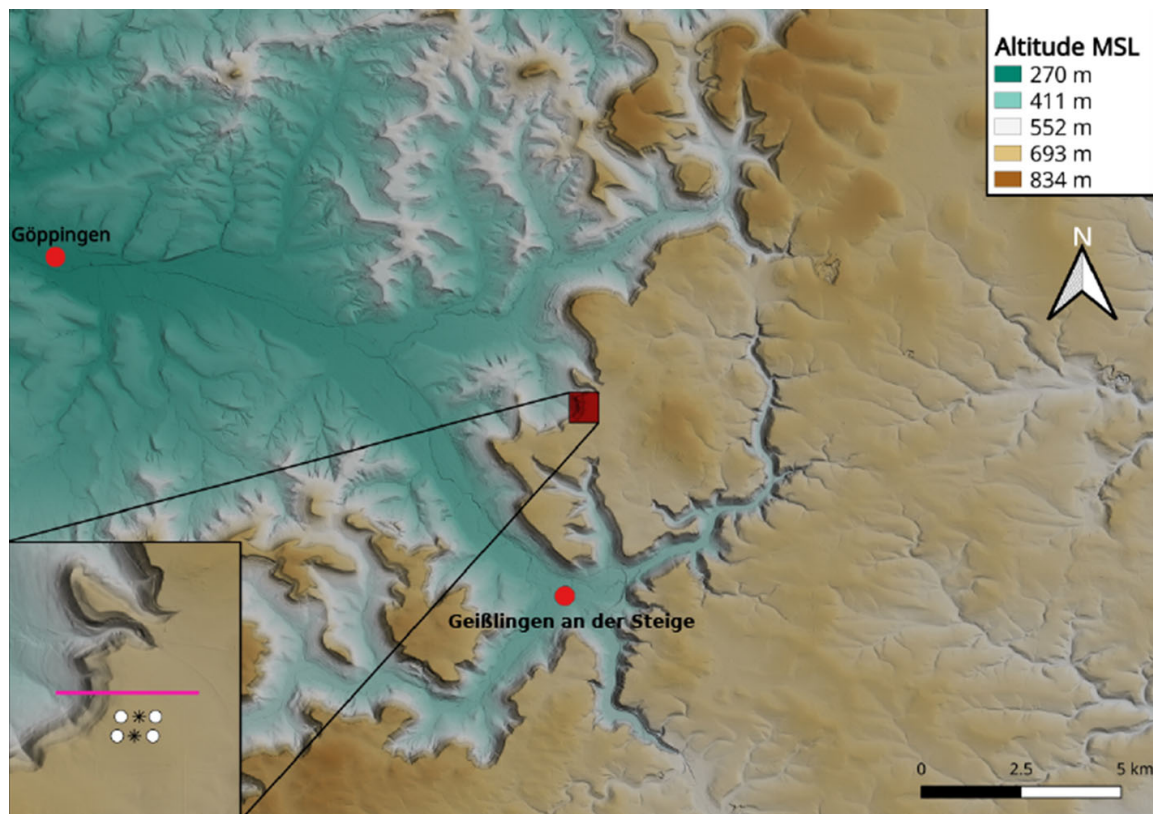


Fig. 1 Digital elevation model of the Albtrauf with the rectangle zooming onto the test site located at 48.664°N , 9.836°E . Height difference displayed in the upper right corner. Zoomed View: white dots = wind measurement masts; black stars = future turbines; pink line = flight path; source: DEM5 (Digital Elevation Model 5 m Resolution) provided by the district office Baden-Württemberg

2.2 Measurement System

The latest version of the MASC, the MASC-3 (Rautenberg et al. 2019), is an autonomously flying UAS with a 4-m wingspan and about 6–8 kg mass. This includes 1 to 1.5 kg of scientific payload (Fig. 2). The flight time can reach up to 2.5 h depending on payload and battery configuration. The autopilot (Pixhawk 2.1 ‘Cube’) is capable of keeping the position within a few metres with respect to its programmed flight path for most conditions. In this study, the airspeed was fixed to 18.5 m s^{-1} by the autopilot system.

The measuring unit is modular and consists of a sensor suite for measuring the wind vector and air temperature at frequencies up to 30 s^{-1} (Rautenberg et al. 2019), and water vapour with frequency of about 0.5 s^{-1} . With the pusher engine at the back of the fuselage, the engines influence on measurements at the front of the UAS is minimized.

The five-hole flow probe measures pressure differences between the holes at the front of the aircraft’s nose. Together with the motion of the aircraft and current position data from the inertial measurement unit (IMU) in the geodetic coordinate system, the wind vector is calculated from

$$\mathbf{v} = \mathbf{v}_{\text{gs}} + M(\mathbf{v}_{\text{tas}} + \boldsymbol{\omega} \times \mathbf{r}), \quad (1)$$

with the wind vector \mathbf{v} (positive eastwards and upwards), ground speed vector \mathbf{v}_{gs} , airspeed vector \mathbf{v}_{tas} , rotation matrix M to convert from an aerodynamic to a geodetic coordinate system, the vector of angular body rates $\boldsymbol{\omega}$, and the lever arm \mathbf{r} between the IMU and five-hole probe. For a more detailed description of wind measurements with the UAS and error estimations,



Fig. 2 The Multi-Purpose Airborne Sensor Carrier, version 3 is a UAS for meteorological measurements in the atmospheric boundary layer. The image shows the UAS with its sensor compartment (Rautenberg et al. 2019). Picture taken by Barbara Altstädter

see Van den Kroonenberg et al. (2008), Wildmann et al. (2014, 2017), and Rautenberg et al. (2018).

3 Methods and Theory

3.1 Measurement Strategy

For the purpose of the flow measurement over the escarpment, flight legs (i.e., straight and level flight paths) at different heights perpendicular to the slope and along the mean wind direction were performed. The lowest flight altitude is 20 m above ground level (a.g.l.) and therefore just above the tree tops. Up to 60 m a.g.l., measurements are performed at vertical intervals of 10 m. Above 60 m the intervals are increased to 20 m and above 120 m each height step is 40 m up to the top height of about 200 m (Fig. 3). Each level consists of at least four straight flight legs on the same path in opposite directions, giving the data more statistical significance.

With a sampling rate of 500 s^{-1} for the raw data and 100 s^{-1} for the processed data, a spatial resolution of 5–6 data points per metre flight path was obtained. The high sampling rate was chosen to counteract the aliasing effect in the output data.

Flight measurements downstream of the edge allow for the analysis of the impact of the escarpment on the flow field. Therefore the flight paths (legs) were chosen to be about 1 km long with 500 m in less disturbed flow above the lowland and another 800 m above the plateau where the future wind turbines will be positioned. Table 1 lists the flights and the metadata for the data used herein.

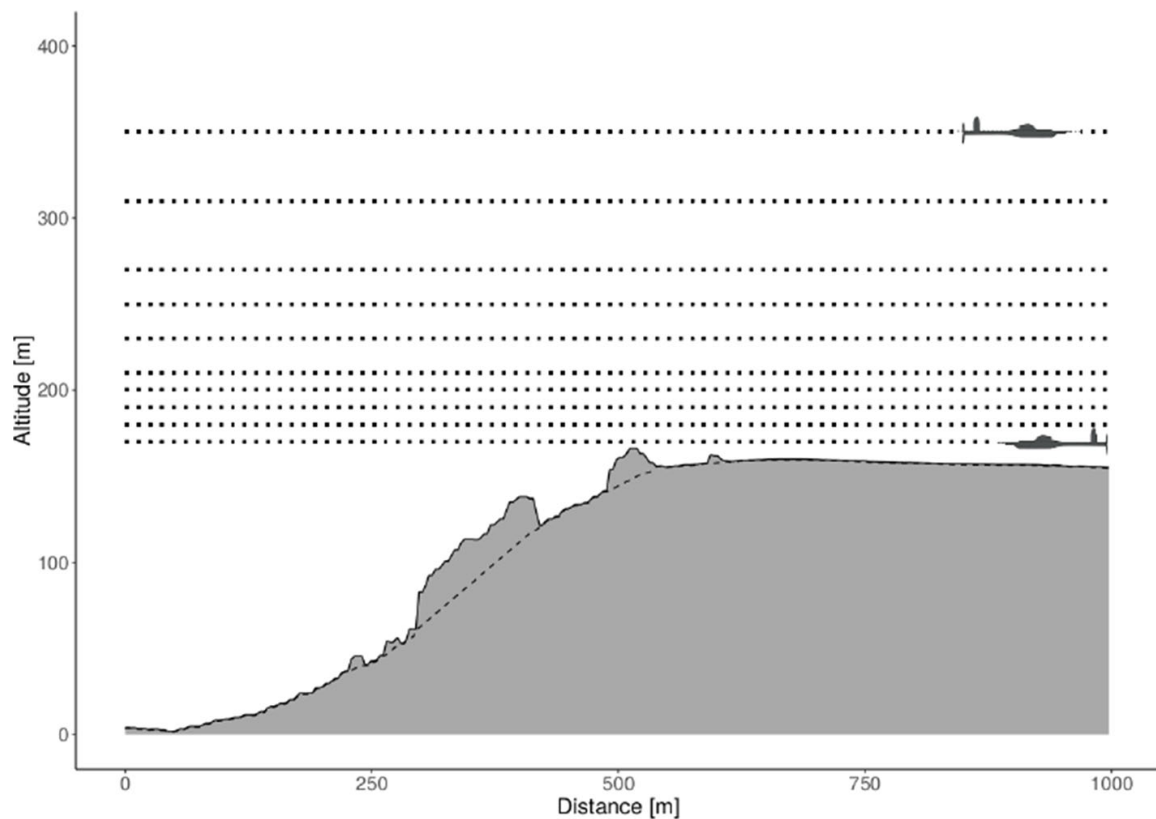


Fig. 3 Measurement strategy for the test site. Legs between 20 and 200 m with more legs flown in lower levels. Escarpment is facing west. The dashed line indicates the terrain without the trees

Table 1 Mean meteorological values and flight plan data for the flights on 21 and 22 September 2018

Name	Flight 1	Flight 2
Date	21/09/2018	22/09/2018
Flight direction	East–west	East–west
Height [m]	20–200	20–200
Mean # of legs per height	4	4
Mean wind dir. [°]	259.3	275.2
Mean wind speed[m s ⁻¹]	9.79	4.44
Mean temperature[°C]	22.2	17.0
Mean rel. humidity[%]	42.8	40.4

Wind direction and speed averaged over all flown flight legs and all heights. Mean temperature and relative humidity at ground level

3.2 Determination of Turbulence Parameters

The wind and fast temperature data are logged at 500 s⁻¹ and scaled down to 100 s⁻¹ using a block mean. These raw 100 s⁻¹ data are then processed using the inertial navigation system (INS) exact position data. The wind speed $|\mathbf{v}_h|$ is calculated by

$$|\mathbf{v}_h| = \sqrt{u^2 + v^2}, \quad (2)$$

using the two velocity components u and v generated by the post-processing software derived from the five-hole probe pressure sensors. In the end, one of the important variables for validating the impact of the escarpment on the flow is TKE, k , which is calculated by taking

the velocity fluctuations from either the variance (Var) or the standard deviation (σ) of all three wind components (u , v , and w)

$$k = \frac{1}{2}(Var_u + Var_v + Var_w) = \frac{1}{2}(\sigma_u^2 + \sigma_v^2 + \sigma_w^2). \quad (3)$$

The variance (Var) of a variable X is calculated, using Reynolds decomposition where the fluctuations X' are separated from the mean \bar{X} , with

$$Var_X = \frac{1}{N-1} \sum_{i=1}^N (X_i - \bar{X})^2. \quad (4)$$

In order to set a proper averaging-window size N , we calculated the turbulent integral length scale (L), i.e., a measure for the size of the largest turbulent eddies in the Kolmogorov inertial sub-range that contribute to the turbulent transport of momentum. The integral length scale, L , of a variable is determined by integration from zero lag to the first root at τ_1 of the autocorrelation function ρ and multiplied with the aircraft's mean true airspeed $|\bar{\mathbf{u}}_a|$ or the ground speed $|\bar{\mathbf{u}}_g|$. The integral length scale of u using the mean true airspeed $|\bar{\mathbf{u}}_a|$, for example, is defined by

$$L = |\bar{\mathbf{u}}_a| \int_0^{\tau_1} \rho_u(\tau) d\tau. \quad (5)$$

An analysis of both flights presented in this paper showed a range of values for L between 43 and 119 m for a single measurement height (see Table 2). The calculation was done for L using the mean ground speed and the mean true airspeed per leg. In conditions with high wind speeds, the ground speed differs between upwind and downwind legs, whereas the mean true airspeed is independent from the wind speed and therefore less subject to fluctuations. To account for this behaviour and to find the maximum integral length scales, the calculation was done with both $|\bar{\mathbf{u}}_a|$ and $|\bar{\mathbf{u}}_g|$ of the UAS, seen in Table 2. The difference in L calculated with the ground speed and mean true airspeed is small for most heights. The biggest difference between those two is 28% at an altitude of 80 m on 21 September 2018. To account for all eddies present during the time of measurement, the window size for calculating k was chosen to be larger than 119.3 m, i.e., based on the highest L calculated from both methods (see Table 2).

The variables mean wind speed \mathbf{v}_h , wind direction φ , TKE k , and inclination angle α shown in Sect. 4 are combined in a data frame after post-processing. The inclination angle is the angle between the horizontal plane in that height and the vertical direction of the wind hitting that plane. Flow coming from below the plane is considered positive while flow from above the plane is considered negative.

Having calculated the variables for the flight, it is possible to derive data for vertical profiles at certain positions over ground and to create a contour plot over the escarpment using interpolation between the horizontal data points. The interpolation method (Eq. 6) chosen for this analysis is the inverse distance weighted interpolation. It is widely used in spatial analysis and the Geographic Information System (Lu and Wong 2008). The principle of calculating the interpolated data points a

$$a(x_0) = \frac{\sum_{i=1}^N \left(\frac{a(x_i)}{d(x_0, x_i)} \right)^p}{\sum_{i=1}^N \left(\frac{1}{d(x_0, x_i)} \right)^p}, \quad (6)$$

Table 2 Data for mean wind speed and mean wind direction for each height on both measurement flights

Height [m]	Flight 1 - 21/09/2018				Flight 2 - 22/09/2018			
	Mean wind dir [°]	Mean wind speed [m s ⁻¹]	L Ground speed [m]	L True air-speed [m]	Mean wind dir [°]	Mean wind speed [m s ⁻¹]	L Ground speed [m]	L True air-speed [m]
20	271	8.6	69.3	64.3	285	3.6	70.5	72.1
30	275	5.8	95.1	93.3	263	3.2	90.2	94.6
40	293	10.6	71.1	55.0	294	6.3	87.0	69
50	268	10.4	60.5	70.5	266	4.4	71.7	65.6
60	280	9.3	43.1	45.0	286	5.5	95.6	111.0
80	278	6.8	117.7	85.0	281	3.6	105.3	105.0
100	254	11.0	60.7	68.2	290	2.9	82.3	76.0
120	255	10.6	57.9	86.3	285	5.5	49.5	46.0
160	254	5.6	98.3	119.3	298	3.7	–	–
200	253	9.5	92.0	84.3	269	5.3	91.0	59.5

The integral length scale (L) is calculated for the mean horizontal wind speed for each flight leg with the mean true airspeed and the mean ground speed. The values are the means of all legs per height

where x_i is the reference point measured by the UAS, x_0 is the interpolated (arbitrary) point, and d is the distance between the reference x_i , the arbitrary x_0 and the power parameter p . For p approaching zero the impact of the direct neighbours onto the interpolated results reduces. A typical value for the power parameter is 2, which has been chosen in this analysis.

3.3 Tower Data

The tower data presented in Sect. 4.1 were derived using 20 s^{-1} data from wind vanes and cup anemometers installed at 10, 34, 45, 59, 86, and 100 m as well as Thies thermometers installed at 3, 23, 45, 72, and 96 m. A block mean of 10 min was applied and faulty values were removed.

3.4 Model Approach

The goal of the model chain is to create a predictive simulation tool that is able to represent several ranges of atmospheric scales in a variety of complex terrains. Three numerical models are coupled: WRF (Skamarock et al. 2008), OpenFOAM (Weller et al. 1998), and FLOWer (Kroll et al. 1999).

The Advanced Research WRF (WRF-ARW) model, version 3.8.1, is used to simulate the flow over the test site and provide the first step of the model-chain. Our set-up is similar to Talbot et al. (2012), who used six model domains nested sequentially where the outer three model nests are run in URANS mode and the three innermost domains are run in LES mode. Due to considerations of computational cost, the sixth model domain has been removed. The innermost nest has a horizontal mesh size of 150 m and consists of $301 \times 301 \times 80$ data points. Vertical grid stretching is applied. The lowest model level is located at 10 m above the ground and Δz close to the ground is 15 m. The model top is defined as about 14.5 km above sea level. The Advanced Spaceborn Thermal Emission and Reflection Radiometer (ASTER) dataset (Schmugge et al. 2003) is used for the topography and the CORINE (Coordination of Information on the Environment) dataset from 2012 for the land-use categories. The initial and boundary conditions are provided by the ECMWF (European Centre for Medium-Range Weather Forecasts) operational analysis. The additional drag caused by trees is parametrized following the approach of Shaw and Schumann (1992). This is of particular importance given that the distance between the test site and the nearest forest is less than 100 m.

The second step of the modelling chain is an OpenFOAM-based (version 6) CFD (computational fluid dynamics) model, which allows for further refinement of both vertical and horizontal resolution. The meso-microscale simulations are conducted with inflow conditions acquired from the WRF model, which stored the data along predefined borders at a 1-min interval. It provides data such as temperature, pressure, velocity, or humidity at the lateral and top boundaries of the meso-microscale domain ($10 \text{ km} \times 10 \text{ km} \times 2.5 \text{ km}$). The meso-microscale model, implemented into the open source code OpenFOAM is based on an unsteady Reynolds-averaged Navier–Stokes approach. The transport equations for mass, momentum, and potential temperature are solved under the Boussinesq approximation, where density is only influenced by buoyancy forces. The turbulent equations are solved using a modified version of the standard $k-\epsilon$ model (El-Bahlouli et al. 2019). The $k-\epsilon$ model uses the TKE k and its dissipation rate ϵ .

The FLOWer simulation results from the third step are only available for a very short time frame of 10 min due to the computational efforts necessary. Hence, an explanation of the model and a comparison to the UAS data were not considered useful herein.

Table 3 Measurement heights flown by MASC-3 for both days in September 2018

Altitude [m]	Flight 1 - 21/09/2018			Flight 2 - 22/09/2018		
	Start [UTC]	End [UTC]	10-min file [UTC]	Start [UTC]	End [UTC]	10-min file [UTC]
20	1058	1104	1100	1324	1336	1330
30	1106	1113	1110	1319	1323	1320
40	1115	1120	1120	1311	1316	1320
50	1136	1140	1140	1344	1350	1350
60	1142	1148	1150	1305	1310	1310
80	1151	1155	1200	1351	1357	1400
100	1155	1204	1200	1257	1303	1300
120	1204	1211	1210	1357	1404	1400
160	1212	1218	1220	1404	1410	1410
200	1219	1227	1230	1413	1416	1420

The columns ‘Start’ and ‘End’ are the times the UAS measured in a single height. The times in ‘10-min file’ are the chosen 10-min files from the models for the comparison against the UAS data

To make a useful comparison between the measurements of the MASC-3 and the results by the first two model chain steps (WRF and OpenFOAM), it was necessary to align the 10-min mean model output data with the measurements from the 1.5-hr flight. To accomplish this, the flight data were split into altitude bins, each bin containing all flight legs of that altitude. Then the start and end time of each altitude bin were calculated in UTC. The model data were available as 10-min means, also in UTC. In the next step, the models 10-min file closest to the corresponding time of each altitude bin of the MASC-3 data was chosen. Table 3 gives an example on how the 10-min files were chosen for the flight on 21 September 2018. The 10-min files contain the values of the previous 10 min.

In the next step, the altitude at which the MASC-3 was flying during that simulation timestep was extracted from the 10-min file (e.g., altitude 20m from the 1100 UTC 10-min file). To get the contour plots from model data in Sect. 4, the model data for each altitude were combined into a single data array to be interpolated and then plotted into a filled contour. The escarpment shape for the models does not show the trees, which makes it seem to be interpolated at different levels when in fact both the measurements and model data are interpolated on the same levels.

4 Results

In the first step, tower data are analyzed to ensure a quasi-steady situation i.e., to make sure there are no sudden variations (e.g., due to micro-fronts or similar events) in wind speed and direction during the flights. In Sect. 4.2, the UAS measurements for 21 and 22 September 2018 for different variables and a comparison to simulation results from the model chain are presented.

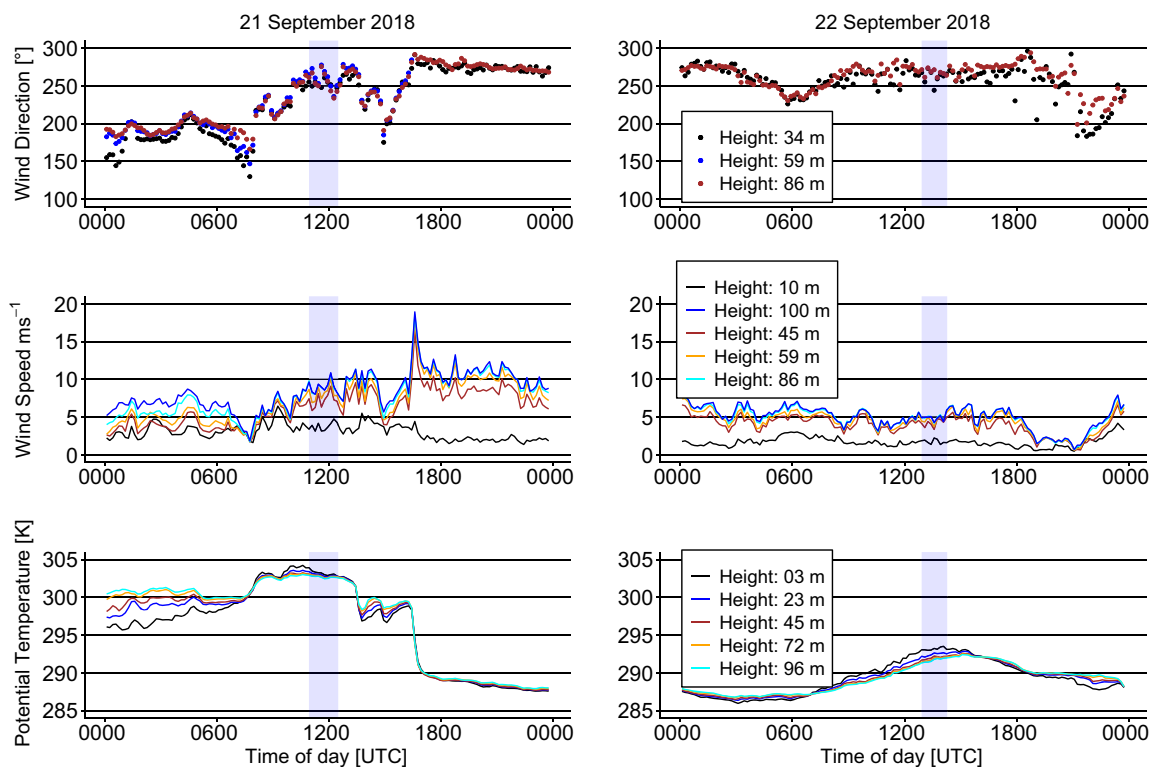


Fig. 4 Mean wind speed and wind direction (10, 34, 45, 59, 86, and 100 m) measured by cup anemometer and wind vanes and a Thies thermometer (3, 23, 45, 72, and 96 m) mounted on the wind measurement mast close to the escarpment on 21 September and 22 September 2018. The blue vertically stretched rectangles indicate the flight duration of the UAS

4.1 Diurnal Variations from Tower Data

An overview of the diurnal variations at the test site for both days is presented in Fig. 4. The data originate from tower instrumentation located on site with measurement heights between 3 and 100 m a.g.l. and shown in UTC. On 21 September 2018, the atmosphere is stably stratified with the potential temperature increasing with height from 296 K in 3 m to 301 K in 96 m. With mainly southern wind directions during this period, wind speed increases with height from 3–4 m s^{-1} at 10 m to around 8 m s^{-1} at 100 m. At 0700 UTC, wind speed at all measurement heights decrease to a mutual point of about 2 m s^{-1} .

After sunrise temperatures increase to 304 K close to the ground and 303 K in 96 m leading to a slightly unstable stratified atmosphere. The wind speed at all levels except the lowest are similar for the next hours, fluctuating between 6 and 12 m s^{-1} . The wind direction changes slowly from south to west during that period. The passage of a cold front at 1630 UTC is marked by a sudden drop in temperature by 10 K, a shift of the wind direction, and a sharp increase in wind speed. During the night, the atmosphere remains neutrally stratified as the wind speed remains above 6 m s^{-1} except for the lowest level. The next day began with westerly winds, wind speeds around 7 m s^{-1} and a neutral stratification. The wind speed is generally lower compared to the previous day and varies between 3 and 7 m s^{-1} . The measurements at 10 m show wind speeds between 1 and 3 m s^{-1} . The wind speed at 10 m above ground differs from measurements at greater heights due to a shadowing effect of the forest. In the early evening, as soon as the wind direction changes to south, the spread between the measurement heights becomes less significant and the wind speeds decrease.

The time periods of the two flights are highlighted by a blue shade in Fig. 4. During the measurement flight on 21 September 2018, the wind direction varies between 260 and 275°, wind speeds fluctuate between 6 and 12 m s⁻¹, and the atmospheric stratification is near neutral. The conditions on the next day are marked by a westerly wind at about 5 m s⁻¹ and a slightly unstable atmosphere with potential temperature values of 293.5 K close to the ground and 292 K at 96 m.

4.2 Measurements and Model Data

21 September 2018 was a mild day with temperatures slightly over 20 °C and a mean westerly wind speed of 8.8 m s⁻¹. On 22 September 2018, the temperature was 5 °C lower with a mean westerly wind speed of 4.4 m s⁻¹ (see Table 1).

The in situ data measured by the UAS and the results from the WRF and OpenFOAM models for 21 September 2018 are illustrated in Figs. 5, 7, 9, and 11, and those for 22 September 2018 in Figs. 6, 8, 10, and 12. To compare the measurements with the model results the approach explained in Sect. 3.4 was used.

For 21 September 2018 (Fig. 5a), the wind speed over the plateau varies from 3.5 to 14 m s⁻¹. The wind maximum is established at a height of 250 m at a distance of 900 m to 1000 m. At 200 m a.g.l. and a distance of 800 m is another area with higher wind speeds peaking at 10 m s⁻¹. The wind speeds above 250 m vary from 4 to 8 m s⁻¹ at a distance between 200 and 500 m and 8 to 12 m s⁻¹ at 500 to 1000-m distance. At the lee side of the tree tops, in the lowest 50 m a.g.l. along the plateau, the horizontal flow is decelerated. This is the area with the highest difference in wind speeds within a few metres vertical extent, ranging from 4 to 10 m s⁻¹.

The measured wind speed on 22 September 2018 is illustrated by Fig. 6a. Wind speeds vary between 4 and 6 m s⁻¹ in a stretch over the full extent of the plateau at heights of 210 to 240 m. Below this strip, at the lee side of the trees, ranging vertically from 180 to 200 m, lower wind speeds between 2 and 4 m s⁻¹ occur. Another area with wind speeds between 2 and 4 m s⁻¹ appears between 240 and 270 m in distance and between 500 and 1000 m. The wind maximum of 8 m s⁻¹ is established at a height of 360 m in a distance of 500 m. The wind speeds above 250 m vary from 4 to 8 m s⁻¹. The mean wind speed measured in the bottom left corner of the plotting plane fluctuates between 2 and 4 m s⁻¹.

The model results for 21 September 2018 and 22 September 2018 are shown in Fig. 5b, c and Fig. 6b, c, respectively. The WRF model in Fig. 5b calculated a streak of wind speeds above 10 m s⁻¹ at heights between 200 and 260 m. Below 200 m height and at distances of more than 600 m, the wind speed decreases to less than 5 m s⁻¹. At a distance of less than 600 m the WRF simulation determines wind speeds between 6 and 10 m s⁻¹. Above 260-m altitude another small patch of wind speeds less than 10 m s⁻¹ can be seen. Between 280 and 400 m, with increasing distance, the wind speed decreases from 15 m s⁻¹ to less than 10 m s⁻¹.

The OpenFOAM model results for the horizontal wind speed illustrated in Fig. 5c shows an area of wind speeds in a range of 14 m s⁻¹ to 16 m s⁻¹ in 250 m altitude and a distance of 400 to 1100 m. Another area with wind speeds around 15 m s⁻¹ is located over the valley in a small band between 190 to 200 m and over the plateau between 180 and 220 m altitude. At distances between 100 and 850 m the wind speed decreases to less than 8 m s⁻¹ in some regions close to the ground and at altitudes between 200 and 240 m. The wind speed at heights above 260 m ranges between 8 m s⁻¹ and 13 m s⁻¹ with lower wind speeds towards the edges of the plot plane.

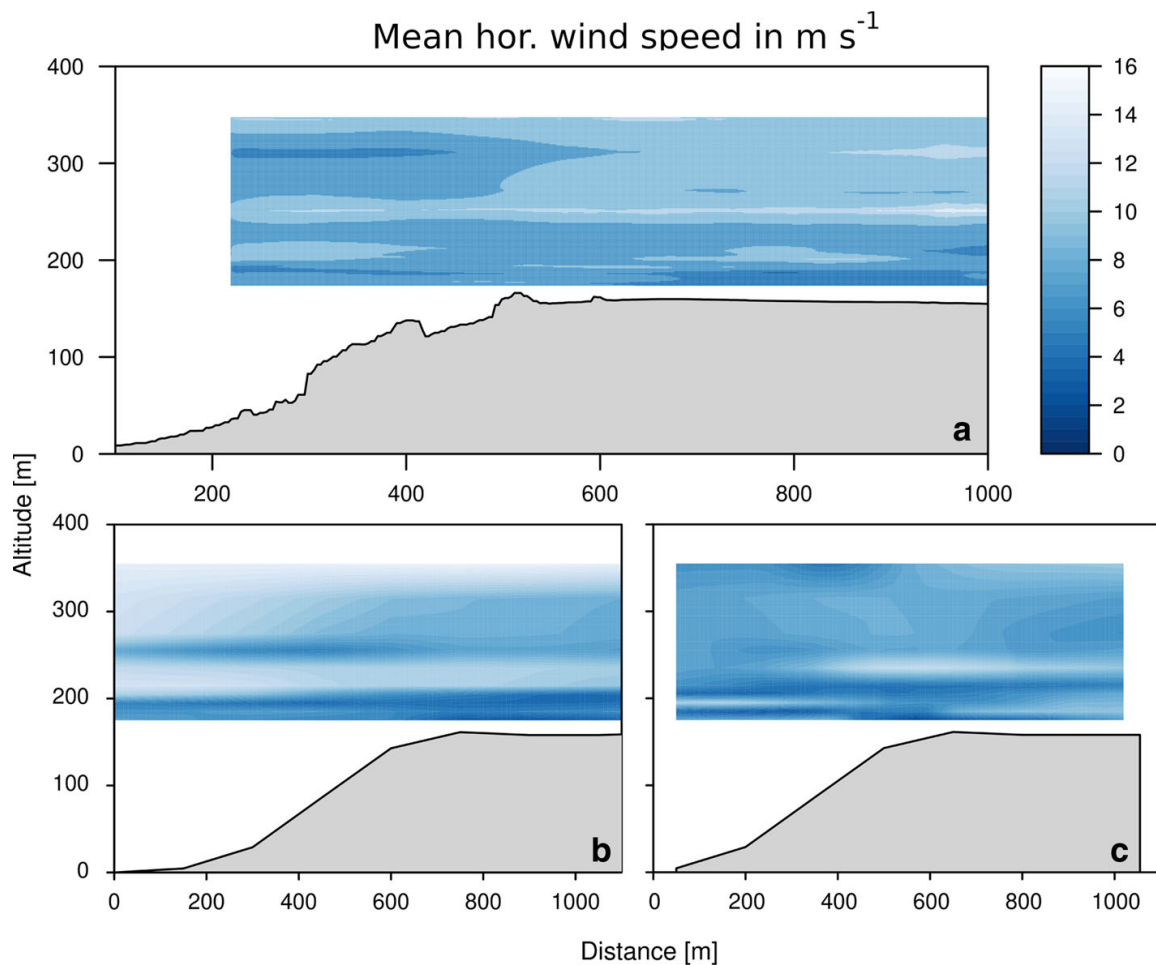


Fig. 5 MASC-3 measurement of the mean wind speed derived through interpolation from horizontal flight legs between 1055–1229 UTC (a) and the mean horizontal wind speed during the UAS flight time calculated by WRF (b) and OpenFOAM (c) models on 21 September 2018. The left side of the plot is facing west. Reference height of zero is at the bottom of the valley

For 22 September 2018 the WRF model in Fig. 6b estimated wind speeds between 1 and 6 m s^{-1} for altitudes between 180 and 250 m. Above 250 m the wind speed increases to values of 6 to 8 m s^{-1} . The lowest wind speeds of 3 m s^{-1} and less are located close to the ground above the plateau in distances between 800 and 1100 m. Two more patches with wind speeds in the range of 2 to 4 m s^{-1} were calculated in heights of 200 and 230 m and a distance between 0 and 600 m.

The OpenFOAM model reported areas of wind speeds less than 3 m s^{-1} close to the ground above the plateau and at a height of 200 m and a distance of 200 m. Patches of wind speeds above 6 m s^{-1} are shown in some areas beginning close to the ground over the escarpment at a distance of 400 m. With increasing altitude, three more areas of wind speeds higher than 6 m s^{-1} can be seen. The most significant ones are at altitudes between 230 and 280 m and 300 and 350 m. Between those two bigger areas of higher wind speeds a small stretch of wind speeds below 5 m s^{-1} was simulated.

For 21 September 2018, Fig. 7a shows a wind-direction change over the plateau from 265° at 190 m to 235° at 360 m above the surface. The strongest direction change appears directly over the escarpment with a difference of 60° to the north between 190 and 270 m above ground. The change in wind direction is less distinct among distances of 700 to 1000 m with wind directions of 260° instead of 285° above the escarpment.

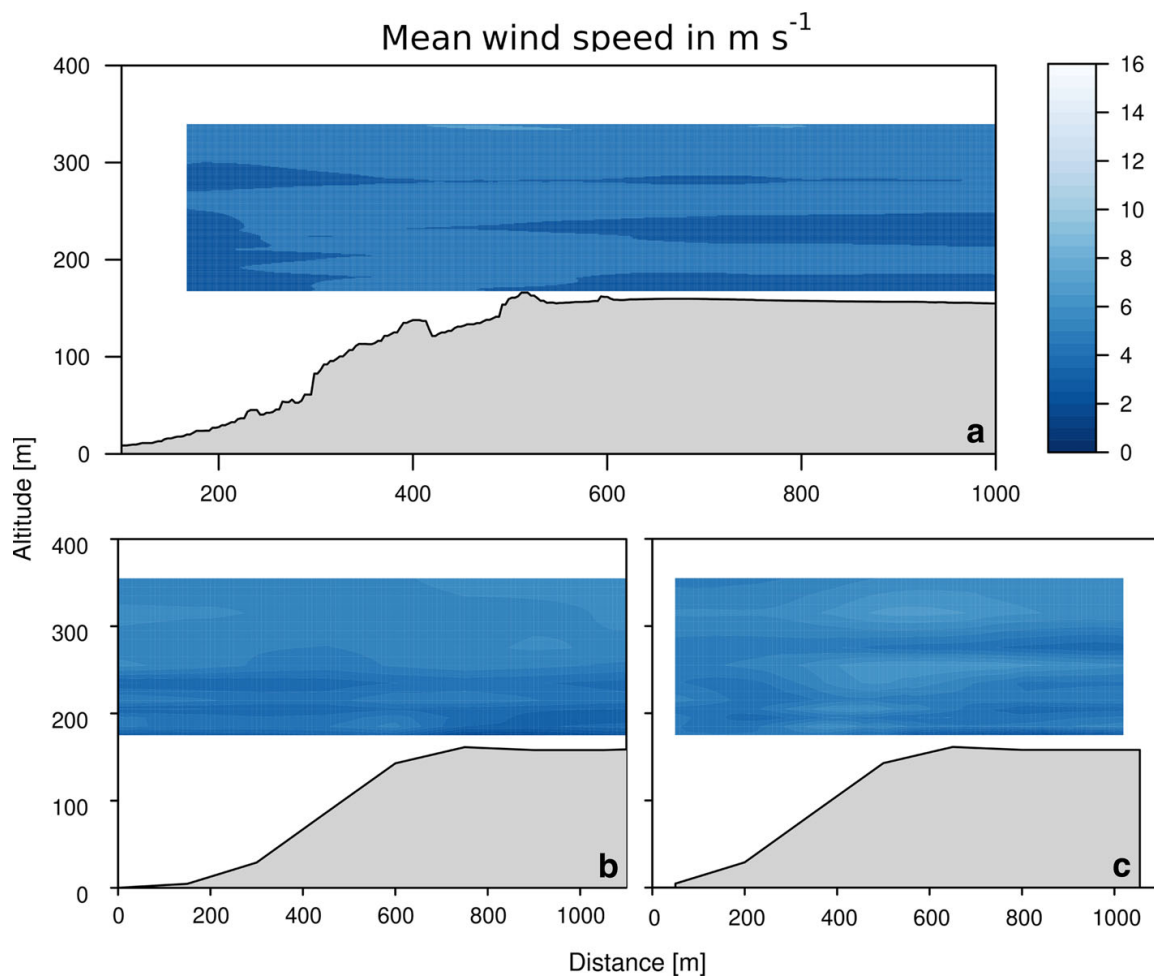


Fig. 6 MASC-3 measurement of the mean wind speed derived through interpolation from horizontal flight legs between 1255–1417 UTC (a) and the mean horizontal wind speed during the UAS flight time calculated by WRF (b) and OpenFOAM (c) models on 22 September 2018. The left side of the plot is facing west. Reference height of zero is at the bottom of the valley

The overall mean wind direction on the 22 September 2018 was 282° , which is 20° different to the measurement on 21 September 2018. The wind direction immediately above the escarpment varies between 280° and 320° , while most of the wind directions in the measured area are within 280° . Another small patch and a larger area with directions beyond 280° occur close to the ground in distances between 650 and 800 m and in heights of 170 to 200 m above the escarpment, respectively.

The WRF model in Fig. 7b shows two areas with a wind direction of up to 290° . The area with a stronger change in wind direction compared to the surrounding area is located at an altitude of 200 m over the escarpment edge in a distance of 500 to 900 m. The second area with a stronger change in wind direction is positioned higher aloft at 240 to 290 m altitude.

The OpenFOAM model shows two areas of wind directions towards 220° at an altitude of 190 m on both ends of the plot plane. Underlying, close to the ground, a wind shear from 220° to more than 260° is visible. Above 220 m the wind direction changes to nearly 280° and back to less than 250° at 350-m altitude.

On 22 September 2018 (Fig. 8b, c) both models predict the wind direction between 280° and 300° . The WRF model, in Fig. 8b, calculated a wind direction exceeding 300° in some small areas above the top edge of the escarpment and the plateau. Approaching the escarpment in distances between 0 and 400 m and heights in the range of 250 to 360 m, the wind direction

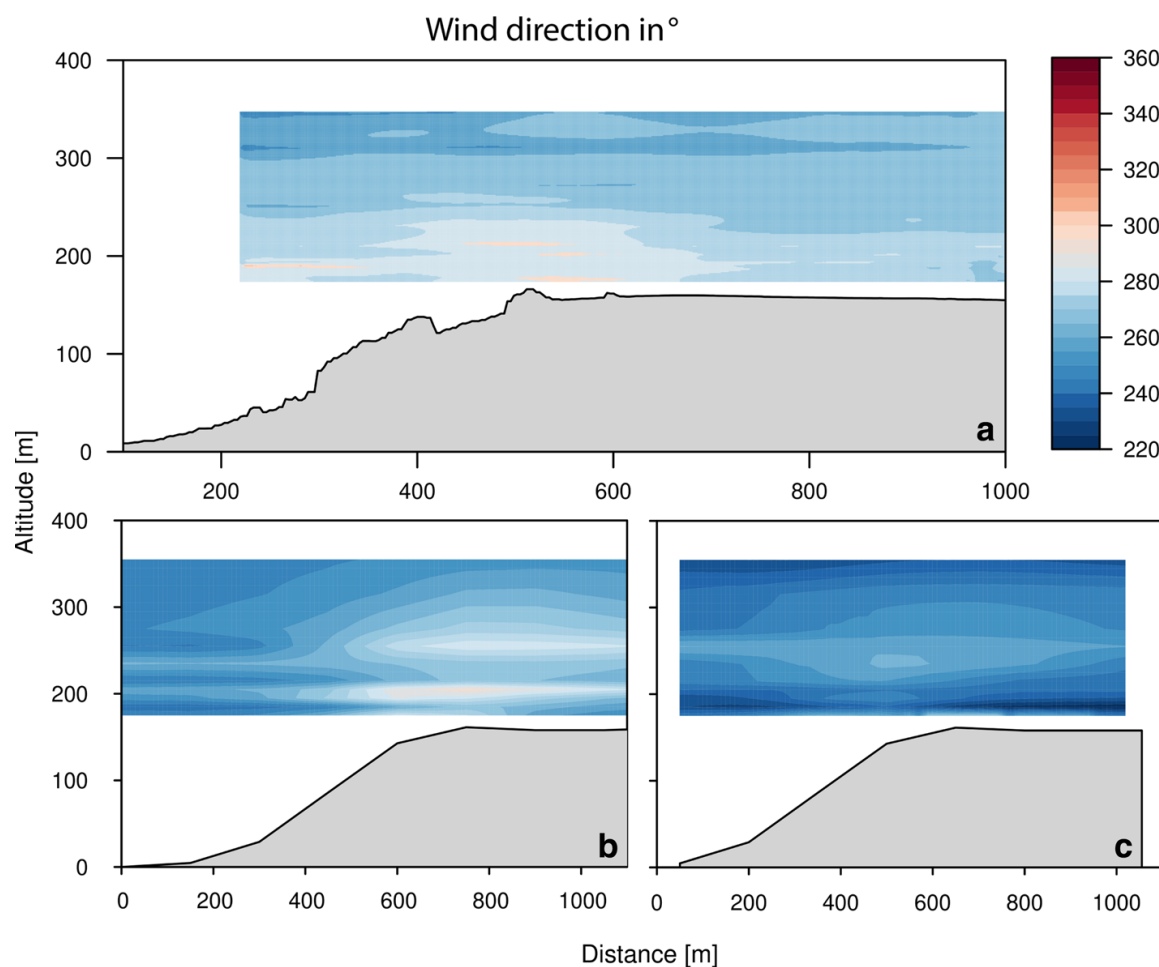


Fig. 7 MASC-3 measurement of the wind direction derived through interpolation from horizontal flight legs between 1055–1229 UTC (a) and the mean wind speed during the UAS flight time calculated by WRF (b) and OpenFOAM (c) models on 21 September 2018. The left side of the plot is facing west. Reference height of zero is at the bottom of the valley

changes from 300° to 280°. This change in wind direction is less distinct in the OpenFOAM model results. Figure 8c shows three thin areas of wind direction around 260°. Two of those are located at heights just below and above 200 m in distances between 100 and 550 m. The third stretch is positioned over the escarpment top in an altitude of 180 m. Apart from a large area at altitudes between 250 and 340 m with a wind direction of 290°, only a small area between 100 and 400 m distance and a height of 180 to 190 m shows wind directions of more than 300°.

The TKE (Fig. 9a) during the time of measurement on 21 September 2018 reaches maximum values of $14 \text{ m}^2 \text{ s}^{-2}$ behind the escarpment and close to the ground. Other areas with values higher than $4 \text{ m}^2 \text{ s}^{-2}$ can be found at heights of 260 to 300 m above ground in a distance 600 to 800 and over the escarpment at a distance of 300 to 500 m and a height of 200 m above the plateau ground level. The latter reaches values of 10 to $14 \text{ m}^2 \text{ s}^{-2}$. The TKE within the other regions varies between 0 and $4 \text{ m}^2 \text{ s}^{-2}$. The long vertical stretch of very low TKE values close to $0 \text{ m}^2 \text{ s}^{-2}$ at the right border are a result of a boundary-value problem within the interpolation.

The TKE (Fig. 10a) during the time of measurement on 22 September 2018 reaches maximum values between 7 and $8 \text{ m}^2 \text{ s}^{-2}$ close to the plateau ground in the lee area of the trees in distances of up to 700 m. The vertical extent of this stretch is up to 230 m above

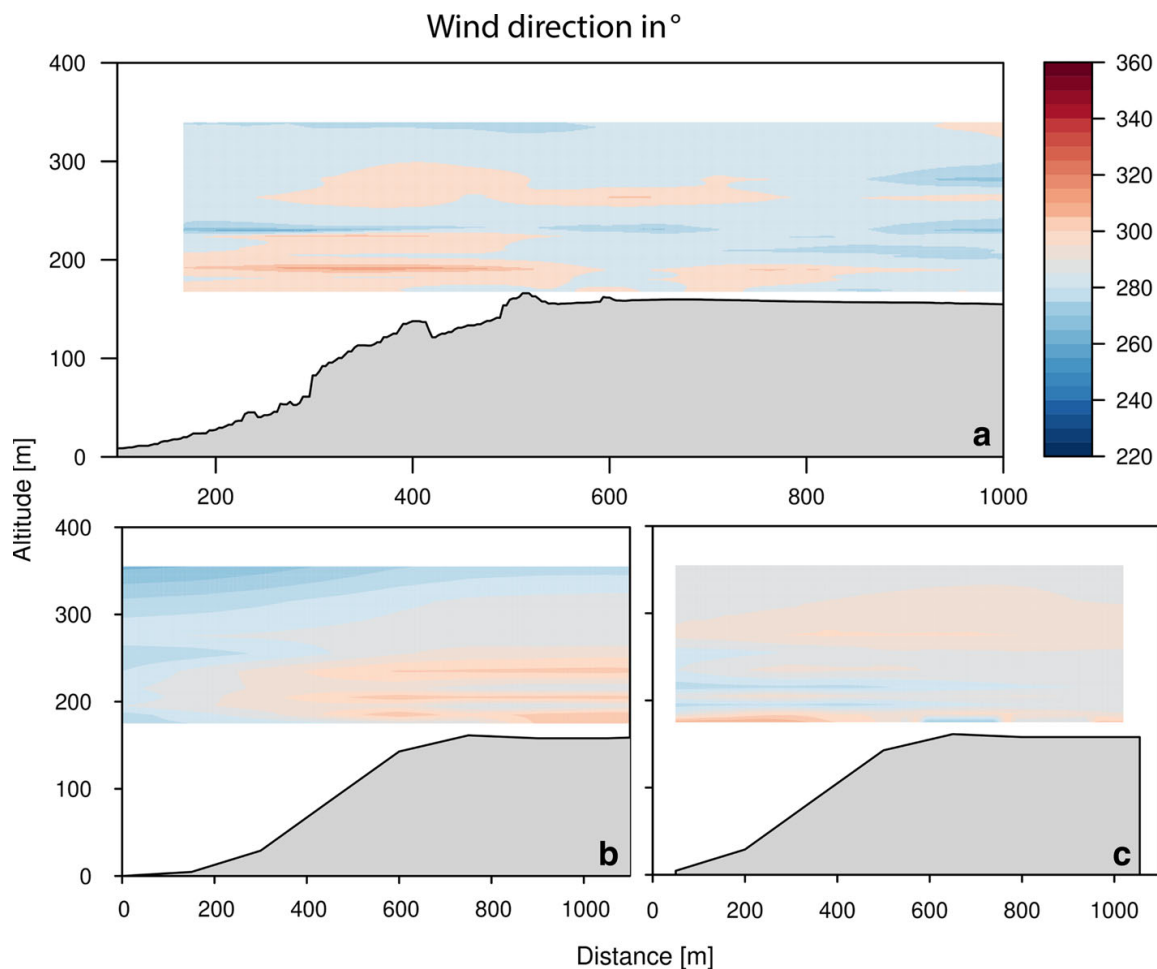


Fig. 8 MASC-3 measurement of the wind direction derived through interpolation from horizontal flight legs between 1255–1417 UTC (**a**) and the mean wind speed during the UAS flight time calculated by WRF (**b**) and OpenFOAM (**c**) models on the 22 September 2018. The left side of the plot is facing west. Reference height of zero is at the bottom of the valley

ground. In other areas k peaks at $2 \text{ m}^2 \text{ s}^{-2}$ with small patches of values up to $4 \text{ m}^2 \text{ s}^{-2}$. In the trees' lee the TKE is up to three times higher compared to the undisturbed flow in front of the escarpment.

Model results for both days are shown in Figs. 9b, c and 10b, c for 21 September 2018 and 22 September 2018, respectively. The WRF model for 21 September 2018 in Fig. 9b calculated values for the TKE between 0 and $5 \text{ m}^2 \text{ s}^{-2}$, with the highest values close to $5 \text{ m}^2 \text{ s}^{-2}$ in a stretch along the plot at a height of 200 m and a larger area between 0 and 550 m distance and altitudes at a range of 240 to 280 m. The lowest 20 m of the plotted data in front of the escarpment show values of less than $2 \text{ m}^2 \text{ s}^{-2}$ for k while the TKE over the plateau is higher with values reaching $3 \text{ m}^2 \text{ s}^{-2}$. The upper left part of the plotting plane also shows TKE close to zero.

The OpenFOAM model in Fig. 9c calculated the TKE of 6 to $8 \text{ m}^2 \text{ s}^{-2}$ for the bottom half of the plotting area, with an exception for the lowest 30 m above the plateau, where the TKE is below $2 \text{ m}^2 \text{ s}^{-2}$. The upper half of the plotted data shows an increase in k with distance from left to right.

On 22 September 2018 the TKE modelled by the WRF model shows values of near $0 \text{ m}^2 \text{ s}^{-2}$ for most of the plot. Only a small patch in 280 m height and 400 m distance together with an area above the plateau and the top of the escarpment has a TKE between 2 and $4 \text{ m}^2 \text{ s}^{-2}$.

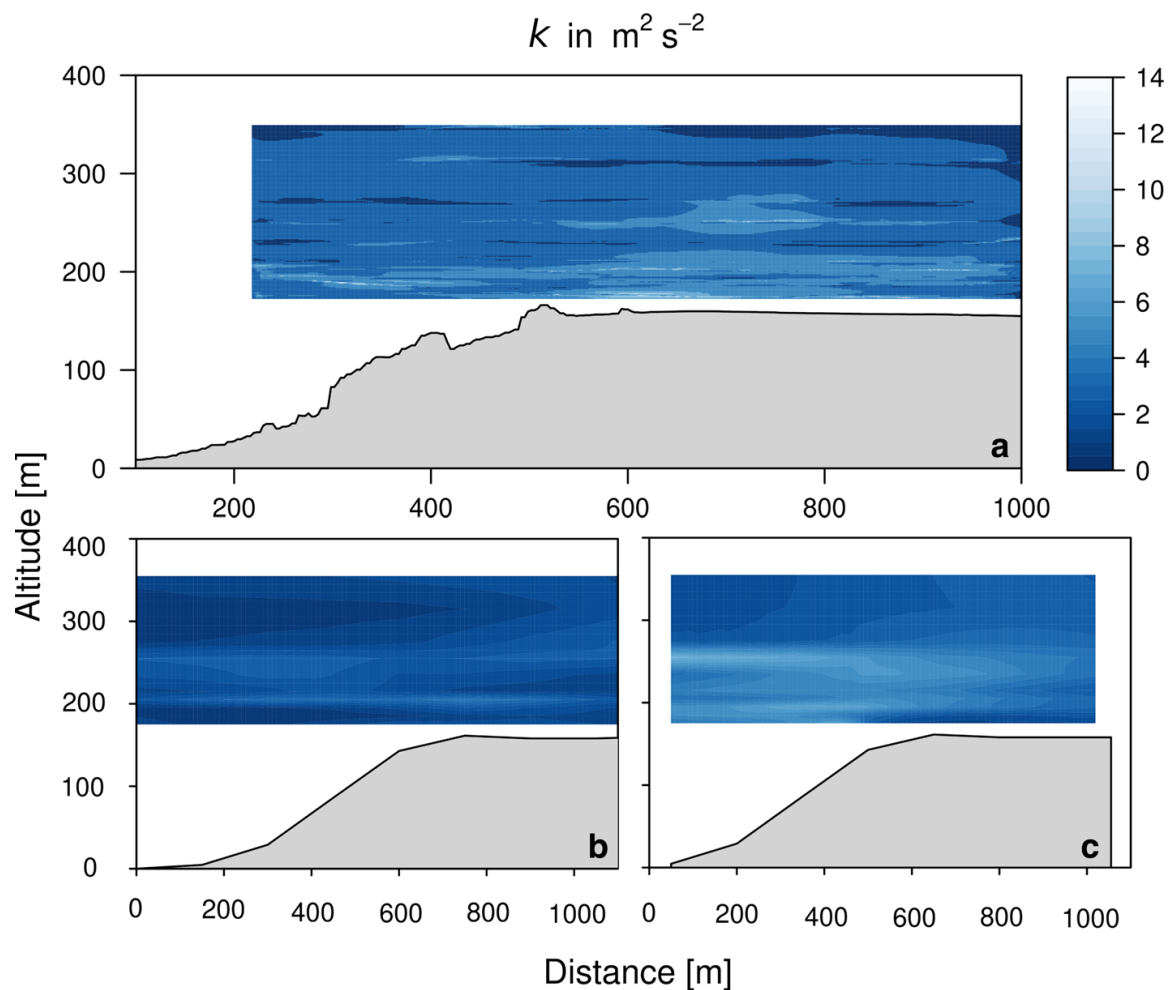


Fig. 9 MASC-3 measurement of the TKE derived through interpolation from horizontal flight legs between 1055–1229 UTC (a) and the mean wind speed during the UAS flight time calculated by WRF (b) and OpenFOAM (c) models on 21 September 2018. The left side of the plot is facing west. Reference height of zero is at the bottom of the valley

The OpenFOAM model in Fig. 10c is again divided in an upper and bottom part. The bottom half of the plot shows a TKE of $2 \text{ m}^2 \text{ s}^{-2}$ with an area of nearly $4 \text{ m}^2 \text{ s}^{-2}$ at a distance between 400 and 700 m and altitudes ranging from 180 to 270 m. In the upper half, k reaches maximum values of $1 \text{ m}^2 \text{ s}^{-2}$.

The change in inclination angle for 21 September 2018 is shown in Fig. 11a. Over the escarpment positive inclination angles of up to 20° are visible at heights between 190 and 260 m. The inclination angle over the plateau varies between 0° and 10° with a few spots of angles towards -10° . In an area in a distance of 700 to 1000 m and a height above ground of 230 to 250 m, negative inclination angles of up to -10° are established.

The change in inclination angle for 22 September 2018 is shown in Fig. 12a. Over the escarpment, positive inclination angles of up to 20° are visible in heights between 190 and 250 m. The inclination angle over the plateau varies between 0° and -10° with a few spots of angles towards -20° at a distance of 1000 m. In general a positive inclination was measured over the escarpment, while the inclination angles above the plateau are mostly negative.

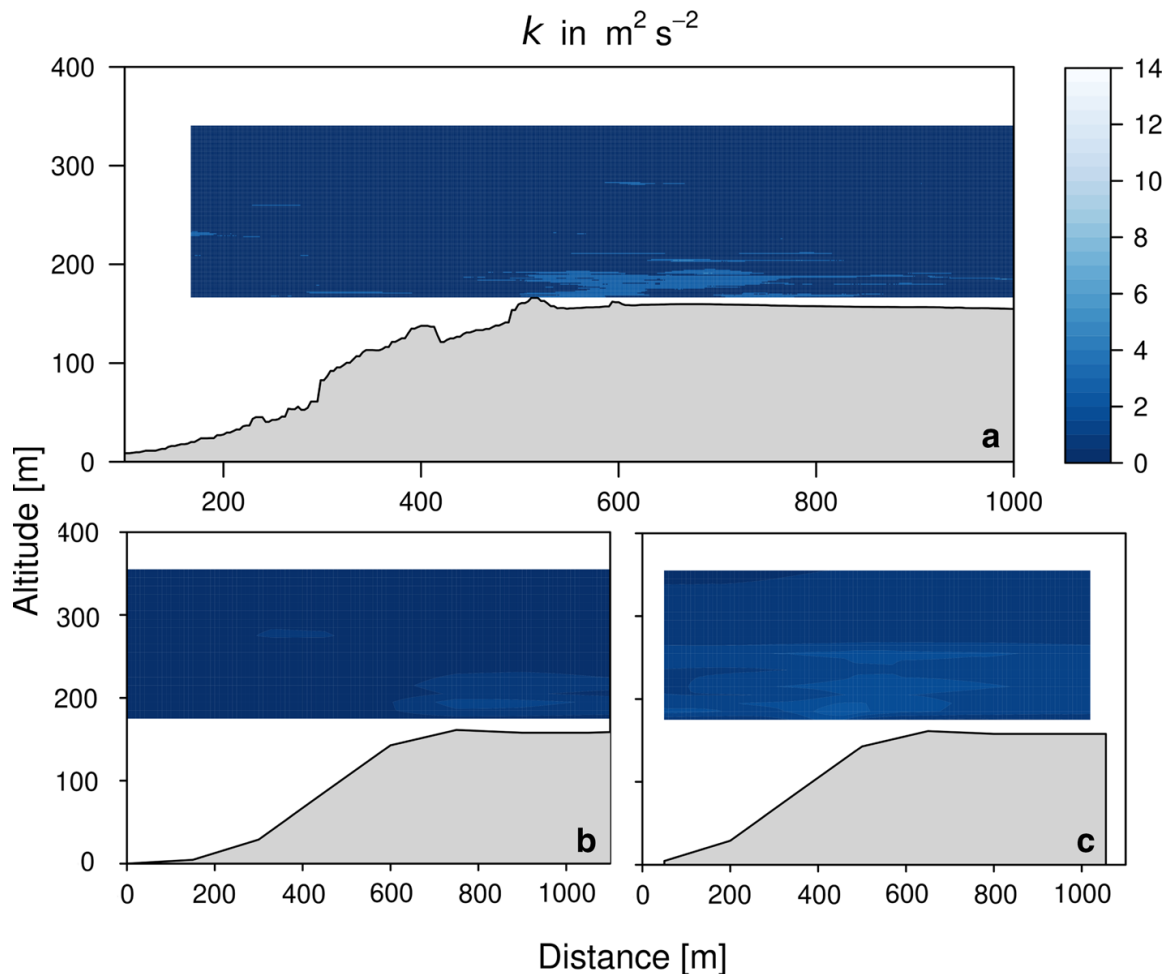


Fig. 10 MASC-3 measurement of the TKE derived through interpolation from horizontal flight legs between 1255–1417 UTC (**a**) and the mean wind speed during the UAS flight time calculated by WRF (**b**) and OpenFOAM (**c**) models on 22 September 2018. The left side of the plot is facing west. Reference height of zero is at the bottom of the valley

Figure 11b shows the WRF results for the inclination angle on 21 September 2018. At a distance of 600 m, above the escarpment top, the plot indicates an upward motion with an inclination of up to 20° . This positive inclination angle can also be seen in another patch 50 m aloft. Between altitudes of 180 and 240 m a negative inclination angle of nearly -10° is visible.

The OpenFOAM model simulated a similar picture with smaller positive and negative changes in the inclination angle. A positive inclination angle of 10° to 20° can be seen in altitudes between 180 and 230 m in a distance of 300 to 400 m. The area with negative inclination angles reaching -6° over the plateau is extended over the whole plateau.

For 22 September 2018 the inclination angle in Fig. 12b, c is more distinct compared to the first day. Negative inclination of up to -10° , and therefore indicating a downward motion, can be seen above the plateau in distances between 700 and 1100 m. The location of positive inclination angles calculated by the WRF model is again above the upper part of the escarpment reaching onto the plateau. Below 200 m the inclination angle reaches more than 20° and therefore its highest positive value. The positive angle is then changing to 0° at 360 m altitude. At a distance of 900 m the inclination angle has negative values of up to -10° at 300 m altitude.

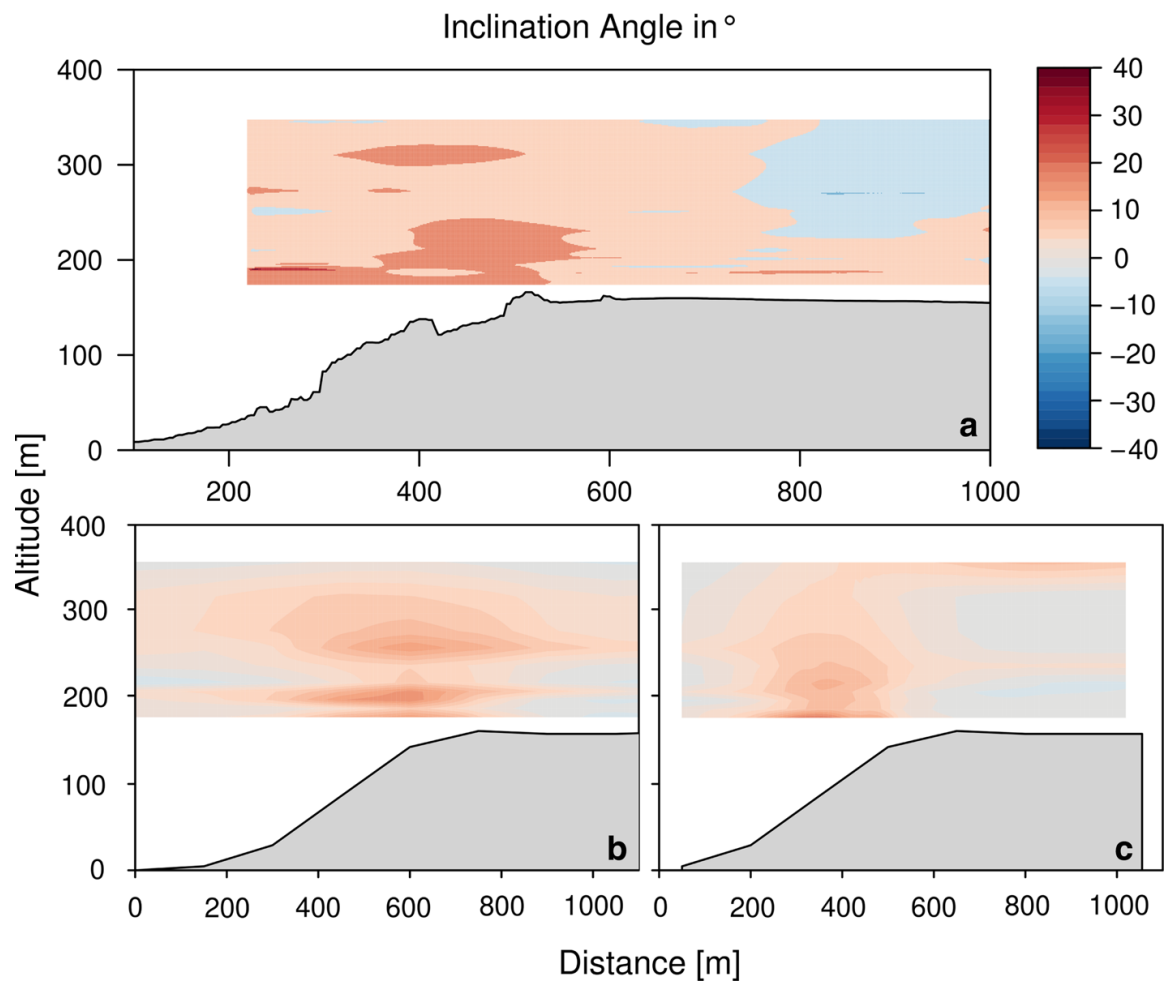


Fig. 11 MASC-3 measurement of the inclination angle derived through interpolation from horizontal flight legs between 1055–1229 UTC **(a)** and the mean wind speed during the UAS flight time calculated by WRF **(b)** and OpenFOAM **(c)** models on 21 September 2018. The left side of the plot is facing west. Reference height of zero is at the bottom of the valley

The location of positive inclination angles from the OpenFOAM model is located at the same spot over the escarpment compared to 21 September 2018. The positive inclination for 22 September 2018 reaches more than 20° in altitudes of 190 to 220 m. With height the inclination angle changes towards 5° , not reaching a neutral position within the plot plane.

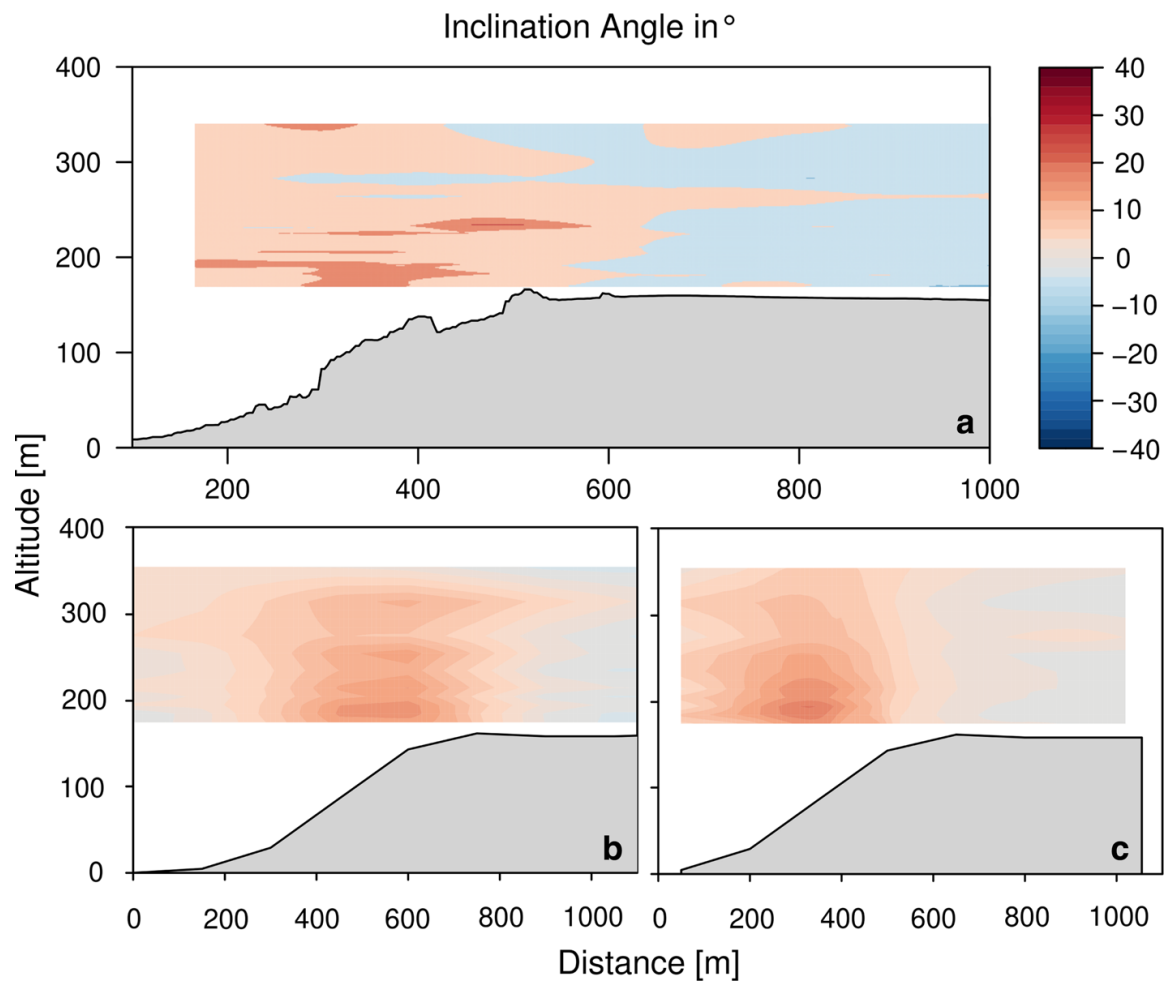


Fig. 12 MASC-3 measurement of the inclination angle derived through interpolation from horizontal flight legs between 1255–1417 UTC (**a**) and the mean wind speed during the UAS flight time calculated by WRF (**b**) and OpenFOAM (**c**) models on 22 September 2018. The left side of the plot is facing west. Reference height of zero is at the bottom of the valley

5 Discussion

5.1 Wind-Field Measurements

This subsection discusses the results from MASC-3. Independent of the different wind speeds, the results obtained from airborne in situ measurements and models presented above show similar flow features for two different days. Heights between 20 and 200 m above the plateau, relevant for the installation and operation of the wind energy converters in their planned locations, were covered. A Bernoulli-like effect of an accelerated flow over an obstacle is expected in regions with complex terrain (Belcher et al. 2012). Such behaviour was observed on both days. The flow accelerated in areas beginning at the top of the escarpment along the plateau in heights between 40 and 80 m above ground. Below and above those areas are zones with reduced wind speeds. In the lee of the trees the wind speed continues to decrease. How distinctive these areas are depends on the mean wind speed and the wind direction. For westerly wind directions the path to overcome the escarpment is 60–80% shorter compared to a flow from the north-west or south-west (Fig. 1). The longer path through the forested escarpment removes energy from the flow, which results in a stronger deceleration in the lee of the trees. Figures 7a and 8a show a wind direction change of more than 20° from

western towards northern winds. This change is a possible result of a channeling flow along the escarpment southward.

After a certain distance we would expect to see a recirculation zone between the accelerated flow due to the escarpment and the decelerated area below (Berg et al. 2011). This phenomena describes a detachment of the flow above the trailing edge of the escarpment and a reattachment (i.e., a downward motion) further downstream the plateau. The distance from the trailing edge where this downward motion happens depends on multiple factors like the shape and height of the obstacle and the speed and direction of the flow (Berg et al. 2011). For 21 September 2018 (Fig. 5a), we see an area at the right end of the plot at a distance of 1000 m that could be the beginning of the flow recirculation. For 22 September 2018 (Fig. 6a), with lower general wind speeds, a recirculation zone would be expected closer to the escarpment, but there is no indication of increased momentum towards the ground. Due to the low wind speeds and the less distinct difference between the areas of accelerated and decelerated flow, a recirculation zone might not be present. Menke et al. (2019) found that during the Perdigão experiment recirculation zones mostly developed in conditions of mean wind speeds $>8 \text{ m s}^{-1}$

Neutral to negative angles above the plateau on both days indicate a downward movement, which facilitates the formation of a recirculation zone over the plateau. However, this conclusion is ambiguous, because Figs. 11a and 12a could as well be interpreted to show the tendency of the flow detaching without recirculating towards the ground. A previous study (Wildmann et al. 2017) used the previous version of MASC over the same area, obtained similar results, but at that time it was not possible to measure below 60 m above the plateau. This gap was filled by using the MASC-3, flying as low as the tree tops covering the upper edge of the escarpment, to show that at canopy height the highest turbulence, generated by the forest, was measured. Another small patch of high TKE has been measured on 21 September 2018 in a distance of 300 m above the escarpment (see Fig. 9a). If a free-flowing atmosphere west of the escarpment is considered, values that high are not expected. One possible explanation is the presence of the single hill upstream (Fig. 1) causing a disturbance and turbulence.

For both days it is difficult to distinguish between an orographically-forced acceleration of the flow and the impact of the stratification (Fig. 4). The air close to the ground was warmer than the air aloft. The difference in potential temperature with height is small, which has an effect on air masses being lifted vertically, but the impact of the escarpment in these cases should be considerably higher.

Despite the large difference in wind speed between the two days, atmospheric phenomena like acceleration of the flow with a recirculation zone over the plateau, the difference in inclination angle above the escarpment and the plateau, and high TKE values downstream of the trees were captured by MASC-3. High TKE close to the ground and along the plateau, together with the inclination angles, and the wind shear along the rotor plane found in similar locations are important factors to improve the modelling efforts for wind-field simulations in complex terrain, especially to resolve the TKE in the lee of the trees for different occurrences, as this directly impacts the fatigue loads onto wind turbines placed in such locations.

In the past, studies by Emeis et al. (1995), Berg et al. (2011), and Lange et al. (2016) investigated the effect of escarpments on flows. The study by Emeis et al. (1995) showed similar features over a smaller escarpment in Hjørdemal, Denmark. The study used 18 measurement masts equipped with cup and sonic anemometers between 5 and 10 m above ground, upstream and downstream of a 16-m high escarpment. A speed-up over the crest was measured for three different thermal stratifications. The results look similar to the measurements conducted in the present study. A small internal boundary layer formed right behind the top of the escarpment. The studies by Berg et al. (2011) and Lange et al. (2016) were both carried

out at the Bolund test site in Denmark. Berg et al. (2011) found a speed-up of 30% over the top of the escarpment and a maximum enhancement of the turbulence intensity of 300% compared to the undisturbed flow in front of the escarpment. A key difference to the present study is the forested escarpment. The effect of trees onto the flow was not investigated in any of these studies. Emeis et al. (1995) also found an impact of the escarpment on the upstream flow and its properties as far down as 400 m. This effect could not be investigated with the measurement set-up in the present study, but should be considered for future measurements. An effect of the escarpment on the wind direction itself was found, but no indications of the wind direction influencing the wake characteristics like TKE and wake length behind the escarpment.

To analyze small turbulent structures and the wind field in more detail, Berg et al. (2011) proposed a measurement approach with a higher temporal and especially a higher spatial resolution by using scanning lidars instead or additionally using masts in fixed locations and heights. This study adds to an approach with UAS providing measurements with high spatial and temporal resolution over a large area of the flow moving over an escarpment and thus is a good tool to validate and improve models in complex terrain.

5.2 Comparison with the Model Chain

To validate the numerical model chain for flow simulation over the escarpment and along the future wind turbines, MASC-3 data from 21 and 22 September 2018 were compared with simulations for the first two model steps (WRF and OpenFOAM).

The coarse WRF model simulation as well as the finer OpenFOAM model are in agreement with the UAS measurements. In particular the inclination angle in Fig. 11b, c and Fig. 12b, c and the mean horizontal wind Figs. 5b, c and 6b, c give promising results when compared with the measurements and are capable of modelling local phenomena such as over-speeding and small changes in inclination angle in complex terrain. The OpenFOAM model predicted the speed-up over the escarpment at similar locations as the MASC-3. These locations are as well in agreement with past research by Emeis et al. (1995) and Chow and Street (2009). The area of higher wind speeds calculated by the WRF model starts at a similar distance, but is located in lower altitudes.

The WRF model is the first step in the model chain and serves as input for the OpenFOAM model. Naturally the OpenFOAM model should be in better agreement with measurements and literature than the WRF model. For the inclination angle (a proxy for the vertical velocity) both models (Fig. 12b, c) gave results in good agreement with the measurements. In small areas above the escarpment the OpenFOAM model performs slightly better. Features like the turnover point from positive to negative inclination angles at 600 m distance were captured by the OpenFOAM model while WRF shows a stronger upward flow at that location. Emeis et al. (1995) also showed the highest vertical velocity close to the top of the escarpment.

The calculations for the TKE and the wind direction need to be adjusted (e.g., using a more detailed implementation of the forest as the main source for turbulence production close to the ground) to be in a better agreement with the measurement and most importantly to make the simulations a trusted tool for site assessment for wind turbines in complex terrain. Berg et al. (2011) found that RANS models, due to their spatial structure, are not ideal to simulate small-scale turbulence in complex terrain. This problem might be intensified by the trees and the additional turbulence introduced by them. Both models parametrize trees on the escarpment in their predictions, but do not use the exact distribution of forest patches along the cross-section. Large-eddy simulation or dynamic reconstruction models as proposed by

Chow and Street (2009) give better results for the prediction of the TKE, but are often, due to the excessive computing resources needed, not applicable for simulations of longer time frames.

A completely new approach to make the simulation data with their short time frame of 10 min comparable to the 1.5 h of flight time was chosen in this study. The results look promising for the task of validating models using unmanned aircraft systems. Some limitations are still not overcome and add uncertainties to the analysis. One limitation of the chosen method is the difference in measurement heights of the UAS and the discrete heights of the model output. To obtain the same heights in the model and measurements, the original model output was interpolated to extract the flown altitudes of the UAS. Another interpolation was done to produce the contour plots. To overcome this issue it would be beneficial to tune the model outputs to give their discrete heights where the UAS was flying or will fly. Together with a higher temporal resolution, it would be possible to compare the measured heights directly with the simulations with identical timestamps. Even problems introduced by mesoscale fluctuations (e.g., a cold front) during the flight would be eliminated, making a comparison with measurements and the validation of models in complex terrain using UAS much easier.

6 Conclusion

The UAS MASC-3 was used to conduct measurements on two consecutive days in September 2018 over the WINSSENT test site. Data from these flights were compared to numerical simulations of two stages of fidelity and the measured wind field was analyzed regarding its impact on the future wind turbines. This work extends the experiment from Wildmann et al. (2017) with a more precise measurement system and the possibility of measuring flow features very close to the ground over the escarpment and the plateau.

The conditions on both days were similar in respect to the wind direction and thermal stratification, with a slight instability on both days (Fig. 4). However, the wind speed for the first day was twice as high with slightly more fluctuations in wind speed and wind direction compared to the second day.

It was shown that the research UAS MASC-3 is capable of measuring a large area alongside the test field in complex terrain and still resolves small changes in all three wind components. Specifically the area above the escarpment and the plateau was of great importance. It was possible to measure down to 20 m above the plateau to get insight into the effect of trees and the additional turbulence they introduce.

Both models produced results in good agreement with the wind-field data measured by the UAS. Despite the coarse spatial resolution of the WRF model, it performed well in terms of predicting the areas of higher wind speeds and the inclination angle above the escarpment and the plateau. The OpenFOAM model gave better results than WRF for the wind speed compared to the measurements, good results for the inclination angle, and needs adjustments for the wind direction. The areas of higher TKE values in the lee of the trees were not captured properly by both models. Areas of high turbulence were located in higher altitudes and in regions before the edge of the slope. Having this in mind, a tuning of the WRF and OpenFOAM model to simulate the turbulence in the lowest 50 m above ground in the lee of the trees would be beneficial for understanding the effect of a forested escarpment onto the local wind field.

The main results are:

- In Wildmann et al. (2017) it was not possible to see the impact of the forest on the flow in the lee of the trees. The measurements conducted in this study showed the capability of the MASC-3 to measure small-scale differences and phenomena of the wind field influenced by a forested escarpment. Features like the intense turbulence at low altitudes over the plateau and an over-speeding above the escarpment introduced by the orography and the forest were found. A recirculation is expected when the flow field is influenced as it is at that site. Despite past studies showing such an effect, a recirculation was not found. We assume the accelerated flow to mix further downstream on the plateau, where data are not available. The negative inclination angles in the east are an indicator for the flow recirculating, but no direct evidence was found.
- The measurements on both days showed an acceleration as well as a change in wind direction of the flow above the escarpment and the plateau close to the ground. Wind shear of more than 4 m s^{-1} with just 100-m difference in altitude above the plateau was found.
- The highest TKE was found to be in the lowest 80 m above ground behind the escarpment with the highest values in the lowest 50 m.
- The wind field measured by the UAS is in good accordance with the results from both the WRF and the OpenFOAM model. The model's turbulence estimation need adjustments to provide better results for the wind field close to the ground in the lee of the trees.

Given the difficulties of comparing the gathered data from the UAS with the model data, the results of the new approach explained in Sect. 3.4 look promising and provide a good basis for future CFD simulations and their validation. However, the comparison is as of now limited to a single cross-section over a period of about 1.5 h.

7 Outlook

To obtain an even better picture of the flow and local phenomena introduced into the flow by the complex terrain, more measurements need to be done. For future campaigns, a slightly extended approach would be beneficial. Specifically, measurements in the undisturbed flow upstream would help understanding of the overall situation. This approach will be realized by a multicopter UAS doing vertical profiles during the next larger flight campaign at the test site during each measurement flight with the MASC-3. Such vertical profiles in the undisturbed flow have a large value for CFD simulations. Furthermore, we aim at performing flights with a second MASC-3 in the valley and the lowland upstream of the escarpment in parallel to the measurements at the test site. Finally, given that the trees at the test site are mostly deciduous, we plan to repeat the experiment during winter to study the impact of leaves on the flow. Also, investigating the flow recirculation further down the plateau is a task for a future measurement campaign.

Acknowledgements We acknowledge support by Projektträger Jülich and the BMWi (Federal Ministry for Economic Affairs and Energy) that funded the WINSENT project (0324129D). We thank the ZSW (Zentrum für Sonnenenergie- und Wasserstoff-Forschung Baden-Württemberg) for supplying the meteorological tower data. For extensive technical support and piloting of the aircraft at the field campaign we want to thank Alexander Rautenberg. The authors also acknowledge the State of Baden-Württemberg through bwHPC (Baden-Württemberg High-Performance-Computing) for providing computational resources.

Funding Open Access funding enabled and organized by Projekt DEAL.

Open Access This article is licensed under a Creative Commons Attribution 4.0 International License, which permits use, sharing, adaptation, distribution and reproduction in any medium or format, as long as you give appropriate credit to the original author(s) and the source, provide a link to the Creative Commons licence, and indicate if changes were made. The images or other third party material in this article are included in the article's Creative Commons licence, unless indicated otherwise in a credit line to the material. If material is not included in the article's Creative Commons licence and your intended use is not permitted by statutory regulation or exceeds the permitted use, you will need to obtain permission directly from the copyright holder. To view a copy of this licence, visit <http://creativecommons.org/licenses/by/4.0/>.

References

- Ayotte G, Davy R, Coppin P (2001) A simple temporal and spatial analysis of flow in complex terrain. *Boundary-Layer Meteorol* 98:275–295. <https://doi.org/10.1023/A:1026583021740>
- Belcher S, Harman I, Finnigan J (2012) The wind in the willows: Flows in forest canopies in complex terrain. *Ann Rev Fluid Mech* 44(1):479–504. <https://doi.org/10.1146/annurev-fluid-120710-101036>
- Berg J, Mann J, Bechmann A, Courtney MS, Jørgensen HE (2011) The Bolund experiment, part i: flow over a steep, three-dimensional hill. *Boundary-Layer Meteorol* 141:219–243. <https://doi.org/10.1007/s10546-011-9636-y>
- Chow FK, Street RL (2009) Evaluation of turbulence closure models for large-eddy simulation over complex terrain: Flow over Askervein Hill. *J Appl Meteorol Clim* 48(5):1050–1065. <https://doi.org/10.1175/2008JAMC1862.1>
- Clifton A, Daniels M, Lehning M (2014) Effect of winds in a mountain pass on turbine performance. *Wind Energy* 17(10):1543–1562. <https://doi.org/10.1002/we.1650>
- El-Bahlouli A, Rautenberg A, Schoen M, zum Berge K, Bange J, Knaus H (2019) Comparison of CFD simulation to UAS measurements for wind flows in complex terrain: Application to the WINSSENT test site. *Energies*. <https://doi.org/10.3390/en12101992>
- El-Bahlouli A, Leukauf D, Platis A, zum Berge K, Bange J, Knaus H (2020) Validating CFD predictions of flow over an escarpment using ground-based and airborne measurement devices. *Energies*. <https://doi.org/10.3390/en13184688>
- Emeis S, Frank H, Fiedler F (1995) Modification of air flow over an escarpment - results from the Hjørdemal experiment. *Boundary-Layer Meteorol* 74:131–161. <https://doi.org/10.1007/BF00715714>
- Hofsaess M, Clifton A, Cheng P (2018) Reducing the uncertainty of lidar measurements in complex terrain using a linear model approach. *Remote Sens*. <https://doi.org/10.18419/opus-10119>
- Knaus H, Hofsaess M, Rautenberg A, Bange J (2018) Application of different turbulence models simulating wind flow in complex terrain: A case study for the WindForS test site. *Computation*. <https://doi.org/10.3390/computation6030043>
- Kroll N, Eisfeld B, Bleecke H (1999) FLOWer. *Notes Numer Fluid Mech* 71:58–68
- Lange J, Mann J, Angelou N, Berg J, Sjöholm M, Mikkelsen T (2016) Variations of the wake height over the Bolund Escarpment measured by a scanning lidar. *Boundary-Layer Meteorol* 159:147–159. <https://doi.org/10.1007/s10546-015-0107-8>
- Letson F, Barthelmie R, Hu W, Pryor S (2018) Characterizing wind gusts in complex terrain. *Atmos Chem Phys* 19:3797–3819. <https://doi.org/10.5194/acp-19-3797-2019>
- Letzger P, Lutz T, Kraemer E (2018) Detached eddy simulations of the local atmospheric flow field within a forested wind energy test site located in complex terrain. *J Phys Conf Ser*. <https://doi.org/10.1088/1742-6596/1037/7/072043>
- Lu GY, Wong DW (2008) An adaptive inverse-distance weighting spatial interpolation technique. *Comput Geo* 34:1044–1055. <https://doi.org/10.1016/j.cageo.2007.07.010>
- Mauz M, Rautenberg A, Platis A, Cormier M, Bange J (2019) First identification and quantification of detached-tip vortices behind a wind energy converter using fixed-wing unmanned aircraft system. *Wind Energy Sci* 4:451–463. <https://doi.org/10.5194/wes-4-451-2019>
- Menke R, Vasiljević N, Mann J, Lundquist J (2019) Characterization of flow recirculation zones at the Perdigo site using multi-lidar measurements. *Atmos Chem Phys* 19(4):2713–2723. <https://doi.org/10.5194/acp-19-2713-2019>
- Rautenberg A, Graf M, Wildmann N, Platis A, Bange J (2018) Reviewing wind measurement approaches for fixed-wing unmanned aircraft. *Atmosphere*. <https://doi.org/10.3390/atmos9110422>
- Rautenberg A, Schoen M, zum Berge K, Mauz M, Manz M, Platis A, van Kesteren B, Suomi I, Kral S, Bange J (2019) The Multi-purpose Airborne Sensor Carrier MASC-3 for wind and turbulence measurements in the atmospheric boundary layer. *Sensors*. <https://doi.org/10.3390/s19102292>

- Schmugge TJ, Abrams MJ, a B Kahle, Yamaguchi Y, Fujisada H, (2003) Advanced spaceborne thermal emission and reflection radiometer (ASTER). Remote Sensing for Agriculture, Ecosystems, and Hydrology IV 4879: <https://doi.org/10.1117/12.469693>
- Shaw RH, Schumann U (1992) Large-eddy simulation of turbulent flow above and within a forest. Boundary-Layer Meteorol 61:47–64. <https://doi.org/10.1007/BF02033994>
- Skamarock WC, Klemp J, Dudhia J, Gill D, Barker D, Duda M, Huang X, Weng W, Powers J (2008) A description of the advanced research WRF version 3. National Center for Atmospheric Research, Tech rep
- Talbot C, Bou-Zeid E, Smith J (2012) Nested mesoscale large-eddy simulations with WRF: Performance in real test cases. J Hydrometeorol 13:1421–1441. <https://doi.org/10.1175/JHM-D-11-048.1>
- Van den Kroonenberg A, Martin T, Buschmann M, Bange J, Voersmann P (2008) Measuring the wind vector using the autonomous mini aerial vehicle M²AV. J Atmos Ocean Technol 25:1969–1982. <https://doi.org/10.1175/2008JTECHA1114.1>
- VDE (2019) DIN EN IEC 61400–1 VDE 0127–1:2019–12; Standards-VDE. VDE Verlag GmbH, Tech rep
- Wagenbrenner N, Forthofer J, Lamb B, Shannon K, Butler B (2016) Downscaling surface wind predictions from numerical weather prediction models in complex terrain with windNinja. Atmos Chem Phys 16:5229–5241. <https://doi.org/10.5194/acp-16-5229-2016>
- Weller HG, Tabor G, Jasak H, Fureby C (1998) A tensorial approach to computational continuum mechanics using object-oriented techniques. Comput Phys 12(6):620–631. <https://doi.org/10.1063/1.168744>
- Wildmann N, Hofsaess M, Weimer F, Joos A, Bange J (2014) MASC - a small remotely piloted aircraft (RPA) for wind energy research. Adv Sci Res 11:55–61. <https://doi.org/10.5194/asr-11-55-2014>
- Wildmann N, Bernard S, Bange J (2017) Measuring the local wind field at an escarpment using small remotely-piloted aircraft. Renew Energy 103:613–619. <https://doi.org/10.1016/j.renene.2016.10.073>
- WindEurope (2019) WindEurope Annual Statistics 2019. <https://windeurope.org/wp-content/uploads/files/about-wind/statistics/WindEurope-Annual-Statistics-2019.pdf>

Publisher's Note Springer Nature remains neutral with regard to jurisdictional claims in published maps and institutional affiliations.

A.2 Seasonal Changes in Boundary-Layer Flow Over a Forested Escarpment Measured by an Uncrewed Aircraft System - Publication II



Seasonal Changes in Boundary-Layer Flow Over a Forested Escarpment Measured by an Uncrewed Aircraft System

Kjell zum Berge¹ · Annika Gaiser^{1,2} · Hermann Knaus³ · Andreas Platis¹ · Jens Bange¹

Received: 2 March 2022 / Accepted: 16 August 2022 / Published online: 1 September 2022
© The Author(s) 2022

Abstract

The uncrewed airborne measurement platform MASC-3 (Multi-Purpose Airborne Sensor Carrier) is used to measure the influence of a forested escarpment with differing leaf area indices (*LAI*) onto the wind field. Data from flight legs between 30 and 200 m above ground with uphill (westerly) wind during summer (July–September) and winter (October–March) seasons between 2018 and 2021 are analyzed. Compared with a low value of *LAI*, it is found that the mean wind speed acceleration is stronger for a high values of *LAI*, and the turbulence is enhanced in the lee of the trees in the lowest 20–60 m above ground. During summer with a high *LAI*, the inclination angle is more clearly defined into an upward motion above the slope and downward motion above the plateau. The results of the airborne dataset fits well into the theoretical and analytical models established in the 1970s and 1980s.

Keywords Complex terrain · Leaf area index · Turbulence measurement · Uncrewed aircraft system · Wind energy

1 Introduction

With a share of 23.7% in 2020, wind energy is one of the main contributors to German electricity production (BMW 2020). This 23.7% of wind energy in Germany is produced by a total power of 54.4 GW (87.6%) from onshore wind turbines and 7.75 GW (12.4%) from offshore wind turbines (BMW 2020). With the ongoing change towards more renewable energies, additional sites are to be developed. Accordingly, not only flat terrain but also complex terrain is coming to the attention of the government and wind turbine operators for fulfilling the needs of renewable energy.

Kjell zum Berge
kjell.zum-berge@uni-tuebingen.de

- ¹ Center for Applied Geoscience, Eberhard-Karls-Universitaet Tuebingen, Schnarrenbergstr. 94-96, 72076 Tübingen, Germany
- ² Meteorology and Air Quality Group, Wageningen University and Research, 6700 AA Wageningen, Netherlands
- ³ Faculty of Science, Energy and Building Services, Esslingen University of Applied Sciences, Kanalstrasse 33, 73728 Esslingen, Germany

With their 1970s studies, Taylor and Gent (1974) and Jackson and Hunt (1975) initiated a larger interest in boundary-layer flows over hills, where the hill height is much smaller than the hill length. They used numerical and analytical linear modelling approaches to determine the flow regimes over low hills. Taylor and Gent (1974) and Jackson and Hunt (1975) extended and improved their own theories over the following years. Within the last 20 years, the development of models and the corresponding computing power has increased greatly. This allows for the simulation of the flow field over more complex structures. However, the underlying theories and models of Taylor et al. (1974, 1987) and Finnigan (1988) still prove to be a strong base for an analytical comparison to measured data.

Finnigan and Brunet (1995) were among the first to look into boundary-layer flows within and above a canopy on low hills. Later studies used their findings in more precise and detailed large-eddy simulations (LESs) for more complex terrain (Dupont et al. 2008; Ross 2008; Wang et al. 2015; Liu et al. 2019). However, research on possible influences of the canopy on the local wind field for the WINSSENT (“Wind Science and Engineering in Complex Terrain”) test site has not yet been performed sufficiently. El-Bahlouli et al. (2019) and Berge zum et al. (2021) suggested a large impact by the deciduous forest onto the flow field in the lowest 60 m above ground. What was not considered in earlier studies is the variation during seasons of the leaf area index (*LAI*) and the resulting effect on the wind field, the turbulence in the lee of the trees, and speed-up over the crest. The impacts of complex terrain on wind speed, turbulence, inclination angle, and wind direction are relevant for the assessment of possible wind energy sites, as they have an influence on the power output, fatigue, and financial and energetic amortization time of wind turbines (Maeda et al. 2004; Schulz et al. 2016a, b; Lutz et al. 2017; El-Bahlouli et al. 2020).

The measurement and characterization of a flow in complex terrain are more challenging compared to flat terrain. The flow behaves less predictably with rapid changes close to the ground, which makes an evaluation with remote sensing devices like lidar and sodar difficult. Due to their large averaging volumes and the heterogeneity of the orography, sodar and lidar are not able to spot small and fast changes in the wind profile. Sonic measurements on towers give a high temporal resolution of the wind speed and direction, but are fixed to one location and are not representative for the immediate vicinity (Ayotte et al. 2001). Fixed wing UASs (uncrewed aircraft system) are able to measure a two-dimensional field of wind, temperature, and humidity with a high spatial and temporal resolution, covering a large area vertically and/or horizontally. This ensures that small phenomena, like turbulent structures, and larger effects, like the speed-up over the crest or recirculation zones downstream of an escarpment, are picked up. With their high resolution data acquisition applied over a large area in multiple heights, UASs are closing the gap between static but high temporal resolution instrumentation on the ground or on towers and remote sensing with its coarser temporal resolution but capabilities of covering large areas.

Where remote sensing requires multiple devices or specialized algorithms (Wildmann et al. 2020) to measure all three wind components or the turbulence kinetic energy (TKE), the UAS does this with a higher temporal resolution over a large area and additionally measures the temperature and humidity at the same time in the same area. This makes a UAS a good tool for measurements in complex terrain.

Considering the trend towards building more wind energy turbines in complex terrain in combination with the effects of this terrain on wind energy production, the project WINSSENT was established. WINSSENT is a research project by the wind energy research cluster WindForS with several southern German research institutions. The main goals of WINSSENT are the characterization of the micro-climate and meteorology at the test site in the Swabian

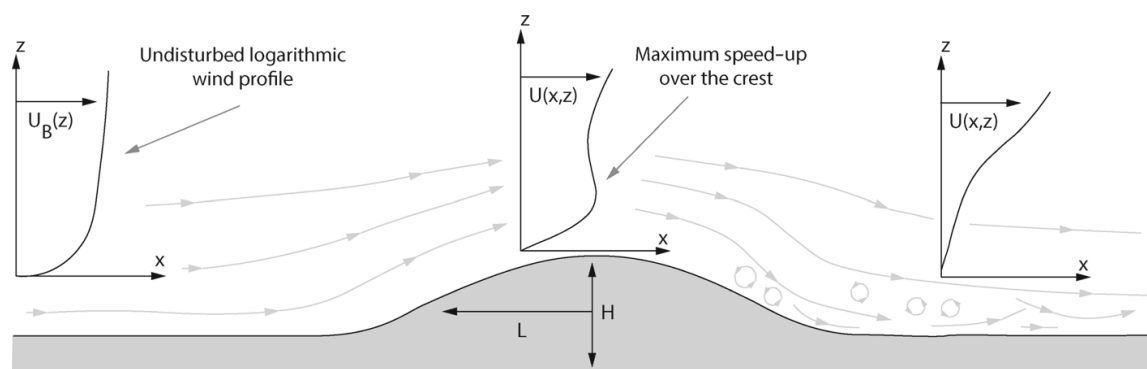


Fig. 1 Ideal hill with its flow features on the findings by Jackson and Hunt (1975). $U_B(z)$ is the undisturbed approaching wind profile

Alps, the preparation and modification of wind energy converters, and the construction and operation of the test site (WindForS 2018).

In the course of the WINSENT project and previous projects, multiple measurements and simulations (Wildmann et al. 2014a, 2017; Knaus et al. 2018; El-Bahlouli et al. 2019, 2020; Letzgus et al. 2018, 2020; Berge zum et al. 2021) were performed at the location of the test site to investigate the influences of complex terrain on the wind field and wind turbines, including the role of the forest. Measurements and simulations showed an accelerated flow over the escarpment with westerly winds.

According to the findings by El-Bahlouli et al. (2019) and Berge zum et al. (2021), the forest at that particular site has a large impact on the turbulence kinetic energy k in the lee of the trees. Blades of modern wind turbines reach into the boundary layer above and behind the tree canopy, an area with increased turbulence. Knaus et al. (2018) found similar results by using Reynolds-averaged Navier-Stokes (RANS) simulations, modelling the flow over the escarpment, where the trees had a significant impact on the turbulence kinetic energy in the lowest 50 m above ground. Thus, this study aims at answering the following questions:

- How strong is the difference in speed-up above the crest and the turbulence kinetic energy k with changing LAI ?
- Are the analytical models from past research applicable for the forested escarpment at the WINSENT test site?

This study compares eight measurement flights in the same area above the escarpment from July–September (summer, high LAI) and six measurement flights between October–March (winter, low LAI) from 2018 to 2021.

2 History of Analytical Flow Models

Over the last decades, a variety of models and approaches have been developed for modelling airflows in complex terrain. The works by Jackson and Hunt (1975) and Finnigan (1988) developed and improved analytical models to describe the flow over (low) hills. A speed-up above the crest of a hill occurs, and this speed-up is dependent on the hill shape and its roughness. The core principle of the model by Jackson and Hunt (1975) was to linearize the equations of motion with a logarithmic background wind profile (Fig. 1). This profile is assumed in a flat and undisturbed area upstream of the hill.

The result of the analysis by Jackson and Hunt (1975) is that the speed-up is much greater than the slope of the hill would suggest (Finnigan et al. 2020). This speed-up is based on the

conventional formula for the fractional speed-up ΔS by Jackson and Hunt (1975),

$$\Delta S(x, z) = \frac{U(x, z) - U_B(z)}{U_B(z)}, \quad (1)$$

where $U(x, z)$ is the wind profile at a location x , which is the lateral distance between the profile and the crest and U_B , the undisturbed approaching wind profile (Fig. 1).

Figure 1 also shows the influence onto the mean flow over a hill incorporating the characteristic mean stream-wise velocity scale $U_0 = U_B(z)$. Above the crest in Fig. 1 a speed-up is expected when compared to the undisturbed upwind profile. This maximum in the mean horizontal wind speed is not visible in the downwind profile. According to Finnigan (1988) this downwind profile is somewhat influenced by the forming of a separation bubble in the lee of the hill (Fig. 1). Based on the findings of Jackson and Hunt (1975) and Taylor and Lee (1984) formulated assumptions for wind-speed changes over low hills. For three-dimensional axially symmetric hills they concluded $\Delta S_{\max} = 1.6\{\frac{H}{L}\}$, for two-dimensional escarpments, $\Delta S_{\max} = 0.8\{\frac{H}{L}\}$ and over two-dimensional ridges, $\Delta S_{\max} = 2\{\frac{H}{L}\}$, where H is the hill height and L is the hill length at the half-height point $H/2$ (Fig. 1). The analytical model by Jackson and Hunt (1975) was later improved by Sykes (1980), Hunt et al. (1988) and Finnigan (1988). The first numerical model by Taylor and Gent (1974) was developed even before the results from Jackson and Hunt (1975) were published. The upcoming numerical models to simulate hill flows adopted the analytical basics from Jackson and Hunt (1975). This led to numerical models like WAsP (Wind energy industry-standard software; Troen and Petersen 1989) that are still used in wind energy site assessment nowadays. With always growing capacities in computing power, existing models by Jackson and Hunt (1975) and Hunt et al. (1988) were improved and new RANS and LES models (Letzgus et al. 2018) were developed but are still using the analytical and numerical basics published by Taylor and Gent (1974) and Jackson and Hunt (1975) in the 1970s (Finnigan et al. 2020). However, these theories only consider low hills with a very small roughness length z_0 and only under neutral thermal stratification.

The first steps towards understanding the impact of a hill covered by canopy onto the flow field were taken in the 1990s with a wind-tunnel experiment by Finnigan and Brunet (1995). They placed a well-studied model canopy on a 2D ridge in a wind tunnel to analyze the impact of the added roughness into the flow field over the low hill. Within the last two decades various other studies on the impact of canopy covered complex terrain onto the flow field above and around hills were performed. However, there is still a lack of real-world experimental datasets. Big field experiments have been carried out in the past, eg., Black Mountain (Bradley 1980), Askervein (Taylor and Teunissen 1987), and Perdigão (Fernando et al. 2019). Most of the experiments only utilized stationary measurements at certain points like the crest and the undisturbed inflow. This set-up can give an insight on the speed-up directly above the crest (but not the full 2D or 3D flow field) and is limited in height.

3 Methods

3.1 Measurement System

For data acquisition the airborne measurement platform MASC-3 (Multi-Purpose Airborne Sensor Carrier) was used. The MASC-3 (Fig. 2) is an UAS that allows for turbulent wind, humidity, and temperature measurements with constant air speed and direction along previously defined flight paths with specific altitudes (Rautenberg et al. 2019). The electrically

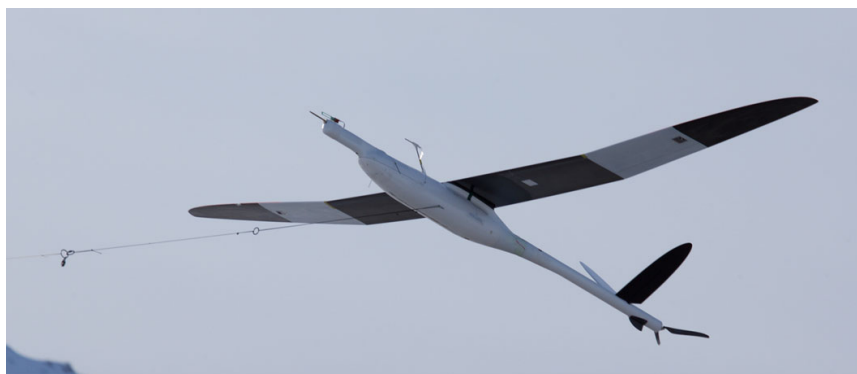


Fig. 2 The MASC-3 UAS equipped with sensor compartment after take-off

powered UAS has a wingspan of 4 m and a takeoff weight of 7–8 kg, depending on the battery load. The speed, direction, and altitude is controlled by the autopilot system (Pixhawk 2.1 Cube) via changing the angle of attack and throttle (Rautenberg et al. 2019).

The sensor compartment consists of a five-hole probe for measuring the wind vector, a fine wire platinum resistance thermometer (Wildmann et al. 2013), two hygrometers (Wildmann et al. 2014b; Mauz et al. 2020), and an inertial measurement unit (IMU) for exact position information. MASC-3 samples the sensors with 100 Hz to measure the three-dimensional wind vector and air temperature with up to 30 Hz (Wildmann et al. 2014a). More detailed information on the MASC-3 and the measurement system were published by Rautenberg et al. (2019).

3.2 Measurement Site and Strategy

The WINSSENT test site is located near Geislingen an der Steige on the Swabian Alb (48.664°N, 9.836°E). The area is characterized by its complex terrain, containing a steep escarpment with a flat plateau (665 m a.s.l.) to the east and a small hill about 1.5 km west of the escarpment (Fig. 3). The escarpment has a slope of up to 40° and a height of approximately 200 m with respect to the valley. The upper 100 m of the escarpment is covered with a dense and mostly deciduous forest (Schulz et al. 2016a; Wildmann et al. 2017). The mean wind direction with approximately 295° is perpendicular to the crest of the escarpment, which makes this area interesting for building the test site. For a more detailed view of height differences in the wider area around the test site, Berge zum et al. (2021) showed a map derived from a digital elevation model.

Figure 4 shows a more detailed view of the escarpment at the test site. Using the analytical model by Hunt et al. (1988) (see Fig. 1) we can estimate ΔS_{\max} using the hill length L and the hill height H . The hill length L is taken as length of the hill at half of the hill height (Hunt et al. 1988). The darker areas of the contour show the trees with a mean height of 23 m. We assume the forest with no foliage in winter to be sparse enough to let the air flow through more freely, while in summer the full foliage cover acts as a vertical extension of the hill shape (red dashed line in Fig. 4). Because we are now using the highest point of the crest itself (blue line) instead of the treetop (red line) the effective hill height from summer to winter is reduced by about 16 m.

To analyze the magnitude of effect of the LAI on the flow field above a forested escarpment, flight legs (i.e., straight and level flight paths) perpendicular to the slope were performed. In total, 14 measurement flights at heights between 30 and 200 m during different seasons

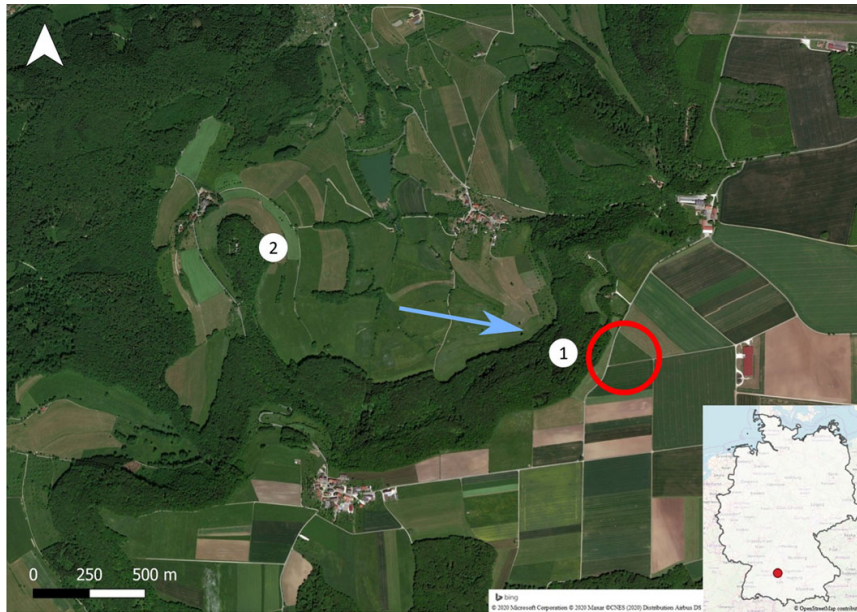


Fig. 3 Satellite picture of the WINSSENT test site (48.664°N , 9.836°E) in southern Germany. The site is east of a forested escarpment (1) with a height of 200 m in respect to the valley. A hill (2) is around 1.5 km west of the escarpment. The blue arrow shows the mean wind direction of all flights combined. The red circle shows the location of the test site. *Sources:* Satellite image: ©2020 Microsoft Corporation ©2020 Maxar ©CNES (2020) Distribution Airbus DS; OSM Standard: ©OpenStreetMap contributors, CC-BY-SA. <https://www.openstreetmap.org/copyright>. <https://www.openstreetmap.org>. <https://www.opendatacommons.org>

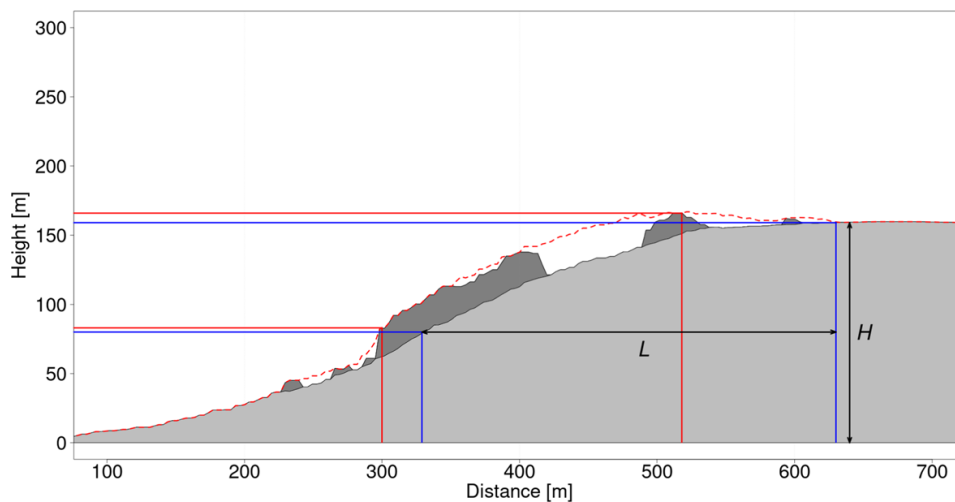


Fig. 4 Cut through the escarpment. The canopy is dark grey. Hill length L and hill height H are displayed following the model of Hunt et al. (1988). Red lines for summer (high LAI) and blue lines for winter (low LAI). The red dashed line shows the assumed hill shape with full foliage in summer

and westerly winds are considered here. The wind speeds during the measurement flights range from 2 m s^{-1} to more than 10 m s^{-1} (Table 1). The height difference between flown altitudes is small close to the ground and increases towards the highest flight altitudes. This measurement strategy ensures that the most decisive area behind the forest is covered by a denser grid of data. For statistical significance, each flight level consists of 2–4 straight flight legs on the same track in opposing directions. The raw data are sampled with 100 Hz which yields 5–6 data points per metre flight path.

To compare measurements from flights with a low LAI to flights with a high LAI , the data are visualized by using line plots on a cross-section (Fig. 5) of the mean vertical velocity



Fig. 5 Flight paths between 30 and 200 m above the plateau. The escarpment is facing west. Source of the satellite image: Google

component U , the turbulence kinetic energy k , and the inclination angle α , for each flown altitude. The inclination, a proxy for the vertical velocity component w , is defined as the vertical deviation of the flow from the x -axis:

$$\alpha = \tan^{-1} \left(\frac{w}{u} \right), \quad (2)$$

with w and u being the velocity components in z and x directions. Due to the fact that some earlier flights (14 August 2018, 21 September 2018, and 22 September 2018) are not covering the same heights later flights did, some altitudes are derived by interpolation. Because the flown altitudes are not evenly distributed, this was done by using the inverse distance interpolation (Lu and Wong 2008). The data for U and k were normalized using their mean values from all flight legs combined at 200 m altitude for each of the 14 measurement flights. Values for U , k , and α were extracted at certain heights (30 m, 40 m, 60 m, 80 m, 100 m, 120 m, 160 m, and 200 m) for each flight. These datasets were then combined and a mean was calculated for each corresponding point on the flight leg along the escarpment and the plateau.

For calculation of the fractional speed-up ΔS_{\max} , an idealized logarithmic wind profile based on the mean wind speed in 200 m above ground was extrapolated downwards using:

$$U_2 = U_1 \frac{\ln \left(\frac{h_2}{z_0} \right)}{\ln \left(\frac{h_1}{z_0} \right)}, \quad (3)$$

with the known wind speed U_1 in 200 m (h_1), the height h_2 of the wind speed U_2 , and the roughness length z_0 with a value of 0.4 (small villages, agricultural land, forests, rough terrain).

For more details on the measurement strategy, the measurement principle, the data structure, and the interpolation method refer to Van den Kroonenberg et al. (2008), Rautenberg et al. (2018), and Berge zum et al. (2021).

3.3 Averaging and Second-Order Moments

The results presented in Sect. 4 are averages of the 14 flights from Table 1. The process starts with single flights that have measured data on altitudes between 30 and 200 m a.g.l. Each of those altitudes consists of multiple legs, typically four. To obtain data for each altitude

Table 1 Lapse rate and bulk Richardson number calculated from flight data for heights between 30 and 200 m, calculated using the equations in Sect. 3.3

Date	Time UTC	LAI	γ (10^{-2} K m^{-1})	RiB	Mean U ($m s^{-1}$)	Mean wind direction ($^{\circ}$)
26/10/2018	1420–1537	Low	0.03	0.033	3.5	285
10/12/2019	1247–1355	Low	-0.20	-0.740	2.0	267
12/12/2019	1352–1458	Low	0.16	0.358	3.1	266
02/11/2020	1446–1609	Low	-0.02	-0.045	5.5	250
10/03/2021	0911–1020	Low	1.24	2.848	6.0	282
10/03/2021	1108–1234	Low	0.30	0.198	5.8	285
14/08/2018	1108–1230	High	-0.37	-3.860	5.3	284
21/09/2018	1055–1229	High	-0.35	-0.089	8.5	262
22/09/2018	1255–1417	High	0.02	0.110	4.5	276
08/07/2019	1251–1416	High	-0.31	-1.435	4.4	297
08/07/2019	1632–1810	High	-0.09	-0.161	4.2	316
29/07/2021	0630–0811	High	0.49	1.051	3.5	252
29/07/2021	0841–1012	High	0.65	2.422	7.2	260
29/07/2021	1636–1803	High	-0.71	-1.552	3.7	300

step within a single flight, the flight data from the flight legs on the same altitude is spatially averaged along the flight path. This results in the 14 flights with data on the discrete heights of 30, 40, 60, 80, 100, 120, 160, and 200 m. To compare the results between the seasons, the data of the six flights in winter and the eight flights in summer is again spatially averaged, e.g., the data at 30 m of the six flights during winter. The standard deviation σ used in Sect. 4.1 was calculated before the first step of averaging took place to make sure no error is introduced by calculating σ from already averaged data. For more information refer to Berge zum et al. (2021).

The mean horizontal wind U and the TKE k in Sect. 4 are normalized. The horizontal wind is normalized using an idealized logarithmic wind profile (Eq. 3) where each measurement altitude was normalized with the corresponding altitude from the logarithmic wind profile. The TKE was normalized using the mean TKE from the measurement in 200 m a.g.l.

To determine the atmospheric stability during the time of flight, the lapse rate,

$$\gamma = \frac{\Delta\theta_v}{\Delta z}, \quad (4)$$

with the difference in virtual potential temperature $\Delta\theta_v$ over the height Δz and the bulk Richardson number,

$$\text{Ri}_B = \frac{\left(\frac{g}{T_v}\right)\Delta\theta_v\Delta z}{(\Delta u)^2 + (\Delta v)^2}, \quad (5)$$

with the the acceleration due to gravity g , the absolute virtual temperature T_v , the virtual potential temperature θ_v , the difference across a layer Δz and the changes in the horizontal wind components Δu and Δv were calculated. The results of the stability estimation are presented in Table 1.

3.4 Leaf Area Index Estimates

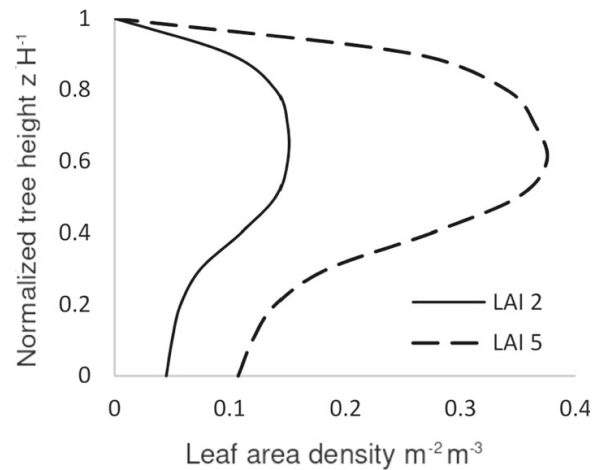
The leaf area index (LAI) is a measure for the one-sided leaf area per ground area (Tian et al. 2004). It varies with forest type, time of the year, and latitude (Tian et al. 2004). The value of LAI of a forest with height h is derived by calculating the parameter integral of the leaf area density (LAD) over height z (Shaw and Schumann 1992):

$$LAI = \int_0^h LAD(z) dz. \quad (6)$$

It is important to note that in its definition, the LAI only considers the leaf area. While this is useful for application in agriculture or climatology, it is insufficient for simulating or measuring the flow components within a forest and above. For this task the branches and the tree trunks are also increasing the drag within and above the forest and therefore need to be considered. Measurements, either from the ground using cameras or from above by satellite imaging are incorporating branches at lower levels within the forest (Verger and Descals 2021).

The forest at the WINSSENT test site consists mainly of deciduous trees. Figure 6 shows the LAD distribution with height in a deciduous forest with a value of LAI of 2 and 5. The variations in LAD with height are lower for a smaller LAI , which is due to most foliage being apparent in the canopy of the forest. This illustration by Shaw and Schumann (1992) was not made for a certain kind of tree but for deciduous trees in general. There are large differences between different kinds of trees. Maple or Oak have branches with a lot of leaves starting

Fig. 6 Distribution of *LAD* with height within a deciduous forest for a *LAI* of 2 and a *LAI* of 5. Source: Shaw and Schumann (1992)



much lower a.g.l. than for example Alder or Pine trees. When using the *LAD* or *LAI* this has to be considered.

The difference in foliage density results in different drag within the forest (Kaimal and Finnigan 1994; Lalic et al. 2003). A high *LAI* results in lower wind speeds within the forest and in the transition zone directly above it (Lalic et al. 2003).

In deciduous forests, changes in *LAI* can be seen in the course of the year. The *LAI* for the forest covering the escarpment was estimated according to the method described by Baret et al. (2010), Confalonieri et al. (2013), and Martin (2015), using vegetation images that are automatically processed and the *LAI* calculated by using the so called ‘gap fraction’ (Confalonieri et al. 2013; Martin 2015):

$$\text{Gap fraction} = \frac{\text{Sky area}}{\text{Total area}}. \quad (7)$$

The pictures were taken from the ground (upward directed photo), using the sky area for the gap fraction in Baret et al. (2010).

Before calculating the gap fraction, the picture is binarized, so sky pixels are assigned the value zero and vegetation pixels the value one by using the ‘histogram-based unimodal threshold method’ (Martin 2015). The *LAI* calculation with the method of Martin (2015) is based on:

$$LAI = - \left(\frac{\cos(\theta_v)}{G(\theta_v, \phi_v)} \right) \log(P_0(\theta_v, \phi_v)). \quad (8)$$

The equation uses the gap fraction $P_0(\theta_v, \phi_v)$, zenith angle θ_v , azimuth angle ϕ_v , and projection function $G(\theta_v, \phi_v)$, which is the fraction of foliage in direction of the view angle (Bréda 2003; Confalonieri et al. 2013). The value of G is set to 0.5 and the value of (θ_v, ϕ_v) to 57.5° , as the angle of the leaves is then negligible according to Weiss et al. (2004).

The values of *LAI* for winter and summer were calculated from spherical photos at 17 different locations along the escarpment transect made at a single representative day in July (summer) and February (winter). For winter, the value of *LAI* in those locations ranged from 0.1 to 1.1, with an overall mean of 0.6 (marked with ‘low *LAI*’ in Table 1). The same locations during summer resulted in a *LAI* ranging from 1.8 to 2.2 and a mean of 2.07 (high *LAI* in Table 1). These results are lower than found by Tian et al. (2004) and Tillack et al. (2014), but are close to the satellite derived data from Copernicus with a *LAI* of 0.6 for winter (low *LAI*) and 3 for summer (high *LAI*) (Copernicus Service information 2021).

4 Results

The atmospheric stability has a strong influence on turbulence production close to the ground. An unstable atmosphere generates buoyancy, which causes turbulence additional to the turbulent shear stress induced by the orographic effect. Table 1 shows the calculated lapse rate γ (Eq. 4), which is a measure of thermal stability, for the times of each flight between 30 and 200 m a.g.l. The lapse rate is negative for four flights with high *LAI* and one flight with low *LAI*. However, they are still very close to zero with a maximum decrease in virtual potential temperature θ_v of -0.71 K over 100 m altitude. The lapse rate during the first flight on 10 March 2021 was clearly larger than zero, meaning the atmosphere was slightly stably stratified. A stable thermal stratification dampens turbulence, but this had a negligible effect on the measured data. Therefore the flight was also included in the analysis. All other flights are considered with a near neutral thermal stratification.

The bulk Richardson number (Ri_B) was also calculated using flight data, similar to the method used in Platis et al. (2021). It is a measure to distinguish between turbulence driven by buoyancy and turbulence driven by vertical shear stress due to the surroundings (mechanically driven). Values above 0 and especially above 0.25, the critical Richardson Number, are considered stable and most of the turbulence is mechanically driven. For negative values the part of buoyancy-driven turbulence is equal or even higher than from mechanical sources like the orographic effect. The data shown in Table 1 evince that during three measurements (14 August 2018, 10 December 2019, and 29 July 2021), the value of Ri_B was significantly below 0 and therefore buoyancy was dominating. The Ri_B values (Eq. 5) were calculated for each altitude segment of the flight data. Table 1 shows Ri_B between the lowest altitude at 30 m and the highest altitude at 200 m. Calculations of the bulk Richardson number indicate that, due to the warm surface, most of the buoyancy-driven turbulence is introduced in the altitudes closest to the ground (not shown), but influences the results for Ri_B over the whole altitude range.

The mean wind speed and wind direction for each flight is shown in Table 1. The wind speed ranges from 2 to 8.5 m s^{-1} with most of the measurements done at $3\text{--}6 \text{ m s}^{-1}$, which is the most common wind speed range for this area. Wind direction was limited to flights with westerly components (Table 1). Complexity to the terrain profile is added by the small hill upstream of the test area, well within the range of accepted wind directions for this analysis (Fig. 3).

4.1 Mean Wind Speed

Figure 7 shows the normalized wind speed for eight heights between 30 and 200 m a.g.l. with the height reference (ground level) on the plateau at a distance of 600 m (Sect. 3.2). Especially at heights below 60 m, a pronounced speed-up over the crest is visible. At heights of 30 m and 40 m a.g.l. right above the escarpment edge, the wind speed in summer (red line) increases to a factor of 1.61 in relation to an idealized logarithmic wind profile (Eq. 3), based on the mean wind speed in 200 m, in a flat area upstream of the crest. In winter (blue line), this factor peaks at 1.13, meaning a speed-up over the crest of 13% compared to the logarithmic wind profile upstream.

The speed-up in winter (blue line) is not as strong in altitudes close to the ground, but still visible when compared to the flow speed further downstream or upstream of the crest. The difference between summer and winter and a speed-up is still visible in 40 m, but already less pronounced.

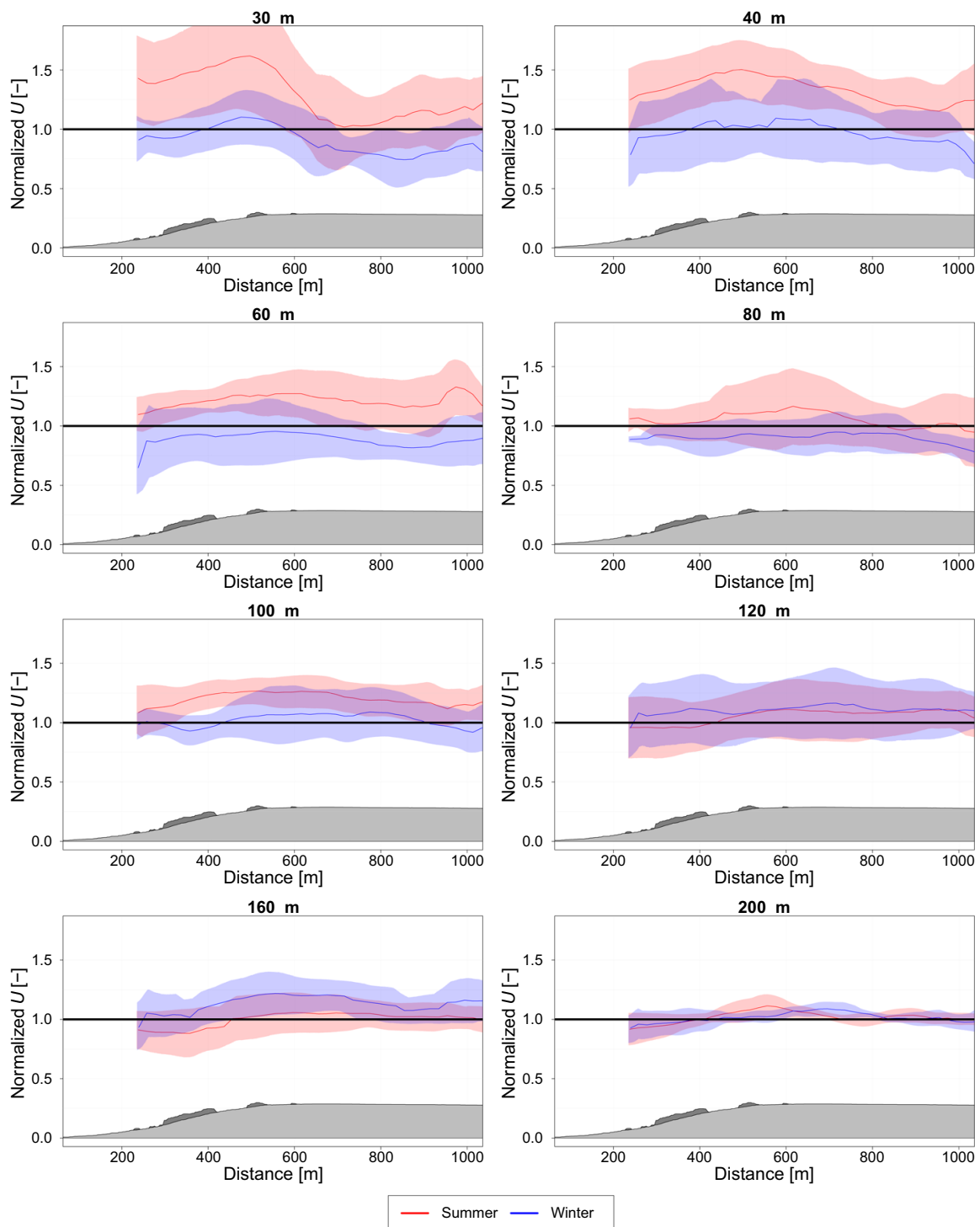


Fig. 7 The mean wind speed calculated from UAS wind data for summer (red) and winter (blue) for altitudes between 30 and 200 m above the plateau and normalized with an idealized logarithmic wind profile upstream of the escarpment (solid lines). The shaded areas are the standard deviation between those flights

Due to the consideration of the hill to be lower in height during winter without the thick foliage and therefore larger parts of the air flowing through the forest instead of being deflected upwards, the maximum speed-up in winter might be lower than 30 m altitude, where the UAS was not able to measure, and thus not visible in the data. The different hill shape due to the forest might also explain the difference in wind speed at the lowest altitudes of 30 m and 40 m between the seasons. In summer, the now steeper hill with the forest acting as a vertical extension (Fig. 4) causes an increased speed-up above the crest compared to winter, where larger amounts of air can flow through the forest instead of above it.

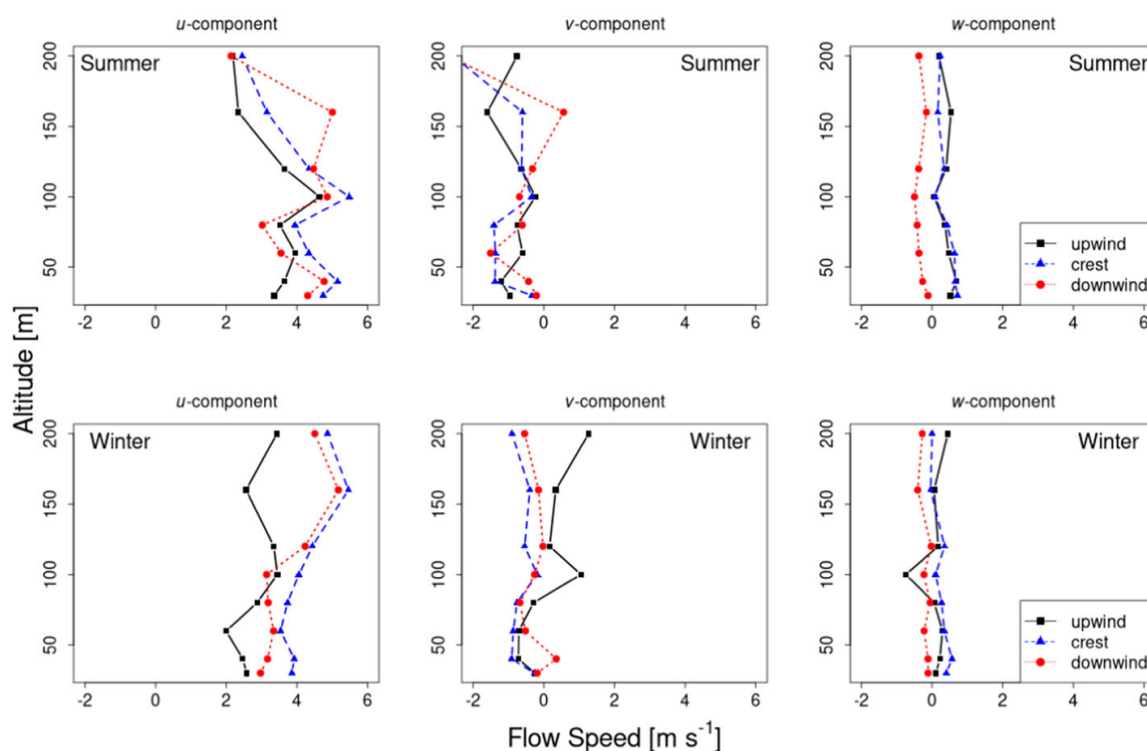


Fig. 8 Vertical profiles off all flights for summer and winter. The first column shows the standard deviation of the u -component of the wind. The middle and right column show the standard deviation of the v - and w -component, respectively. The data have not been normalized

At 80 m and above, no distinctive speed-up over the crest is visible (Fig. 7). At altitudes of 100 m and 160 m the measurements show higher values in normalized wind speeds for summer and winter, respectively. This might also be another speed-up effect caused by the upstream hill (labelled with No. 2 in Fig. 3) and shifted up in altitude with distance over the valley. This effect of accelerated winds in 100–140 m was already visible in a case study done with UAS at the same site by Berge zum et al. (2021). Here the numerical models and the measurements showed an additional layer in those altitudes with faster flowing air masses when compared with neighbouring streamlines above and below.

The standard deviation between flights, plotted as shaded areas, also decreases with height. The trailing edge of the forest, but also the orography itself are causing perturbations in the wind components in altitudes of up to 80 m a.g.l. These perturbations are also in accordance with the measurements by Berge zum et al. (2021) and simulations by Knaus and Dürr (2015) and Knaus et al. (2018).

The vertical profiles in Fig. 8 shows the three meteorological wind components u , v , and w . The vertical profiles in Fig. 8, extracted from the horizontal legs in Fig. 7 are plotted for the three wind components during both seasons at three locations to reference the locations of theoretical data in Fig. 1. Due to not having the wind components, the upwind location is not the idealized logarithmic wind profile (Eq. 3), but the furthest flight data available to the west. The downwind data originates from the flight measurements furthest to the east. Already above the slope (upwind) in the lowest altitudes smaller perturbations are visible, especially for u and v . They are more pronounced over the crest and the plateau. The speed-up over the crest is mostly visible in the u -component. During winter, the flow speed of the v -component is much higher above the plateau. Also visible here is the second flow maxima at heights of 100 m a.g.l.

Figure 9 shows the standard deviation for more locations along the escarpment and the plateau. Each graph consists of data points within ± 15 m around the points at 200, 300,

400, 500, 600, 700, and 800 m distance (x axis) along the slope and the plateau. The lowest altitude with measurement data is 30 m. We can see stronger perturbations for the lowest three altitudes at 30, 40, and 60 m. The escarpment influences especially the horizontal components u and v , while the vertical component w shows smaller fluctuations due to smaller values of w . Directly above the slope, the deviation in the signal is stronger for w compared to the area above the plateau. This can also be seen in the inclination angle α , a proxy for the vertical velocity w , which is discussed in Sect. 4.3.

Simulations and wind-tunnel experiments by Liu et al. (2019) showed a very similar behaviour for the horizontal components u and v over a model hill with stronger perturbations in the lowest data points above the crest. Figure 7 also indicates the earlier mentioned second speed-up in altitudes above 100 m, especially in winter. The standard deviations observed for v in Fig. 9 at the altitudes of 30–60 m are more pronounced when compared with u and therefore have a larger impact on the seasonal differences. This is contrary to the findings by Hunt et al. (1988), where the v -component is causing less perturbation when compared with u . These differences can be explained with the non-ideal terrain, a 3D environment and the canopy. Especially for wind directions with a northern component, the wind is deflected by the escarpment towards the measurement site (Fig. 3) causing stronger perturbations in the v component.

4.2 Turbulence Kinetic Energy

The turbulence kinetic energy per mass, k , was calculated separately for each measurement height within each flight and then the individual flights were averaged the same way as the standard deviation σ of the wind components in Sect. 4.1. Values of σ (shaded areas) reaching into negative plot regions in altitudes at 100 m and above in Fig. 10 are caused by the always positive standard deviation in some locations being larger than the TKE base value.

The TKE displayed in Fig. 10 shows a strong dependence on the height a.g.l. At 30 m and 40 m above the plateau, in the lee of the forest edge, strong turbulence develops, five times higher in summer and three times higher in winter compared to the undisturbed flow at 200 m altitude. To a certain degree the slightly unstable thermal stratification on some days in summer will have an impact onto the turbulence production on the plateau, but the fact that the largest TKE is measured directly at the crest in the lee of the forest shows that the main contributor is the orography and the canopy. Above 60 m altitude, the TKE in both seasons is nearly equal and no second peak is visible at heights where there was another speed-up in the horizontal wind measured. The orographic effect on the TKE is to be expected in the lowest altitudes above the crest (Liu et al. 2019). This can be seen in the UAS measurements as well, but especially in summer the turbulence production by the foliage seems to superimpose the orographic effect. In winter this superimposition is less pronounced and more of the actual orographic effect can be measured when the flow can move through the canopy more easily.

Figure 11 shows the difference in TKE for the summer (left) and winter (right) measurements. The higher production in summer due to the high LAI and a longer and thicker wake over the plateau is clearly visible. Berg et al. (2011) and Lange et al. (2016) found an enhancement of the turbulence of up to 300% for the Bolund test site in Denmark. Since the Bolund test site has no forested slope, this supports the assumption that the forest at the WINSSENT test site has little influence on TKE production in winter, and therefore low LAI , and that most of the turbulence is generated by the orography through shear stresses between the decreased wind speed in the lee of the crest and the speed-up above it.

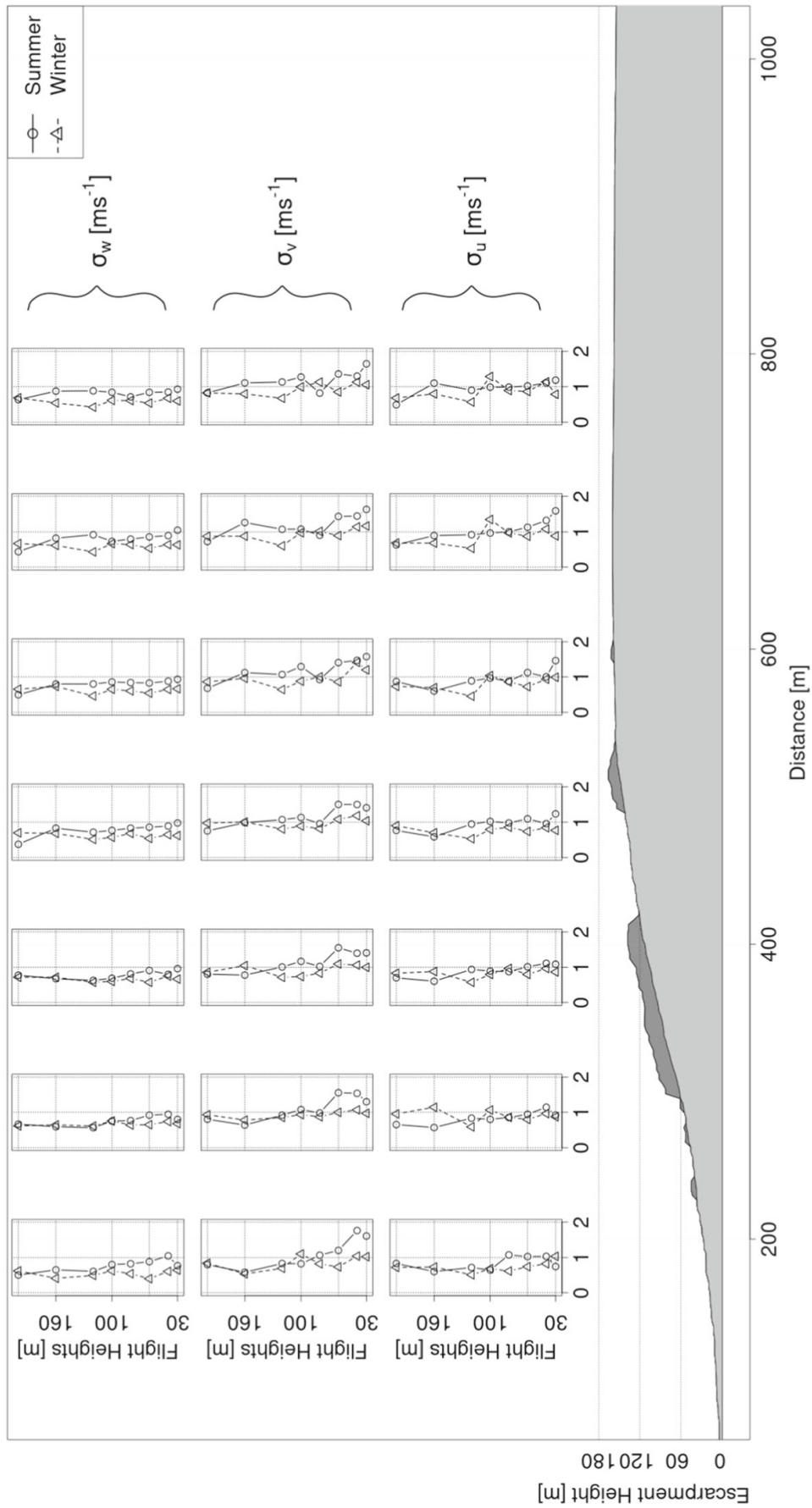


Fig. 9 Vertical profiles of all flights for summer and winter. The lowest row shows the standard deviation of the u -component of the wind. The middle and top row show the standard deviation of the v - and w -component, respectively. The data have not been normalized

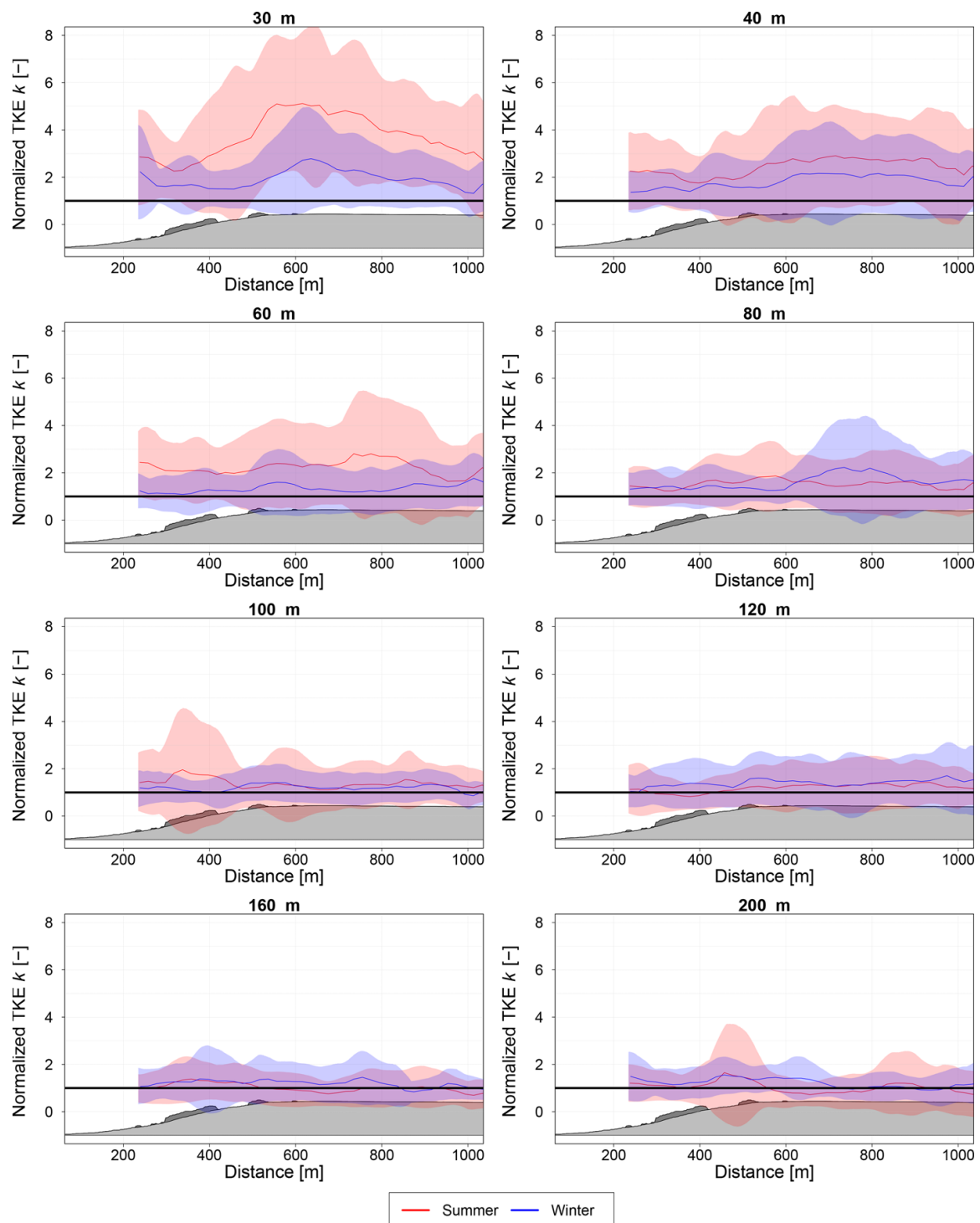


Fig. 10 Turbulence kinetic energy calculated from UAS wind data for summer (red) and winter (blue) for altitudes between 30 and 200 m above the plateau and normalized with the 200 m altitude data. The solid lines show the mean of all flights for each season and the shaded areas are the standard deviation between those flights

4.3 Inclination Angle

The inclination angle α (Eq. 2), the inclination of the horizontal wind caused by the vertical wind component w , is typically positive above the hill slope and negative or neutral on the hill's lee side. The escarpment at the WINSSENT test site does not have a lee side, but a long plateau. Figure 12 presents the measured data for summer and winter. The difference in α is

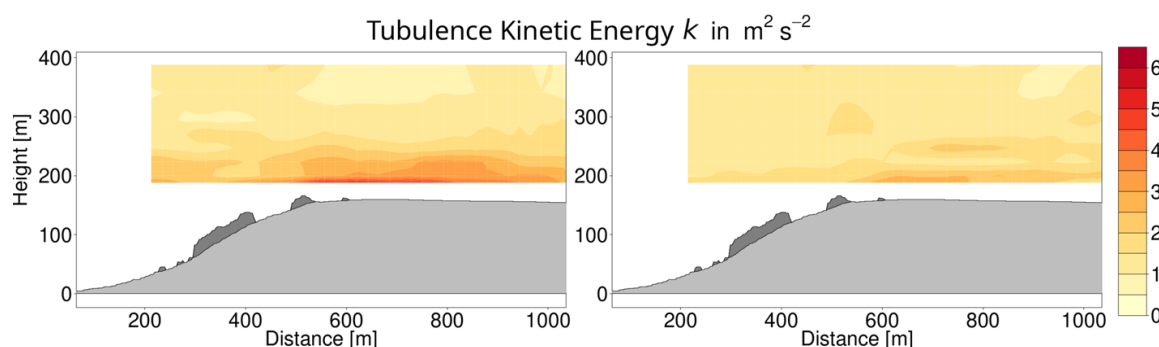


Fig. 11 Contour plots of the turbulence kinetic energy of all flights for summer (left) and winter (right). The darker shaded areas on the hill slope is the canopy

Table 2 Calculated ΔS_{\max} using the suggested equations for certain hill shapes by Taylor and Lee (1984) with the defined hill length L from Hunt et al. (1988)

Hill shape	Equation	WINSSENT test site ΔS_{\max} – Summer	WINSSENT test site ΔS_{\max} – Winter
2D escarpment	$\Delta S_{\max} = 0.8 \frac{H}{L}$	0.58 (0.61)	0.39 (0.13)
3D axially symmetric	$\Delta S_{\max} = 1.6 \frac{H}{L}$	1.14	0.79
2D ridges	$\Delta S_{\max} = 2 \frac{H}{L}$	1.43	1

Measured values for ΔS_{\max} are written in brackets behind the calculated values for a 2D escarpment

strongest at the lowest altitudes with 10° over the slope and 0 to -8° over the plateau. In altitudes above 120 m, the difference in inclination between slope and plateau has decreased.

The values 30 m above the plateau especially indicate a strong variation between the single flights in summer and winter. The lowest altitudes are still strongly influenced by the canopy causing larger variations in vertical wind w (Liu et al. 2019). In general the inclination angle does not depict a strong dependence on the seasons and therefore the LAI . Above the slope and the crest, the values for summer are higher at 30 m, 60 m, and 80 m when compared to the data from winter. Only at an altitude of 120 m the α in winter is constantly higher. It is not clear why there is an offset between summer and winter in that altitude. The data shows larger variations in 120 m possibly caused by single flights with significantly lower inclination angles in summer.

4.4 Comparison to Past Literature

Theories and past experiments predict a speed-up effect close to the ground over the crest of a hill (Bradley 1980; Taylor et al. 1987) when compared with the undisturbed flow higher up or upwind of the crest. This effect is also visible in Fig. 7. The increased wind speed in low altitudes in summer fits well to measurements done with a single tower at the crest of Black Mountain by Bradley (1980), with a maximum speed-up found in a height of 28 m above the canopy and a displacement height of 7 m.

For the WINSSENT test site the calculated ΔS_{\max} , using the equation for a 2D escarpment by Taylor and Lee (1984), reaches a value of 0.58 for summer and 0.39 for winter meaning the maximum wind speed above the crest is 58% and 39% higher in summer and winter, respectively. Table 2 shows the calculated values for the site specific terrain for all equations suggested by Taylor and Lee (1984). The measured values for the escarpment at the WINSSENT test site are written in brackets behind the calculated values from theory.

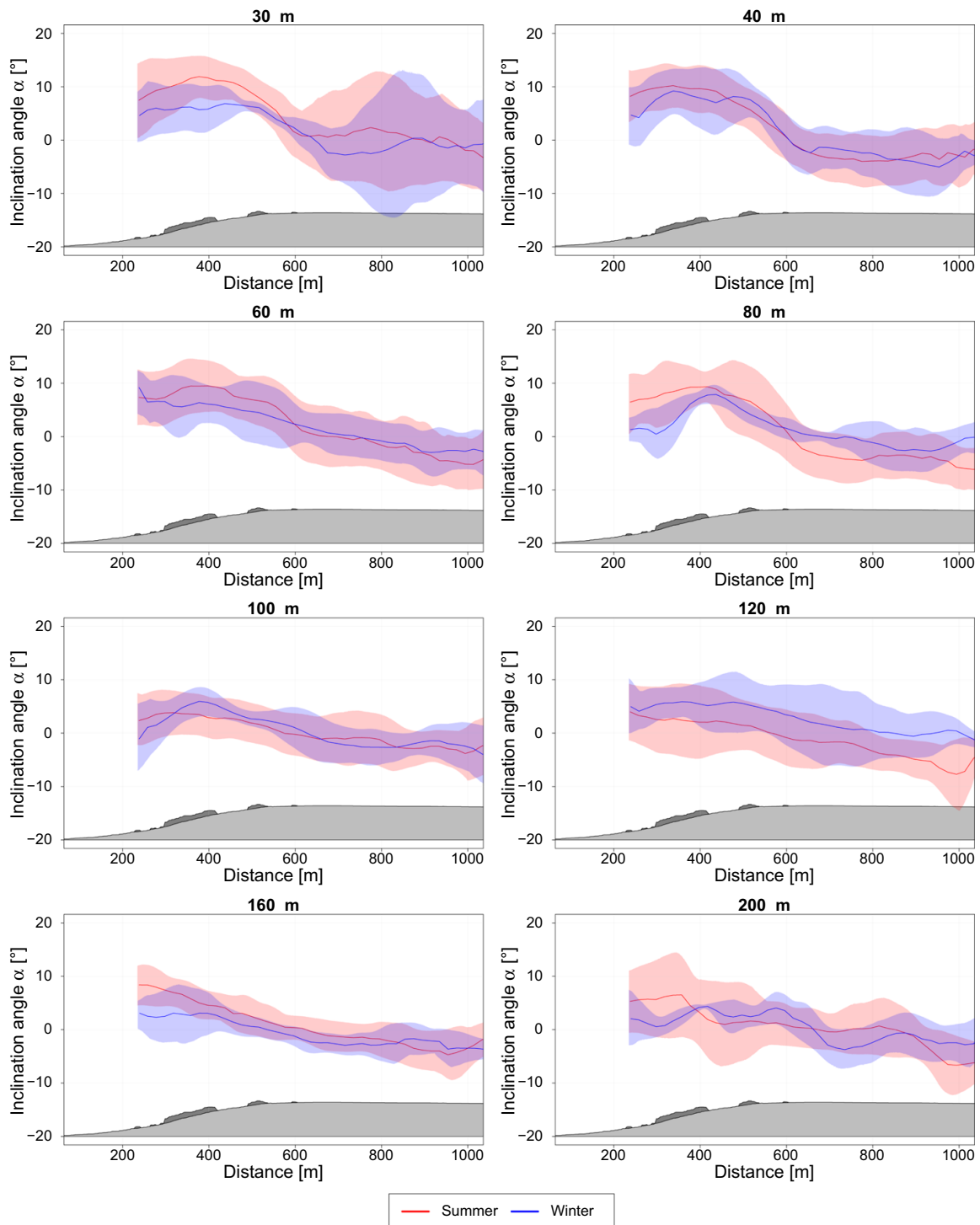


Fig. 12 Inclination angle α calculated from UAS wind data for summer (red) and winter (blue) for altitudes between 30 and 200 m above the plateau. The solid lines show the mean of all flights for each season and the shaded areas are the standard deviation between those flights

The fractional speed-up ΔS_{\max} derived from the measurements (Fig. 7) for the WINSSENT test site is 0.61 (red line) for summer and 0.13 (blue line) for winter, using the idealized undisturbed wind profile upstream of the crest for each altitude. The fractional speed-up for the measurements during summer above the crest in the heights listed in Table 3 fits well in the ranges for 2D escarpments proposed by Taylor and Lee (1984) in Table 2. With the modification to the hill shape in Fig. 4, the calculated ΔS_{\max} for winter is at a maximum value of 0.39 and thus three times higher than the measured value of 0.13.

Table 3 ΔS_{\max} for the WINSENT test site and the Black Mountain experiment Bradley (1980) describing the maximal speed-up close to the ground above the crest when using the idealized logarithmic wind profile

Field experiment	Hill height H (m)	Hill length L (m)	ΔS_{\max}	Height of ΔS_{\max} (m)	Hill type
Black mountain	170	275	1.07	27 ^a	Ridge
WINSENT summer	166	232	0.61	30–40	Escarpment
WINSENT winter	150	302	0.13	30–60 ^b	Escarpment

^aRelative to displacement height of 7 m

^bThe actual ΔS_{\max} might be lower than 30 m

The analysis by Taylor and Lee (1984) was done for hills without a canopy and for idealized terrain. Such idealized topography is of course very rare in the real world. In this case a more complex terrain and a large canopy on the escarpment play major roles in the formation of the wind field. Despite these limitations our results fit well with the theoretical foundations by Taylor and Lee (1984). The results by Bradley (1980) for Black Mountain with its similar hill length L and hill height H predict the speed-up in the same range of altitude above the crest, but resulted in a much higher ΔS_{\max} of 1.07, a 107% higher wind speed compared to the undisturbed measurement (Table 3). Because Black Mountain is not an escarpment, but a ridge, the speed-up is higher according to the theories and models.

5 Conclusion

The MASC-3 UAS was used to measure the wind field over the WINSENT test site during 14 flights in high and low LAI conditions. Data from those flights were compared to theories and experiments by Jackson and Hunt (1975), Bradley (1980), Taylor et al. (1987), Taylor and Teunissen (1987), and Hunt et al. (1988). Those theories were developed for low hills with more gentle slopes and neutral conditions, but most of the features they predict are evident in the presented dataset by airborne measurements over a more complex terrain with a forested slope. The mean velocity and velocity perturbations above the hill crest are in accordance with the theories by Jackson and Hunt (1975).

These studies often only analyzed the impact of a hill or a hill covered with a canopy on the wind field. However, at least for deciduous forests in a moderate climate a large difference in drag and shear exists between the seasons. This difference is estimated by the leaf area index. The present study aimed at answering the question if there is a difference in the velocity components and the turbulence of the flow field between the seasons in complex terrain and finding a link to the theories and models developed decades ago. Those differences are important for the installation, energy production and interpretation of the data collected with wind energy converters in complex terrain in general and especially with the research wind energy converters that are going to be installed at the WINSENT test site.

A clear difference in wind speed over the WINSENT test site was found between the seasons. The lowest altitudes between 30 and 60 m are strongly influenced by the foliage density. The maximum speed-up ΔS_{\max} measured above the crest in summer was 0.61 or 61% using as reference an idealized logarithmic wind profile upstream. The speed-up in winter was slightly lower with a factor of 0.13. When using the undisturbed logarithmic wind profile upstream, the assumptions by Taylor et al. (1987) for a 2D escarpment using the hill shape for summer (Fig. 4) agree very well. In winter, with the hill having a lower profile due to the low LAI (missing foliage), the calculations with the equations in Table 2 yield a value of 0.39 being three times higher than the measured value of 0.13 or 13%. The differing

hill shape during the seasons (Fig. 4) might also be a possible explanation for the stronger winds in heights of 30 m and 40 m during summer. The very sparse forest in winter without any foliage and thus a low *LAI* lets air flow more freely through the forest and is therefore a smaller obstacle than the forest during summer with its high *LAI* and a dense foliage acting as a hill extension increasing the speed-up above the crest.

At higher altitudes this difference in speed-up is not visible, except for a band between 120 and 160 m a.g.l. In this area the wind speed picks up again with the data from winter being higher. This might be the influence of the upstream hill (see Fig. 3) disturbing the wind field and causing a speed-up that was advected upwards over the valley before reaching the crest of the escarpment.

The different amplitude in speed-up above the crest during the seasons is explainable with the forest itself. During winter with no foliage and therefore a very low *LAI* of 0.6, the air can flow more freely through the forest while in summer the dense canopy forces a large part of the flow above it artificially making the escarpment higher. If we consider this in the equations by Hunt et al. (1988) we get a lower ΔS_{\max} for winter.

Same as the wind speed, the turbulence kinetic energy is largely impacted by the *LAI*. In 30 m and 40 m a.g.l. the measurements in summer showed a 40% higher TKE than in winter. The turbulence decreases with height, but the foliage dependence is clearly visible.

The main results are:

- A clear difference in speed-up over the crest (up to 61% in summer) and a strong difference in TKE in the lee of the trees on top of the escarpment were found. The highest values were reached close to the ground in altitudes of 40 m and below.
- Despite the complex terrain and the high canopy, the analytical models and theories from the 1970s and 1980s are still evident. Especially the measurement flights during summer (high *LAI*) resulted in a good agreement with the theoretical calculations using the equations by Taylor and Lee (1984) done for the WINSENT test site. The measurements during winter resulted in a fractional speed-up that is only one third of the calculated speed-up from the theories. However, it is important to note that the theories and analytical models only covered hills without or a small canopy. Especially the forest edge, which was included in any past model discussed here, has a large influence on turbulence production in the lowest altitudes a.g.l.

This study showcased the influence of the leaf area index (foliage) onto the flow field over an escarpment. The difference in flow features for different seasons have a large impact on life time calculations and power output for wind energy applications in complex terrain. To obtain a better picture of the flow phenomena in complex terrain during different seasons more experiments are needed and model calculations should take into account the different foliage in the corresponding seasons to obtain more reliable results for modelling the wind field in complex terrain. It would also be beneficial to compare future measurements during different thermal stability conditions and compare those results to the analytical models.

Acknowledgements We acknowledge support by PTJ (Projekträger Jülich) and the BMWi (Federal Ministry for Economic Affairs and Energy) that funded the WINSENT project (FKZ 0324129D). We thank the two reviewers for their helpful and constructive comments. For extensive technical support and piloting of the aircraft at the field campaign we want to thank our pilots and Martin Schön.

Funding Open Access funding enabled and organized by Projekt DEAL.

Data Availability The dataset of raw data used during and/or analyzed during the current study will be publicly available on PANGAEA.

Declarations

Conflict of interest The authors declare that they have no conflict of interest.

Open Access This article is licensed under a Creative Commons Attribution 4.0 International License, which permits use, sharing, adaptation, distribution and reproduction in any medium or format, as long as you give appropriate credit to the original author(s) and the source, provide a link to the Creative Commons licence, and indicate if changes were made. The images or other third party material in this article are included in the article's Creative Commons licence, unless indicated otherwise in a credit line to the material. If material is not included in the article's Creative Commons licence and your intended use is not permitted by statutory regulation or exceeds the permitted use, you will need to obtain permission directly from the copyright holder. To view a copy of this licence, visit <http://creativecommons.org/licenses/by/4.0/>.

References

- Ayotte G, Davy R, Coppin P (2001) A simple temporal and spatial analysis of flow in complex terrain. *Boundary-Layer Meteorol* 98:275–295. <https://doi.org/10.1023/A:1026583021740>
- Baret F, de Solan B, Lopez-Lozano R, Ma K, Weiss M (2010) GAI estimates of row crops from downward looking digital photos taken perpendicular to rows at 57.5° zenith angle: Theoretical considerations based on 3D architecture models and application to wheat crops. *Agric For Meteorol* 150(11):1393–1401
- Berg J, Mann J, Bechmann A, Courtney MS, Jørgensen HE (2011) The Bolund experiment, part I: flow over a steep, three-dimensional hill. *Boundary-Layer Meteorol* 141:219–243. <https://doi.org/10.1007/s10546-011-9636-y>
- Berge zum K, Schoen M, Mauz M, Platis A, van Kesteren B, Leukauf D, El Bahlouli A, Letzgas P, Knaus H, Bange J (2021) A two-day case study: comparison of turbulence data from an unmanned aircraft system with a model chain for complex terrain. *Boundary-Layer Meteorol*
- BMW (2020) Erneuerbare Energien-Die Energieträger der Energiewende. visited: 10-January-2022
- Bradley E (1980) An experimental study of the profiles of wind speed, shearing stress and turbulence at the crest of a large hill. *Q J Roy Meteorol Soc* 106(447):101–123. <https://doi.org/10.1002/qj.49710644708>
- Bréda N (2003) Ground-based measurements of leaf area index: a review of methods, instruments and current controversies. *J Exp Bot* 54(392):2403–2417
- Confalonieri R, Foi M, Casa R, Aquaro S, Tona E, Peterle M, Boldini A, De Carli G, Ferrari A, Finotto G, Guarneri T, Manzoni V, Movedi E, Nisoli A, Paleari L, Radici I, Suardi M, Veronesi D, Bregaglio S, Cappelli G, Chiodini M, Dominoni P, Francone C, Frasso N, Stella T, Acutis M (2013) Development of an app for estimating leaf area index using a smartphone. Truthness and precision determination and comparison with other indirect methods. *Comput Electron Agric* 96:67–74
- Copernicus Service information (2021) Copernicus global land service—LAI dataset. visited: 25-November-2021
- Dupont S, Brunet Y, Finnigan J (2008) Large-eddy simulation of turbulent flow over a forested hill: validation and coherent structure identification. *Q J R Meteorol Soc* 134:1911–1929
- El-Bahlouli A, Rautenberg A, Schoen M, Berge K, Bange J, Knaus H (2019) Comparison of CFD simulation to UAS measurements for wind flows in complex terrain: application to the WINSSENT test site. *Energies*. <https://doi.org/10.3390/en12101992>
- El-Bahlouli A, Leukauf D, Platis A, Berge K, Bange J, Knaus H (2020) Validating CFD predictions of flow over an escarpment using ground-based and airborne measurement devices. *Energies*. <https://doi.org/10.3390/en13184688>
- Fernando HJS, Mann J, Palma JMLM, Lundquist JK, Barthelmie RJ, Belo-Pereira M, Brown WOJ, Chow FK, Gerz T, Hocut CM, Klein PM, Leo LS, Matos JC, Oncley SP, Pryor SC, Bariteau L, Bell TM, Bodini N, Carney MB, Courtney MS, Creegan ED, Dimitrova R, Gomes S, Hagen M, Hyde JO, Kigle S, Krishnamurthy R, Lopes JC, Mazzaro L, Neher JMT, Menke R, Murphy P, Oswald L, Otarola-Bustos S, Pattantyus AK, Rodrigues CV, Schady A, Sirin N, Spuler S, Svensson E, Tomaszewski J, Turner DD, van Veen L, Vasiljević N, Vassallo D, Voss S, Wildmann N, Wang Y (2019) The Perdigão: peering into microscale details of mountain winds. *Bull Am Meteorol Soc* 100(5):799–819. <https://doi.org/10.1175/BAMS-D-17-0227.1>
- Finnigan J (1988) Air flow over complex terrain. In: Steffen WL, Denmead OT (eds) *Flow and transport in the natural environment: advances and applications*. Springer, Berlin, pp 183–229

- Finnigan J, Brunet Y (1995) Turbulent airflow in forests on flat and hilly terrain. Cambridge University Press, Cambridge
- Finnigan J, Ayotte K, Harman I, Katul G, Oldroyd H, Patton E, Poggi D, Ross A, Taylor P (2020) Boundary-layer flow over complex topography. *Boundary-Layer Meteorol* 177:247–313. <https://doi.org/10.1007/s10546-020-00564-3>
- Hunt JCR, Leibovich S, Richards KJ (1988) Turbulent shear flows over low hills. *Q J Roy Meteorol Soc* 114(484):1435–1470. <https://doi.org/10.1002/qj.49711448405>
- Jackson PS, Hunt JCR (1975) Turbulent wind flow over a low hill. *Q J Roy Meteorol Soc* 101(430):929–955. <https://doi.org/10.1002/qj.49710143015>
- Kaimal J, Finnigan J (1994) Atmospheric boundary-layer flows—their structure and measurement. Oxford University Press, New York, Oxford. ISBN: 0-19-506239-6. <https://doi.org/10.1007/BF00712396>
- Knaus H, Dürr B (2015) Numerical simulation including model validation of wind flow in alpine terrain in eastern Switzerland. *Prog Comput Fluid Dyn Int J* 15(3):168–176. <https://doi.org/10.1504/PCFD.2015.069577>
- Knaus H, Hofsaess M, Rautenberg A, Bange J (2018) Application of different turbulence models simulating wind flow in complex terrain: a case study for the WindForS test site. *Computation*. <https://doi.org/10.3390/computation6030043>
- Lalic B, Mihailovic D, Rajkovic B, Arsenic I, Radlovic D (2003) Wind profile within the forest canopy and in the transition layer above it. *Environ Modell Softw* 18:943–950
- Lange J, Mann J, Angelou N, Berg J, Sjöholm M, Mikkelsen T (2016) Variations of the wake height over the Bolund escarpment measured by a scanning lidar. *Boundary-Layer Meteorol* 159:147–159. <https://doi.org/10.1007/s10546-015-0107-8>
- Letzger P, Lutz T, Kraemer E (2018) Detached eddy simulations of the local atmospheric flow field within a forested wind energy test site located in complex terrain. *J Phys Conf Ser*. <https://doi.org/10.1088/1742-6596/1037/7/072043>
- Letzger P, El Bahlouli A, Leukauf D, Hofsaß M, Lutz T, Krämer E (2020) Microscale CFD simulations of a wind energy test site in the Swabian Alps with mesoscale based inflow data. *J Phys Conf Ser* 1618(062):021
- Liu Z, Hu Y, Fan Y, Wang W, Zhou Q (2019) Turbulent flow fields over a 3D hill covered by vegetation canopy through large eddy simulations. *Energies*. <https://doi.org/10.3390/en12193624>
- Lu GY, Wong DW (2008) An adaptive inverse-distance weighting spatial interpolation technique. *Comput Geo* 34:1044–1055. <https://doi.org/10.1016/j.cageo.2007.07.010>
- Lutz T, Schulz C, Letzger P, Rettenmeier A (2017) Impact of complex orography on wake development: simulation results for the planned WindForS test site. *J Phys Conf Ser* 854(012):029
- Maeda T, Homma S, Ito Y (2004) Effect of complex terrain on vertical wind profile measured by Sodar technique. *Wind Eng* 28(6):667–678
- Martin C (2015) LAI: calculate indirect leaf area index (LAI) from images. R package version 0.0.0.9004
- Mauz M, van Kesteren B, Junkermann W, Berge K, Schön M, Platis A, Bange J (2020) Miniature high-frequency chilled-mirror hygrometer for atmospheric measurements aboard fixed wing UAS. *Meteorol Z* 29(6):439–449. <https://doi.org/10.1127/metz/2020/1026>
- Platis A, Hundhausen H, Lampert A, Emeis S, Bange J (2021) The role of atmospheric stability and turbulence in offshore wind-farm wakes in the German bight. *Boundary-Layer Meteorol*. <https://doi.org/10.1007/s10546-021-00668-4>
- Rautenberg A, Graf M, Wildmann N, Platis A, Bange J (2018) Reviewing wind measurement approaches for fixed-wing unmanned aircraft. *Atmosphere*. <https://doi.org/10.3390/atmos9110422>
- Rautenberg A, Schoen M, Berge K, Mauz M, Manz M, Platis A, van Kesteren B, Suomi I, Kral S, Bange J (2019) The multi-purpose airborne sensor carrier MASC-3 for wind and turbulence measurements in the atmospheric boundary layer. *Sensors*. <https://doi.org/10.3390/s19102292>
- Ross A (2008) Large-eddy simulations of flow over forested ridges. *Boundary-Layer Meteorol* 128:59–76
- Schulz C, Hofsaß M, Anger J, Rautenberg A, Lutz T, Cheng P, Bange J (2016a) Comparison of different measurement techniques and a CFD simulation in complex terrain. *J Phys Conf Ser* 753(082):017
- Schulz C, Klein L, Wehling P, Lutz T (2016b) Investigations into the interaction of a wind turbine with atmospheric turbulence in complex terrain. *J Phys Conf Ser* 753(032):016
- Shaw RH, Schumann U (1992) Large-eddy simulation of turbulent flow above and within a forest. *Boundary-Layer Meteorol* 61:47–64. <https://doi.org/10.1007/BF02033994>
- Sykes RI (1980) An asymptotic theory of incompressible turbulent boundary-layer flow over a small hump. *J Fluid Mech* 101(3):647–670. <https://doi.org/10.1017/S002211208000184X>
- Taylor P, Gent P (1974) A model of atmospheric boundary-layer flow above an isolated two-dimensional hill: an example of flow above gentle topography. *Boundary-Layer Meteorol* 7:349–362. <https://doi.org/10.1007/BF00240837>

- Taylor P, Teunissen H (1987). Askervein hill project: overview and background data. <https://doi.org/10.1007/BF00121863>
- Taylor P, Mason PJ, Bradley E (1987) Boundary-layer flow over low hills. *Boundary-Layer Meteorol* 39:107–132. <https://doi.org/10.1007/BF00121870>
- Taylor PA, Lee R (1984) Simple guidelines of estimating wind speed variation due to small scale topographic features. *Climat Bull* 18:3–32
- Tian Y, Dickinson RE, Zhou L, Zeng X, Dai Y, Myneni RB, Knyazikhin Y, Zhang X, Friedl M, Yu H, Wu W, Shaikh M (2004) Comparison of seasonal and spatial variations of leaf area index and fraction of absorbed photosynthetically active radiation from Moderate Resolution Imaging Spectroradiometer (MODIS) and common land model. *J Geophys Res Atmos* 109(D1)
- Tillack A, Clasen A, Kleinschmit B, Förster M (2014) Estimation of the seasonal leaf area index in an alluvial forest using high-resolution satellite-based vegetation indices. *Remote Sens Environ* 141:52–63
- Troen I, Petersen E (1989) *The European wind atlas*. Riso National Lab, Roskilde
- Van den Kroonenberg A, Martin T, Buschmann M, Bange J, Voersmann P (2008) Measuring the wind vector using the autonomous mini aerial vehicle M²AV. *J Atmos Ocean Technol* 25:1969–1982. <https://doi.org/10.1175/2008JTECHA1114.1>
- Verger A, Descals A (2021) Copernicus global land operations “vegetation and energy”—algorithm theoretical basis document. visited: 14-January-2022
- Wang X, Wang C, Li Q (2015) Wind regimes above and below a temperate deciduous forest canopy in complex terrain: interactions between slope and valley winds. *Atmosphere* 6:60–87
- Weiss M, Baret F, Smith G, Jonckheere I, Coppin P (2004) Review of methods for in situ leaf area index (LAI) determination part II. estimation of LAI, errors and sampling. *Agric For Meteorol* 121:37–53
- Wildmann N, Mauz M, Bange J (2013) Two fast temperature sensors for probing of the atmospheric boundary layer using small remotely piloted aircraft (RPA). *Atmos Meas Tech*. <https://doi.org/10.5194/amt-6-2101-2013>
- Wildmann N, Hofsaess M, Weimer F, Joos A, Bange J (2014a) MASC: a small remotely piloted aircraft (RPA) for wind energy research. *Adv Sci Res* 11:55–61. <https://doi.org/10.5194/asr-11-55-2014>
- Wildmann N, Kaufmann F, Bange J (2014b) An inverse-modelling approach for frequency response correction of capacitive humidity sensors in ABL research with small remotely piloted aircraft (RPA). *Atmos Meas Tech* 7(9):3059–3069. <https://doi.org/10.5194/amt-7-3059-2014>
- Wildmann N, Bernard S, Bange J (2017) Measuring the local wind field at an escarpment using small remotely-piloted aircraft. *Renew Energy* 103:613–619. <https://doi.org/10.1016/j.renene.2016.10.073>
- Wildmann N, Päsche E, Roiger A, Mallaun C (2020) Towards improved turbulence estimation with doppler wind lidar velocity-azimuth display (VAD) scans. *Atmos Meas Tech* 13(8):4141–4158. <https://doi.org/10.5194/amt-13-4141-2020>
- WindForS (2018) WINSSENT and WINSSENT-BW. WindForS—Windenergie Forschungscluster

Publisher's Note Springer Nature remains neutral with regard to jurisdictional claims in published maps and institutional affiliations.

A.3 Evaluation of Engineering Models for Large Scale Cluster Wakes with the Help of in Situ Airborne Measurements - Publication III

This publication is currently under review in round two.

1 RESEARCH ARTICLE

2 Evaluation of Engineering Models for Large Scale Cluster Wakes with
3 the Help of in Situ Airborne Measurements

4 Kjell zum Berge*¹ | Gabriele Centurelli² | Martin Dörenkämper³ | Jens Bange¹ | Andreas Platis¹

¹Geo- and Environmental Sciences,
Eberhard-Karls-Universitaet Tuebingen,
Baden-Württemberg, Germany

²ForWind-Wind Energy Research
Center, Carl von Ossietzky University
of Oldenburg, Niedersachsen, Germany

³Fraunhofer Institute for Wind Energy
Systems, Fraunhofer, Oldenburg,
Germany

Correspondence

*Kjell zum Berge, Center for Applied
Geoscience, Eberhard-Karls-Universitaet
Tuebingen, Schnarrenbergstr. 94-96,
72076 Tuebingen, Germany
Email: kjell.zum-berge@uni-tuebingen.de

Summary

The planned expansion of wind energy in the German Bight is creating much more densely staggered wind farms and wind farm clusters. This results in a significantly greater influence of the generated wakes on energy production of neighboring wind farms. The Dornier-128 research aircraft operated by the Technische Universität of Braunschweig was used to measure the wind field in the lee of single and multiple wind farm clusters in the German Bight on four days during July 2020, and July 2021. The data at 120 m aMSL (above mean sea level) was analyzed to identify wake areas and the wind speed decrease behind the wind farm clusters. The observations were then compared to a range of numerical data including the mesoscale model WRF applying a wind farm parametrization (WRF-WF) to model wake effects and an engineering model with different setups. A model calibrated on a single wind farm is established as the baseline. A modification with a lower wake recovery, the TurbOPark model, and a WRF-coupled model make up the three additional declinations considered. Overall, the models compared well to the measurement data in the direct vicinity of the wind farms and up to 20-30 km downstream of the wind farm clusters. The accuracy in wind speed prediction of the model results decreased with distance to the wind farms, where the mesoscale model (WRF-WF) exhibited a more consistent performance across varying distances.

KEYWORDS:

Wind Energy, Airborne Measurements, Wakes, Mesoscale Models, Engineering Models

6 1 | INTRODUCTION

7 The global push for renewable energy has made wind power one of the key players in a low-carbon future. In 2021, wind energy production
8 surpassed 830 GW, with 93% of that total coming from onshore systems and 7% from offshore systems¹. Germany, with its current 8.4 GW
9 of installed offshore wind capacity (07-2023), accounts for 13.3% of the global offshore total^{2,3}. While onshore wind energy technology is
10 well-developed, offshore wind energy is still in the early stages of expansion, with only 19 countries currently utilizing offshore wind turbines¹.

11 The expansion of offshore wind energy is crucial for achieving Germany's and the world's energy goals. As such, the German government plans
12 to significantly accelerate its expansion. By 2045, a capacity of at least 70 GW is planned to be installed, which is almost a tenfold increase from
13 current levels⁴. To reach this capacity, large wind farm clusters will be installed in the North Sea and Baltic Sea. However, the increasing scarcity
14 of available space in the North Sea, due to factors such as competing interests and potential nature conservation areas, means that wind farms
15 must be located closer together. This has both economic advantages, such as the ability to share infrastructure, and negative effects on overall
16 energy production, such as reduced power output due to wake impacts from upstream wind farms^{5,6,7}.

17 Over the past two decades, the wakes behind offshore wind turbines and wind farms have been the subject of intense research. Most of

18 this research has relied on SCADA (Supervisory Control and Data Acquisition) data⁸ and remote sensing techniques, such as Doppler lidar
19 (Light Detection and Ranging)^{9,10,11,12}, or Doppler radar (Radio Detection and Ranging)^{13,14}. In addition to these measurements, wakes have
20 been studied in terms of numerical modelling on different scales and fidelity levels. From fast engineering models⁷, over models using RANS
21 (Reynolds averaged Navier-Stokes) methodologies^{15,16} to turbulence-resolving large-eddy simulations (LES)^{17,18} and mesoscale models to cover
22 even regional scales^{19,20,21,22,23}. Higher fidelity models, such as LES, and also lower fidelity engineering models have the ability to represent
23 individual turbines, unlike WRF (Weather Research and Forecasting Model) with its grid sizes of 1 km and more. This is especially true for wind
24 farms with a dense wind farm layout¹⁶. On the other hand, WRF can model the entire wind field around multiple wind farm clusters and their wake
25 with a variety of parameterizations²⁴, whereas LES are often limited to smaller regions encompassing a single wind farm cluster due to the shear
26 computational power required; and engineering models do not resolve well the behaviour of cluster wakes on a large scale²⁵.

27 As wind farm clusters continue to grow in size, measurement methods such as satellite-based synthetic aperture radar (SAR)^{26,27} and airborne
28 measurements^{28,6,7} are becoming more common. Large wind farm cluster wakes over distances of more than 10 km were first observed using
29 SAR data^{29,27,26}. In situ airborne data from the WIPAFF campaign even observed wakes as long as 70 km during thermally stable conditions^{28,6}.

30 Recent studies show that the thermal stratification of the marine boundary layer has a major impact on the development of wind turbine and
31 cluster wakes³⁰. A well mixed boundary layer during neutral and unstable stratification leads to faster wake recovery^{21,31}, while long-lasting
32 wakes are typically observed under stable conditions²⁸.

33 For instance, Canadillas et al.³² used a Doppler lidar system, airborne data, and the WRF model to study the interaction between two wind
34 farm clusters in the North Sea. They found a strong wind speed deficit of up to 30% 1.5 km downstream of the wind farm cluster and a reduction
35 in power yield of another downstream wind farm of up to 0.5%⁷ for distances of 30 km. The wind speed reduction was strongly dependent on
36 stability and wind direction. Although Doppler lidar measurements are useful for long-term monitoring, they are limited in their ability to cover
37 areas larger than 10 km. Therefore, lidar and radar are not suitable to study the full cluster wake development, that during stable conditions can
38 stretch more than 50 km in length. For this task, airborne measurements or SAR data can be valuable tools as they cover significantly larger areas.
39

40 In the past, comparisons between mesoscale, engineering models and measurements (SCADA, lidar, radar) were based on averages over long
41 periods of time⁷. In the current manuscript we assess model performance against the data of measurement flights, whose time period is limited to
42 a few hours. Engineering models are particularly challenged by this type of comparison. Normally, calibrations of engineering models are derived
43 over a large sample of scenarios, and they should not be expected to provide accurate results in modeling situations spanning few consecutive
44 hours. Furthermore, no inflow measurements concurrent with the flight is available. This leads to inaccuracies in the determination of the inflow
45 parameters, as they have to be derived with strong assumptions from either downstream conditions or climate models. On the other hand, fast
46 engineering models are currently used to support the wind capacity expansion of the German Bight by forecasting the impact on the yield of spe-
47 cific sites by existing or planned wind farms. More understanding of the model behavior when applied to the simulations of such large scenarios
48 is yet to be acquired in order to frame the accuracy of its results.

49 The aim of this study is a comparison between engineering models and a mesoscale model (WRF-WF) with regard to the wake propagation of
50 wind farm clusters in the German Bight by means of in situ flight measurements and to answer the following questions:
51

- 52 • Are engineering and mesoscale models capable of simulating large scale cluster wakes over very long distances?
- 53 • Can engineering models give comparable results without the input of long term data sets for the inflow conditions?
- 54 • What is the influence of mesoscale effects when only looking on single case studies and how to overcome this?

55 The study is organized as follows. In Section 2, we introduce the methodology, experimental setup, and measurement area in the North Sea, as
56 well as the data processing and model setup. In Section 3, we present four cases of flight data and compare these results to simulation runs of
57 engineering and mesoscale models, discussing the quality of the measurement data and the performance of the models under different conditions
58 within the four cases. Finally, in Section 4, we summarize the findings of this study.

59 2 | SITE AND METHODS

60 This section gives an overview of the data sources and model setups that has been used in this study. Measurements were conducted using the
61 Dornier-128 aircraft of the Technische Universität (TU) Braunschweig^{28,6} for wake measurements and 10-minute SCADA data for information in
62 the wind farm clusters. Numerical models used in this study are the engineering model FOXES (Farm Optimization and eXtended yield Evaluation
63 Software) and the mesoscale model WRF and WRF-WF (WRF with wind farm parametrization). Four cases in July 2020 and July 2021 have been
64 identified (³³) to serve as a model comparison.

2.1 | Wind Farms in the German Bight

The main focus of the 49 measurement flights in the German Bight conducted within the X-Wakes project in 2020 and 2021 was to measure the atmospheric conditions, wake propagation and other phenomena like the global blockage effect around the three wind farm clusters N2, N3 and N4 (Fig. 1). The clusters N2 and N3 are 50 and 35 km off of the German coast, respectively, just north of the East-Frisian islands. Cluster N4 is located further north-east towards the German-Danish border. The horizontal distance between cluster N2 and N3 is below 25 km which makes an interaction between these two clusters more likely, due to the mean prevailing wind direction between south-west (SW) and west (W) ⁽³⁰⁾. The distances of clusters N2 and N3 to cluster N4 are much larger with 120 km and 65 km, respectively.

For modelling the wind farm wakes, it is important to know the key characteristics of the wind farms in question. In the scope of this paper, information of the wind turbines in cluster N2 and N3 are most important and listed in Tab. 1.

Table 1 Wind farm properties of clusters N2 and N3. "Wind Farm" denotes the name of the wind farm given by the operator, "No. of WTs" is the total number of wind turbines in a single wind farm, "WT Type" is the wind turbine type, h is the hub height, D is the rotor diameter, P_{rated} is the rated power of each turbine type and "SCADA" denotes if SCADA data was available.

Cluster	Wind Farm	No. of WTs	Manufacturer	h [m]	D [m]	P_{rated} [MW]	SCADA Data Available
N2	Merkur	66	GE	102	150	6	Yes
N2	Borkum Riffgrund 1 (BRK I)	78	Siemens	83	120	4	Yes
N2	Borkum Riffgrund 2 (BRK II)	56	Vestas	83	154	4	Yes
N2	Trianel Wind Farm Borkum 1 (TW I)	40	Adwen	87	116	5	Yes
N2	Trianel Wind Farm Borkum 2 (TW II)	32	Senvion	111	164	6.3	No
N2	Alpha Ventus (AV)	6/6	Senvion/Adwen	92/90	126/116	5	Yes
N3	Nordsee 1 (NO)	54	Senvion	90	126	6.2	Yes
N3	Gode Wind 1 (GOW I)	55	Siemens	110	154	6	Yes
N3	Gode Wind 2 (GOW II)	42	Siemens	110	154	6	Yes
N4	Nordsee Ost (NE)	48	Senvion	100	126	6	Yes
N4	Amrumbank West (AW)	80	Siemens	90	120	3.8	Yes
N4	Meerwind Süd-Ost	80	Siemens	89	120	3.6	No

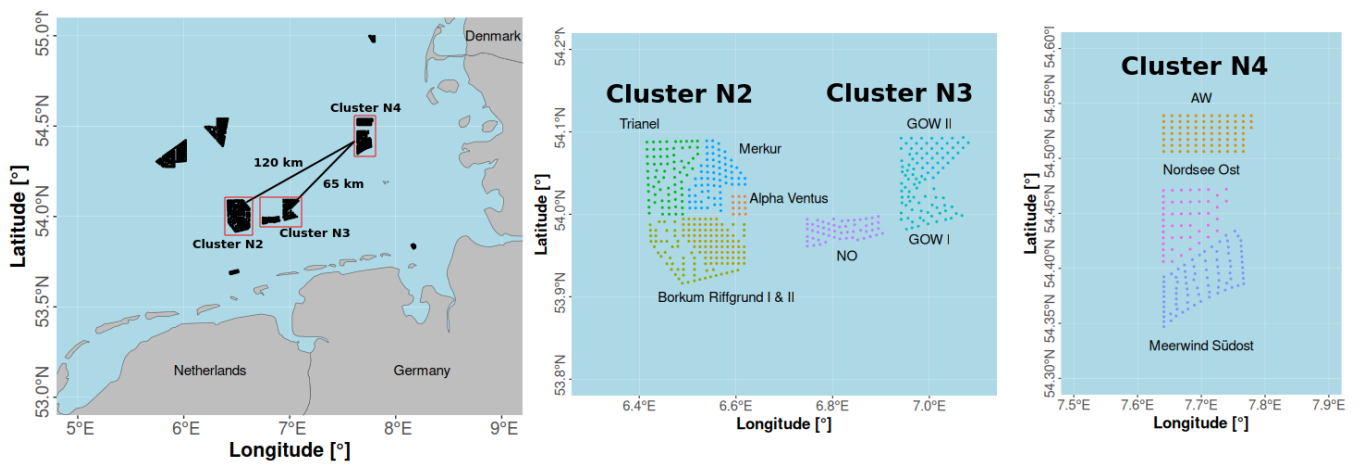


Figure 1 Wind farms cluster in the German Bight as of 2021. Distances shown between clusters N2, N3 and N4

2.2 | Measurement System and Strategy

To investigate a large spatial extent of a wake formed in the lee of a wind farm or a wind farm cluster (Fig. 1) the research aircraft DO-128³⁴ is used. The DO-128 is capable of measuring the 3D wind vector with an accuracy of $\pm 0.5 \text{ m s}^{-1}$ for the horizontal wind speed³⁵ as well as other meteorological values like air temperature, air pressure and relative humidity with a sampling rate of 100 Hz³⁶. This enables the aircraft to measure with a spatial resolution of a few meters along its flight path over the North Sea. Apart from the meteorological sensors mounted in a nose boom at the front of the aircraft, a laser scanner measuring wave heights and downward facing sensors measuring the sea surface temperature (SST) are located underneath the fuselage. More details on the instrumentation and the data processing are available in Platis et al.²⁸ and Lampert et al.³⁴. The flight tracks were always aligned perpendicular to the wind direction during the measurement and consisted of multiple legs (straight and leveled flight sections) with a length of 40–50 km up- and downstream of single wind farms and clusters. This flight pattern assures to cross the wakes on each leg and also to measure the undisturbed flow at the boundaries of each flight leg. To get information of the atmospheric stratification before, during and after the actual measurement pattern, vertical profiles from 30 m above the sea surface to 1000 m altitude were flown. The altitude during the horizontal flight legs was between 110 and 120 m aMSL, which is slightly above the hub height of the wind turbines in cluster N2, N3 and N4 (see Tab. 1). Figure 2 shows the flight patterns of the four measurement flights examined in this study in July 2020 and July 2021. The black arrow depicts the mean wind direction during each of the measurements. Generally the flight path is always orthogonal to the mean wind direction during the flight.

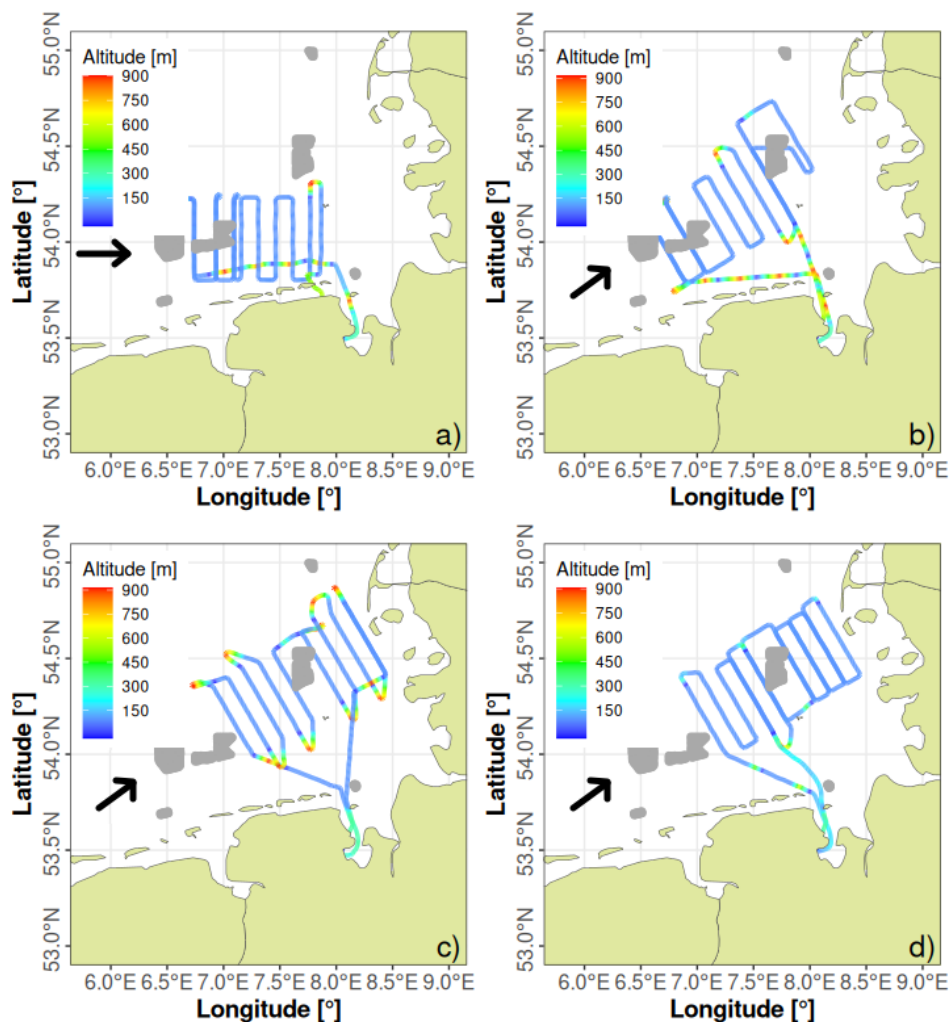


Figure 2 Flight patterns for the four investigated measurement flights. a) 14.07.2020; b) 23.07.2020; c) 27.07.2021 and d) 30.07.2021. The different color on each flight track shows the altitude changes. The black arrow shows the mean wind direction during the measurements. Wind farms are depicted by the grey areas

Table 2 The rounded distances between the single measurement legs for all four flights

14.07.2020		23.07.2020		27.07.2021		30.07.2021	
Leg	Distance [km]	Leg	Distance [km]	Leg	Distance [km]	Leg	Distance [km]
1 - 2	13	1 - 2	13	1 - 2	10	1 - 2	10
2-3	10	2-3	10	2-3	10	2-3	10
3-4	13	3-4	10	3-4	10	3-4	10
4-5	10	4-5	10	4-5	10	4-5	10
5-6	10	5-6	10	5-6	20	5-6	20
		6-7	9	6-7	10	6-7	10
		7-8	27	7-8	10	7-8	10
				8-9	10	8-9	10

89 2.3 | Model Setup

90 In this study, results from the mesoscale model WRF with wind farm parametrization (WRF-WF) and the engineering model FOXES are compared
91 with aircraft data. Below the models, their specific setup and related data sources are described.

92 2.3.1 | Weather Research and Forecasting Model (WRF)

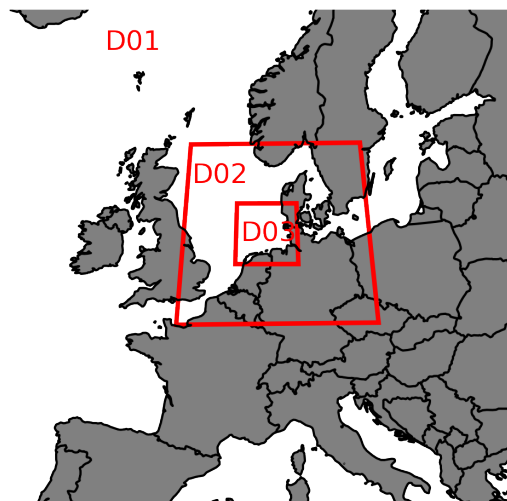
93 Mesoscale wake simulations were conducted with the WRF model (version 4.2.1) developed by the National Center of Atmospheric Research⁽³⁷⁾.
94 The model is widely applied in wind energy research and industrial applications e.g.^{38,39,7}. The set-up applied was developed in several research
95 projects with the aim of optimizing the model results for offshore wind energy applications (e.g.^{38,40,39,41}). Parts of the set-up are based on the
96 extensive sensitivity studies carried out in the framework of the NEWA (New European Wind Atlas) project^(40,39). Internal refinements of the
97 setup were done by comparison to the wind measurements of several offshore met masts in the North Sea. The model's boundary conditions for
98 the atmospheric variables were prescribed by the ERA5 (Fifth Generation of the European Reanalysis) data set⁽⁴²⁾ and with OSTIA (Operational
99 Sea Surface Temperature and Sea Ice Analysis) data set⁽⁴³⁾ for the sea surface variables. The wind turbines were parameterized with the Fitch wind
100 farm parametrization that models the turbines as a wind speed-dependent sink of momentum and source of turbulence⁽⁴⁴⁾. The model domain
101 always covered the whole German Bight area, including all turbines that were commissioned at the investigated situations in time. Figure 3 shows
102 the three domains for the WRF simulation, with the innermost domain D03 covering the whole area of interest for this study.
103 Hereafter, we refer to WRF-WF when using data from this described setup, instead the acronym WRF will now be used to refer to the same set-up
104 without wind farm parameterisation. These type of simulations were required to initialize one of the engineering model set-up considered, clarified
105 in Sec. 2.3. The model results were post-processed to make those comparable to e.g. the flight height measurements. To compare the WRF results
106 for each of the four cases in July 2020 and 2021 with the corresponding flight data, the wind speed at the exact coordinates and the same time
107 frame (mean of the whole flight leg for the 10 minute WRF data) of the flight transect were extracted and directly compared to the wind speed
108 measured by the aircraft at the same grid points.

109 2.3.2 | WRF-WF Timeshift Estimation

110 The WRF model is driven by ERA5 and OSTIA boundary conditions on a six-hourly interval. As a result, inaccuracies, in particular phase errors,
111 may appear if there are significant changes in the weather situation during this time period and e.g. wind ramp events such as fronts move
112 faster/slower in the model than in reality. To account for this well-known inaccuracy, it may be necessary to correct the WRF-WF results for time
113 differences due to atmospheric changes not captured with the last model run. In order to determine the corresponding time shift for each of the
114 four flights, each of the measurement legs flown was compared with the results of the WRF-WF simulation at times up to three hours before and
115 three hours after the measurement time. The WRF results with wind farm parameterization were chosen to determine the time shift between
116 measurement and model, as this is more consistent for the subsequent analysis of the results and the time shift of the WRF and WRF-WF runs
117 should not differ, as this is independent of the parameterization. An alternative to evaluate the time shift could be the use of FINO1 data. This
118 option was not selected because the met mast is located on the eastern side of the N2 wind farm cluster and could therefore be disturbed by the
119 turbines in terms of both wind direction and wind speed.

Table 3 Parameters of the WRF model set-up. More information on the different models and schemes are summarized on the WRF Users Page⁴⁵

Parameter	Setting
WRF model version	4.2.1
Land use data	MODIS
Surface layer scheme	MYNN
Microphysics scheme	WRF single-moment five-class
Wind farm parametrization	Fitch et al., ⁴⁴
Planetary boundary layer (PBL) scheme	MYNN level 2.5
Shortwave and long-wave radiation	RRTMG
Atmospheric boundary conditions	ERA5
Sea surface conditions	OSTIA
Horizontal resolution	18, 6 and 2 km
Vertical Resolution	60 eta level
Land surface model	Unified Noah Land Surface Model
Simulation duration	240 (+24 spin-up) hours
Nudging	Grid nudging above PBL
Model output interval	10 min
Nesting	One-way

**Figure 3** The three WRF model domains (D01, D02, D03) over the North Sea and the German Bight with a grid sizes of 18, 6 and 2 km, respectively.

121 Figure 4 shows as an example the first measurement leg (leg 1 in Figure 3.2.1) of the flight on 14.07.2020 between 13:07 and 13:17 UTC as
 122 a solid black line and results from multiple WRF-WF results at certain time steps, from which the decision was made which best fits the aircraft
 123 data. The blue triangles show the results of the WRF-WF simulation closest to the flight period (13:10 UTC) at the same interpolated coordinates.
 124 The red rectangles and the black circles show the WRF-WF results 2:40 h before and after the time of the measurement. In this case, the black
 125 circles show the best agreement with the flight data in the waked region, which is why a time offset of about -2:40 h can be assumed. Compared
 126 to the time steps closer to the time of measurement, the results for -2:40 h also give the best results for the waked area. This time step was also
 127 consistently better than the other time steps during this flight. Therefore, the WRF-WF results for the 14.07.2020 flight period were corrected
 128 accordingly. The simulation results for the other days were also analysed and corrected using the same scheme (see Table 4).

Table 4 The time shift of all four measurement flights. The time shift is the same for all flight legs within each of the measurement flights.

Date	Time	Time Shift
14.07.2020	1230 - 1600 UTC	- 2:40h
23.07.2020	1200 - 1530 UTC	- 1:10h
27.07.2021	1030 - 1415 UTC	- 1:30h
30.07.2021	0830 - 1200 UTC	1:30h

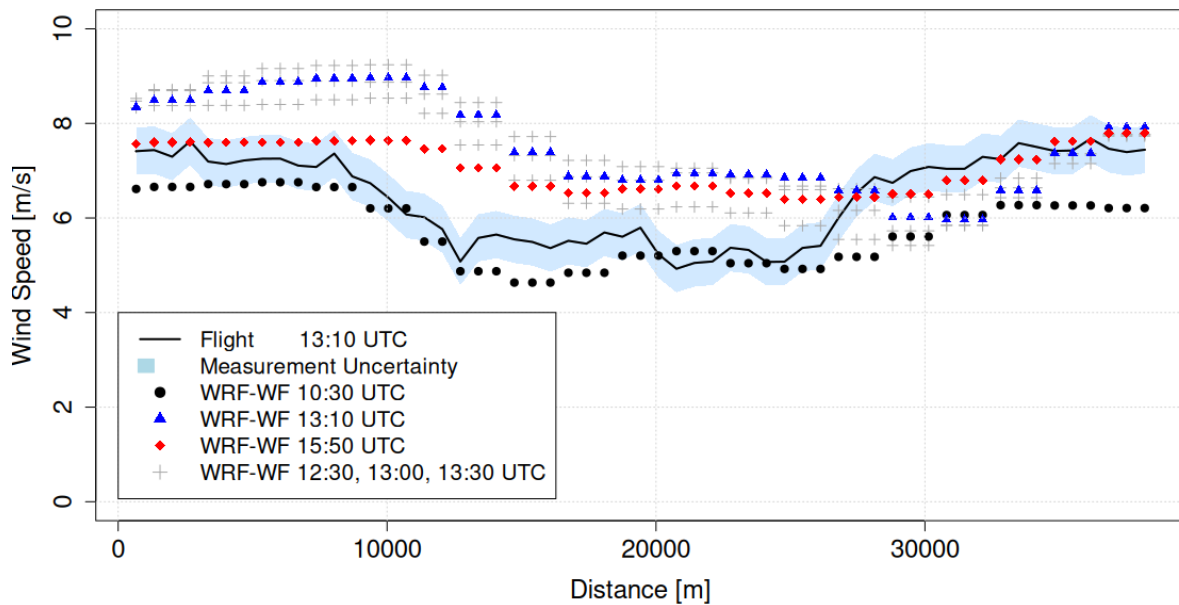


Figure 4 Wind speed of leg 1 of the measurement flight on the 14.07.2020 (black line) with the measurement uncertainty of $\pm 0.5 \text{ m s}^{-1}$ (blue shade) compared to results from WRF-WF for different 10-minute wind speed data. The blue triangles represent the WRF-WF data for the time of measurement. The black dots and red rectangles are WRF-WF results for 2:40h before and after the measurement on that flight leg, respectively. The grey crosses are additional WRF-WF results around the time of measurement

129 2.3.3 | Engineering Model

130 In addition to the WRF-WF results, the considered cases have been simulated with an engineering-type model (EM) for the wind farm yield cal-
 131 culation. The model used is the open source code FOXES⁴⁶ developed at "Fraunhofer IWES". Within the engineering model, the wake of every
 132 single turbine is described according to an analytical wake model, e.g. the well-established *Jensen*⁴⁷ or *Bastankhah*⁴⁸ models. A wake recovery co-
 133 efficient dependent on local turbulence intensity (TI) in combination with a wake superposition strategy take care of describing the wake effects
 134 at the farm level. In this way, the engineering model avoids the solution of any differential flow equations, removing the need for a solving grid. On
 135 the one hand, this feature maintains computational costs low allowing for the calculation of wake effects across several inflow conditions at hun-
 136 dreds of turbines. On the other, it makes the model particularly unreliable for representing single situations. So far, engineering models have been
 137 demonstrated to agree well with single situations simulated in LES⁴⁹ and with production data (SCADA) over longer period of simulated time⁵⁰
 138 when correctly calibrated.

139 For this purpose, we consider four different analytical methods for calculating wind farms' performance in the engineering model framework: A
 140 standard engineering model with a baseline calibration (EM-BL), a calibration aiming at strongly dampening wake recovery (EM-LR), the TurbOPark
 141 model of Ørsted (EM-TP), and an engineering model coupled with WRF (EM-WRF). The following describes the four models in details.

142 The baseline model (EM-BL) is established as the wake model of Bastankhah and Porté-Agel 2016⁵¹. In this model, the wake velocity deficit,
 143 $\delta(\vec{x})$, is treated differently according to the downward distance from the wake-causing turbine. Further downstream, the so called far-wake exhibits
 144 self-similarity and it is modeled with a Gaussian velocity deficit. In the near-wake, instead, the velocity deficit is characterized by a uniform velocity

145 deficit core that progressively decreases in diameter as the wake diffuses radially. The transition between the core and the free flow is modeled
 146 again through the Gaussian profile. The end of the near-wake is obtained when the uniform deficit core collapses, and it is represented by a certain
 147 distance from the rotor x_0 , which reads

$$\frac{x_0}{d_0} = \frac{1 + \sqrt{1 - C_T}}{\sqrt{2(\alpha Tl_{loc} + \beta(1 - \sqrt{1 - C_T}))}} \quad (1)$$

148 with α and β being model parameters, C_T the thrust coefficient, d_0 the rotor diameter. The local turbulence intensity Tl_{loc} is intended at the
 149 location of the turbine's rotor causing the wake and is computed as

$$Tl_{loc} = \sqrt{Tl_{amb}^2 + \max(Tl_{add,i})^2} \quad (2)$$

150 with i being, all the wakes reaching the location of interest. The turbulence intensity added by a generic turbine, Tl_{add} , is modeled after Crespo
 151 and Hernandez 1999⁵².

152 The wake velocity deficit of a generic turbine j at any locations in the wake frame identified by x , downstream distance from the center of the
 153 rotor, and r , the radial distance from the wake center-line, in the far-wake reads:

$$\delta_j(\vec{x}) = \frac{\Delta U(x)}{U_{\infty,j}(\vec{x})} = \left(1 - \sqrt{1 - \frac{C_{T,j}}{8 \left(\frac{1}{\sqrt{8}} + k^* \frac{x-x_0}{d_0} \right)^2}} \right) \exp \left(- \frac{r^2}{2d_0^2 \left(\frac{1}{\sqrt{8}} + k^* \frac{x-x_0}{d_0} \right)^2} \right), \quad (3)$$

with $U_{\infty,j}$ being the undisturbed velocity the turbine's rotor location. Equation 3 bears the assumption of no yaw misalignment and an axis-
 symmetric wake expansion coefficient k^* . To introduce dependency on TI for the wake recovery, k^* is determined thanks to: $k^* = k_{TI} TI^* + k_b$,
 in agreement with Niayifar and Porté-Agel⁴⁹. The turbulence intensity, TI^* , is either the ambient turbulence intensity Tl_{amb} in the far wake or the
 local turbulence intensity Tl_{loc} in the near wake. This choice stems from the fact that the turbulence intensity added by the wake decays much
 faster than the velocity deficit.

We used linear superposition of the wake velocity deficit to determine the velocity modified by the wind farms at any location as:

$$U(\vec{x}) = U_{\infty}(\vec{x}) \left(1 - \sum_{i=1}^{N_t} \delta_i(\vec{x}) \right) \quad (4)$$

154 with N_t the total number of turbines.

155 The parameters k_{TI} , k_b , α , and β controls how the wake recovers downstream. The baseline calibration we used for these coefficient is $k_{TI} = 0.23$,
 156 $k_b = 0.003$, $\alpha = 1.4$, and $\beta = 0.077$, found to determine the best agreement between the engineering model and wind farm production data at a
 157 real wind farm in the German Bight by von Brandis et al.⁵³

158 The calibration was derived neglecting the effect of the ground, normally represented by mirroring all the turbines at the ground, so that an
 159 identical wind farm is simulated under the ground⁵⁴.

160 The baseline calibration, focusing on maximize the accuracy at a single wind farm, is expected to be biased toward underestimating the velocity
 161 deficit far downstream the wind farms in the cluster wake. Therefore, we introduced a "low wake recovery" calibration for the same Porté-Agel
 162 wake model (EM-LR). In this calibration, the coefficients k_{TI} and k_b are set to a value of 0.05 and 0.0, respectively.

Since the calibration of (EM-LR) has not been validated yet, we considered the implementation of the TurbOPark model proposed by Pedersen
 et al.⁵⁵ in FOXES (EM-TP). This wake model was tailored to increase the accuracy of the wake deficit calculation at larger downstream distances.
 The wake deficit in the TurbOPark model is also assumed to distribute as a Gaussian, but there is no differentiation between near- and far-wake.
 However, the model is supposed to improve the representation of the wake recovery by injecting a direct dependency of the wake expansion
 coefficient to the TI found at the particular location of interest:

$$\frac{d\sigma_w}{dx} = A Tl_{loc}(\vec{x}) \quad (5)$$

note that $Tl_{loc}(x)$ is calculated according to Eq. 2. However, before it always referred to the value at the turbine's rotor causing the wake. Along the
 same line, also the velocity deficit of the generic turbines is referenced to the actual location at which it is computed, rather than to the undisturbed
 velocity at the wake causing rotor.

$$\delta_j(\vec{x}) = \frac{\Delta U(x)}{U_{\infty}(\vec{x})} = \left(1 - \sqrt{1 - \frac{C_{T,j}}{8 (\sigma_{w,j}(x)/D_j)^2}} \right) \exp \left(- \frac{r^2}{2\sigma_{w,j}^2(x)} \right), \quad (6)$$

TurbOPark requires the use of a quadratic superposition for the velocity deficit:

$$U(\vec{x}) = U_{\infty}(\vec{x}) \left(1 - \sqrt{\sum_{i=1}^{N_t} \delta_i(\vec{x})^2} \right) \quad (7)$$

163 Furthermore, the ground effect has to be considered, the turbines are therefore mirrored at the ground. This model features a total of three tunable parameters. The chosen values are provided in table 5, together with a summary of the models used and their calibrations.

Case	Wake model	Calibration	Wake Frame	WS superposition
EM-BL	Porté-Agel ⁵¹	$k_{T1} = 0.23, k_b = 0.003, \alpha = 1.4, \beta = 0.077$	rotor wind	linear
EM-LR	Porté-Agel ⁵¹	$k_{T1} = 0.05, k_b = 0.0, \alpha = 1.4, \beta = 0.077$	rotor wind	linear
EM-TP	TurbOPark ⁵⁵	$A = 0.04, c1 = 1.5, c2 = 0.8$	rotor wind	quadratic
EM-WRF	Porté-Agel ⁵¹	$k_{T1} = 0.23, k_b = 0.003, \alpha = 1.4, \beta = 0.077$	streamlines	linear

Table 5 The four different engineering model simulations set-up

164
165 The last engineering model considered is the WRF-coupled streamline wake model presented in von Brandis et al. 2023⁵³ (EM-WRF). The
166 derivation of realistic inflow conditions for the engineering model, detailed in Sec. 2.3.4, can introduce a lot of uncertainty in the EM results.
167 Coupling EM-WRF is expected to provide a significantly better framework to run simulations where multiple very large wind farms or wind farm
168 clusters are involved.

169 The EM-WRF is set up with the same wake model, calibration, and superposition strategy of the EM-BL, however the wake frame of reference
170 for any turbine wake uses as the downstream coordinate the streamline evolving from the Nacelle of the wake causing turbine. In this way, the
171 wakes propagate not according to a straightline oriented as the wind direction at the wake causing rotor, but they are supposed to propagate as
172 a passive scalar would within the undisturbed flow. A full description of the procedure is provided in⁵³ and the implementation is provided in the
173 open source version of FOXES.

174 Such a model requires the knowledge of the heterogeneous undisturbed flow field to initialize turbines WS and WD, and to derive the
175 streamline path within each considered timestep. Therefore, the simulations performed with WRF-WF were also repeated without the wind
176 farm parameterisation (WRF). The results of WRF are provided as input background flow field to FOXES, so that wakes are calculated by the
177 engineering model framework and superimposed to the WRF results. Every timestep in the WRF timeseries becomes completely independent
178 from one another in the engineering model framework, so that the classical fully-developed and steady-state flow assumptions used in analytical
179 wake models still hold. Concerning with the T1 value for the wake models, despite being estimated by the WRF model, we preferred to fix the
180 same 5% value used in the other engineering models. In order to focus solely on whether the EM-WRF could improve the engineering model
181 result via a better initialization of turbines free-stream and turbine wake propagation.

182
183 In all the engineering models above described we did not include an induction model to account for wind farm blockage. We believe it would
184 offer negligible improvement in the calculation of wake effects downstream a wind farm.

185 We also did not account for uncertainty in the wind direction when simulating a single situation. As the results are later presented in moving
186 average we claim that accounting for such uncertainty would not introduce significant differences in our results.

187 2.3.4 | Determination of Inflow Conditions

188 The most critical point in the simulations with the engineering model is the inflow definition. During the aircraft flights considered there has been
189 no further measurement that focused on the inflow conditions for the different wind farm clusters. Therefore to determine the undisturbed velocity
190 necessary for the initialization of the engineering model we can only rely on the measurements available, i.e. SCADA or the aircraft data.

191 Taking values of inflow wind speed and direction from the SCADA of the turbines in the first row is a common practice in model calibration
192 procedures at a single wind farm. However, the spatial extension of the current scenarios implies that the advection time cannot be neglected. This
193 means that to compare the model prediction against the measurements at a single leg, it is not possible to use the SCADA of the turbine in "free-
194 stream" at the same time the aircraft flew along the given leg. Instead, it is necessary to account for the advection time between the considered
195 leg and any of the turbines in the farm. However, the wake effects strongly depend on inflow velocity, and such a procedure would introduce
196 too much uncertainty in the model results. Therefore, to compare the model against the measured data, the inflow conditions of wind speed and
197 direction have been derived leg by leg, as average of the free-stream portion of each leg (see section 2.4 for details). For the turbulence intensity
198 value, according to²⁸, it is possible to derive it from the aircraft measurements. However, very small values around 3% were sampled. Upon initial

199 testing, with such a low value the wake models overestimate too much the wake deficit. Eventually, it was preferred to fix a value of 5% for TI, that
 200 is very representative for the German Bight and likely to be used by modelers when information on TI are missing.
 201 In this way, the advection time had to be considered only for the operating status of each turbine. The turbines' wakes affecting the velocity
 202 sampled by the aircraft were generated at a different time than when the sampling happens. We assume it is possible to calculate the time difference
 203 between any turbine and the aircraft leg of interest as

$$\Delta t_{\text{advec}} = \frac{\Delta x}{\bar{U}_{\text{leg}}} \quad (8)$$

204 Subtracting Δt from the average time at which each leg is collected, we derive the time at which the operating status of each turbine has to
 205 be determined. Knowing the operating status allows to correctly specify the level of thrust the turbines was operating at, e.g. avoiding to simulate
 206 wakes for non operational turbines. We define the degree of curtailment of a turbine from the ratio of the power produced and the power it is
 207 expected at the wind speed measured by the nacelle anemometer. Whenever the ratio between the two power was less than 0.75, than the turbine
 208 was considered curtailed. Furthermore, the blade pitch angle is taken into consideration to determine turbines completely stopped, however it has
 209 not been used to determine the degree of curtailment as it was found to be in some farms inconsistent with the level of power produced by the
 210 turbines. In FOXES, the degree of curtailment is used to recalculate the thrust coefficient. The procedure encompass the following step: the non
 211 curtailed turbine Power and Ct are computed according to the power and thrust curves, the thrust is then recalculated from the power according to
 212 1D momentum theory to define a correction coefficient to be applied when computing Ct from the Power, finally the curtailment degree is applied
 213 to the turbine Power, the curtailed power is finally used to derive Ct from 1D momentum and the value is corrected according to the correction
 214 coefficient.

215 In its current status, the derivation of the advection times entails a lot of uncertainty as many simplification assumptions were taken. Most
 216 notably, it is assumed that no wind direction change happens during the advection. However, in internal tests, we observed the results of the
 217 engineering model for the cluster wake to depend on the correct definition of the operating status of the turbines to a lower degree than the
 218 values of wind direction and wind speed. In initial testing of the engineering simulations, it appeared clear that a further source of uncertainty was
 219 represented by the existence of wind speed gradients across the wind speed profiles sampled on the leveled measurements legs. As explained in
 220 sec. 2.3, one simulation for each day considered is also initialized with mesoscale data (WRF), to check if these gradients in the inflow could
 221 be captured by the two models combination.

222 A further benefit of this procedure is to compensate for the lack of information about the vertical shear as the inflow wind speed is defined
 223 from a single horizontal leg at a time. The vertical distribution of velocity can impact the power output of every single turbine and hence the wakes
 224 produced. In the classical engineering modeling framework, information about shear are commonly missing. For this reason, it is good practice to
 225 initialize the simulation with hub height velocity. Unfortunately, the hub-height of most of the turbine simulated (see table 1) is below the altitude
 226 aMSL of the aircraft during the straight and leveled measurements legs. Figure 5 shows the mean wind speed of all vertical profiles combined for
 227 each of the four measurement flights. The upper line at 120 m aMSL is the aircrafts altitude, the line at 90 m aMSL is the lower altitude of most
 228 of the turbines in cluster N2, N3 and N4. The vertical profiles show that the wind speed difference between those two heights is negligible and
 229 within the uncertainty of the aircraft wind measurement.

230 2.4 | Data Processing and Meteorological Data

231 The aircraft data considered in this study are the three wind components u , v and w , the air temperature T , the relative humidity ϕ and the absolute
 232 air pressure p . These values are available with a temporal resolution of 10–100 Hz. The mean horizontal wind speed vector \mathbf{u}

$$\vec{u} = \vec{v}_{\text{gs}} + \mathbf{M}(\vec{v}_{\text{tas}} + \vec{\Omega} \times \vec{s}), \quad (9)$$

233 is calculated using the ground speed vector \vec{v}_{gs} , the air speed vector \vec{v}_{tas} , the rotation matrix \mathbf{M} from the aircraft's aerodynamic fixed coordinate
 234 system to the meteorological coordinate system, the angular rotation vector $\vec{\Omega}$ and the lever arm \vec{s} between the IMU (inertial measurement unit)
 235 and the flow probe.

236 To determine the atmospheric stability, the lapse rate γ

$$\gamma = \frac{\Delta \theta_v}{\Delta z} \quad (10)$$

237 with the difference in virtual potential temperature $\Delta \theta_v$ over the height Δz is used as it can be considered to be the most robust and representative
 238 stability criteria in the German Bight according to Platis et al. 2022³⁰. It was calculated between the lowest flight altitude (20 m aMSL) and hub
 239 height (120 m aMSL) and in another interval above between 120 m aMSL and the highest flight altitude, mostly 1000 m aMSL.

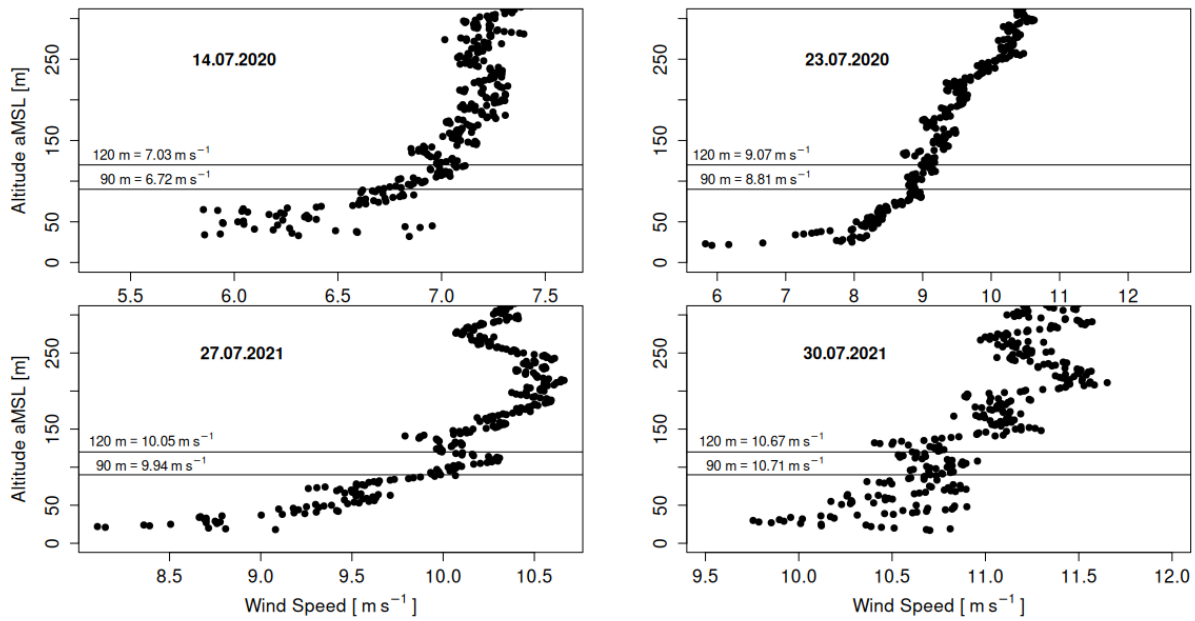


Figure 5 The mean wind speed during all vertical profiles for each of the four measurement flights up to a height of 300 m aMSL. The two lines show the heights of 90 m and 120 m aMSL with the corresponding wind speeds.

240 To include mesoscale effects when processing the aircraft data, meteorological data from the measurement mast FINO1 at the eastern edge of
 241 cluster N2 (Fig. 1) was considered. It features wind, temperature, pressure and humidity measurements at various heights of 30, 40, 50, 70, and
 242 90 m. Looking at the meteorological data of the complete day and not only at the time of an aircraft measurement, reveals mesoscale effects that
 243 could have been misinterpreted for other, e.g. wind farm related, effects. Additionally, WRF-WF results are considered to reflect changes in the
 244 mesoscale situation during aircraft measurements and the whole day.

245 To identify wake effects, a clear differentiation between the wake area and the undisturbed or free flow is essential. An estimation of the expected
 246 position of the cluster wake can be provided by assuming it as a self-similar profile with Gaussian feature like in⁷. A mean direction is computed
 247 across all the points at "hub-height" altitude sampled by the aircraft in one flight. The wake of each cluster is then assumed to propagate along the
 248 mean direction for 90 km and with a lateral extension expanding in a linear manner downstream: $W_{\text{cluster wake}} = W_{\text{cluster}} + 0.04 \cdot \Delta x$ with Δx being
 249 the windward distance from the last turbine in the cluster. With such an approximation of the cluster wakes, it is possible to define the portion of
 250 the legs that should be in free-stream. Table 6 shows the mean values for each flight in the columns "Flight Data".

251 As a second source of data to define the wind speed in the free flow, SCADA data was used. Depending on the wind direction the first row
 252 of turbines, for the wind farms where SCADA data was made available by the operators, was identified, and the wind speed measured by the
 253 instrumentation on each turbine analyzed and averaged (Tab. 6). All measurement data in this study are in Coordinated Universal Time (UTC).

Table 6 Comparison between wind speed and wind direction measured by first row turbines of all available SCADA data and flight data.

Date	Wind Speed [m s ⁻¹]		Wind Direction [°]	
	SCADA	Flight Data	SCADA	Flight Data
14.07.2020	6.8	6.5	268.6	260.4
23.07.2020	9.2	9.3	233.0	225.8
27.07.2021	6.5	9.4	233.9	237.7
30.07.2021	9.4	10.8	232.4	241.9

3 | RESULTS

This section presents the aircraft data on four days in July 2020 and July 2021 over the German Bight in westerly winds between and in the lee of the wind farm clusters N2, N3 and N4 (Fig. 1). Afterwards, a range of engineering models with different setups (2.3.3) and the WRF-WF simulation using the method by Fitch⁴⁴ were compared to the aircraft data. To get an overview on the mesoscale situation during the days of measurement, the following subsection describes data from the meteorological measurement mast FINO1, located at the eastern edge of the N2 cluster.

3.1 | Meteorological Conditions and Stability Estimation

In Fig. 6 the measured values for wind direction and wind speed from FINO1 data are plotted for the 14.07.2020, 23.07.2020, 27.07.2021 and 30.07.2021. The blue shaded areas are indicating the time of flight measurement during each day.

As FINO1 is located within the wind farm cluster N2, more precisely in the eastern half, the wind speed data should be treated with caution. This is especially true for wind directions from the west⁵⁶. For this reason, the measurement data shown in Figure 6 should only be seen as a consideration of the overall situation on each of the measurement days. Mesoscale phenomena e.g. changes in wind speed during the time of measurement, which are important for interpreting the results, are clearly visible from the FINO1 data.

On the 14.07.2020 during the aircraft measurements the wind speed shows a small magnitude of variation between 5 m s^{-1} and 6 m s^{-1} and wind direction changes from 250° to 270° . On the 23.07.2020 the wind speed is varying around 7 m s^{-1} during the day but is dropping from $7\text{-}8 \text{ m s}^{-1}$ to 6 m s^{-1} around noon, back again to $7\text{-}8 \text{ m s}^{-1}$ towards the end of the aircraft measurements (Fig. 6b). The wind direction changes from southern direction at sunrise to $210\text{-}240^\circ$ during the flight.

The wind direction on the 27.07.2021 (Fig. 6c) ranges between 200° and 240° with stronger changes in the early hours of the day. The wind speed peaked in the morning and evening at around 9 m s^{-1} while slowly decreasing from 6 m s^{-1} to 3 m s^{-1} during the measurement.

During flight time on the 30.07.2021 (Fig. 6d), wind speed and wind direction are similar to the 27.07.2021, with a wind direction of close to 240° and a decreasing wind speed from 8 m s^{-1} to 4 m s^{-1} during the aircraft measurement.

Table 7 The mean lapse rate of all vertical profiles during each measurement flight between the lowest altitude and hub height and above hub height to the highest altitude calculated using equation 10.

Date	Lapse rate < hub height [K/100 m]	Lapse rate > hub height [K/100 m]	Thermal stratification
14.07.2020	0.18	0.23	stable
23.07.2020	0.31	0.14	stable
27.07.2021	0.43	0.31	stable
30.07.2021	0.14	0.27	stable

Table 7 shows the lapse rate calculated from aircraft data during vertical profiles (see Fig. 2) for the heights of the lowest altitude at 60 m to hub height at 120 m and for altitudes above hub height to the maximum altitude of 1000 m. The lapse rate for all measurement days shows a stable stratification, when evaluated according to the definition by Platis et al.³⁰. The strongest stable stratification was found on the measurement days of 23.07.2020 and 27.07.2021 with lapse rates of 0.31 and 0.43 from the lowest measurement to hub height, respectively. None of the days show a very stable stratification, but are stable enough to produce visible wakes.



Figure 6 FINO1 data for wind speed and wind direction for the four measurement days in July 2020 and 2021 at various tower levels. The wind speed (solid lines) and wind direction (dotted lines) for the measurement days 14.07.2020, 23.07.2020, 27.07.2021 and 30.07.2021 are shown in sub figure a) to d), respectively.

280 3.2 | Wind Speed Analysis and Turbine Status Visualization

281 The plots shown in the following subsections are structured as follows: The upper section provides an overview of the wind speeds from aircraft
 282 measurements and simulations at the same coordinates behind the wind farm clusters N2, N3, and N4 (see Table 1 and Figure 1 for comparison).
 283 In addition to the wind speeds plotted along the flight path, the turbine statuses during the measurement period are also displayed. Black dots
 284 represent turbines for which no measurement data were available. Red dots indicate turbines that were not operational at the time of the mea-
 285 surements. Beige dots represent turbines operating within the power curve, while orange dots represent turbines that are curtailed (operating at
 286 less than 75 % capacity). The plot area below shows the measurement and model data of each flight leg again, depicted as lines for a more detailed
 287 comparison. The research aircraft's measurement results are represented by a gray line. For better comparison, a running average was calculated
 288 from these high-resolution data, depicted as a black line. Surrounding this line is a blue shadow indicating the measurement accuracy of the aircraft
 289 measurements. The colored lines represent the model results for each individual measurement leg and all models presented earlier.

290 The values calculated in the tables 8 to 11 represent the deviations of the model results from the flight measurements in the wake region and out-
 291 side in the free flow. To calculate the deviations, each flight leg was divided into up to 500 sections (depending on the leg length). The deviation
 292 between measurement data and model was then determined for each of these sections. The wind speeds shown in the table are the means of
 293 these individual calculations within the aforementioned regions.

294 The expected wake areas of each of the wind farm clusters is indicated by dashed and dotted lines in the lower plot panel. It is important to note
 295 that the length of the flight leg always starts at zero and does not reflect the position in geocoordinates.

296 3.2.1 | Measurement Flight - 14.07.2020

297 Figure 7 shows the measurement flight on 14.07.2020 between 1230 UTC and 1600 UTC. The flight data show significant reductions in wind speed
 298 behind clusters N2 and N3. On "Leg 1", which is located in the lee about 6km away from cluster N2, the measured wind speed drops from more than

299 7 m s^{-1} to almost 5 m s^{-1} . In the wake, EM-WRF provides the best agreement with the flight data (see Table 8). In the free flow, this model has
 300 the lowest agreement. WRF-WF and EM-LR overestimate the wind speed deficit in the wake. On the contrary, EM-BL and EM-TP underestimate
 301 the wake deficit, with the latter performing significantly better, having a deviation less than half the one of the former model. Outside the wake,
 302 the EM initialized with the free stream derived on the leg offer the best results, as no intrinsic gradients in the undisturbed flow existed.

303 "Leg 2" shows two clear minima in the flow speed, although this flight leg is located before the Godewind wind farms with its two clear peaks
 304 (markers 1 and 2). The lower minimum (marker 3) is located directly behind the NE wind farm. EM-BL and EM-TP overestimate the wind speed in
 305 the wake on this leg, while EM-LR overestimate the deficit behind NE wind farm but underestimate the wake of cluster N2. WRF-WF is agreeing
 306 better with the measurements, however the two deficit peaks are not so distinct. EM-WRF delivers the best results. Outside the wake, WRF-WF
 307 and EM-WRF underestimate the flow speed by almost 2 m s^{-1} .

308 "Leg 3" is located in the lee very close to wind farm cluster N3. This results in a clear deficit behind the northern and southern extensions of the
 309 GOW wind farms (markers 1 and 2). The significantly lower wind speed in the northern wake of only 3.5 m s^{-1} is striking, while the reduction in
 310 the southern wake is only down to 4.6 m s^{-1} . The best results are again provided by EM-WRF together with the mesoscale simulation from WRF-
 311 WF. It's interesting to observe, how the mesoscale model (WRF-WF), not resolving directly for the presence of the turbines tends to smooth out
 312 wake gradients connected to the wind farm layout, as again the two peaks of wake deficit are less distinct in WRF-WF than in EM-WRF.

313 EM-LR significantly overestimates the minima of the two wakes; the much less pronounced southern wake (marker 2) in particular is overesti-
 314 mated by around 2 m s^{-1} . EM-TP and EM-BL perform better in the south part of the leg, while they underestimate the velocity deficit of 1.5 m s^{-1}
 315 and 1.8 m s^{-1} , respectively, in the north part. Outside the wake, the wind speed is significantly underestimated by all models in the southern area.
 316

Table 8 Deviation of the model data from the flight data for each leg on the 14.07.2020, divided into the inner region (wake area) and the outer region.

flight_leg	WRF-WF		EM_BL		EM_WRF		EM_LR		EM_TP	
	Inner	Outer	Inner	Outer	Inner	Outer	Inner	Outer	Inner	Outer
1	0.47	0.71	0.62	0.33	0.31	1.09	0.55	0.33	0.27	0.33
2	0.65	0.91	1.20	0.45	0.67	0.74	0.39	0.45	0.75	0.45
3	0.65	0.92	0.46	0.88	0.78	0.96	1.05	0.57	0.49	0.74
4	1.35	0.93	1.33	0.39	1.65	1.31	0.67	0.41	1.08	0.24
5	0.82	0.86	1.01	0.56	0.87	1.16	0.72	0.81	0.88	0.63
6	1.28	1.16	0.62	0.49	2.05	2.52	0.62	0.48	0.62	0.49

317 The deficit is still clearly present on the flight legs "Leg 4" and "Leg 5", although the two wakes have almost merged and now only represent
 318 a single wake, which has shifted slightly to the north. The wind speed minimum on "Leg 4" is 3 m s^{-1} . On "Leg 5", the wind speed in the wake
 319 increases to just under 5 m s^{-1} . As the distance between the flight legs increases, an area of increased wind speed moves northwards from the
 320 area south of the measurement area. This is not fully captured by the models (compare Table 8). WRF-WF in particular underestimates the wind
 321 speed, although the mesoscale effects should be better modelled here. The wakes on "Leg 4" and "Leg 5" are only partially captured by the models.

322 EM-BL, EM-TP and EM-WRF overestimate the flow velocity up to around 3 m s^{-1} on "Leg 4" and $1.5 - 2 \text{ m/s}$ on "Leg 5" for the EM-BL that
 323 performs the worst in the comparison. EM-LR and WRF-WF capture a deficit more comparable to the measurements, but are still underestimating
 324 the peak by about 1 m s^{-1} . The EM also compute a shape of the wake different than the measurement. This could be the results of considering
 325 a straightline wake propagation, homogeneous across all the turbines. EM-WRF is supposed to improve the description of the wake propagation
 326 over standard engineering models. In this particular case, the shape of the defect is better understood by the EM-WRF. However, having the same
 327 wake model calibration of the EM-BL that largely underestimates the deficit observed by the measurements, it does provide the extent of the wake
 328 deficit suggested by the measurements.

329 "Leg 6" does not show a clear wake in the aircraft data. The area of increased wind speed (marker 4) has shifted further north and lost intensity. The
 330 EM-BL, EM-LR and EM-TP models calculate a deficit not where the cluster wake is expected, but only in the southernmost area of the measurement
 331 leg (marker 5). There, they better agree with the measured wind speed. WRF-WF and EM-WRF are particularly noticeable on this flight leg. With
 332 the exception of a small area, WRF-WF consistently delivers wind speeds that are too high. Although, the profile of the EM-WRF is similar to the
 333 course of the flight measurement, it calculates wind speeds of more than 9 m s^{-1} that are at maximum more than 5 m s^{-1} off the aircraft data.
 334 However, it's important to remind that EM-WRF results several Km downstream the clusters, like at Leg 6, are almost uniquely influenced by the

input flow field of WRF. Why both WRF-WF and WRF simulations determine significantly different results and with too high values on this flight leg it could not be clarified. This may be due to the influence of changes in the general weather situation or local effects like clouds in the vicinity.

From the previous comparison, we observe that as the distance to wind farm clusters increases, the quality of the model results decreases. This is also reflected in the speed deviations in Table 8. EM-LR tends to overestimate the deficit in the wake, especially in a closer range to the wind farms. EM-BL and EM-TP underestimate the deficit, with the latter having normally a smaller deviation, as the wake recovery is slower than the EM-BL.

3.2.2 | Measurement Flight - 23.07.2020

Figure 8 shows the measurement and model data from a flight on 23.07.2020 between 1200 UTC and 1530 UTC with southwesterly wind direction and wind speeds of 10 m s^{-1} (compare Table 6). The individual measurement legs show only a slight reduction of wind speed in the lee of the wind farms and wind farm clusters. This could be on one hand due to the wind direction and therefore less overlapping of wakes and on the other hand to a more effective wake recovery, which could be enhanced by a lower lapse rate above the turbines creating a stronger energy entrainment from the top of the waked area.

On 'Leg 1', the flight data shows two areas with reduced wind speeds of 8 and 8.5 m s^{-1} (markers 1 and 2). The southern minimum is more pronounced than the northern minimum, which is directly behind cluster N2 and should therefore have a much stronger deficit. The models forecast a wake with up to 3 m s^{-1} less wind speed for EM-BL and EM-TP in that area. The EM-LR model overestimates the reduction in wind speed even more at approximately 4 m s^{-1} . The WRF-WF and EM-WRF models provided the best results, with a difference of only 1.7 m s^{-1} from the aircraft measurement. This significant difference between the models can likely be attributed to mesoscale effects, which can only be accurately modelled by a mesoscale model such as WRF. In the undisturbed area at the southern end of the measurement section, all models produced results that were either within or just outside the measurement uncertainty of the aircraft measurement.

'Leg 2' demonstrates a comparable wind speed progression with a minor wake behind the 'NE' wind farm (marker 3). There is a small area of reduced wind speed further south (marker 4), but it is not situated in the lee of any of the wind farm clusters. The wind measurement also shows significantly lower fluctuations. The reason for this reduction is unclear, and the models do not support this trend. However, all models show the presence of a wake in the lee of 'NO', while the extent of cluster N3 and the expected wake are not discernible in the aircraft data (marker 3). In the northern area (marker 1), EM-LR overestimates the wake by almost 5 m s^{-1} , EM-TP by 3 m s^{-1} , and EM-BL by 2.5 m s^{-1} . EM-WRF and WRF-WF exhibit the best results with a deviation of 0.5 to 1 m s^{-1} .

Table 9 Deviation of the model data from the flight data for each leg on the 23.07.2020, divided into the inner region (wake area) and the outer region.

flight_leg	WRF-WF		EM_BL		EM_WRF		EM_LR		EM_TP	
	Inner	Outer	Inner	Outer	Inner	Outer	Inner	Outer	Inner	Outer
1	0.94	0.67	1.27	0.28	0.43	0.71	1.88	0.28	1.56	0.28
2	1.34	0.77	1.91	0.58	1.21	1.51	2.70	0.65	2.33	0.61
3	0.96	1.22	1.03	1.03	0.73	1.08	1.68	1.44	1.27	1.21
4	0.58	0.34	0.32	1.15	0.50	0.44	0.69	1.91	0.52	1.52
5	0.72	0.44	1.29	0.84	0.68	0.50	1.46	1.19	1.41	0.98
6	0.58	0.31	0.57	1.63	0.38	0.17	0.59	2.41	0.59	2.03
7	0.45	1.26	1.24	0.65	0.76	0.75	1.24	0.66	1.24	0.66
8	0.43	1.58	0.73	0.28	0.44	0.75	2.08	0.28	1.25	0.28

'Leg 3' is situated 4-5 km behind the northern extension of cluster N3 (marker 4). The flight measurement at this location shows a minimum wind speed of 9 m/s , with a significant increase in wind speed to the south of the wake. This is in contrast to the significant reduction observed on 'Leg 2' and could indicate an acceleration of the air masses to the south along the GOW I wind farm. This area is only partially covered by WRF-WF and EM-WRF. Both models capture the reduction in wind speed in the wake, but with some discrepancies. EM-BL overestimates the wake by around 1 m s^{-1} in the upper area, while EM-TP and EM-LR overestimate it by 1.5 and 3 m s^{-1} , respectively, in the northern area. There is still a clear wake at the northern end of the measuring leg according to the model data from EM-LR, EM-TP and EM-BL.

The measurement legs labelled 'Leg 4', 'Leg 5', and 'Leg 6' exhibit minimal change when compared to 'Leg 3'. In the flight data, the wake of cluster N3 dissipates relatively quickly, and the wind speed increases to almost 12 m s^{-1} . The WRF-WF and EM-WRF models determine the entire course

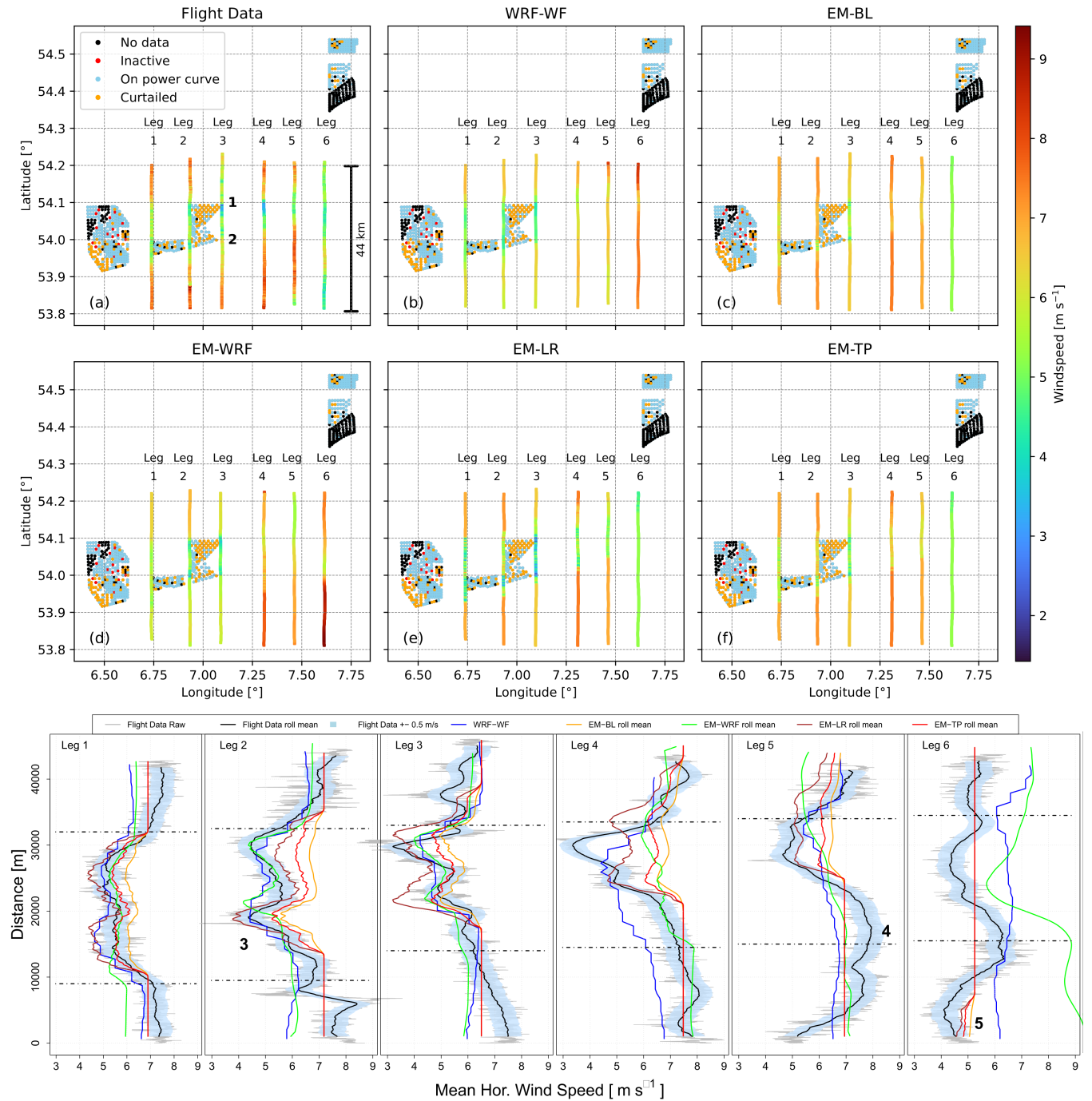


Figure 7 Top Part: The measurement area in the German Bight with the wind farm clusters N2, N3 and N4 on the 14.07.2020 between 1230 UTC and 1600 UTC. The dots represent the individual turbines and their status during the total measurement time. a) shows the results of the flight measurements on six flight legs with a mean wind direction of 270°. b), c), d), e) and f) show the results of the model calculations on the coordinates of the flight paths corresponding to WRF-WF, EM-BL, EM-WRF, EM-LR and EM-TP, respectively. The lower plot area shows the flight legs as line plots with running mean values for direct comparison. The dashed lines are the estimated wake area

368 of these legs, with only slight deviations, often less than 0.5 m s⁻¹ (see Table 9). EM-TP, EM-LR, and EM-BL still clearly identify the wake of cluster
 369 N3 and even cluster N2 (marker 5).

370 On Leg 7, located directly in front of cluster N4, wind speed increases to 12 m s⁻¹ in the uppermost area and decreases to below 8 m s⁻¹ in the
 371 southernmost area. WRF-WF and EM-WRF capture the scenario well, with very small deviations from the measurement. Table 9 shows the mean

372 deviations inside and outside the expected wake, where there is no longer a wake present and the entire area can be considered outside the wake.
 373 EM-TP and EM-LR continue to calculate a wake in the northern area of the flight leg, despite being more than 60 km away from cluster N2 (Table 2).
 374 The largest difference to the flight measurements are recorded in the EM-LR, in average around 3 m s^{-1} . EM-BL also simulates a slight reduction
 375 in wind speed in this area. These three models mentioned show no change in wind speed outside of the potential wake.
 376 "Leg 8" is located approximately 4-5 km behind the northern end of "AW" (marker 6). The wind measurements of the research aircraft show only a
 377 slight or no reduction in wind speed, similar to the measurements taken behind cluster N3. The WRF-WF and EM-WRF models slightly overestimate
 378 the wind speed along the flight leg by $0.5\text{-}1 \text{ m s}^{-1}$. The EM-TP and EM-LR models indicate a very strong wake of around 3.5 m s^{-1} at the minimum
 379 and a large lateral extent. EM-BL is more accurate, with a deviation in the wake range of approximately 1 m s^{-1} . All three methods provide results
 380 that do not deviate from the initialization speed below or above the wake, due to the large distance of these areas from an upstream wind farm.

3.2.3 | Measurement Flight - 27.07.2021

382 Figure 9 shows the measurement flight on 27.07.2021 between 1030 UTC and 1415 UTC with a south-westerly wind direction and wind speed
 383 of 10 m s^{-1} (compare table 6). On this day, the measurement paths between clusters N2 and N3 were omitted in order to also being able to carry
 384 out more measurements behind wind farm cluster N4 at different distances.

385 Accordingly, 'Leg 1' was flown 4 km behind cluster N3. A wake is clearly visible in the northern area (marker 1), as identified by the EM-BL,
 386 EM-TP, and EM-LR models. However, EM-LR overestimates the deficit by almost 3 m/s, EM-BL underestimates it by $0.5\text{-}1 \text{ m s}^{-1}$, while EM-TP
 387 reproduces accurately the measurements in the area (marker 1). WRF-WF and EM-WRF identify the minimum in the wake with a deviation of
 388 less than 0.5 m s^{-1} . However, both models are already 2 m s^{-1} below the measured wind speed of 10 m s^{-1} outside the wake. Outside the wake
 389 of cluster N3, WRF-WF and EM-BL deliver the best results in the upper part. EM-TP and EM-LR show a wind speed approximately 2 m s^{-1} and
 390 1 m s^{-1} , respectively, lower than the measured wind speed. The EM-WRF model calculates a wind speed of just under 6 m s^{-1} in the upper
 391 section of the measuring leg. The reason for the significant deviation of this model from the measurement in marker 2 is not entirely clear. One
 392 possible explanation is the course of WRF-WF, which also tends to have lower wind speeds and thus strongly affects the results of EM-WRF. It is
 393 unlikely that the calculated wake from cluster N2 is the cause, as otherwise the EM-BL model would also have shown a stronger wake deficit.

394 The flight legs "Leg 2", "Leg 3" and "Leg 4" show a very similar progression of wind speed with distance as already seen in "Leg 1". The wake is less
 395 pronounced in these measurements, but relatively constant at $7.5\text{-}8.2 \text{ m s}^{-1}$ with an undisturbed flow velocity of $10\text{-}12 \text{ m s}^{-1}$. EM-LR again
 396 shows a strong wake, which overestimates the measured one by about $1.5\text{-}2 \text{ m s}^{-1}$. EM-BL again overestimates the wind speed in the wake by
 397 around 1 m s^{-1} . On "Leg 4" and "Leg 5", EM-BL also shows almost no deviations from the initialisation speed. EM-TP performs consistently better
 398 than the previous models in reproducing the wake of N3. However, all the engineering models initialized with homogenous free-stream conditions
 399 underestimate the wind speed in the northerly undisturbed flow. WRF-WF does not manage to simulate the wake in any of the measurements
 400 on "Leg 2" to "Leg 4". Instead, an increased wind speed was determined in these areas (markers 3 and 4). Only on "Leg 5" are the results for the
 401 lower half of the measurement in the range of 0.5 m s^{-1} deviation from the measurements. In the upper part, the wind speed is underestimated
 402 by around 2 m s^{-1} .

403

Table 10 Deviation of the model data from the flight data for each leg on the 27.07.2021, divided into the inner region (wake area) and the outer region.

flight_leg	WRF-WF		EM_BL		EM_WRF		EM_LR		EM_TP	
	Inner	Outer	Inner	Outer	Inner	Outer	Inner	Outer	Inner	Outer
1	0.74	1.19	0.51	0.46	1.10	2.68	1.35	1.02	0.49	0.72
2	0.95	0.95	0.26	0.32	0.46	1.94	0.96	0.89	0.43	0.56
3	1.14	1.39	0.62	0.75	0.76	2.36	0.67	1.42	0.32	1.00
4	0.80	0.70	0.25	1.30	0.64	1.41	0.74	1.76	0.32	1.49
5	0.65	1.09	0.32	0.89	0.87	1.89	1.22	1.20	0.62	1.05
6	0.91	0.89	1.24	0.45	0.77	0.28	2.46	1.02	1.58	0.65
7	0.85	1.37	0.53	0.23	1.19	0.49	1.71	0.84	0.96	0.32
8	0.82	0.78	0.43	1.08	0.86	0.64	1.51	1.36	0.74	1.16
9	0.76	0.35	0.58	0.14	0.54	0.71	1.19	0.76	0.78	0.26

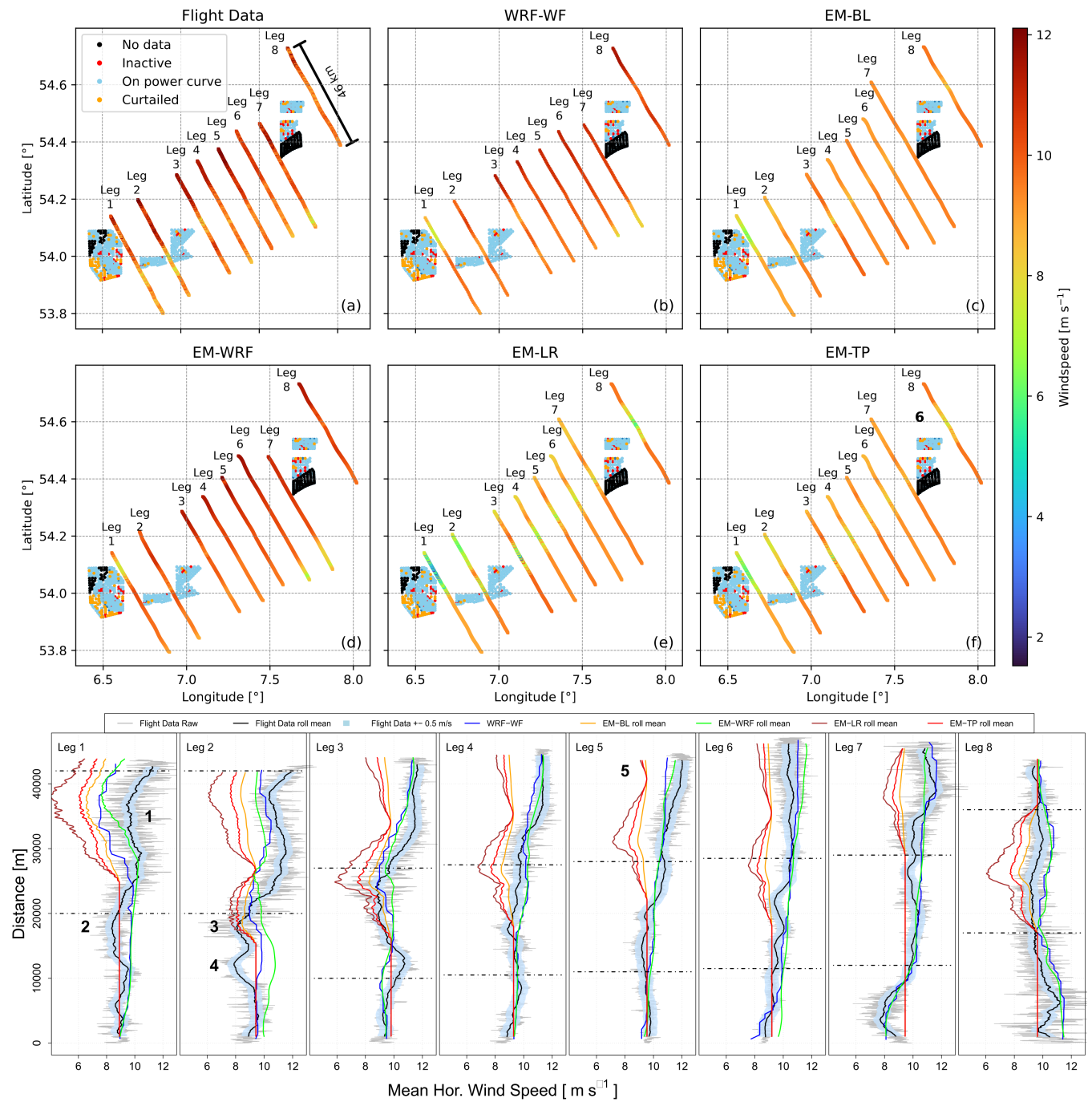


Figure 8 Top Part: The measurement area in the German Bight with the wind farm clusters N2, N3 and N4 on the 23.07.2020 between 1200 UTC and 1530 UTC. The dots represent the individual turbines and their status during the total measurement time. a) shows the results of the flight measurements on six flight legs with a mean wind direction of 230° . b), c), d), e) and f) show the results of the model calculations on the coordinates of the flight paths corresponding to WRF-WF, EM-BL, EM-WRF, EM-LR and EM-TP, respectively. The lower plot area shows the flight legs as line plots with running mean values for direct comparison. The dashed lines are the estimated wake area

404 "Leg 6" to "Leg 9" are located behind the wind farm cluster N4. Two clear wakes are recognisable on "Leg 6". These show a reduction in wind
 405 speed of 1 m s^{-1} (marker 5) and 1.5 m s^{-1} (marker 6). The wind speed is underestimated by EM-LR over the entire length of the measuring leg,
 406 and the deficit in the wake is overestimated. The other EM models and WRF-WF perform similarly and follow the course of the flight leg better,
 407 with a deviation of $0.3\text{-}1 \text{ m s}^{-1}$. WRF-WF also successfully simulates the measured wind speed with minimal deviation in the upper part of 'Leg 6'.

408 On the following measurement legs ("Leg 7", "Leg 8" and "Leg 9"), the wind speeds slowly recover and approach the undisturbed current. Flight
 409 data from 'Leg 7' still clearly shows the presence of two wakes. The models, with the exception of WRF-WF and EM-WRF, also predict wakes at
 410 the same positions. WRF-WF only detects the upper wake. At the height of the lower wake (marker 7), a wind speed that is too high is displayed,
 411 similar to what was observed during 'Leg 3'. The results of EM-WRF show a deviation of only around 2 m s^{-1} compared to the two wakes. However,
 412 EM-TP overestimates the deficit by $2\text{-}3 \text{ m s}^{-1}$. Leg 8 presents a similar picture, with EM-BL showing hardly any deviation from the initialisation
 413 speed. WRF-WF and EM-WRF are closer to the measured wind speed over the entire leg.
 414 "Leg 9" displays a small minimum in the upper leg area, which may no longer necessarily be the wake of cluster N4. WRF-WF, EM-WRF, and EM-BL
 415 produce comparable results to those of "Leg 8". However, EM-TP and EM-LR underestimate the wind speed by up to 2 m s^{-1} even at a distance
 416 of 30 km from cluster N4.
 417 For a more detailed breakdown of the deviations inside and outside the wake, please refer to the corresponding table 10.

418 3.2.4 | Measurement Flight - 30.07.2021

419 Figure 10 shows the measurement flight on 30.07.2021 between 0830 UTC and 1200 UTC with a south-westerly wind direction and wind speed
 420 of 10 m s^{-1} (compare table 6). This measurement flight is very comparable with the flight on 27.07.2021.
 421 The measurement on "Leg 1" shows a small deficit of 2.3 m s^{-1} in the southern area behind the northern extension of cluster N3. All models
 422 record this wake at the same point, with EM-BL showing very good results with deviations of less than 0.5 m s^{-1} both inside and outside the
 423 wake. EM-LR, instead largely overestimates the reduction in wind speed with a maximum deviation of around 2.5 m s^{-1} in the region of nearest
 424 to N3. EM-TP seats again in between these two models. WRF-WF and EM-WRF overestimate the wind speed in the leg by around 1 m/s , except
 425 for the southernmost part (marker 1).
 426 "Leg 2" presents results that are almost identical to those of "Leg 1". In this case, the simulation results of the EM-BL model are again the closest to
 427 the measurement data, EM-TP falls shortly behind, and EM-LR overestimate the deficit in the wake or underestimate the wind speed in general.
 428 Similarly, EM-WRF and WRF-WF overestimate the wind speed everywhere except for the southernmost part of the flight leg.
 429

Table 11 Deviation of the model data from the flight data for each leg on the 30.07.2021, divided into the inner region (wake area) and the outer region.

flight_leg	WRF-WF		EM_BL		EM_WRF		EM_LR		EM_TP	
	Inner	Outer	Inner	Outer	Inner	Outer	Inner	Outer	Inner	Outer
1	0.69	0.73	0.35	0.29	1.19	0.87	1.63	0.66	0.46	0.46
2	0.68	0.90	0.45	0.27	0.78	0.98	1.29	0.87	0.65	0.52
3	0.60	0.95	0.24	0.38	0.64	0.98	1.65	0.89	0.65	0.60
4	0.77	0.96	0.77	0.36	0.78	1.02	0.70	0.34	0.52	0.23
5.00	0.28	0.75	0.31	0.25	0.22	0.71	0.72	0.56	0.25	0.39
6	0.60	0.35	0.60	0.55	0.60	0.50	1.95	2.11	0.89	0.94
7	0.61	1.42	0.56	0.38	0.73	1.15	0.72	0.55	0.24	0.22
8	0.90	0.62	0.22	0.34	0.83	1.31	0.81	0.83	0.26	0.40
9	1.25	1.57	0.39	0.33	1.86	1.70	0.48	0.43	0.34	0.23

430 The measurement data on "Leg 3", "Leg 4" and "Leg 5" no longer show a clearly identifiable wake in the measurement data. On "Leg 3" and "Leg
 431 4", WRF-WF and EM-WRF follow the same pattern. On the lower part of the legs the speed is underestimated, on the upper part it is overesti-
 432 mated. EM-LR still sees pronounced wakes (markers 2 and 3), which are no longer present. However, on "Leg 4" and "Leg 5" the general wind speed
 433 is no longer so clearly underestimated. The model EM-BL delivers the results with the smallest deviations on all three flight legs (compare Table 11).
 434 "Leg 6" is situated directly behind the northern end of cluster N4, where "AW" wind farm is placed. The flow data shows two wakes, identified by
 435 markers 4 and 5. The more northerly wake is more pronounced, with a deficit of just over 2 m s^{-1} . In this measurement leg, all the models but
 436 EM-LR produce comparable results, with deviations in the wake of 0.6 m s^{-1} (TableTable 11). Outside the wake, the measurement data agrees
 437 very well, with differences of less than 1 m s^{-1} . Only EM-LR show a strong overestimation of approximately 2.5 m s^{-1} in the wake areas."
 438 On "Leg 7", "Leg 8" and "Leg 9", no clearly recognisable wakes can be identified. Although EM-BL, EM-TP and EM-LR still show wakes (markings
 439 6 and 7), these are not recognisable as such in the flight measurements. EM-BL performs the best on all three legs. WRF-WF and EM-WRF

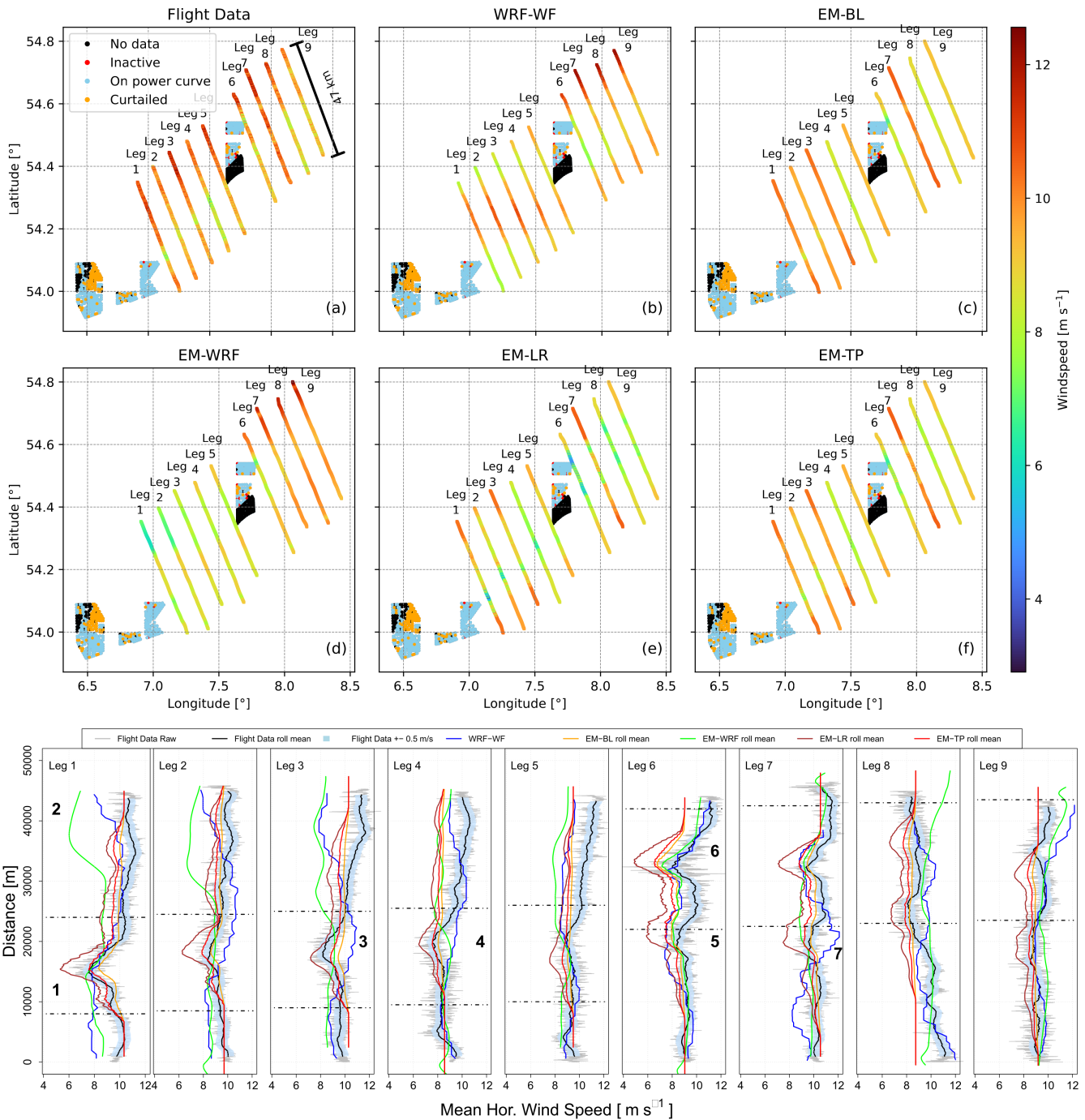


Figure 9 Top Part: The measurement area in the German Bight with the wind farm clusters N2, N3 and N4 on the 27.07.2021 between 1030 UTC and 1450 UTC. The dots represent the individual turbines and their status during the total measurement time. a) shows the results of the flight measurements on six flight legs with a mean wind direction of 230°. b), c), d), e) and f) show the results of the model calculations on the coordinates of the flight paths corresponding to WRF-WF, EM-BL, EM-WRF, EM-LR and EM-TP, respectively. The lower plot area shows the flight legs as line plots with running mean values for direct comparison. The dashed lines are the estimated wake area

440 underestimate the wind speed, except for a small part in the middle of "Leg 7".

441

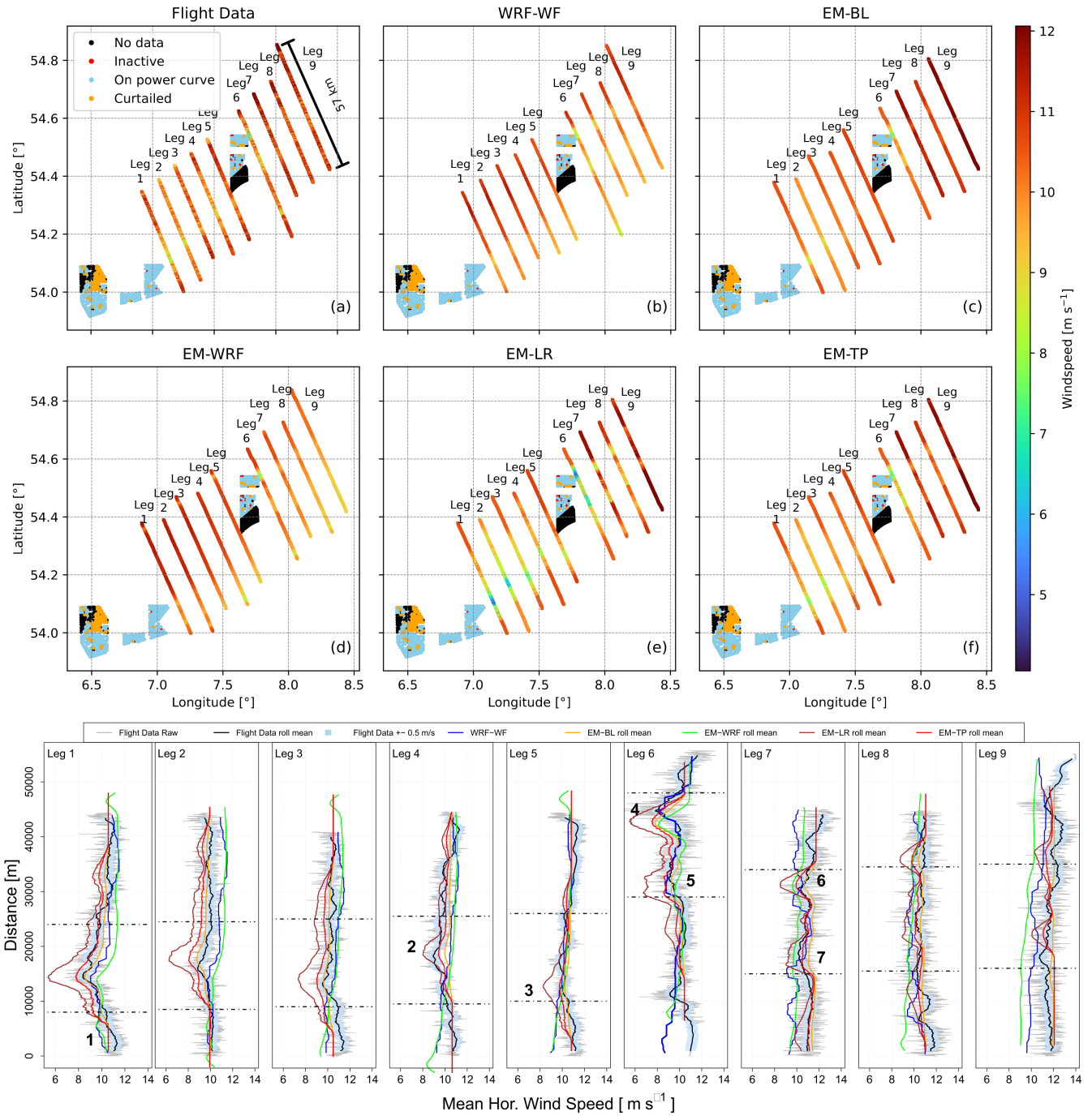


Figure 10 Top Part: The measurement area in the German Bight with the wind farm clusters N2, N3 and N4 on the 27.07.2021 between 1030 UTC and 1450 UTC. The dots represent the individual turbines and their status during the total measurement time. a) shows the results of the flight measurements on six flight legs with a mean wind direction of 230°. b), c), d), e) and f) show the results of the model calculations on the coordinates of the flight paths corresponding to WRF-WF, EM-BL, EM-WRF, EM-LR and EM-TP, respectively. The lower plot area shows the flight legs as line plots with running mean values for direct comparison. The dashed lines are the estimated wake area

4 | DISCUSSION

The procedure shown in this study is an innovative method to treat the SCADA data information that - to the knowledge of the authors - has not been attempted yet elsewhere. However, as simulations on the scale of multiple wind farm clusters are becoming normality in the planning of future scenarios, it's paramount to raise awareness and dedicate attention to the correct use of SCADA data.

4.1 | Wake Measurement

This subsection discusses the results of the aircraft measurements and the extent of the wakes during the four measurements in July 2020 and 2021. The measurements of the research aircraft of the project partner TU Braunschweig were performed behind the wind farm clusters N2, N3 and N4 (see Figure 1 and Figure 2) perpendicular to the wind in a meandering flight pattern. The distances between the individual flight legs were 10-20 km, and the shortest distances behind the wind farms were about 4-5 km. This made it possible to measure the particularly long wakes of more than 50 km in stable conditions^{28,6}.

Wind farm clusters N2, N3 and N4 are a collection of individual wind farms that together form large areas of wind energy production in the German Bight. Depending on their size, the distance between the individual wind turbines within a wind farm and their orientation, these clusters result in wakes of varying intensity. For example, measurements have shown that the deficit is greatest in the lee of the eastern extensions of GOW I and II and AW. In particular, the AW wind farm at the northern end of cluster N4 often shows the largest wind speed deficit in the wake due to the small distance between the turbines (see Figures 1 and 2).

Wakes were found on each of the four flights. The severity of the wind speed deficit and the length of the wakes were always different. While the flights on 14 July 2020 and 27 July 2021 showed clear wakes even at greater distances, the wakes in the same areas on the flights on 23 July 2020 and 30 July 2021 were much less pronounced and persistent. The 27 July 2021 flight even showed a wake extending from cluster N3 to the southern extensions of cluster N4. In other words, it extends over a distance of about 60 - 65 km. The wakes from cluster N2 are generally shorter than the wakes behind cluster N3, or there is no distinct wake at all in the measured data.

Although all flights were performed under stable atmospheric conditions^{57,58,7,30} (Table 7), the measured data did not always show wakes at the locations where they would have been expected. In the measurements on 23 July 2020, with the wind direction from the southwest and the prevailing atmospheric stability, one would have expected a clear wake behind cluster N2. This area (marker 1 on "Leg 1" in figure 8) shows a decrease in wind speed, but at 10 m s^{-1} it is higher than the area further south on the same flight leg (marker 2) at 8 m s^{-1} . However, this section of the leg is not behind a wind farm and should therefore have a higher wind speed. One might assume that most of the turbines in cluster N2 are shut down or curtailed, but this is not the case as can be seen from the turbine data in figure 8. It is difficult to identify a reason for the differences in the measured wind speeds. A possible explanation is the influence of the general weather situation or the coast, which causes generally lower wind speeds in the southern part of the measurement area. This area of lower wind speeds along all flight legs can be seen in both the flight measurement data and the WRF-WF simulation in Figure 8a) and b). This also highlights a problem with airborne measurements. In addition to the advantages of in-situ measurements, such as high temporal resolution over long distances or large areas, this type of measurement always represents a single point in time. To cover the large scales of the resulting wakes, each leg can only be measured 1-2 times. This leads to low statistical significance and makes comparisons with other measurement methods, and especially with model results, difficult. In addition to the low statistical significance, the long duration of a single measurement also causes problems. Several hours elapse between the start and end of the measurement flights analyzed in this study. This significant time difference between the measurement on the first and the last flight leg can extend over the change in atmospheric conditions due to synoptic events. This complicates the interpretation of the measurement results and should always be taken into account when analyzing the measurement data. On 14 July 2020 (Figure 7), the measured wind speed of $4\text{-}6.5 \text{ m s}^{-1}$ on "Leg 6" is significantly higher than the undisturbed flow at the beginning of the measurement flight on "Leg 1". There may have been a local change in weather conditions (e.g. due to the formation of rain clouds and the associated change in the wind field). These problems could be reduced by repeating the measurements on the same flight paths, but this always involves a loss of measurement area covered, or greatly increases the cost if several measurement aircraft are used.

4.2 | Model Evaluation

The engineering model FOXES in four different configurations as well as the WRF model with wind farm parameterization⁴⁴ were evaluated using the flight measurements. A direct comparison of the wind speed at the coordinates of each measurement leg showed the performance of the models in the near and far wake behind the mentioned wind farm cluster. Looking at the average deviations of each model from the flight data over all legs of all flights, EM-BL shows the smallest deviations in the wake of 0.69 m s^{-1} . EM-TP, EM-WRF, and WRF-WF perform similarly with 0.77 , 0.82 , and 0.79 m s^{-1} , respectively. EM-LR is the worst performer with wake wind speed deviations of 1.19 m s^{-1} . Looking at the area

488 outside the wake, EM-BL is again the best performers with deviations from the measured data of 0.57 m s^{-1} . EM-WRF is the worst performer
489 with a global deviation of 1.10 m s^{-1} . It should be noted that the wake areas are exemplary defined areas based on the extent of the wind farms
490 and the prevailing mean wind direction, which do not necessarily reflect the real wake area. Overall, this quantitative differences may not well
491 represent the level of fidelity of the models.

492 The EM-BL, EM-LR and EM-TP models perform better than WRF-WF and EM-WRF outside the wake in some cases because they are initialized
493 with the undisturbed flow and do not change on the more distant flight legs outside the wake. As a result, these three models can provide better
494 average values, while failing in modeling individual maxima and minima. Within the cluster wake, EM-BL is often found to underestimate the
495 extent of the wake deficit unless in the very near vicinity of the turbines ("Leg 1" on 27 July 2021 Figure 9). EM-LR almost always overestimate the
496 deficit. On the more distant legs, the model predicts can calculate a deficit larger than 2 m s^{-1} and sometimes up to 5 m s^{-1} what suggested by
497 the measurements. EM-TP across all the legs comparisons seems to offer the most balance calibration for describing the cluster wakes from few
498 hundreds of meters downstream the turbines till the very far wake. However, in internal testing not shown here for sake of clarity, we observed
499 that including the ground effect into the EM-BL achieves very similar results to the EM-TP in the cluster wake.

500 Considering the behavior of EM-WRF and WRF-WF in the cluster wake region, it is sometime possible to observe that modeling the wind farm
501 through an engineering model can provide a better trace of the wind farm layout effects. WRF-WF has also the tendency to smear sharp velocity
502 gradients in the horizontal plane, often failing in capturing the sharp minima in velocity observed on legs closer to the clusters outlet, e.g. "Leg
503 3" on 14 July 2020 Figure 7. However, in some situations and on some legs, EM-WRF produces model results that differ significantly from the
504 measured data and also from the other models. This is particularly noticeable on "Leg 6" on 14 July 2020, where the wind speed follows the
505 measurement, but with a large bias of more than 5 m s^{-1} (Figure 7 marker 5). Something similar can be seen on the first two flight legs "Leg 1"
506 and "Leg 2" on 27 July 2021. At marker 2 the wind speed is underestimated by about 5 m s^{-1} . WRF-WF, on the other hand, follows the measured
507 data with only a small deviation. The reason for these deviations from WRF-WF is unclear. It is possible to speculate, that the gradients imposed
508 in the wind field by the wakes instigate sufficient mixing to modify the wind fields of WRF-WF, with respect to the one of WRF, on the scale of
509 one transversal extension of the cluster wake to its sides. Furthermore, tests have shown that even small deviations in the time stamp of the WRF
510 data lead to sometimes significant changes in the course of the EM-WRF data. If the time shift of the WRF-WF data is changed, the results for
511 the EM-WRF data are in some cases better, but the WRF-WF data deviate significantly further. As the WRF-WF data are the basis, the time shift
512 was optimized for the WRF-WF data and used accordingly for EM-WRF and not vice versa.

513
514 For further tuning of the engineering models and a deeper understanding of how the models react to certain input parameters it would be
515 beneficial to compare the models against more measurement flights in variable conditions as well as having a detailed look into more SCADA data
516 and a comparison of this with engineering models.

517 5 | CONCLUSION

518 In this study, four measurement flights in July 2020, and July 2021 were used for comparison with the WRF-WF model and different setups of the
519 FOXES engineering model. The DO-128 Ibuf research aircraft of the TU Braunschweig was used to measure and evaluate the wind field in the
520 German Bight in front of and behind several wind farm clusters. The flights took place at 120 m aMSL in order to identify the wake as efficiently
521 as possible. It has already been shown that wakes can reach lengths of more than 70 km under stable atmospheric stratification²⁸. Van der Laan et
522 al.¹⁶ analyzed a RANS-based wind farm parameterization between wind farms off the south british coast with a distance of 26 km . However, the
523 use of engineering models (EM) for the validation of wakes longer than 30 km has not yet been attempted. Due to the actual field of application
524 of engineering models in the area of long-term prediction of the energy yield of a wind farm, they are rather unsuitable to accurately describe
525 wind farm wakes at single situations like the one collected by the flight measurement. Because of the ever-increasing expansion of wind energy
526 in the German Bight and the resulting overlapping of wakes, a simulation of the resulting effects on the power output is essential. For this to be
527 successful, the wake structure and length must be known.

528 The results have shown that engineering models and also lower resolution models such as WRF-WF can satisfactorily determine the wakes of
529 individual wind farms and wind farm clusters, but not consistently. In the range up to about 15 km downwind, the majority of the models predict
530 with fair accuracy the velocity deficit. However, the engineering model calibrated with a low wake recovery suffers from often overestimating the
531 cluster wake at this close range. For distances in the lee beyond this, the comparisons are also more difficult as evidence of the wake is not always
532 found in the measurements. The engineering model calibrated on a single wind farm (EM-BL) often predicts too little velocity deficit where the
533 measurements do suggest bigger deficits. In this cases, EM-TP and EM-LR are sometimes better. On the other hand, EM-LR also often overesti-
534 mates the deficit and predicts a deficit not sampled by the measurements. The engineering model driven by the mesoscale WRF model, EM-WRF,
535 overall gave comparable results to WRF-WF. In general, we believe that informing the EM with gradients in the flow field greatly improves their

536 predictions when applied on the scale of multiple wind farm clusters. As demonstrated by the fact that even calibrating the homogeneous inflow
537 for the EM-BL/LR/TP leg by leg a deviation comparable to the one of WRF can be observed outside the waked area.

538 A crucial point to be discussed when comparing EM to measurements over these large scales is the advection time. The air mass which the
539 aircraft flies through at the end of a flight measurement is not the same as the air mass which flows through the wind farm or wind farm cluster
540 at that moment. However, in addition to the condition of the individual turbines, this is exactly what is decisive for determining the wakes. By
541 calculating the air mass at the time and place of the measurement back to a time in the past when exactly this air mass flowed through the wind
542 farm, the quality of the model results increased significantly. Nevertheless, as the engineering models here used lack any type of dynamic wake
543 development, there are strong limits to further consider advection time.

- 545 • This study was able to show that engineering models with appropriate tuning can simulate wakes satisfactorily up to distances of up to
546 30 km behind wind farm clusters. However, at distances beyond this, the quality of the results drops rapidly.
- 547 • The synoptic influence of the large-scale weather situation or the effect of the coast has a great effect on the wakes and is clearly visible in
548 the measured data (Figure 8). A reduction in wind speed in the southern part of the measurement area, as was clearly visible on 23.07.2020,
549 makes it more difficult to identify the wake. This problem is also reflected in the model results. The models do not always manage to capture
550 the mesoscale changes in detail. Sometimes a wake is simulated where none is visible in the measured data, and sometimes no wake is
551 recorded where the measurement data shows one. Consequently, best results in such situations are provided by WRF-WF and the EM-WRF.

552 **Author Contributions** Both K.z.B. and G.C. wrote the manuscript and evaluated and prepared most of the figures. G.C. performed the EM simula-
553 tions. M.D. performed the WRF-WF simulations. All authors contributed intensively to an internal review. All authors have read and agreed to the
554 published version of the manuscript.

555 **Acknowledgements** We acknowledge support by PTJ (Projekträger Jülich), the Open Access Publication Fund of the University of Tübingen
556 and the BMWK (Federal Ministry for Economic Affairs and Climate Action) that funded the X-Wakes project (FKZ 03EE3008). The authors also
557 gratefully acknowledge the computing time granted by the North-German Supercomputing Alliance (HLRN) that have contributed to the research
558 results reported in this paper. For extensive technical support and providing the aircraft data, we want to thank the project partners from the TU
559 Braunschweig. We thank the wind farm operators Nordsee One, Ørsted, RWE Offshore Wind and Trianel Windpark Borkum for giving us access
560 to the wind farm production data for the specific flight dates. The alpha ventus SCADA data was made available by the RAVE (research at alpha
561 ventus) initiative, which was funded by the German Federal Ministry of Economic Affairs and Climate Action on the basis of a decision by the
562 German Bundestag and coordinated by Fraunhofer IWES (see: www.rave-offshore.de)

563 **Data Availability Statement** The dataset of raw data used during and/or analyzed during the current study is publicly available
564 on PANGAEA³³. The wind farm production data can not be made available. WRF <https://github.com/wrf-model/WRF> and FOXES
565 <https://github.com/FraunhoferIWES/foxes> are open-source models that can be downloaded from the respective repositories.

566 **Conflict-of-Interest Statement** All authors declare that they have no conflicts of interest.

570 References

- 571 1. Bojek P. Wind Electricity, <https://www.iea.org/reports/wind-electricity>. visited: 03-November-2022 2022.
- 572 2. Deutsche WindGuard GmbH . German Wind Energy in Numbers, <https://www.wind-energie.de/english/statistics/statistics-germany/>. visited:
573 03-November-2022 2022.
- 574 3. Deutsche WindGuard GmbH . Status des Offshore-Windenergieausbaus in Deutschland Erstes Halbjahr 2023, [https://www.windguard.de/id-1-halbjahr-2023.html?file=files/cto_layout/img/unternehmen/windenergiestatistik/2023/Halbjahr/Status%20des%20Offshore-
575 Windenergieausbaus_Halbjahr%202023.pdf](https://www.windguard.de/id-1-halbjahr-2023.html?file=files/cto_layout/img/unternehmen/windenergiestatistik/2023/Halbjahr/Status%20des%20Offshore-Windenergieausbaus_Halbjahr%202023.pdf). visited: 19-September-2023 2023.
- 576 4. Press and Information Office of the Federal Government . More wind energy at sea, <https://www.bundesregierung.de/breg-en/issues/offshore-wind-energy-act-2024112>. visited: 03-November-2022 2022.
- 577 5. Schneemann J, Rott A, Dörenkämper M, Steinfeld G, Kühn M. Cluster wakes impact on a far-distant offshore wind farm's power. *Wind Energy
578 Science* 2020; 5: 29-49. doi: 10.5194/wes-5-29-2020

- 581 6. Platis A, Bange J, Bärfuss K, et al. Long-range modifications of the wind field by offshore wind parks? results of the project WIPAFF.
582 *Meteorologische Zeitschrift* 2020; 29(5): 355-376. doi: 10.1127/metz/2020/1023
- 583 7. Cañadillas B, Foreman R, Barth V, et al. Offshore wind farm wake recovery: Airborne measurements and its representation in engineering
584 models. *Wind Energy* 2020; 23(5): 1249-1265. doi: <https://doi.org/10.1002/we.2484>
- 585 8. Barthelmie RJ, Jensen LE. Evaluation of wind farm efficiency and wind turbine wakes at the Nysted offshore wind farm. *Wind Energy* 2010;
586 13(6): 573-586. doi: <https://doi.org/10.1002/we.408>
- 587 9. Aitken ML, Banta RM, Pichugina YL, Lundquist JK. Quantifying Wind Turbine Wake Characteristics from Scanning Remote Sensor Data. *Journal*
588 *of Atmospheric and Oceanic Technology* 2014; 31(4): 765 - 787. doi: 10.1175/JTECH-D-13-00104.1
- 589 10. Trabucchi D, Trujillo JJ, Kühn K. Nacelle-based Lidar Measurements for the Calibration of a Wake Model at Different Offshore Operating
590 Conditions. *Energy Procedia* 2017; 137: 77-88. doi: <https://doi.org/10.1016/j.egypro.2017.10.335>
- 591 11. Bodini N, Zardi D, Lundquist JK. Three-dimensional structure of wind turbine wakes as measured by scanning lidar. *Atmospheric Measurement*
592 *Techniques* 2017; 10(8): 2881-2896. doi: 10.5194/amt-10-2881-2017
- 593 12. Carbajo Fuertes F, Markfort CD, Porté-Agel F. Wind Turbine Wake Characterization with Nacelle-Mounted Wind Lidars for Analytical Wake
594 Model Validation. *Remote Sensing* 2018; 10(5). doi: 10.3390/rs10050668
- 595 13. Nygaard NG, Newcombe AC. Wake behind an offshore wind farm observed with dual-Doppler radars. *Journal of Physics: Conference Series*
596 2018; 1037(7): 072008. doi: 10.1088/1742-6596/1037/7/072008
- 597 14. Hirth BD, Schroeder JL, Gunter WS, Guynes JG. Coupling Doppler radar-derived wind maps with operational turbine data to document wind
598 farm complex flows. *Wind Energy* 2015; 18(3): 529-540. doi: <https://doi.org/10.1002/we.1701>
- 599 15. Laan v. dMP, García-Santiago O, Kelly M, et al. A new RANS-based wind farm parameterization and inflow model for wind farm cluster
600 modeling. *Wind Energy Science* 2023; 8(5): 819-848. doi: 10.5194/wes-8-819-2023
- 601 16. Laan v. dMP, García-Santiago O, Sørensen NN, Troldborg N, Risco JC, Badger J. Simulating wake losses of the Danish Energy Island wind farm
602 cluster. *Journal of Physics: Conference Series* 2023; 2505(1): 012015. doi: 10.1088/1742-6596/2505/1/012015
- 603 17. Vollmer L, Steinfeld G, Kühn M. Transient LES of an offshore wind turbine. *Wind Energy Science* 2017; 2(2): 603-614. doi: 10.5194/wes-2-
604 603-2017
- 605 18. Maas O, Raasch S. Wake properties and power output of very large wind farms for different meteorological conditions and turbine spacings:
606 a large-eddy simulation case study for the German Bight. *Wind Energy Science* 2022; 7(2): 715-739. doi: 10.5194/wes-7-715-2022
- 607 19. Churchfield MJ, Lee S, Michalakes J, Moriarty PJ. A numerical study of the effects of atmospheric and wake turbulence on wind turbine
608 dynamics. *Journal of Turbulence* 2012; 13. doi: 10.1080/14685248.2012.668191
- 609 20. Abkar M, Porté-Agel F. Influence of atmospheric stability on wind-turbine wakes: A large-eddy simulation study. *Physics of Fluids* 2015; 27(3).
610 doi: 10.1063/1.4913695
- 611 21. Dörenkämper M, Witha B, Steinfeld G, Heinemann D, Kühn M. The impact of stable atmospheric boundary layers on wind-turbine wakes
612 within offshore wind farms. *Journal of Wind Engineering and Industrial Aerodynamics* 2015; 144: 146-153. doi: [https://doi.org/10.1016/j](https://doi.org/10.1016/j.jweia.2014.12.011)
613 [.jweia.2014.12.011](https://doi.org/10.1016/j.jweia.2014.12.011)
- 614 22. Lignarolo LE, Mehta D, Stevens RJ, et al. Validation of four LES and a vortex model against stereo-PIV measurements in the near wake of an
615 actuator disc and a wind turbine. *Renewable Energy* 2016; 94: 510-523. doi: <https://doi.org/10.1016/j.renene.2016.03.070>
- 616 23. Vollmer L, Steinfeld G, Heinemann D, Kühn M. Estimating the wake deflection downstream of a wind turbine in different atmospheric stabilities:
617 an LES study. *Wind Energy Science* 2016; 1(2): 129-141. doi: 10.5194/wes-1-129-2016
- 618 24. Ali K, Schultz DM, Revell A, Stallard T, Ouro P. Assessment of Five Wind-Farm Parameterizations in the Weather Research and Forecasting
619 Model: A Case Study of Wind Farms in the North Sea. *Monthly Weather Review* 2023; 151(9): 2333 - 2359. doi: 10.1175/MWR-D-23-0006.1

- 620 25. Fischereit J, Schaldemose Hansen K, Larsén XG, Laan v. dM, Réthoré PE, Murcia Leon JP. Comparing and validating intra-farm and farm-to-
621 farm wakes across different mesoscale and high-resolution wake models. *Wind Energy Science* 2022; 7(3): 1069–1091. doi: 10.5194/wes-7-
622 1069-2022
- 623 26. Djath B, Schulz-Stellenfleth J, Cañadillas B. Impact of atmospheric stability on X-band and C-band synthetic aperture radar imagery of offshore
624 windpark wakes. *Journal of Renewable and Sustainable Energy* 2018; 10(4). doi: 10.1063/1.5020437
- 625 27. Hasager CB, Vincent P, Badger J, et al. Using Satellite SAR to Characterize the Wind Flow around Offshore Wind Farms. *Energies* 2015; 8(6):
626 5413–5439. doi: 10.3390/en8065413
- 627 28. Platis A, Siedersleben SK, Bange J, et al. First in situ evidence of wakes in the far field behind offshore wind farms. *Scientific Reports* 2018; 8.
628 doi: 10.1038/s41598-018-20389-y
- 629 29. Christiansen MB, Hasager CB. Wake effects of large offshore wind farms identified from satellite SAR. *Remote Sensing of Environment* 2005;
630 98(2): 251-268. doi: <https://doi.org/10.1016/j.rse.2005.07.009>
- 631 30. Platis A, Hundhausen M, Lampert A, Emeis S, Bange J. The Role of Atmospheric Stability and Turbulence in Offshore Wind-Farm Wakes in the
632 German Bight. *Boundary Layer Meteorology* 2022; 182. doi: 10.1007/s10546-021-00668-4
- 633 31. Lee S, Vorobieff P, Poroseva S. Interaction of Wind Turbine Wakes under Various Atmospheric Conditions. *Energies* 2018; 11(6). doi:
634 10.3390/en11061442
- 635 32. Cañadillas B, Beckenbauer M, Trujillo JJ, et al. Offshore wind farm cluster wakes as observed by long-range-scanning wind lidar measurements
636 and mesoscale modeling. *Wind Energy Science* 2022; 7(3): 1241–1262. doi: 10.5194/wes-7-1241-2022
- 637 33. Rausch T, Bärfuss K, Hankers R, et al. In-situ airborne measurements of atmospheric and sea surface parameters related to offshore
638 wind parks in the German Bight, Flight 20210724_1427_cessna406. In: PANGAEA. 2023. In: Rausch, T et al. (2023): In-situ air-
639 borne measurements of atmospheric and sea surface parameters related to offshore wind parks in the German Bight. PANGAEA,
640 <https://doi.org/10.1594/PANGAEA.955382>
- 641 34. Lampert A, Bärfuss K, Platis A, et al. In situ airborne measurements of atmospheric and sea surface parameters related to offshore wind parks
642 in the German Bight. *Earth System Science Data* 2020; 12(2): 935–946. doi: 10.5194/essd-12-935-2020
- 643 35. Brümmer B, Kruspe G, Rump B, et al. Berichte aus dem Zentrum für Meeres- und Klimaforschung: Arktis 91 Report on the Field Phase with
644 Examples of Measurements.; 2012
- 645 36. Corsmeier U, Hankers R, Wieser A. Airborne turbulence measurements in the lower troposphere onboard the research aircraft Dornier 128-6,
646 D-IBUF. *Meteorologische Zeitschrift* 2001; 10(4): 315-329. doi: 10.1127/0941-2948/2001/0010-0315
- 647 37. Skamarock W, Klemp J, Dudhia J, et al. A description of the advanced research WRF version 3. Technical Report, 162 pages NCAR/TN-
648 556+STR, NCAR - National Center for Atmospheric Research; Boulder, Colorado, USA: 2019
- 649 38. Dörenkämper M, Optis M, Monahan A, G. S. On the Offshore Advection of Boundary-Layer Structures and the Influence on Offshore Wind
650 Conditions. *Boundary Layer Meteorology* 2015; 155. doi: 10.1007/s10546-015-0008-x
- 651 39. Dörenkämper M, Olsen BT, Witha B, et al. The Making of the New European Wind Atlas – Part 2: Production and Evaluation. *Geosci. Model*
652 *Dev.* 2020; 13: 5079–5102. doi: 10.5194/gmd-13-5079-2020
- 653 40. Hahmann AN, Sile T, Witha B, et al. The making of the New European Wind Atlas – Part 1: Model sensitivity. *Geoscientific Model Development*
654 2020; 13(10): 5053–5078. doi: 10.5194/gmd-13-5053-2020
- 655 41. Gottschall J, Dörenkämper M. Understanding and mitigating the impact of data gaps on offshore wind resource estimates. *Wind Energy Science*
656 2021; 6(2): 505–520. doi: 10.5194/wes-6-505-2021
- 657 42. Hersbach H, Bell B, Berrisford P, et al. The ERA5 global reanalysis. *Quarterly Journal of the Royal Meteorological Society* 2020; 146(730): 1999-
658 2049. doi: <https://doi.org/10.1002/qj.3803>
- 659 43. Donlon CJ, Martin M, Stark J, Roberts-Jones J, Fiedler E, Wimmer W. The Operational Sea Surface Temperature and Sea Ice Analysis (OS-
660 TIA) system. *Remote Sensing of Environment* 2012; 116: 140-158. Advanced Along Track Scanning Radiometer(AATSR) Special Issuedoi:
661 <https://doi.org/10.1016/j.rse.2010.10.017>

- 662 44. Fitch AC, Olson JB, Lundquist JK, et al. Local and Mesoscale Impacts of Wind Farms as Parameterized in a Mesoscale NWP Model. *Monthly*
663 *Weather Review* 2012; 140(9): 3017 - 3038. doi: 10.1175/MWR-D-11-00352.1
- 664 45. Press and Information Office of the Federal Government . WRF Model Physics Options and References. *visited: 22-September-2023* 2023.
- 665 46. Schmidt J, Vollmer L, Dörenkämper M, Stoevesandt B. FOXES: Farm Optimization and eXtended yield Evaluation Software. *Journal of Open*
666 *Source Software* 2023; 8(86): 5464. doi: 10.21105/joss.05464
- 667 47. Jensen N. A note on wind turbine interaction. *Riso-M-2411, Risoe National Laboratory, Roskilde, Denmark* 1983: 16.
- 668 48. Bastankhah M, Porté-Agel F. A new analytical model for wind-turbine wakes. *Renewable Energy* 2014; 70: 116–123. doi:
669 10.1016/j.renene.2014.01.002
- 670 49. Niayifar A, Porté-Agel F. A new analytical model for wind farm power prediction. *Journal of Physics: Conference Series* 2015; 625: 012039. doi:
671 10.1088/1742-6596/625/1/012039
- 672 50. Nygaard NG, Poulsen L, Svensson E, Pedersen JG. Large-scale benchmarking of wake models for offshore wind farms. *Journal of Physics:*
673 *Conference Series* 2022; 2265(2): 022008. doi: 10.1088/1742-6596/2265/2/022008
- 674 51. Bastankhah M, Porté-Agel F. Experimental and theoretical study of wind turbine wakes in yawed conditions. *Journal of Fluid Mechanics* 2016;
675 806: 506–541. doi: 10.1017/jfm.2016.595
- 676 52. Crespo A, Hernández J, Frandsen S. Survey of modelling methods for wind turbine wakes and wind farms. *Wind Energy* 1999; 2(1): 1–24. doi:
677 10.1002/(sici)1099-1824(199901/03)2:1<1::aid-we16>3.3.co;2-z
- 678 53. Brandis vA, Centurelli G, Schmidt J, Vollmer L, Djath B, Dörenkämper M. An investigation of spatial wind direction variability and its
679 consideration in engineering models. *Wind Energy Science* 2023; 8(4): 589–606. doi: 10.5194/wes-8-589-2023
- 680 54. Lissaman PB. Energy effectiveness of arbitrary arrays of wind turbines. *Journal of energy* 1979; 3(6): 323–328.
- 681 55. Pedersen JG, Svensson E, Poulsen L, Nygaard NG. Turbulence Optimized Park model with Gaussian wake profile. *Journal of Physics: Conference*
682 *Series* 2022; 2265(2): 022063. doi: 10.1088/1742-6596/2265/2/022063
- 683 56. Foreman RJ, Cañadillas B, Neumann T, Emeis S. Measurements of heat and humidity fluxes in the wake of offshore wind turbines. *Journal of*
684 *Renewable and Sustainable Energy* 2017; 9(5): 053304. doi: 10.1063/1.5003811
- 685 57. Emeis S. A simple analytical wind park model considering atmospheric stability. *Wind Energy* 2010; 13(5): 459-469. doi:
686 <https://doi.org/10.1002/we.367>
- 687 58. Nygaard NG, Newcombe AC. Wake behind an offshore wind farm observed with dual-Doppler radars. *Journal of Physics: Conference Series*
688 2018; 1037(7). doi: 10.1088/1742-6596/1037/7/072008